Developing Ecofriendly Nano-Particulate Adsorbents using Iron-Plant Polyphenols, Understanding the Molecular Properties and their Environmental Applications

Thesis submitted in partial fulfilment of the

requirements for the degree of

DOCTOR OF PHILOSOPHY

by

Jinat Aktar

(Roll No. 156152011)

Centre for the Environment

Indian Institute of Technology Guwahati

Guwahati-781039, Assam, India

April, 2022

Dedicated to my parents

…… Jinat Aktar

CENTRE FOR THE ENVIRONMENT

Indian Institute of Technology Guwahati

Guwahati – 781039, Assam, India

STATEMENT

I do hereby declare that the content embodied in this thesis entitled "Developing ecofriendly nano-particulate adsorbents using iron-plant polyphenols, understanding the molecular properties and their environmental applications" is the result of investigations carried out by me at me in the Centre for the Environment and Department of Chemistry, Indian Institute of Technology Guwahati, India under the supervision of Prof. Manabendra Ray, Department of Chemistry, and Prof. Saswati Chakraborty, Department of Civil Engineering, Indian Institute of Technology Guwahati, India.

In keeping with the general practice of reporting observations, due acknowledgements have been made wherever the work described is based on the findings of other investigations.

Date: Jinat Aktar

CERTIFICATE

This is to certify that the thesis entitled **"Developing ecofriendly nano-particulate adsorbents using iron-plant polyphenols, understanding the molecular properties and their environmental applications"** submitted by **Ms. Jinat Aktar (Roll No. 156152011)**, a research scholar in the Centre for the Environment, Indian Institute of Technology Guwahati, for the award of the degree of Doctor of Philosophy, is a record of the original research work carried out by her under my supervision and guidance. The thesis has fulfilled all requirements as per the regulations of the institute and, in my opinion, has reached the standard needed for submission. The work documented in this thesis has not been submitted to any other University or Institute for the award of any degree.

(Prof. Saswati Chakraborty)

Department of Civil Engineering

Indian Institute of Technology Guwahati

Guwahati - 781039, Assam, India

(Prof. Manabendra Ray)

Department of Chemistry

Indian Institute of Technology Guwahati

Guwahati - 781039, Assam, India

Acknowledgment

This Ph.D. thesis would not have been possible to complete without the help and support of many individuals associated directly or indirectly with the research work. It is my utmost pleasure to pen down these names and acknowledge them for their unconditional care and efforts.

At the very onset, I would like to extend my sincere sense of gratitude to my supervisor Prof. Saswati Chakraborty, Department of Civil Engineering, IIT Guwahati for letting me work independently and always being supportive in every step. I am grateful to my Co-supervisor Prof. Manabendra Ray Department of Chemistry for his continuous guidance, support, and motivation during my Ph.D. tenure at IIT Guwahati. Their immense help throughout has encouraged me to materialize the research ideas, which eventually led to the successful completion of this work. I am forever thankful to them for providing a very healthy and friendly working environment. I am glad to have worked under their supervision and will be forever grateful to them.

I am also thankful to my honorable doctoral committee members, Prof. Mohammad Jawed, Prof Sharad Gokhale, Prof. Animes Kr. Goldar, for providing highly valuable suggestions, relevant insights and thought-provoking ideas during the seminars that helped me to significantly improve my research work.

I am thankful to the Institute, Indian Institute of Technology Guwahati, for providing me with the state-of-the-art infrastructure and facilities for advanced research.

My sincere regards to all the technical and official staff, of Centre for the Environment, including Partha Pratim Bakal, Rajib Gogoi, Kaustav Rakshit, and Dr Deepmoni Deka. I would also like to thank Central Instruments Facility (CIF), IIT Guwahati, for providing me the facility of high-end and sophisticated instruments, which were necessary for this research work.

The financial support from Department of Science and Technology (DST)-INSPIRE, New Delhi is duly acknowledged.

I would like to thank my present group members, Tanmay Dutta, Sayanti Ghosh, L. Chan and Somnath Paik, for their timely help, support, and the wonderful time we shared during this period.

I would like to thank Atanu Kumar Paul, Dr. Chandan Mukherjee, Rajendra Adak, and Kaustav Banerjee for their help in my journey.

I would like to specially thank to Abhishek N Srivastava, Bidisha Buragohain, Sounak Bhattachariya, and Sana Gafar, for their constant support in my journey.

I also express my sincere thanks to my senior and junior members of Centre for the Environment Dr. Papu Kumar Naik, Rahul Verma, Dr. D Narendra Naik, Dr. Mothe Gopi Kiran, Rajasekhar Ravula, Sudeshna Gupta, Deepa Sachan, Dharitri Saikia, Pulakeswar Basumatary, Nidhi bharti, Dr. Smruti Ranjan Dash, Priyanka Adhikari.

I would like to thank my friends of IIT Guwahati for their constant support and care, Sushma Chakraborty, Dr. Himali Horo, Anupama Bora, Kajal Ingtipi, Nehal Zehra, Anjali Dahiya, Arnab Ghosh, Jaya Krishnan, Paulomi Bose, Poulami Dutta.

I would like to thank Dr. Anwesha Mahanta, ma'am, for all the positivity. I also thank Mandar da, Arunangsu, Abhra da, Sumon da. I also acknowledge the doctors and medical team of IIT Guwahati and Juri Deka for the care.

I also want to express my gratitude to my teachers, Prof. Apurba Ratan Ghosh and Prof. Naba Kumar Mondal, Department of Environmental Science, The University of Burdwan.

I extend my sincerest special thanks to my childhood friend Chinmayee Sain and Sukla Hazra for their support.

Last but not the least, I am forever grateful to all of my family members, especially to my Father (Sk Aktar Hossain), Mother (Atia Begum), Sisters (Wasifa Aktar and Rifa Aktar), Cousin (Asif Jalal), and Grandma (Anwara Begum) for their constant encouragements and moral supports during my research work.

.....Jinat Aktar

Abstract

Removing pollutants using adsorbents made from natural ingredients is an exciting proposition from the standpoint of their cost-effectiveness and safety. In this respect, materials from plant polyphenols and iron salts attracted our interest. Polyphenols are class of chemicals widely distributed in leaves, seeds, and other parts of plants. They are known for their health benefits and antioxidant properties. Iron is one of the common elements in earth crust and metalloenzymes. Iron(III) is known to bind strongly with catechol, which is part of polyphenols as well. Thus, understanding the chemical nature of material synthesized from plant polyphenols and iron would also be relevant to chemical science.

Chapter 1. Introduction and Literature Review

This chapter includes the literature on the green synthesis of nanoparticles and their environmental applications. Literature survey revealed that the chemistry of polyphenols with iron is multifaceted. Depending upon the pH, oxidation state of iron, metal-ligand ratio, and presence of oxygen, polyphenols can react in a number of different ways with metals, and the type of possible product also changes. Based on literature studies, the research gap, objectives of the thesis were defined.

Chapter 2. Synthesis and Characterization of Iron-Plant Polyphenol Complexes

Two iron(III) based new materials were synthesized from tannic acid (Mat-1) and guava leaf extract (Mat-2) in ~10 g scale under identical conditions (Scheme 1). The iron-polyphenol ratio would play a role in determining the type of complexation; the ratio was fixed at 1:1. To pursue this, the polyphenol content of guava leave extract was determined as the gallic acid equivalent using the Folin Ciocalteu reagents and calculated the iron salt necessary to maintain 1:1 ratio. On the other hand, tannic acid sourced from gall nut is an ester of 10 units of gallic acid with a central sugar unit. The iron: tannic acid was fixed at 10:1, which is equivalent to iron: gallic

acid unit of 1:1. With tannic acid, we have synthesized another material (Mat-3) with Fe(III) salt as starting material. This was used as a control. All the syntheses were performed at room temperature, and the final pH of the solutions 7, maintained using dilute NaOH. Materials were isolated after centrifugation for 5 min at 8000 rpm and stored over silica gel at 0-5° C. At these conditions, the materials do not change any of the properties for over a year.

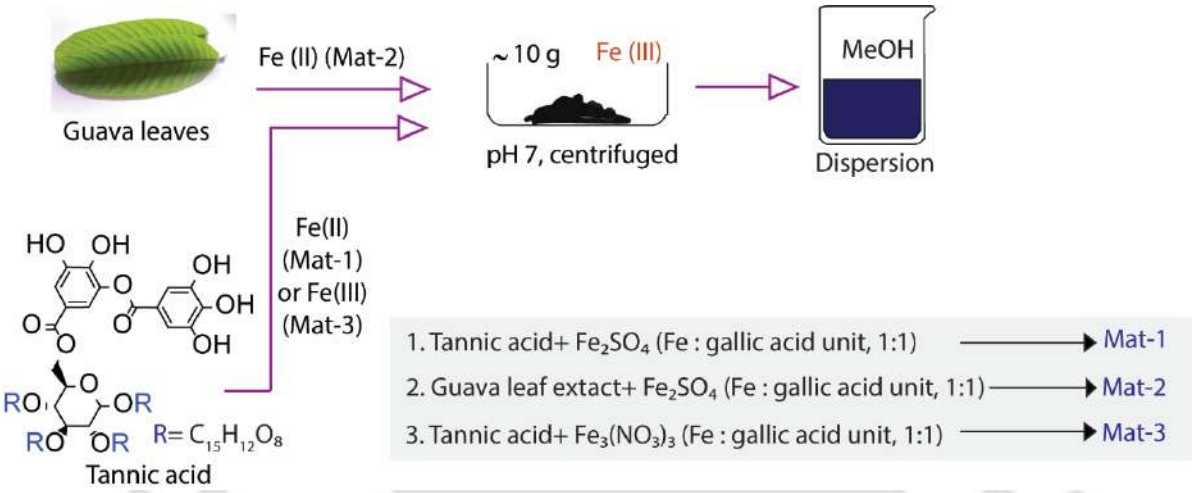

Scheme 1. The scheme of synthesis of Mat-1, Mat-2, and Mat-3.

The physical properties, surface properties, chemical properties of all three materials were analyzed using FESEM, FETEM, DLS, BET, pH_{zpc}, CHNS analysis, Magnetic susceptibilities, EPR, XPS, Mass analysis, TGA, PXRD, FTIR. The results of FESEM and TEM confirm the irregular-shaped particles of Mat-1 and Mat-2 within 20-100nm size range, present in an agglomerated form. The ESI mass spectra of tannic acid showed a sequential fragmentation pattern with successive loss of all 10 gallic acid units. MALDI mass spectra of tannic-iron complex (Mat-1) showed the loss of 205.5 mass units could be assigned to iron(III) bound to gallic acid. From the ESI mass spectra of guava extract, we identified multiple polyphenols (Figure 1a). Using isotopic abundance fitting, some of the peaks could be identified in MALDI mass spectra of oxo iron complexes (Figure 1b-f). Similar evidence of iron complex and oxo-

iron complex was found in corresponding tannic acid material (Mat-1) as well. Mat-3, synthesized from iron(III) and tannic acid, fragmented less under our experimental condition.

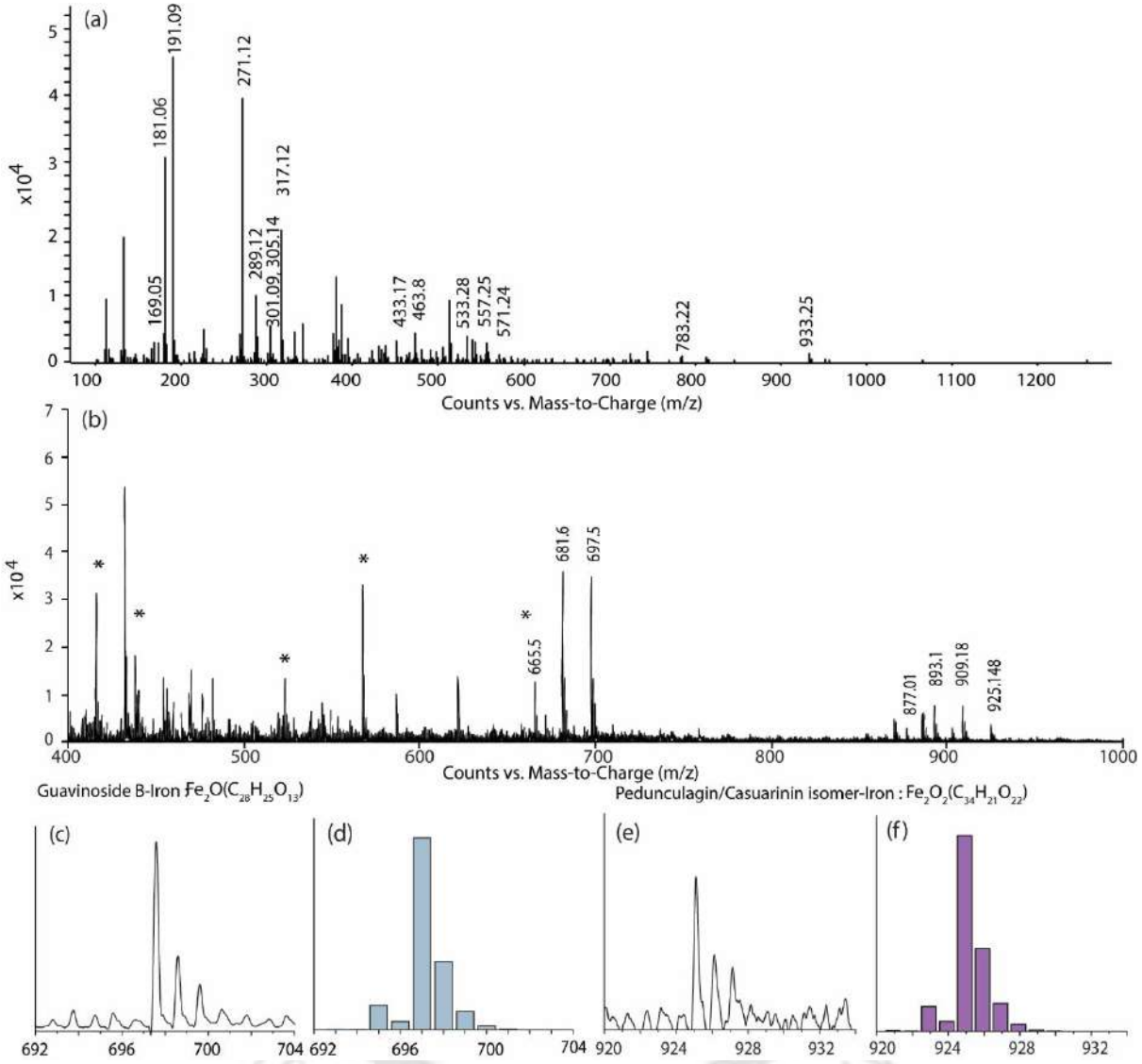

Figure 1. (a) ESI mass of guava leaf extract (b) MALDI mass analysis of Mat-2 in HCCA matrix, Observed and calculated isotopic distribution of Guavinoside b-Iron complex (c) and (d) and Pedunculagin/Casuarinin Iron complex (e) and (f) respectively.
(* Peak of matrix used in measurement)

The EPR spectra of all three materials at room temperature showed a characteristic peak for Fe (III). However, at lower temperatures, the signal for Mat-1 and Mat-2 reduced significantly. One plausible explanation for this is that Mat-1 and Mat-2 have antiferromagnetically coupled oxo-bridged iron(III) while Mat-3 has non-coupled iron(III) center. Magnetic susceptibility of

Mat-3 (6.8×10^{-5} cm^3 g^{-1}) is significantly higher than the other two ($1.6 – 2.1 \times 10^{-5}$ cm^3 g^{-1}). This also supports the presence of oxo-bridged iron(III) in Mat-1 and Mat-2 but not in Mat-3. The XPS spectra of both Mat-1 and Mat-2 showed the presence of Fe(III) as a major component with some iron(II). In Mat-3, Fe(III) form was present only.

Chapter 3. Methylene Blue Removal Using Materials Synthesized in Chapter 2

In this chapter, the dye removal property of Mat-1 and Mat-2 were investigated. Both the materials were tested on six different dyes, and a detailed study with methylene blue (MB) was carried out. Batch processes were carried out with different pH (2, 3, 4, 5, 7, 8); concentration of dye (1, 5, 10, 20, 40, 80, 150 mg/L); dose of adsorbent (0.5, 1, 2, 4 g/L) and time (5, 15, 30, 60, 120 min). Mat-1 and Mat-2 showed maximum adsorption capacities of 187 and 255 mg/g, respectively, at 150 mg/L of dye concentration (Figure 2a, 2b). Mat-2 reached equilibrium within 30 min with ~100% removal. The removal capacity of materials was also compared with commercially available activated charcoal. Mat-2 can match performance with activated charcoal even though these materials have 1/6 times surface area than activated carbon. Isotherm models (Figure 2c, 2d) and kinetic models are also applied to a better understanding of the mechanism. The desorption study was carried out using solvents and salts. Desorption is most effective with H-bond donor solvents methanol, and MB can act as H-bond acceptor at the imine N or charged S. In the presence of Na^+, K^+, Ca^{+2}, $Ba^{+2,}$ and Al^{+3} salts, with the higher charge, larger cations are increasingly more effective to displace dye from the adsorbent. The desorption study revealed that dye binding on adsorbents has a significant contribution from ionic interaction. The H-bonding, along with aromatic π–π interaction, as well contributed to adsorption.

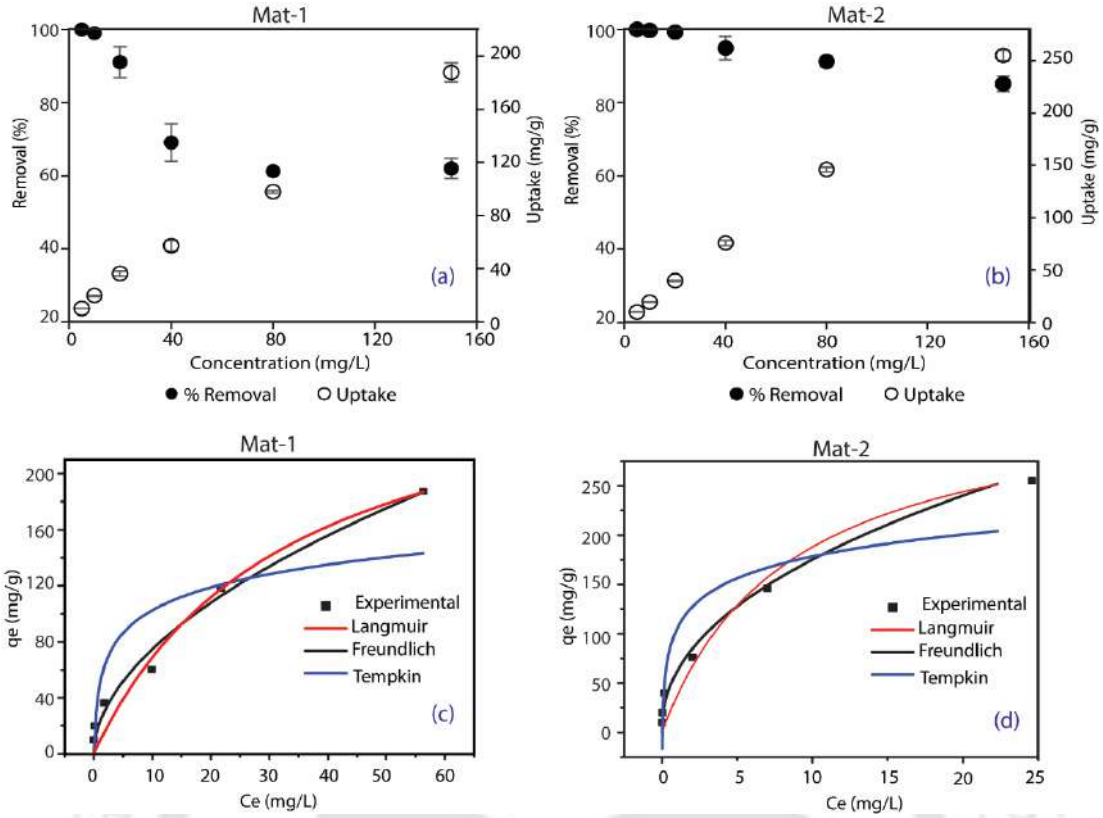

Figure 2. (a), (b) Effect of initial concentration on removal percentage and adsorption capacity of MB by Mat-1 and 2, respectively. (Conditions: C0=5-150 mg/L, pH= 7, Adsorbent dose=0.5g/L, rpm=250, t=60min). (c), (d) Isotherm plot of MB removal by Mat-1 and Mat-2, respectively.

Chapter 4. Bismarck brown dye removal capacity and cytotoxic effect

In this chapter, the removal capacity of Mat-1 and Mat-2 was investigated against another cationic dye, Bismarck brown (BB). It was reported that azo dyes were capable of showing carcinogenic nature and inducing genetic abnormalities. Since post-treated water will be used for different purposes, it is important to check the toxicity of the post-treated water due to the possibility of residual toxicity. This also aimed to investigate the toxic effect of BB dye on chromosomal level, using *A. cepa,* and also checked the reduction of toxicological impact post-treated dye solution with Mat-1 and Mat-2. Batch processes were executed with different concentration of dye (10, 20, 40, 80, 100, 200, 400 mg/L) (Figure 3a, 3b); dose of adsorbent (0.5, 1, 1.5, 2, 3 g/L) and time (5, 10, 15, 30, 60, 120 minutes). Both materials showed > 80%

removal of BB in a wide range of dye concentrations, from 20-400 mg/L with very high adsorption capacities of 652 mg/g and 680 mg/g of Mat-1 and Mat-2, respectively(Figure 3a, 3b). Isotherm and kinetic studies were also carried out for a better understanding of dye removal. The desorption of BB was carried out using methanol, followed by the adsorption process. With increasing cycle, the desorption percentage was also increased from 75% to 99% for Mat-1 and 71% to 86% for Mat-2 at 0.5g/L of material dose (Figure 3d).

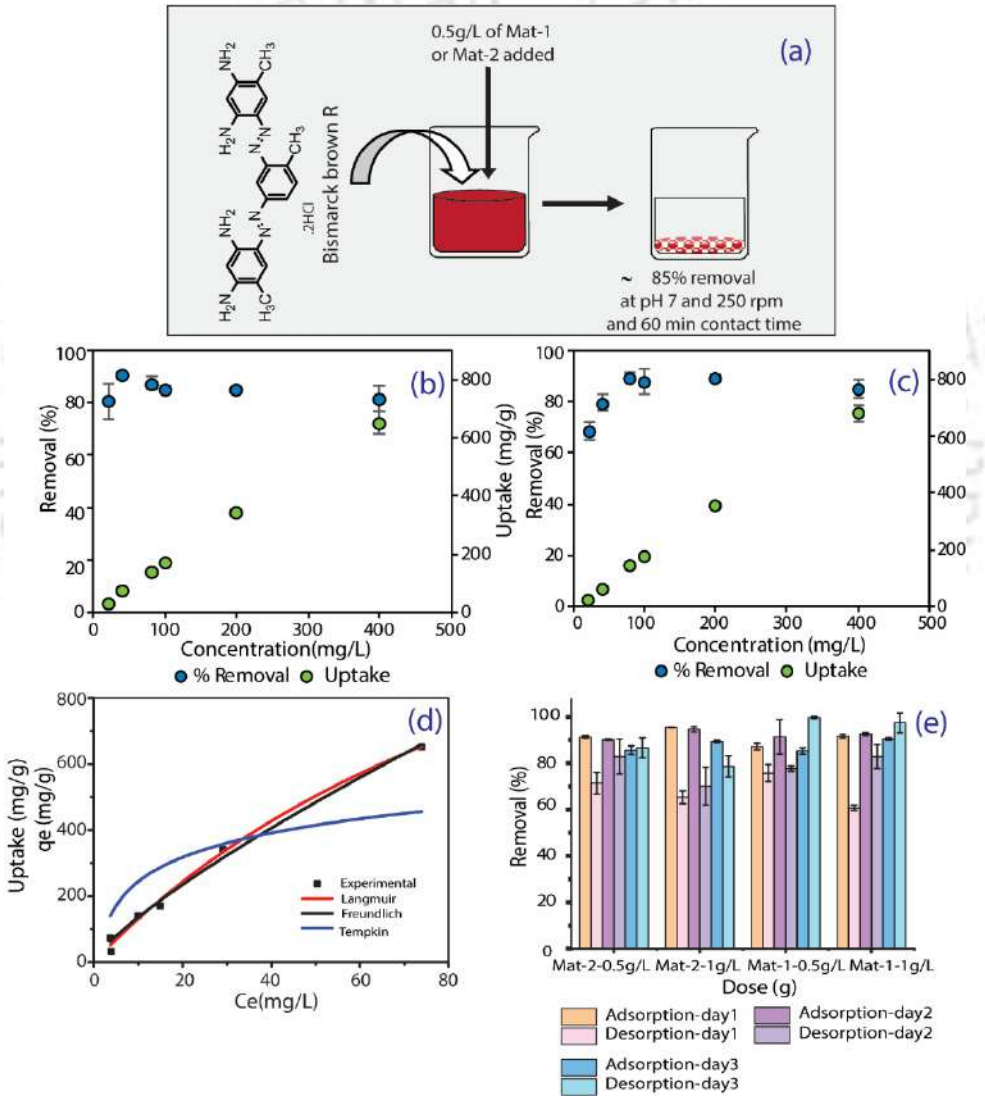

Figure 3. (a) Scheme of BB adsorption by Mat-1 and Mat-2 (b) BB removal by Mat-1 and (c) Mat-2 at different concentrations with the dose of 0.5 g/L,(d)Isotherm study of Mat-1, and (e) Adsorption-desorption study of Mat-1 and Mat-2.

To check the cytotoxic effect of BB dye, *A. cepa* was treated for five different treatments: one with distilled water, two with residual dye solution after removal by Mat-1 and Mat-2, and two with direct BB stock solution of 200 and 400 mg/L concentration. Mitotic index (MI) and chromosomal aberration were studied, and it was observed that the BB dye could cause cell and chromosomal deformations (Figure 4). However, BB solution after treatment of Mat-1 and Mat-2 did not show such negative effects in terms of MI or cell deformation (Figure 4a-d). With the increase of dye concentration, the change in cell structure, as well as elongated cells, was observed (Figure 4h). The direct application of BB dye at 200 and 400 mg/L of concentration, decreased mitotic stages, and cellular deformation were observed. (Figure 4h).

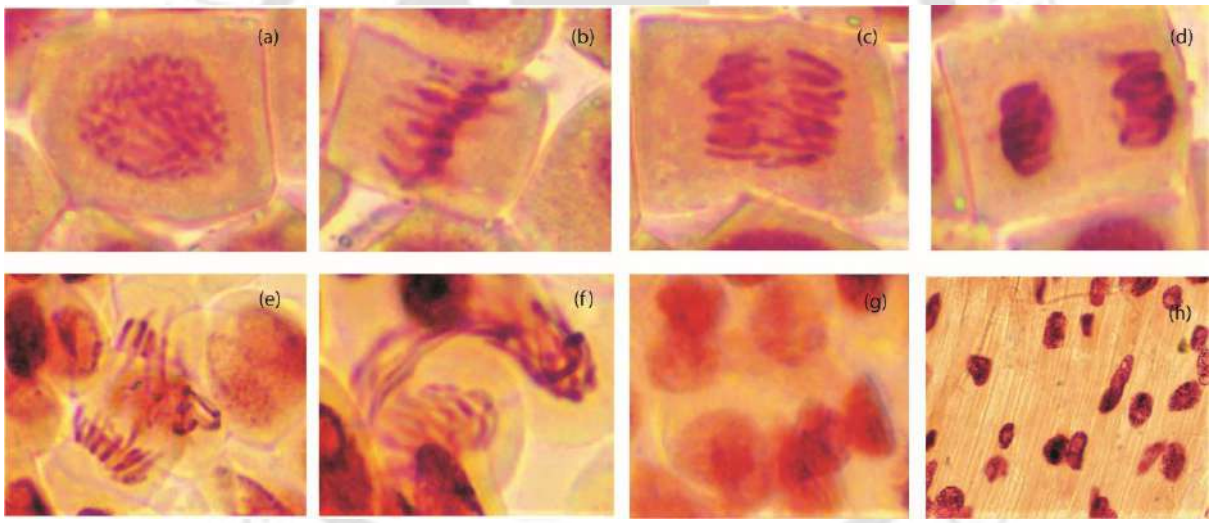

Figure 4. Chromosomal observation of *A. cepa* cell. (a) normal prophase; (b) normal metaphase; (c) normal anaphase; (d) normal telophase; (e) anaphase with chromosomal aberration in exposure of BB; (f) chromosomal deformation chromosomal aberration, (g) cellular agglomeration with cell wall degradation; and (h) cell elongation.

Chapter 5. Fluoride removal using Mat-1 and Mat-2

In the previous chapter, it was observed that both adsorbents were capable of removing cationic dyes from an aqueous solution at pH 7. Below pH_{zpc} values, materials can remove negatively charged ions like fluoride as the material's surfaces are positively charged. We choose fluoride

as adsorbate in this chapter to check the removal capability of Mat-1 and Mt-2. The fluoride concentration in the solution was measured using Ion-Selective Electrode (ISE). Batch processes were carried out at different pH, concentrations, dose, and contact times. Adsorption isotherm, kinetics, and desorption studies were also investigated. Both materials showed ~70% removal of 10 mg/L of fluoride concentration at pH 2 and 1h of contact time. With increasing dose, the removal increased, and decrease of uptake was observed (Figure 5a, 5b). The maximum fluoride uptake capacities of Mat-1 and Mat-2 were 12.3 and 7.5 mg/g at 40 mg/L of fluoride concentration. (Figure 5a, 5b). For authentication of the Mat-1 and Mat-2 on fluoride removal capacity, all of the materials were applied to real fluoride contaminated water from 15 sites in Guwahati, Assam.

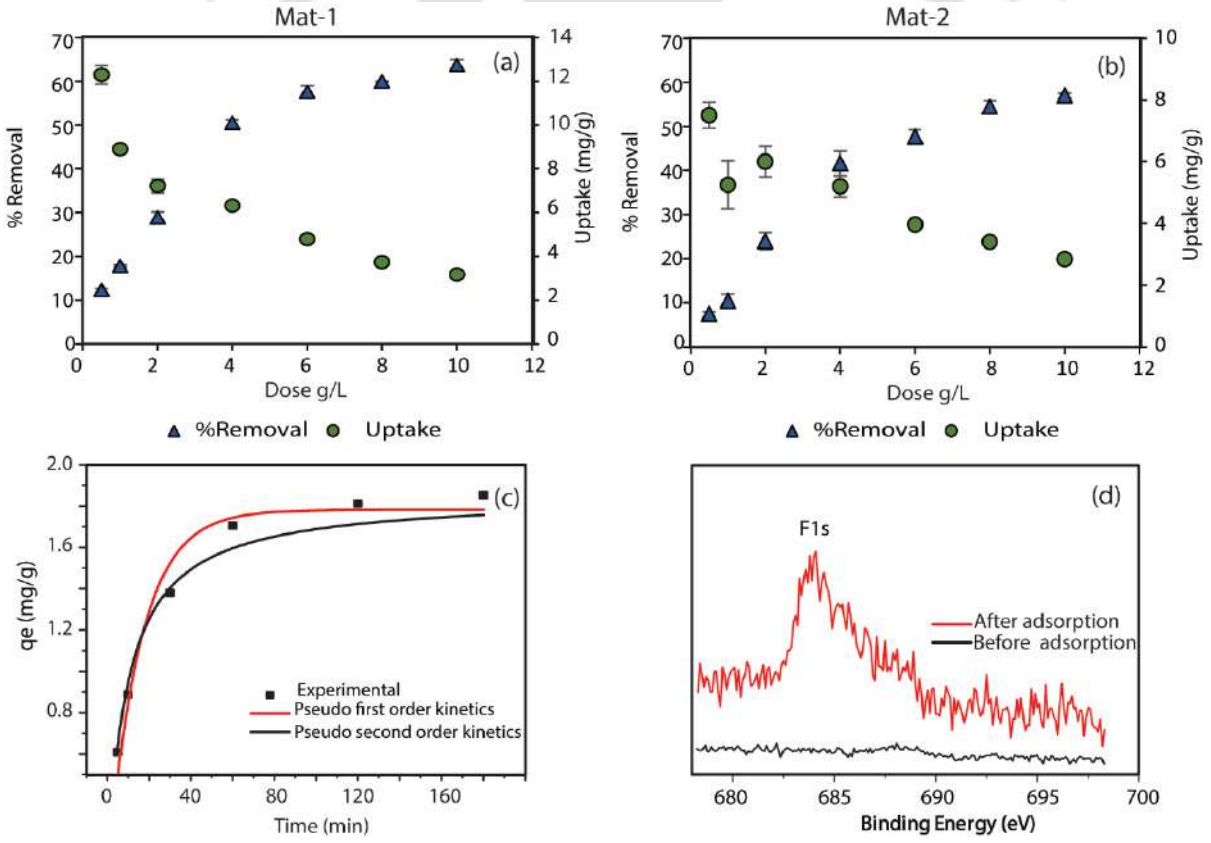

Figure 5. Effect of (a) Mat-1 and (b) Mat-2 dose on fluoride removal at pH 2, 1h contact time, (c) Kinetics of Mat-1, and (d) XPS spectra (F1s) of Mat-1 before and after adsorption.

Among them, six sites were identified as fluoride contaminated sites. Samples of 4 contained fluoride site were reached below the WHO recommended permissible limit (1.5 mg/L) with 2

g/L dose of Mat-1 and Mat-2 with a contact time of 1 h. After increasing the dose to 4 g/L, the rest two samples also reached within the permissible limit. After the removal process, the fluoride adsorbed samples were further analyzed, and the presence of fluoride was confirmed by XPS (Figure 5d) and EDS spectra.

Chapter 6. In Vitro Investigation of Mat-1 and Mat-2 on Physio-Chemical Responses in *Vigna radiata* and Antimicrobial Activity Against Pathogenic Bacteria

In this chapter, the biosafety of Mat-1 and Mat-2 was checked on mung beans (*Vigna radiata*) and bacteria. The seed germination, seedling morphology, microscopic study, membrane stability, biochemical parameters (chlorophyll, carotenoid, proline, polyphenol) were analyzed to investigate the phytotoxicity of Mat-1, Mat-2, and tannic acid on mung bean (*Vigna radiata*). This chapter also highlights the antibacterial characteristics of materials in terms of minimum inhibitory concentrations (REMA method) and zone of inhibition (disc diffusion) on eight disease-causing bacteria. This study contributed to the utilization of iron polyphenol complexes in agriculture and the assessment of environmental safety.

Results showed the increase in root-shoot length, biomass, productivity in Mat-1 and Mat-2 treated plants signified the positive impact of iron-polyphenol complexes on plants. In addition, the microscopic view showed no deformation in the epidermis, cortex, peri circle, xylem, and phloem in Mat-1 and Mat-2 treated plants (Figure 6). However, tannic acid-treated plants showed increased stress, decreased growth, and changes in physiological and biological parameters, which eventually affect plant health. The microscopic view of the root section showed deformation of the xylem and phloem, and aggregated form of xylem-phloem was observed (Figure 6).

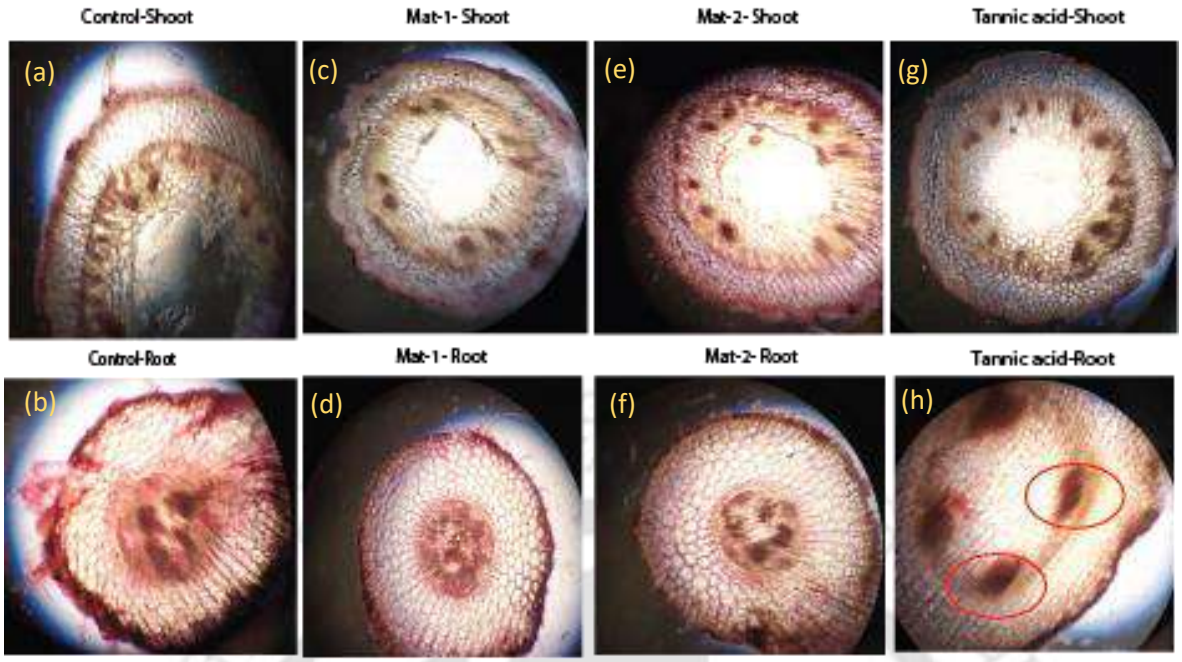

Figure 6. Transverse section of shoots and roots of (a), (b)control, (c), (d) Mat-1, (e),(f) Mat-2 and (g), (h) TA treated plants.

On the other side, after the complexation with iron, i.e., iron-tannic acid complex (Mat-1) changes the whole behavioral pattern with *Vigna radiata*, it reduces the stress level and increases the productivity of plants.

The antimicrobial property was checked against four Gram-positive and four Gram-negative bacteria (Table 1). In REMA method, all materials (Mat-1, Mat-2, tannic acid) showed antimicrobial activity against all eight disease-causing bacteria. In contrast, tannic acid showed better results in some bacteria (Table 1). The disc diffusion method did not fit well in our case as the materials were partially dispersible in nature.

Table 1. The minimum inhibitory concentration and zone of inhibition of materials against eight bacteria.

Bacteria	MIC (mg/mL)			ZOI (mm)		
	Tannic	Mat -1	Mat -2	Tannic	Mat -1	Mat -2
Gram-negative bacteria						
Escherichia coli	0.39	6.25	3.13	20	14	13
Klebsiella pneumoniae	3.13	6.25	6.25	19	-	-
Enterococcus aerogenes	3.13	6.25	6.25	23	9	9
Pseudomonas aeruginosa	0.39	6.25	6.25	17	-	-
Gram-positive bacteria						
Micrococcus luteus	0.39	6.25	6.25	19	-	-
Staphylococcus aureus	6.25	3.13	3.13	22	9	9
Staphylococcus epidermidis	6.25	6.25	6.25	22	12	9
Bacillus subtilis	0.39	6.25	3.13	17	-	-

Results suggested that Mat-1 showed inhibition against *Staphylococcus aureus* at the dose of 3.13 mg/mL with 9 mm of ZOI, while with the higher dose of 6.25 mg/mL, it showed the ZOI of 14 mm against *E. coli*. Mat-2 showed inhibition against *E. coli*, *Staphylococcus aureus*, and *Bacillus subtilis* with the dose of 3.13 mg/mL and exhibited the ZOI of 13, 9, 9 mm, respectively.

Contents

List of Table *Page no.*

List of Figure *Page no.*

List of Scheme ***Page no.***

Nomenclature

Symbols/ Abbreviations	Brief Description
°	Degree
λ	Lambda
%	Percent
±	Plus-minus
Δ	Delta
mM	Millimolar
nm	Nanometer
mm	Millimeter
cm^{-1}	Wave number
mL	Microliter
L	Litre
pH	Potential of Hydrogen
c	Concentration
mg	Milligram
g	Gram
mg/L	Milligram/Litre
w/w	Weight/weight
v/v	Volume/volume
wt%	Weight percent
s	Second
min	Minutes
h	Hours
A	Absorbance
% T	Transmittance
rpm	Rotation per minute
pHzpc	pH of zero-point charge
NPs	Nanoparticles
TA	Tannic Acid
GA	Gallic acid
HCCA	α-Cyano-4-hydroxycinnamic acid
MB	Methylene Blue
BB	Bismarck brown R

F	Fluoride
Chl-a	Chlorophyll-a
Chl-b	Chlorophyll-b
EDS	Energy-Dispersive X-Ray Spectroscopy
FTIR	Fourier Transform Infrared Sepctroscopy
FESEM	Field Emission Scanning Electron Microscopy
FETEM	Field Emission Transmission Electron Microscopy
TGA	Thermogravimetric Analysis
BET	Brunauer–Emmett–Teller
XPS	X-ray photoelectron spectroscopy
EPR	Electron paramagnetic resonance
XRD	X-Ray Diffraction Analysis
DLS	Dynamic light scattering
ESI	Electrospray ionization
MALDI	Matrix-assisted laser desorption/ionization
REMA	Resazurin microtitre assay
MIC	Minimum Inhibitory Concentration
ZOI	Zone of Inhibition

Chapter I

Introduction and Literature Review

1.1. Overview

In the twenty-first century, the world's population is confronted with serious water quality challenges. Despite the fact that water is the most vital natural resource, just 1% of it is suitable for human use [1]. Approximately 1.1 billion people do not have access to safe drinking water, according to the World Health Organization (WHO, 2015). The water issue is exacerbated by poor water management, the generation of a massive volume of hazardous waste, and its improper disposal [2]. The inevitability of wastewater treatment reinforces the need to develop sustainable treatment options. Pollutants released in wastewaters can be hazardous to aquatic life and able to change the condition of the aquatic ecosystem [3]. Various approaches for purifying wastewater have been developed, such as sedimentation, membrane filtration, flotation, precipitation, adsorption, ion exchange coagulation, oxidation, etc. [4–6]. Among them, adsorption is a much simpler and attractive procedure in comparison to other methods due to its high efficiency and ease of handling. Besides, it shows good efficiency in low concentrations of pollutants. Traditional methods for removing contaminants from wastewater are not cost-effective, particularly at low pollutant concentrations [7]. Moreover, adsorption has also been in practice for decades in the treatment of wastewater from distinct sources [8–10]. Additional benefits include the recovery of pure metal for recycling and the reuse of the adsorbent [11]. However, conventional adsorbents are chemically modified, susceptible to secondary effects, and expensive. Therefore, in the current scenario, there is an obvious need for sustainable, cost-effective, energy-efficient, and green adsorbent. My research is an attempt towards contributing to the water treatment process using eco-friendly efficient bioadsorbant.

Adsorption by biomaterials, commonly known as biosorption, is a popular approach where different parts of plants, dry leaves, shoot powder, barks, agricultural wastes, fruit shells, and a variety of other biological materials have all been investigated over the years (Table 1.1). Bioadsorbents have been the subject of a recent flurry of research articles due to their simple process, biodegradability, low cost, nontoxic, ecofriendly, and year-round availability. Some of the selected bioabsorbents used for the removal of different kinds of pollutants from wastewater are enlisted in the following table.

Table 1.1. Selected list of different bio-adsorbent used in pollutant removal.

Adsorbent	**Pollutant**	**References**
Rice hull ash	Lead (II)	[12]
NaOH treated rice husk	Malachite green	[13]
Wheat bran	Chromium (VI)	[8]
Ocimum americanum L. seed pods	Chromium (VI)	[14]
Aegle marmelos correa (Bael fruit)	Chromium (VI)	[15]
Okra, pumpkin, grape, and squash	Copper ions	[16]
Sugarcane bagasse	Cu^{2+}, $Cd^{2+,}$ and Pb^{2+}	[9]
Sugarcane bagasse	Rhodamine B (RhB) and Basic Blue 9	[17]
Iron oxyhydroxide NP coated rice husk	Fluoride	[18]
Azadirachta indica (Neem)	Lead (II)	[19]
Rambutan peel based activated carbon	Remazol Brilliant Blue R	[20]
Phoenix tree leaf powder	Methylene blue	[21]
Pea peels	Bismarck brown	[22]
Coconut husk	Mercury (Hg^0)	[23]
Activated carbon from coconut coil	Methylene blue	[24]
Eichhornia crassipes (Water hyacinth)	Phosphorus	[25]
Water hyacinth was modified by citric acid	Ni (II), Cu (II), and Cr (VI)	[26]
Bamboo dust carbon	Methylene blue	[27]
Tea extract mediated nanoparticles	Malachite green, rhodamine B	[28]

It can be concluded from the above table that different parts of plants, different agro-waste, water hyacinth, etc., in dry or powder form, in some modified form, after converting in charcoal were used for adsorption of different heavy metals, dyes, and other pollutants present in wastewater. However, in many literature activated charcoal from different biomaterials were used for water treatment purposes but, energy consumption and air pollution is an adverse side of it.

The use of biomaterial's extract and different precursor salts for the synthesis of different metal-ligand complexes is another well-known area of study regarding environmental application and environmental chemistry.

The presence of polyphenol in different parts of plants like root [29], shoot, leaves, seed [30], bulk, etc., acts as a ligand and makes complexation in the presence of different precursor metal salts. The specific components that cause plant-mediated metal complex synthesis and the mechanism of action are still unknown. Different secondary metabolites such as flavonoids, polyphenols, terpenoids, and heterocyclic compounds have been suggested to react with metal salts and produce plant mediated-metal complex [31,32]. Different polyphenols like moin, hyprine, flavonone, naringenin, gallic acid, ellagic acid, etc., present in plant extracts are soluble in water, and some organic solvents react with precursor iron salt solutions (Figure 1.1).

Polyphenols are chemically interesting due to their redox activity, which is the origin of their function as an antioxidant. Polyphenols are structurally diverse, and their reactivity depends on pH. The size distribution of these synthesized materials usually belongs within nano ranges [28,33,34]. Due to their high surface-to-volume ratio, nanoparticles are well known for their application in water treatment.

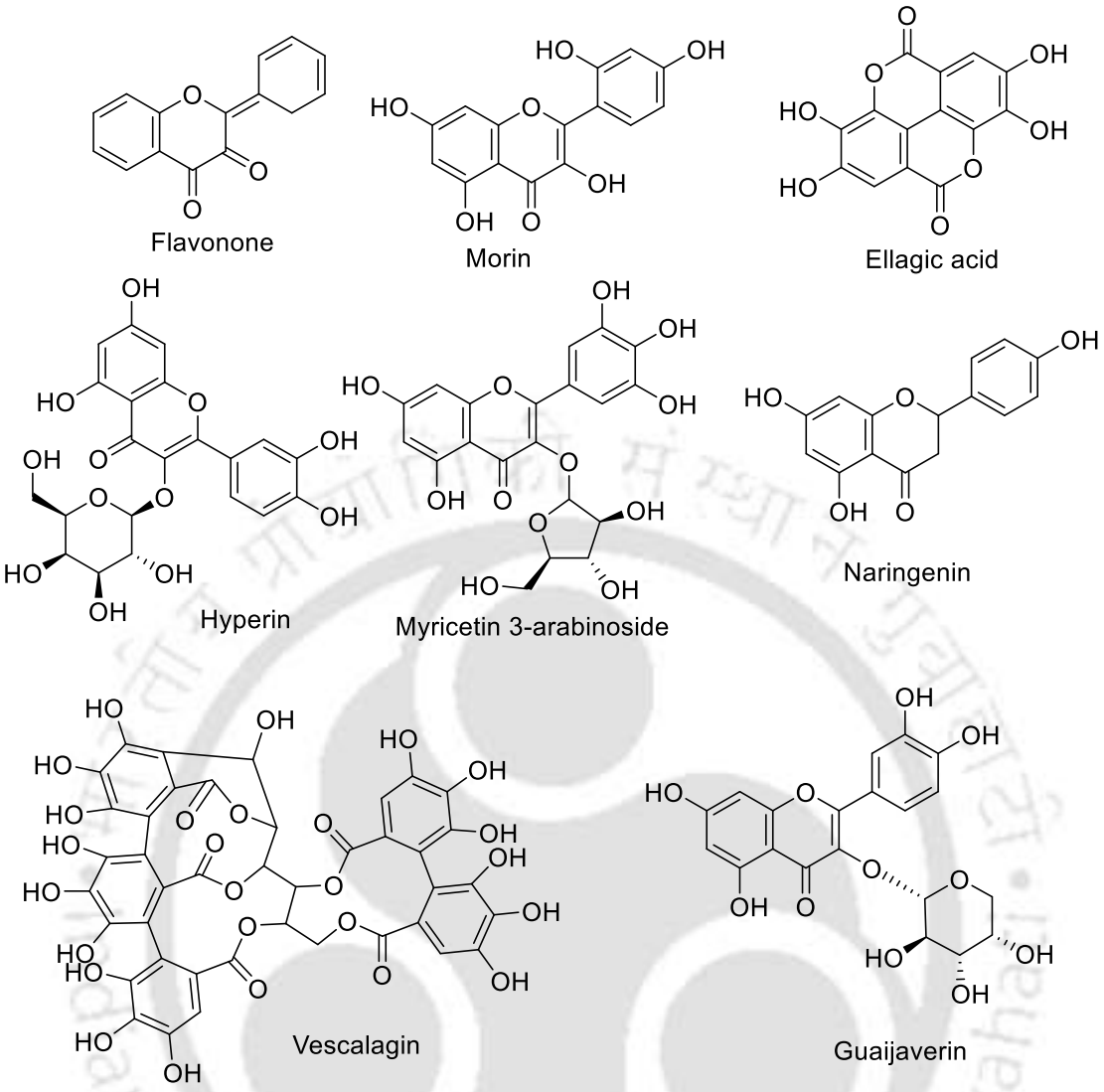

Figure 1.1. Structure of selected plant polyphenols.

Hence, these materials are also well known as green synthesized nanoparticles. The small size ranges of the materials possess increased surface area, which helps in the adsorption of pollutants due to increments of active sites. Moreover, the use of plant materials for the green synthesis of nanoparticles is useful for its cost-effectiveness, bulk production, and effective reproducibility process. Table 1.2 represents various plant parts utilized in different literature for synthesizing metal-based nanomaterials.

The production of green nanoparticles provides numerous advantages over traditional methods that include no energy requirement, significant affordability, and eco-friendliness as no toxic

byproducts are produced [35]. The benefit of green produced nanoparticles synthesis is that they do not require synthetic reducing agents, which are detrimental to the environment. Additional benefits of green synthesis over traditional ones include the possibility of bulk scale production, no requirement of external conditions such as high pressure and energy [36].

Table 1.2. Literature of plant-mediated synthesis of the nanoparticles.

Plant name	**Plant part**	**Metal salt**	**Application**	**References**
Benjamina	Leaf	Silver	Cadmium	[33]
Trigonella foenum-graecum	Leaf	Silver	Reactive blue 19 and Reactive yellow 186	[37]
Terminalia bellerica kernel	Fruit	Silver	Methyl orange, Eosin yellow	[38]
Palm tree (*Phoenix dactylifera*)	Leaf	Copper–silver	Methylene blue	[39]
Mussaenda glabrata	Leaf	Gold and silver	Rhodamine B, methyl orange	[40]
Stemona tuberosa Lour		Gold	4-nitrophenol, methylene blue, methyl orange and methyl red	[41]
Lagerstroemia speciosa	Leaf	Gold	methyl orange, bromophenol blue and bromocresol green, and 4-nitropheno	[42]
Hibiscus sabdariffa	Flower	Copper	Nitrate	[43]
Citrofortunella microcarpa	Leaf	Copper	Rhodamin B	[44]
Moringa oleifera	Leaf	Iron	Nitrate removal,	[45]
Dodonaea viscosa	Leaf	Iron	Antimicrobial	[46]
Laurus nobilis L	Leaf	Iron	Antimicrobial against *Listeria monocytogenes* bacterium.	[47]
Carica papaya	Leaf	Iron	Remazol yellow RR dye degradation	[48]
Tea	Leaf	Iron	Malachite green, rhodamine B and methylene blue dye removal	[28]
Simmondsia	seed	Iron	Fluoride removal	[49]

chinensis				
Nettle and Thyme	Leaf	Iron	Cephalexin (CEX) antibiotic removal	[50]
Azadirachta indica	Leaf	Iron	ammonia nitrogen, COD	[51]
Eucalyptus teretiornis,	Leaf	Iron	Dye removal	[52]
Eucalyptus globules	Leaf	Iron	Chromium	[53]
oolong tea	Leaf	Iron	Malachite green	[54]
Green tea		Iron	Methylene blue and methyl orange	[55]
Lantana camara	Leaf	Iron	Ni (II)	[34]
Oak, mulberry and cherry	Leaf	Iron	Arsenic (III), Chromium	[56]
Eichhornia crassipes, *Lantana camara* and *Mimosa pudica*	Leaf	Iron	Nitrate and phosphate	[57]
Vaccinium corymbosum	Shoot and leaf	Iron	Arsenic	[58]
Tea extract	Leaf	Iron	Bromothymol blue	[59]

Table 1.2 summarizes the utilization of several plant species for the synthesis of plant-mediated metal nano complexes. Different precursor metal salts like silver, gold, copper, nickel, iron were used for complexation purposes. Among them, some metal salts are quite costly, which makes the synthesized materials expensive, and some have some toxic effects on the environment. However, the use of iron salt for synthesis makes the material cost-effective and environmentally friendly. Apart from it, iron is a common earth element also very essential for the growth of the living body. Iron forms strong bonds with the phenolic –OH group of the polyphenols to form a complex. Iron after complexation generally prefers the Fe(III) oxidation state, but in a mixture, some amount of Fe(II) could also be present.

1.2. Iron-Polyphenol Interaction

Polyphenols can react in various ways depending on pH, iron oxidation state, metal-ligand ratio, and oxygen present. Depending upon pH, polyphenols and polyphenolic-metal complexes can be varied structurally, show different coordination modes. The speciation of iron-catechol changes with the change in the pH. In the complexation of catechol : iron, in the ratio of 2: 1 at the pH of 6-7, the formation of bis species is observed with a λ_{max} of 570nm. Additionally, the tris species is formed in solutions with a pH > 9.5 and a UV–vis maximum of 490 nm. At low pH (<4.5), the occurrence of a sea-green Fe(cat) species with a λ_{max} of 714 nm was observed (Figure 1.2) [60–62]. The pKa value of most of the polyphenol was 9-10, bellow that pH, in the presence of iron, catechol deprotonates and forms a stable iron-polyphenol complex [63].

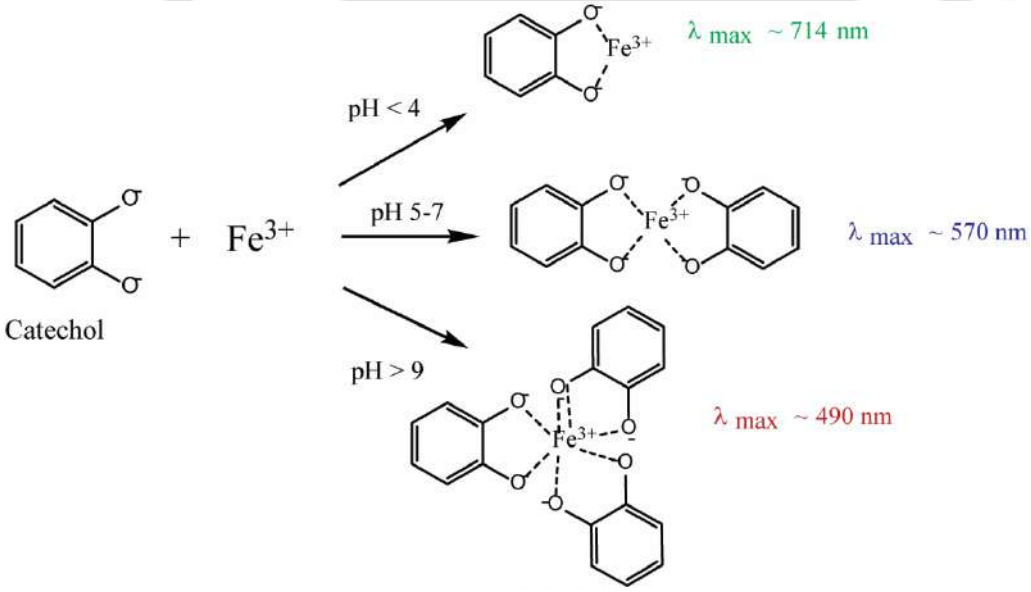

Figure 1.2. Iron catechol complexation at different pH.

Iron binds to polyphenol due to the antioxidant actions of polyphenols [64]. After the displacement of the proton, polyphenols act as hard Lewis bases, and after the interaction with Fe(III) (hard Lewis acid), they show higher stability constant of 40-49 [65]. However, in

interaction, polyphenols with Fe (II) (borderline Lewis acid) exhibit lower stability constant in comparison to Fe (III) complex.

Oxygen also plays an important role in iron-polyphenol complexation. In previous literature, it is also observed that due to the autooxidation process, in the presence of oxygen, the catechol and gallic acid complexes of Fe(II) are oxidized to Fe (III) complexes (Figure 1.3 a) [66,67]. In aerobic conditions, the oxidation of Fe (II) is a slow process. However, in the interaction of polyphenol-iron, the rate of the oxidation of iron is increased [68].

Previous literature shows that Fe (III) reduces to Fe (II) after binding with a polyphenolic compound, forming a semiquinone as an intermediate to finally give a quinone form. This happens due to the oxidation of polyphenol (Figure 1.3b).

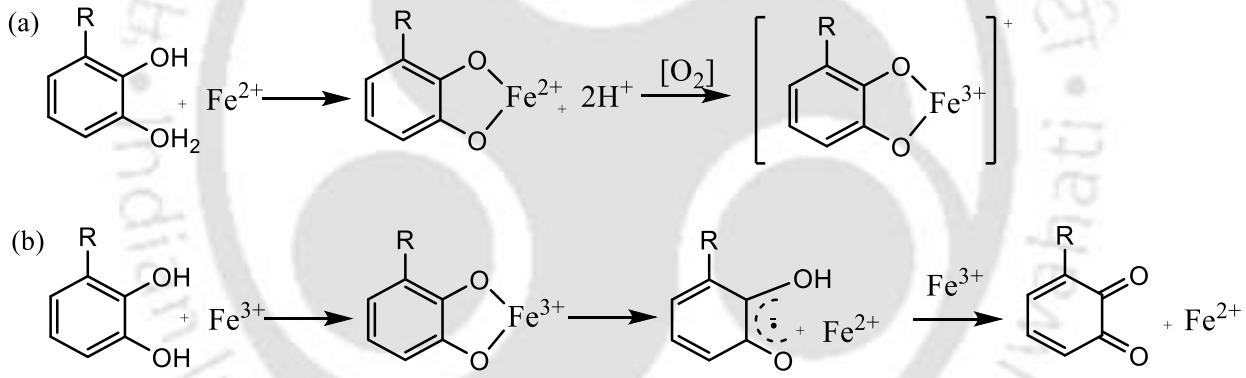

Figure 1.3. (a) Iron (II)-polyphenol reaction in the presence of oxygen, (b) reduction of iron (III) in iron polyphenol interaction.

1.3. Structure of Iron Polyphenol Complexes

In literature, very few reports are available explaining the structure of the iron-polyphenol complexes. Among them, most are proposed structures of iron polyphenols. Feller and Cheetham (2006) conducted the reaction with gallic : iron in 1:1 ratio [69]. Synthesis was performed in an autoclave at 100°C for 72 h, which yielded a blue-black rod-shaped single crystal, which was found to be similar to the previously reported work by Wunderlich [70].

The valency of the Fe(III) was confirmed by Mössbauer and XANES spectroscopies. Similarly, Ponce et al. (2016) reported the study in hydrothermal reaction conditions at 125°C under autogenous pressure for 48h (Figure 1.4.a) [71]. The crystalline iron-gallate was formed with trigonal $Fe(C_7O_5H_3).\ xH_2O$ structure. Single crystal X-ray was used to analyze the structure, and Mössbauer spectra of the crystals supported the presence of Fe(III) ions with the absence of Fe(II) component. Krekel (1999) reported the synthesis of historic ink using gallic acid: iron in 1:1 ratio. This study also proposed a structure of Fe(III) octahedral gallic acid complex. In literature, the quercetin-iron complex was synthesized in 1:2 ratio in the presence of methanol (Figure 1.4.c) [73]. Another proposed structure of iron polyphenol nanoparticles was given by Wang et al. (2013) [52]. This study experimented with eucalyptus leaves to synthesize iron nanoparticles and applied them for Acid Black 194 removal. The polyphenol-iron ratio in the synthesis of the material was adopted as 3: 1 (Figure 1.4.d).

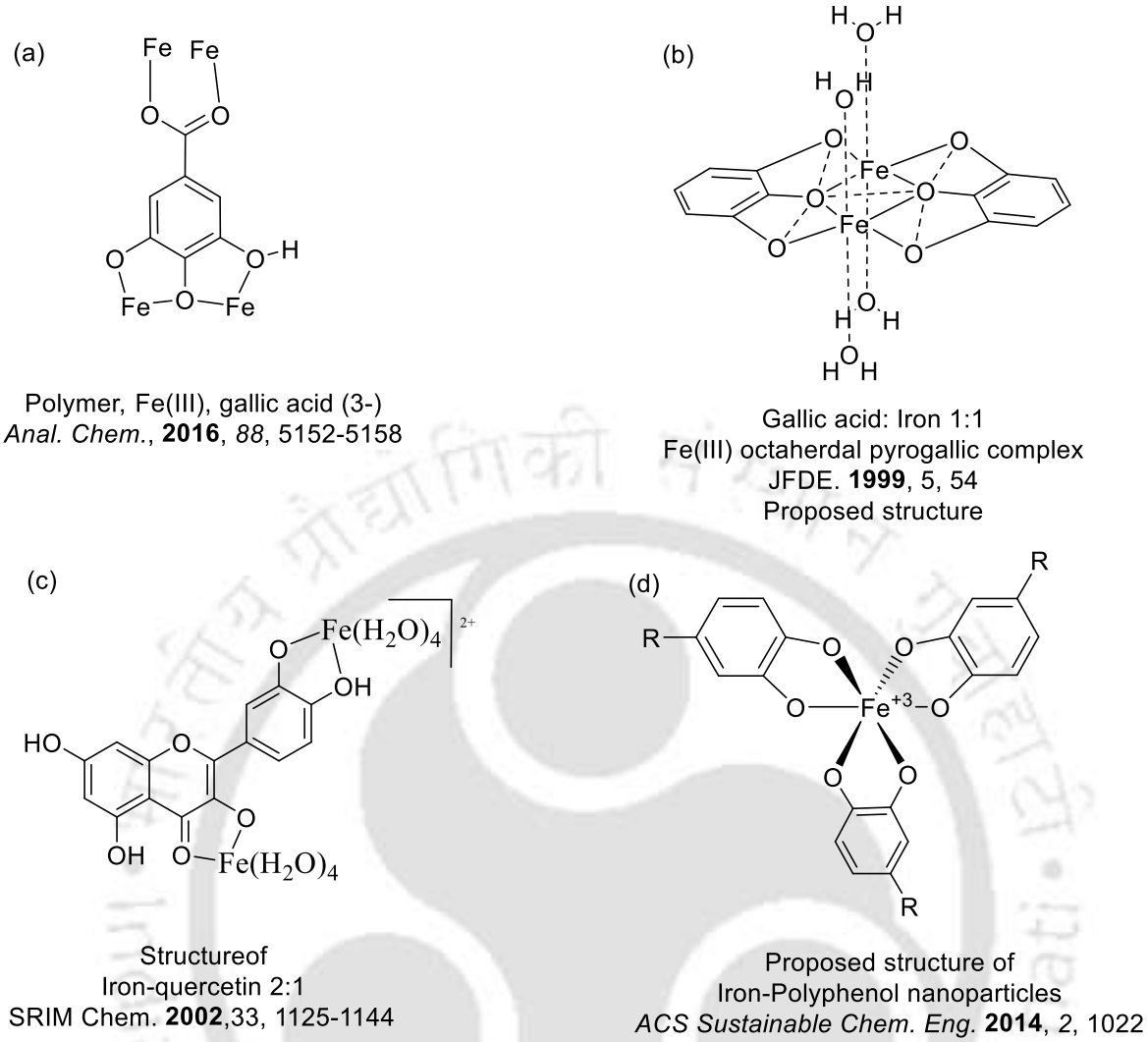

Figure 1.4. Structure of iron-polyphenol complexes (a) structure of gallic-iron complex (b) proposed structure of the iron complex (c) proposed structure of iron-eucalyptus nanoparticles.

1.4. Application of Iron-Plant Polyphenol Complexes

1.4.1. Wastewater Treatment

Zhu et al. (2018) used green tea extract was utilized for the synthesis of zero-valent iron/Cu nanoparticle synthesis at N_2 atmosphere and employed for the removal of Cr (VI) from aqueous solutions [74]. At pH 5, zero-valent iron/Cu nanoparticles were capable of 94.7 % removal of 5 mg/L of Cr (VI) solution. The material was characterized by FESEM, FTIR, and PXRD (peak is unclear, polyphenol not measured, no iron-polyphenol ratio). Pan et al. (2019) used peanut

skin for iron-based nanoparticles synthesis purposes [75]. This study described the core-shell structure of nano complex with Fe (0) in the core, surrounded by the biomolecule layer. The material was characterized using PXRD, FTIR, XPS, and UV-spectroscopy. Moreover, SEM images showed agglomeration of the particle. Materials showed 100% removal of 10 mg/L of Cr (VI) at pH 4.7 and 2 g/L of dose. Similarly, Jin et al. (2018) synthesized zero-valent iron nanoparticles using eucalyptus leaf extract and applied them for chromium removal [76]. The experiment was executed with 10 mg/L of chromium solution, at pH 4, nanoparticle dose of 1.4 g/L, 30°C. Results showed 86% removal of total chromium.

Ehrampoush et al. (2015) utilized tangerine peel extract, which acted as a stabilizing agent for the synthesis of iron oxide nanoparticles by co-precipitation method and utilized for cadmium adsorption [77]. The average size of the particles in DLS was 200 nm. Moreover, the removal experiment showed 88% removal of 20 mg/L of Cd at 4 pH, with a material dose of 4 g/L.

Machado et al. (2017) utilized the oak leaves to synthesize nanoscale zero-valent iron and analyzed the degradation of a popular antibiotic and amoxicillin in wastewater [78]. They studied the degradation of 100% of amoxicillin occurred at 95 min of contact time in an aqueous solution with amoxicillin and nanoparticle in the ratio of 1:15. Apart from these, *Lantana camara* fruit extract was used by Nithya et al. (2018) for the synthesis of iron oxide nanoparticles and applied for the removal of Ni(II) [34]. With the dose of the nanoparticle of 1.2 g/L, 99% removal of 100 mg/L of the solution was observed at pH 7. Manquián-Cerda et al. (2017) employed the plant leaves and shoots extract of *Vaccinium corymbosum* to synthesize iron nanoparticles and apply them for arsenate removal [58]. Nanoparticles were characterized using TEM, SEM (52 nm), BET, PXRD. They reported that the maximum removal of 76% of 200 mg/L arsenates was observed at pH 4, and 120 min of reaction time. Furthermore, Sajadi et al. (2016) utilized the plant seeds of *Silybum marianum* L. for the synthesis of copper-supported iron nanoparticles and applied them against nitrobenzene

reduction [79]. Materials were characterized by XRD, TEM, EDS, and UV–vis spectroscopy. Maximum removal of 96% was observed for 1 mmol of concentration at 90 min of reaction time. The following tables show the summary of plant-mediated iron-nano complexes synthesized by using different plants, characterized, and applied to remove pollutants from wastewater.

Table 1.3. Use of plant-mediated nanoparticles in wastewater treatment.

Plant name	Application	Condition	Removal or uptake	Comment	References
Green tea, Eucalyptus leaf	Nitrate	20 mg/L, 1g dose	50 and 35%	Total phenol not measured. EDS only. PXRD peak not clear	[80]
Nephrolepis auriculata	Chromium (VI)	50 mg/L of	90%	XPS, EDS, Fe^{+3}, Fe^{+2}, Fe^{0} Nitrogen atmosphere for synthesis. The dose is not clear.	[81]
Citrus maxima peels	Chromium (VI)	100 mg/L, 90 min,	99%	TEM, EDS, XPS, IR, DLS. Nanoparticles in solution phase. The dose of material is not clear. Removal was not checked with varying conditions.	[82]
Oak, mulberry and cherry NPs	Arsenic (III),		300 mg/g 200 mg/g and 250 mg/g	Polyphenol not measured, no characterization for the state of iron. Claim Zero valent NPs	[56]
Tangerine peel extract	Cadmium	4 pH, 4 g/L of dose, 20 mg/L of Cd	88%	No polyphenol estimation. SEM, DLS only. In removal, no triplicates	[77]
Nettle and Thyme leaf	Cephalexin antibiotic	25 mg/L, 0.1g dose	80%	Powder XRD, peaks of different state of Fe were there. Claim Zero valent NPs	[50]

Cupressus sempervirens leaf	Methyl orange dye	25 mg/L, with H_2O_2, 1 g/L dose	95%	Polyphenol not measured. PXRD	[31]
Hibiscus flower petals	Rodamine B		20 mg/g	Synthesis and characterization not cleared, EDS done. Claim Zero valent NPs	[83]
Eucalyptus leaf	Acid black 194 COD, N		71% and 84% removal	Iron-Polyphenol complex	[84]
Oolong tea	Malachite green	50 mg/L conc, 0.01g dose, in 40min.	73%	EDS, PXRD. NP in solution phase	[85]
Iron-polyphenol with Eucalyptus and 2 other plants	Acid red 94 and MB	2000 mg/L initial conc. 24hr contact time.	Uptake is 463 mg/g for acid red and 64 mg/g for MB	IR, TEM only. NPs in solution used. Not in powder form. Dose and other parameters not clear	[86]
Iron-polyphenol with Eucalyptus leaf	Acid black 194	1300 mg/L of 2000 mg/L initial conc. 24h contact time. pH 3-9	> 80% removal.	UV, IR NPs in solution used. Not in powder form. Dose and other parameters not clear	[52]
Tea leaf	Malachite green (MG), methylene blue (MB), and	0.01 g of dose, 50 mg/L initial conc.	Uptake of 190.3 mg/g, 186.93 mg/g and	IR, XPS, zeta potential. Only kinetics study	[28]

	rhodamine B (RB)		182.4 mg/g, respective		
Fe-zero with Guava leaf	MB	50 mg/L conc, 2.4g/L dose.	> 94% removal	UV-TEM-IR. Claim Zero valent NPs	[87]
Tea leaf-Iron, NZVI activated carbon comparison	Real textile water	Initial-350 mg/L conc. dose 0.7g. pH 5 for NZVI, 8 for AC, and 7 for green nano.	72% removal for AC, 85% removal for green nano. And 71% for nZVI	XRD, SEM, EDX, different modeling. UV peak not mentioned.	[88]
Fe_3O_4 coated-tea polyphenol	MB removal	3.5 mg/L conc, dose 1g/L, pH >7.	Uptake 5mg/g	ESI mass, PXRD, raman, VSM, BET surface area 126	[89]

It was observed that no confined protocol was followed for synthesis purposes. In different reports, various kinds of synthesis processes were used. Thus, there exists a scarcity of knowledge regarding detailed analysis of zero-valent iron, irrespective of results reported in various literature. In some literature, the formation of zero-valent iron was claimed without proper characterization of the materials. However, in some literature, iron complexes were separated using centrifugation and applied as a powder form. Whereas, according to some other experimental results, materials were present in the suspension phase. So to say, basically, in all the studies, the efficiency of iron-polyphenol complexes in pollutant removal was studied.

1.4.2. Application in Agriculture

Iron is an important element for plant growth, photosynthesis capacities, as well as different biochemical processes. It is also crucial for the structure of chloroplasts, as well as Fe-S group is essential to ensure electron flow in the thylakoid membrane [90]. Iron also has an important role in synthesizing chl-b from chl-a [91]. In different literature, iron-based nanomaterials improved plant growth in terms of biomass, root-shoot growth, photosynthesis capacity, productivity, etc. [92,93]. However, some literature reported the negative impact on the plants, like the accumulation of iron nanoparticles in the root surface and cause the suppression of water uptake, suppression on growth, induce stress, etc. [94–96]. Table 1.4. summarises different studies on the effect of iron-based nanoparticles on plant species.

Table 1.4. Positive and negative effects of different metal complexes on different plant species.

Materials	Species	Analysis	Comment	References
Iron oxide NPs	Lemna minor	No. of leaves, dry weight, Fe accumulation in the root, chlorophyll, Lipid peroxidation were measured.	At high concentration, chlorophyll content decrease, MDA production increased. Showed toxicity on plant and kill plants within 7 days in all concentration range.	[97]
Iron (III) oxide NPs	*Vigna radiata*	Dry biomass, root-shoot growth, Fe and As analysis, proline test, H_2O_2 content, total antioxidant capacity, SEM, etc., were measured.	The effect of Seedlings raised in AsO_4^{3-} and Fe_2O_3-NPs, and in combined conditions were evaluated in this study. AsO_4^{3-} reduces the seedling growth. Fe_2O_3-NPs showed resistance to arsenic toxicity.	[98]
Micro and nano-sized iron	*Lepidium sativum*, *Sinapis alba*,	Germination index, elongation, biomass, microscopic	No significant phytotoxicity effects could be detected. Increased seedling length	[92]

	and *Sorghum saccharatum*	observation was checked.	and biomass production were observed.	
Fe_3O_4 nanoparticle	Cucumber and lettuce	Root elongation, germination index, relative seed germination was checked.	Decrease in root growth and germination index.	[99]
Zero-valent iron	Cattail and hybrid poplars plant species	Root-shoot weight, length were measured. FESEM, EDX, TEM were also checked.	The result showed the toxic effect on cattail species at >200mg/L of concentration. While at a lower concentration, it enhances plants growth.	[100]
FeO_x NPs	*Lactuca sativa*	Germination test, root shoot length	1mg/L dose helped in germination and growth. However, 20mg/L dose suppressed the germination of seeds.	[101]
Zero-valent iron nanoparticle	*Oryza sativa* cv	Germination test, growth, hydrolytic enzyme activities, antioxidant, proline, chlorophyll.	Increased root-shoot length, biomass, and chlorophyll. absence of membrane damage, decrease in proline content.	[102]
Zero-valent iron nanoparticle	Peanut	Germination test, growth, TEM	40 and 80 μmol/L of dose better of growth of plants.	[103]

In the above table, it could be seen that iron complexes were able to show positive effects by increasing the plants' productivity, growth, and biomass. On the other hand, some literature showed the negative influence of iron complexes on plants, such as the deposition of iron nanoparticles in the root surface, which reduces the water intake, affects growth rate, and induces stress.

1.4.3. Antimicrobial Activity

The application of iron complexes on nanomaterials has significant potential in the inhibition of various diseases causing bacteria and fungi. Although the mechanism of these metal nano compounds, antimicrobial properties are yet to be known. A number of the proposed mechanisms of antimicrobial activities have been suggested, including breakage of the cell membrane, damage of DNA, etc. Lee et al. (2008) studied the effect of zero-valent iron on *E. Coli* and studied the severe physical disruption of membranes which could have induced the oxidative stress and showed the high antimicrobial effects of dissolved iron [104]. However, the absence of a harmful effect of nZVI on the species was observed by Stefaniuk et al. (2016), and further growth of Gram-positive bacteria was found [105]. The following table shows the summary of the inhibition effect of iron polyphenol complexes on different microbes.

Table 1.5. Antimicrobial activity of iron nanoparticles.

Materials	Species	Comments	References
Iron oxide NPs with *Cynometra ramiflora* leaf extract	*E. coli* and *S. epidermidis*	Kirby-Bauer diffusion assay with 70 µL of material. (dose is not clearly mentioned). The exact area of ZOI is not mentioned.	[106]
Gallic-Aluminium and gallic-iron complex	*E. coli*	Only iron-gallic acid complex is effective in showing inhibition. ZOI of the iron-gallic complex is 12.00 ± 0.25 mm with 50µL of genotoxic dose.	[107]
Iron oxide NPs with tannic acid	*Trichothecium roseum, Cladosporium herbarum, Penicillium chrysogenum, Alternaria alternata, and Aspergillus niger.*	With 0.5 mg/ml dose of iron nano, the ZOI of the different fungi are as follows: *T. roseum*, (22 mm) *C. herbarum*, (18 mm) *P. chrysogenum*,(28 mm) *A. alternate* (21 mm) and A. niger (26 mm).	[108]

Iron oxide magnetic NPs with *Argemone mexicana* L. leaf extract	*E. coli*, *P. mirabilis* and *B. subtilis*	8 mm ZOI with 12.5 µg/disc of dose.	[109]
Iron oxide NPs	*Staphylococcus aureus*, *Escherichia coli*, and *Pseudomonas aeruginosa*	With a dose of 0.15 mg/mL of NPs, the ZOI against S. aureus, E. coli, and P. aeruginosa is 29,26,28 mm.	[110]
Iron oxide NPs	*Bacillus subtilis* and *E. coli*	Showed antimicrobial activity at > 50 µM. relatively at high concentrations	[111]
Fe_3O_4-NPs	*Bacillus cereus* and *Klebsiella pneumoniae*	With 5 µg/mL of MIC, against *K. pneumoniae* and *B. cereus* showed 26 mm and 22 mm zone of inhibitions, respectively. MBC for these strains was observed at 40 µg/mL of Fe3O4-NPs, showing 40–50% loss in viable bacterial cells and 80 µg/mL of concentration exhibiting 90–99% loss.	[112]

This table summarizes the capabilities of different types of iron nano-complexed against various microorganisms to check their inhibition. Different kinds of methods were used for the estimation of the antimicrobial activity of iron-based materials. The phytochemicals are capable of showing antimicrobial activity and fight against several pathogenic diseases [113]. Literature showed the formation of reactive oxygen species (ROS) that breaks the DNA stand and also causes the death of the cells [111]. The mechanism of inhibition varies from species to species. Considering the small size of the iron complex, it can easily penetrate the bacterial membrane due to the adhesion and deposition of the materials, as a result of which cytolysis occurs [114].

1.5. Summary of Literature Survey

I. Multiple reports on nanomaterial from iron and plant extract are available for investigating pollutant removal.

II. Reported materials employed different conditions and different sets of spectroscopic tools, which limit the understanding of the identity of active ingredients responsible for the synthesis of the material.

III. Multiple literatures report the formation of Fe(0) using plant extract as a reducing agent. However, considering the metal-ligand ratio, pH of solutions, state of iron, the type of possible products also changed.

IV. In multiple reports, it is seen that the synthesized materials are generated in the dispersion phase without isolation of materials.

1.6. Research Gap

- In plant extract, multiple numbers of components are present. With the change of season and geographical location, the type and quantity of the active biological components of the same plant species also vary. Therefore, the identification of active components responsible for nanomaterial synthesis is important.
- Different bioactive substances react differently with metal solutions. Therefore, identification of the state of the metal and possible structure of the metal-polyphenol complex is important, but the insufficiency of literature focusing on this issue is noticed.
- Comparative studies between iron polyphenol complex synthesized with different types of polyphenols have not been reported before.
- The toxicological study, fate, and transit of iron-polyphenol complexes in the environment have not yet been explored enough. There are many more aspects that need detailed research for better comprehension of the topic.

1.7. Objectives

i. Optimization and standardization for the synthesis of iron-polyphenol materials using two different types of polyphenols under identical conditions.

ii. Reproducibility and bulk synthesis of the materials.

iii. Materials were synthesized using plant extract (mixture of polyphenols) and a single component polyphenol (tannic acid) with known formula and analysis of the similarities and differences of synthesized materials using multiple spectroscopic techniques.

iv. Comparative assessment of materials efficacy as adsorbent with both cationic and anionic pollutants.

v. Toxicity test of the synthesized materials to investigate the safety with respect to individual interaction with plant and bacterial life forms.

References

[1] A.S. Adeleye, J.R. Conway, K. Garner, Y. Huang, Y. Su, A.A. Keller, Engineered nanomaterials for water treatment and remediation: Costs, benefits, and applicability, Chem. Eng. J. 286 (2016) 640–662. https://doi.org/10.1016/j.cej.2015.10.105.

[2] E.N. Zare, M.M. Lakouraj, N. Kasirian, Development of effective nano-biosorbent based on poly m-phenylenediamine grafted dextrin for removal of Pb (II) and methylene blue from water, Carbohydr. Polym. 201 (2018) 539–548. https://doi.org/10.1016/j.carbpol.2018.08.091.

[3] A. Bhatnagar, M. Sillanpää, Utilization of agro-industrial and municipal waste materials as potential adsorbents for water treatment-A review, Chem. Eng. J. 157 (2010) 277–296. https://doi.org/10.1016/j.cej.2010.01.007.

[4] M.M. Ayad, A.A. El-nasr, Adsorption of Cationic Dye (Methylene Blue) from Water Using Polyaniline Nanotubes Base, J. Phys. Chem. 114 (2010) 14377–14383.

[5] C. Santhosh, V. Velmurugan, G. Jacob, S.K. Jeong, A.N. Grace, A. Bhatnagar, Role of nanomaterials in water treatment applications: A review, Chem. Eng. J. 306 (2016) 1116–1137. https://doi.org/10.1016/j.cej.2016.08.053.

[6] S. De Gisi, G. Lofrano, M. Grassi, M. Notarnicola, Characteristics and adsorption capacities of low-cost sorbents for wastewater treatment: A review, Sustain. Mater. Technol. 9 (2016) 10–40. https://doi.org/10.1016/j.susmat.2016.06.002.

[7] B. Volesky, Biosorbents for metal recovery, Trends Biotechnol. 5 (1987) 96–101. https://doi.org/10.1016/0167-7799(87)90027-8.

[8] K. Kaya, E. Pehlivan, C. Schmidt, M. Bahadir, Use of modified wheat bran for the removal of chromium(VI) from aqueous solutions, Food Chem. 158 (2014) 112–117. https://doi.org/10.1016/j.foodchem.2014.02.107.

[9] O. Karnitz, L.V.A. Gurgel, J.C.P. de Melo, V.R. Botaro, T.M.S. Melo, R.P. de Freitas Gil, L.F. Gil, Adsorption of heavy metal ion from aqueous single metal solution by chemically modified sugarcane bagasse, Bioresour. Technol. 98 (2007) 1291–1297. https://doi.org/10.1016/j.biortech.2006.05.013.

[10] L. Bulgariu, L.B. Escudero, O.S. Bello, M. Iqbal, J. Nisar, K.A. Adegoke, F. Alakhras, M. Kornaros, I. Anastopoulos, The utilization of leaf-based adsorbents for dyes

removal: A review, J. Mol. Liq. 276 (2019) 728–747. https://doi.org/10.1016/j.molliq.2018.12.001.

[11] F.M.A.A. Arshad I. Esmael, Minerva E. Matta, Hisham A. Halim, Adsorption of Heavy Metals from Industrial Wastewater using Palm Date Pits as Low Cost Adsorbent, Int. J. Eng. Adv. Technol. 3 (2014) 71–76.

[12] L.-H. Wang, C.-I. Lin, Adsorption of Lead(II) Ion from Aqueous Solution Using Rice Hull Ash, Ind. Eng. Chem. Res. 47 (2008) 4891–4897. https://doi.org/10.1021/ie071521z.

[13] S. Chowdhury, R. Mishra, P. Saha, P. Kushwaha, Adsorption thermodynamics, kinetics and isosteric heat of adsorption of malachite green onto chemically modified rice husk, Desalination. 265 (2011) 159–168. https://doi.org/10.1016/j.desal.2010.07.047.

[14] L. Levankumar, V. Muthukumaran, M.B. Gobinath, Batch adsorption and kinetics of chromium (VI) removal from aqueous solutions by Ocimum americanum L. seed pods, J. Hazard. Mater. 161 (2009) 709–713. https://doi.org/10.1016/j.jhazmat.2008.04.031.

[15] J. Anandkumar, B. Mandal, Removal of Cr(VI) from aqueous solution using Bael fruit (Aegle marmelos correa) shell as an adsorbent, J. Hazard. Mater. 168 (2009) 633–640. https://doi.org/10.1016/j.jhazmat.2009.02.136.

[16] A. Al Bsoul, L. Zeatoun, A. Abdelhay, M. Chiha, Adsorption of copper ions from water by different types of natural seed materials, Desalin. Water Treat. 52 (2014) 5876–5882. https://doi.org/10.1080/19443994.2013.808593.

[17] Z. Zhang, I.M. O'Hara, G.A. Kent, W.O.S. Doherty, Comparative study on adsorption of two cationic dyes by milled sugarcane bagasse, Ind. Crops Prod. 42 (2013) 41–49. https://doi.org/10.1016/j.indcrop.2012.05.008.

[18] P. Pillai, Y. Lakhtaria, S. Dharaskar, M. Khalid, Synthesis, characterization, and application of iron oxyhydroxide coated with rice husk for fluoride removal from aqueous media, Environ. Sci. Pollut. Res. 27 (2020) 20606–20620. https://doi.org/10.1007/s11356-019-05948-8.

[19] K.G. Bhattacharyya, A. Sharma, Adsorption of Pb(II) from aqueous solution by Azadirachta indica (Neem) leaf powder, J. Hazard. Mater. 113 (2004) 97–109.

https://doi.org/10.1016/j.jhazmat.2004.05.034.

[20] M.A. Ahmad, R. Alrozi, Optimization of rambutan peel based activated carbon preparation conditions for Remazol Brilliant Blue R removal, Chem. Eng. J. 168 (2011) 280–285. https://doi.org/10.1016/j.cej.2011.01.005.

[21] R. Han, Y. Wang, X. Zhao, Y. Wang, F. Xie, J. Cheng, M. Tang, Adsorption of methylene blue by phoenix tree leaf powder in a fixed-bed column: experiments and prediction of breakthrough curves, Desalination. 245 (2009) 284–297. https://doi.org/10.1016/j.desal.2008.07.013.

[22] T.A. Khan, R. Rahman, E.A. Khan, Decolorization of bismarck brown R and crystal violet in liquid phase using modified pea peels : non-linear isotherm and kinetics modeling, Model. Earth Syst. Environ. 2 (2016) 1–11. https://doi.org/10.1007/s40808-016-0195-6.

[23] K. Johari, N. Saman, S.T. Song, C.S. Chin, H. Kong, H. Mat, Adsorption enhancement of elemental mercury by various surface modified coconut husk as eco-friendly low-cost adsorbents, Int. Biodeterior. Biodegradation. 109 (2016) 45–52. https://doi.org/10.1016/j.ibiod.2016.01.004.

[24] Y.C. Sharma, Uma, S.N. Upadhyay, Removal of a cationic dye from wastewaters by adsorption on activated carbon developed from coconut coir, Energy and Fuels. 23 (2009) 2983–2988. https://doi.org/10.1021/ef9001132.

[25] X. Chen, X. Chen, X. Wan, B. Weng, Q. Huang, Water hyacinth (Eichhornia crassipes) waste as an adsorbent for phosphorus removal from swine wastewater, Bioresour. Technol. 101 (2010) 9025–9030. https://doi.org/10.1016/j.biortech.2010.07.013.

[26] W. Qu, D. He, Y. Guo, Y. Tang, J. Shang, L. Zhou, R. Zhu, R.J. Song, Modified Water Hyacinth Functionalized with Citric Acid as an Effective and Inexpensive Adsorbent for Heavy Metal-Ion Removal, Ind. Eng. Chem. Res. 58 (2019) 18508–18518. https://doi.org/10.1021/acs.iecr.9b03401.

[27] N. Kannan, M.M. Sundaram, Kinetics and mechanism of removal of methylene blue by adsorption on various carbons - A comparative study, Dye. Pigment. 51 (2001) 25–40. https://doi.org/10.1016/S0143-7208(01)00056-0.

[28] C. Xiao, H. Li, Y. Zhao, X. Zhang, X. Wang, Green synthesis of iron nanoparticle by tea extract (polyphenols) and its selective removal of cationic dyes, J. Environ. Manage. 275 (2020) 111262. https://doi.org/10.1016/j.jenvman.2020.111262.

[29] V.A. Niraimathee, V. Subha, R.S.E. Ravindran, S. Renganathan, Green synthesis of iron oxide nanoparticles from Mimosa pudica root extract, Int. J. Environ. Sustain. Dev. 15 (2016) 227. https://doi.org/10.1504/IJESD.2016.077370.

[30] S. Venkateswarlu, Y.S. Rao, T. Balaji, B. Prathima, N.V.V. Jyothi, Biogenic synthesis of Fe3O4 magnetic nanoparticles using plantain peel extract, Mater. Lett. 100 (2013) 241–244. https://doi.org/10.1016/j.matlet.2013.03.018.

[31] A. Ebrahiminezhad, S. Taghizadeh, Y. Ghasemi, A. Berenjian, Green synthesized nanoclusters of ultra-small zero valent iron nanoparticles as a novel dye removing material, Sci. Total Environ. 621 (2018) 1527–1532. https://doi.org/10.1016/j.scitotenv.2017.10.076.

[32] M.K. Satapathy, P. Banerjee, P. Das, Plant-mediated synthesis of silver-nanocomposite as novel effective azo dye adsorbent, Appl. Nanosci. 5 (2015) 1–9. https://doi.org/10.1007/s13204-013-0286-x.

[33] K.M. Al-Qahtani, Cadmium removal from aqueous solution by green synthesis zero valent silver nanoparticles with Benjamina leaves extract, Egypt. J. Aquat. Res. 43 (2017) 269–274. https://doi.org/10.1016/j.ejar.2017.10.003.

[34] K. Nithya, A. Sathish, P. Senthil Kumar, T. Ramachandran, Fast kinetics and high adsorption capacity of green extract capped superparamagnetic iron oxide nanoparticles for the adsorption of Ni(II) ions, J. Ind. Eng. Chem. 59 (2018) 230–241. https://doi.org/10.1016/j.jiec.2017.10.028.

[35] M. Herlekar, S. Barve, R. Kumar, Plant-Mediated Green Synthesis of Iron Nanoparticles, J. Nanoparticles. 2014 (2014) 1–9. https://doi.org/10.1155/2014/140614.

[36] M.I. Din, A. Zahoor, Z. Hussain, R. Khalid, A review on green synthesis of iron (Fe) nanomaterials, its alloys and oxides, Inorg. Nano-Metal Chem. 0 (2020) 1–17. https://doi.org/10.1080/24701556.2020.1862229.

[37] J. Singh, V. Kumar, S. Singh Jolly, K.-H. Kim, M. Rawat, D. Kukkar, Y.F. Tsang,

Biogenic synthesis of silver nanoparticles and its photocatalytic applications for removal of organic pollutants in water, J. Ind. Eng. Chem. 80 (2019) 247–257. https://doi.org/10.1016/j.jiec.2019.08.002.

[38] L. Sherin, A. Sohail, U.-S. Amjad, M. Mustafa, R. Jabeen, A. Ul-Hamid, Facile green synthesis of silver nanoparticles using Terminalia bellerica kernel extract for catalytic reduction of anthropogenic water pollutants, Colloid Interface Sci. Commun. 37 (2020) 100276. https://doi.org/10.1016/j.colcom.2020.100276.

[39] J. Al-Haddad, F. Alzaabi, P. Pal, K. Rambabu, F. Banat, Green synthesis of bimetallic copper–silver nanoparticles and their application in catalytic and antibacterial activities, Clean Technol. Environ. Policy. 22 (2020) 269–277. https://doi.org/10.1007/s10098-019-01765-2.

[40] S. Francis, S. Joseph, E.P. Koshy, B. Mathew, Green synthesis and characterization of gold and silver nanoparticles using Mussaenda glabrata leaf extract and their environmental applications to dye degradation, Environ. Sci. Pollut. Res. 24 (2017) 17347–17357. https://doi.org/10.1007/s11356-017-9329-2.

[41] B. Bonigala, B. Kasukurthi, V.V. Konduri, U.K. Mangamuri, R. Gorrepati, S. Poda, Green synthesis of silver and gold nanoparticles using Stemona tuberosa Lour and screening for their catalytic activity in the degradation of toxic chemicals, Environ. Sci. Pollut. Res. 25 (2018) 32540–32548. https://doi.org/10.1007/s11356-018-3105-9.

[42] B.C. Choudhary, D. Paul, T. Gupta, S.R. Tetgure, V.J. Garole, A.U. Borse, D.J. Garole, Photocatalytic reduction of organic pollutant under visible light by green route synthesized gold nanoparticles, J. Environ. Sci. 55 (2017) 236–246. https://doi.org/10.1016/j.jes.2016.05.044.

[43] R.M. Paixão, I.M. Reck, R. Bergamasco, M.F. Vieira, A.M.S. Vieira, Activated carbon of Babassu coconut impregnated with copper nanoparticles by green synthesis for the removal of nitrate in aqueous solution, Environ. Technol. (United Kingdom). 39 (2018) 1994–2003. https://doi.org/10.1080/09593330.2017.1345990.

[44] M. Rafique, F. Shafiq, S.S. Ali Gillani, M. Shakil, M.B. Tahir, I. Sadaf, Eco-friendly green and biosynthesis of copper oxide nanoparticles using Citrofortunella microcarpa leaves extract for efficient photocatalytic degradation of Rhodamin B dye form textile wastewater, Optik (Stuttg). 208 (2020) 164053.

https://doi.org/10.1016/j.ijleo.2019.164053.

[45] L. Katata-Seru, T. Moremedi, O.S. Aremu, I. Bahadur, Green synthesis of iron nanoparticles using Moringa oleifera extracts and their applications: Removal of nitrate from water and antibacterial activity against Escherichia coli, J. Mol. Liq. 256 (2018) 296–304. https://doi.org/10.1016/j.molliq.2017.11.093.

[46] S.C.G. Kiruba Daniel, G. Vinothini, N. Subramanian, K. Nehru, M. Sivakumar, Biosynthesis of Cu, ZVI, and Ag nanoparticles using Dodonaea viscosa extract for antibacterial activity against human pathogens, J. Nanoparticle Res. 15 (2013) 1319. https://doi.org/10.1007/s11051-012-1319-1.

[47] M. Jamzad, M. Kamari Bidkorpeh, Green synthesis of iron oxide nanoparticles by the aqueous extract of Laurus nobilis L. leaves and evaluation of the antimicrobial activity, J. Nanostructure Chem. 10 (2020) 193–201. https://doi.org/10.1007/s40097-020-00341-1.

[48] S. Hossen, M. Yusuf, S. Chandra, T. Das, O. Saha, M. Rahaman, J. Islam, Green synthesis of iron oxide nanoparticle using Carica papaya leaf extract : application for photocatalytic degradation of remazol yellow RR dye and antibacterial activity, Heliyon. 6 (2020) e04603. https://doi.org/10.1016/j.heliyon.2020.e04603.

[49] S. Kumari, S. Khan, Defluoridation technology for drinking water and tea by green synthesized Fe3O4/Al2O3 nanoparticles coated polyurethane foams for rural communities, Sci. Rep. 7 (2017) 1–12. https://doi.org/10.1038/s41598-017-08594-7.

[50] M. Leili, M. Fazlzadeh, A. Bhatnagar, Green synthesis of nano-zero-valent iron from Nettle and Thyme leaf extracts and their application for the removal of cephalexin antibiotic from aqueous solutions, 3330 (2018). https://doi.org/10.1080/09593330.2017.1323956.

[51] C.P. Devatha, A.K. Thalla, S.Y. Katte, Green synthesis of iron nanoparticles using different leaf extracts for treatment of domestic waste water, J. Clean. Prod. 139 (2016) 1425–1435. https://doi.org/10.1016/j.jclepro.2016.09.019.

[52] Z. Wang, Iron complex nanoparticles synthesized by eucalyptus leaves, ACS Sustain. Chem. Eng. 1 (2013) 1551–1554. https://doi.org/10.1021/sc400174a.

[53] V. Madhavi, T.N.V.K.V. Prasad, A.V.B. Reddy, B. Ravindra Reddy, G. Madhavi,

Application of phytogenic zerovalent iron nanoparticles in the adsorption of hexavalent chromium, Spectrochim. Acta - Part A Mol. Biomol. Spectrosc. 116 (2013) 17–25. https://doi.org/10.1016/j.saa.2013.06.045.

[54] L. Huang, X. Weng, Z. Chen, M. Megharaj, R. Naidu, Synthesis of iron-based nanoparticles using oolong tea extract for the degradation of malachite green, Spectrochim. Acta - Part A Mol. Biomol. Spectrosc. 117 (2014) 801–804. https://doi.org/10.1016/j.saa.2013.09.054.

[55] T. Shahwan, S. Abu Sirriah, M. Nairat, E. Boyacı, A.E. Eroğlu, T.B. Scott, K.R. Hallam, Green synthesis of iron nanoparticles and their application as a Fenton-like catalyst for the degradation of aqueous cationic and anionic dyes, Chem. Eng. J. 172 (2011) 258–266. https://doi.org/10.1016/J.CEJ.2011.05.103.

[56] S.S. Poguberović, D.M. Krčmar, S.P. Maletić, Z. Kónya, D.D.T. Pilipović, D. V. Kerkez, S.D. Rončević, Removal of As(III) and Cr(VI) from aqueous solutions using "green" zero-valent iron nanoparticles produced by oak, mulberry and cherry leaf extracts, Ecol. Eng. 90 (2016) 42–49. https://doi.org/10.1016/j.ecoleng.2016.01.083.

[57] R. Prabhakar, S.R. Samadder, Aquatic and terrestrial weed mediated synthesis of iron nanoparticles for possible application in wastewater remediation, J. Clean. Prod. 168 (2017) 1201–1210. https://doi.org/10.1016/j.jclepro.2017.09.063.

[58] K. Manquián-Cerda, E. Cruces, M. Angélica Rubio, C. Reyes, N. Arancibia-Miranda, Preparation of nanoscale iron (oxide, oxyhydroxides and zero-valent) particles derived from blueberries: Reactivity, characterization and removal mechanism of arsenate, Ecotoxicol. Environ. Saf. 145 (2017) 69–77. https://doi.org/10.1016/j.ecoenv.2017.07.004.

[59] H. Xin, X. Yang, X. Liu, X. Tang, L. Weng, Y. Han, Biosynthesis of Iron Nanoparticles Using Tie Guanyin Tea Extract for Degradation of Bromothymol Blue, J. Nanotechnol. 2016 (2016). https://doi.org/10.1155/2016/4059591.

[60] J. Bijlsma, W.J.C. de Bruijn, J.A. Hageman, P. Goos, K.P. Velikov, J.P. Vincken, Revealing the main factors and two-way interactions contributing to food discolouration caused by iron-catechol complexation, Sci. Rep. 10 (2020). https://doi.org/10.1038/s41598-020-65171-1.

[61] M.J. Sever, J.J. Wilker, Visible absorption spectra of metal – catecholate and metal – tironate, (2004) 1061–1072.

[62] M. Elhabiri, C. Carrër, F. Marmolle, H. Traboulsi, Complexation of iron(III) by catecholate-type polyphenols, Inorganica Chim. Acta. 360 (2007) 353–359. https://doi.org/10.1016/j.ica.2006.07.110.

[63] R.C. Hider, Z.D. Liu, H.H. Khodr, Metal chelation of polyphenols, in: 2001: pp. 190–203. https://doi.org/10.1016/S0076-6879(01)35243-6.

[64] N.R. Perron, J.L. Brumaghim, A review of the antioxidant mechanisms of polyphenol compounds related to iron binding, Cell Biochem. Biophys. 53 (2009) 75–100. https://doi.org/10.1007/s12013-009-9043-x.

[65] L.D. Loomis, K.N. Raymond, Solution Equilibria of Enterobactin and Metal-Enterobactin Complexes, Inorg. Chem. 30 (1991) 906–911. https://doi.org/10.1021/ic00005a008.

[66] K. Chvátalová, I. Slaninová, L. Březinová, J. Slanina, Influence of dietary phenolic acids on redox status of iron: Ferrous iron autoxidation and ferric iron reduction, Food Chem. 106 (2008) 650–660. https://doi.org/10.1016/j.foodchem.2007.06.028.

[67] H. El Hajji, E. Nkhili, V. Tomao, O. Dangles, Interactions of quercetin with iron and copper ions: Complexation and autoxidation, Free Radic. Res. 40 (2006) 303–320. https://doi.org/10.1080/10715760500484351.

[68] T. Kawabata, V. Schepkin, N. Haramaki, R.S. Phadke, L. Packer, Iron coordination by catechol derivative antioxidants, Biochem. Pharmacol. 51 (1996) 1569–1577. https://doi.org/10.1016/0006-2952(96)00101-3.

[69] R.K. Feller, A.K. Cheetham, Fe(III), Mn(II), Co(II), and Ni(II) 3,4,5-trihydroxybenzoate (gallate) dihydrates; a new family of hybrid framework materials, Solid State Sci. 8 (2006) 1121–1125. https://doi.org/10.1016/j.solidstatesciences.2006.04.013.

[70] C. -H Wunderlich, R. Weber, G. Bergerhoff, Über Eisengallustinte, ZAAC - J. Inorg. Gen. Chem. 598 (1991) 371–376. https://doi.org/10.1002/zaac.19915980134.

[71] A. Ponce, L.B. Brostoff, S.K. Gibbons, P. Zavalij, C. Viragh, J. Hooper, S. Alnemrat, K.J. Gaskell, B. Eichhorn, Elucidation of the Fe(III) Gallate Structure in Historical

Iron Gall Ink, Anal. Chem. 88 (2016) 5152–5158. https://doi.org/10.1021/acs.analchem.6b00088.

[72] C. Krekel, Chemistry of Historical Iron Gall Inks, Int. J. Forensic Doc. Exam. 5 (1999) 54–8. https://www.ncjrs.gov/App/abstractdb/AbstractDBDetails.aspx?id=186065.

[73] R.F.V. De Souza, E.M. Sussuchi, W.F. De Giovani, Synthesis, electrochemical, spectral, and antioxidant properties of complexes of flavonoids with metal ions, Synth. React. Inorg. Met. Chem. 33 (2003) 1125–1144. https://doi.org/10.1081/SIM-120023482.

[74] F. Zhu, S. Ma, T. Liu, X. Deng, Green synthesis of nano zero-valent iron/Cu by green tea to remove hexavalent chromium from groundwater, J. Clean. Prod. 174 (2018) 184–190. https://doi.org/10.1016/j.jclepro.2017.10.302.

[75] Z. Pan, Y. Lin, B. Sarkar, G. Owens, Z. Chen, Green synthesis of iron nanoparticles using red peanut skin extract: Synthesis mechanism, characterization and effect of conditions on chromium removal, J. Colloid Interface Sci. 558 (2019) 106–114. https://doi.org/10.1016/j.jcis.2019.09.106.

[76] X. Jin, Y. Liu, J. Tan, G. Owens, Z. Chen, Removal of Cr(VI) from aqueous solutions via reduction and absorption by green synthesized iron nanoparticles, J. Clean. Prod. 176 (2018) 929–936. https://doi.org/10.1016/j.jclepro.2017.12.026.

[77] M.H. Ehrampoush, M. Miria, M.H. Salmani, A.H. Mahvi, Cadmium removal from aqueous solution by green synthesis iron oxide nanoparticles with tangerine peel extract, J. Environ. Heal. Sci. Eng. 13 (2015) 1–7. https://doi.org/10.1186/s40201-015-0237-4.

[78] S. Machado, J.G. Pacheco, H.P.A. Nouws, J.T. Albergaria, C. Delerue-Matos, Green zero-valent iron nanoparticles for the degradation of amoxicillin, Int. J. Environ. Sci. Technol. 14 (2017) 1109–1118. https://doi.org/10.1007/s13762-016-1197-7.

[79] S.H. Ali, T.E. Jassim, Thermodynamics and Kinetic study of Bismarck Brown R Dye Adsorption from Aqueous Solution using Sewage Sludge, xxx (2020).

[80] T. Wang, J. Lin, Z. Chen, M. Megharaj, R. Naidu, Green synthesized iron nanoparticles by green tea and eucalyptus leaves extracts used for removal of nitrate in aqueous solution, J. Clean. Prod. 83 (2014) 413–419.

https://doi.org/10.1016/J.JCLEPRO.2014.07.006.

[81] Y. Yi, G. Tu, P. Eric, S. Xiao, Z. Fang, Green synthesis of iron-based nanoparticles from extracts of Nephrolepis auriculata and applications for Cr (VI) removal, Mater. Lett. 234 (2019) 388–391. https://doi.org/10.1016/j.matlet.2018.09.137.

[82] Y. Wei, Z. Fang, L. Zheng, L. Tan, E.P. Tsang, Green synthesis of Fe nanoparticles using Citrus maxima peels aqueous extracts, Mater. Lett. 185 (2016) 384–386. https://doi.org/10.1016/j.matlet.2016.09.029.

[83] Z. Khan, S.A. Al-Thabaiti, Green synthesis of zero-valent Fe-nanoparticles: Catalytic degradation of rhodamine B, interactions with bovine serum albumin and their enhanced antimicrobial activities, J. Photochem. Photobiol. B Biol. 180 (2018) 259–267. https://doi.org/10.1016/j.jphotobiol.2018.02.017.

[84] Z. Wang, C. Fang, M. Megharaj, Characterization of iron-polyphenol nanoparticles synthesized by three plant extracts and their fenton oxidation of azo dye, ACS Sustain. Chem. Eng. 2 (2014) 1022–1025. https://doi.org/10.1021/sc500021n.

[85] L. Huang, X. Weng, Z. Chen, M. Megharaj, R. Naidu, Synthesis of iron-based nanoparticles using oolong tea extract for the degradation of malachite green, Spectrochim. Acta - Part A Mol. Biomol. Spectrosc. 117 (2014) 801–804. https://doi.org/10.1016/j.saa.2013.09.054.

[86] Z. Wang, C. Yu, C. Fang, M. Megharaj, Removal of acid red 94 and methylene blue using iron-polyphenol nanomaterials synthesized by various plant leaves: A comparison study, Proc. 2014 Int. Conf. Nanosci. Nanotechnology, ICONN 2014. (2014) 39–42. https://doi.org/10.1109/ICONN.2014.6965256.

[87] P. Somchaidee, K. Tedsree, Green synthesis of high dispersion and narrow size distribution of zero-valent iron nanoparticles using guava leaf (Psidium guajava L) extract, Adv. Nat. Sci. Nanosci. Nanotechnol. 9 (2018). https://doi.org/10.1088/2043-6254/aad5d7.

[88] A. Karam, K. Zaher, A.S. Mahmoud, Comparative Studies of Using Nano Zerovalent Iron, Activated Carbon, and Green Synthesized Nano Zerovalent Iron for Textile Wastewater Color Removal Using Artificial Intelligence, Regression Analysis, Adsorption Isotherm, and Kinetic Studies, Air, Soil Water Res. 13 (2020).

https://doi.org/10.1177/1178622120908273.

[89] K.K. Singh, K.K. Senapati, K.C. Sarma, Synthesis of superparamagnetic Fe3O4 nanoparticles coated with green tea polyphenols and their use for removal of dye pollutant from aqueous solution, J. Environ. Chem. Eng. 5 (2017) 2214–2221. https://doi.org/10.1016/j.jece.2017.04.022.

[90] J.F. Briat, C. Dubos, F. Gaymard, Iron nutrition, biomass production, and plant product quality, Trends Plant Sci. 20 (2015) 33–40. https://doi.org/10.1016/j.tplants.2014.07.005.

[91] A. Tanaka, R. Tanaka, Chlorophyll metabolism, Curr. Opin. Plant Biol. 9 (2006) 248–255. https://doi.org/10.1016/j.pbi.2006.03.011.

[92] G. Libralato, A. Costa Devoti, M. Zanella, E. Sabbioni, I. Mičetić, L. Manodori, A. Pigozzo, S. Manenti, F. Groppi, A. Volpi Ghirardini, Phytotoxicity of ionic, micro- and nano-sized iron in three plant species, Ecotoxicol. Environ. Saf. 123 (2016) 81–88. https://doi.org/10.1016/j.ecoenv.2015.07.024.

[93] J. Trujillo-Reyes, S. Majumdar, C.E. Botez, J.R. Peralta-Videa, J.L. Gardea-Torresdey, Exposure studies of core-shell Fe/Fe3O4 and Cu/CuO NPs to lettuce (Lactuca sativa) plants: Are they a potential physiological and nutritional hazard?, J. Hazard. Mater. 267 (2014) 255–263. https://doi.org/10.1016/j.jhazmat.2013.11.067.

[94] X. Ma, A. Gurung, Y. Deng, Phytotoxicity and uptake of nanoscale zero-valent iron (nZVI) by two plant species, Sci. Total Environ. 443 (2013) 844–849. https://doi.org/10.1016/j.scitotenv.2012.11.073.

[95] D. Martínez-Fernández, D. Barroso, M. Komárek, Root water transport of Helianthus annuus L. under iron oxide nanoparticle exposure, Environ. Sci. Pollut. Res. 23 (2016) 1732–1741. https://doi.org/10.1007/s11356-015-5423-5.

[96] C.O. Dimkpa, J.E. McLean, N. Martineau, D.W. Britt, R. Haverkamp, A.J. Anderson, Silver nanoparticles disrupt wheat (Triticum aestivum L.) growth in a sand matrix, Environ. Sci. Technol. 47 (2013) 1082–1090. https://doi.org/10.1021/es302973y.

[97] L.R.R. Souza, L.E. Bernardes, M.F.S. Barbetta, M.A.M.S. da Veiga, Iron oxide nanoparticle phytotoxicity to the aquatic plant Lemna minor: effect on reactive oxygen species (ROS) production and chlorophyll a/chlorophyll b ratio, Environ. Sci. Pollut.

Res. 26 (2019) 24121–24131. https://doi.org/10.1007/s11356-019-05713-x.

[98] N. Shabnam, M. Kim, H. Kim, Ecotoxicology and Environmental Safety Iron (III) oxide nanoparticles alleviate arsenic induced stunting in Vigna radiata, Ecotoxicol. Environ. Saf. 183 (2019) 109496. https://doi.org/10.1016/j.ecoenv.2019.109496.

[99] R. Barrena, E. Casals, J. Colón, X. Font, A. Sánchez, V. Puntes, Evaluation of the ecotoxicity of model nanoparticles, Chemosphere. 75 (2009) 850–857. https://doi.org/10.1016/j.chemosphere.2009.01.078.

[100] X. Ma, A. Gurung, Y. Deng, Phytotoxicity and uptake of nanoscale zero-valent iron (nZVI) by two plant species, Sci. Total Environ. 443 (2013) 844–849. https://doi.org/https://doi.org/10.1016/j.scitotenv.2012.11.073.

[101] R. Liu, H. Zhang, R. Lal, Effects of Stabilized Nanoparticles of Copper, Zinc, Manganese, and Iron Oxides in Low Concentrations on Lettuce (Lactuca sativa) Seed Germination: Nanotoxicants or Nanonutrients?, Water, Air, Soil Pollut. 227 (2016) 42. https://doi.org/10.1007/s11270-015-2738-2.

[102] T. Guha, K.V.G. Ravikumar, A. Mukherjee, A. Mukherjee, R. Kundu, Nanopriming with zero valent iron (nZVI) enhances germination and growth in aromatic rice cultivar (Oryza sativa cv. Gobindabhog L.), Plant Physiol. Biochem. 127 (2018) 403–413. https://doi.org/10.1016/j.plaphy.2018.04.014.

[103] X. Li, Y. Yang, B. Gao, M. Zhang, Stimulation of peanut seedling development and growth by zero-valent iron nanoparticles at low concentrations, PLoS One. 10 (2015). https://doi.org/10.1371/journal.pone.0122884.

[104] C. Lee, J.E.E.Y. Kim, W.O.N.I.L. Lee, K.L. Nelson, Bactericidal Effect of Zero-Valent Iron Nanoparticles on Escherichia coli, (2008) 4927–4933. https://doi.org/10.1021/es800408u.

[105] M. Stefaniuk, P. Oleszczuk, Y.S. Ok, Review on nano zerovalent iron (nZVI): From synthesis to environmental applications, Chem. Eng. J. 287 (2016) 618–632. https://doi.org/10.1016/j.cej.2015.11.046.

[106] S. Groiss, R. Selvaraj, T. Varadavenkatesan, R. Vinayagam, Structural characterization, antibacterial and catalytic effect of iron oxide nanoparticles synthesised using the leaf extract of Cynometra ramiflora, J. Mol. Struct. 1128 (2017)

572–578. https://doi.org/10.1016/j.molstruc.2016.09.031.

[107] J.M. Barcelo, M. Guieb, A. Ventura, A. Nacino, H. Pinasen, L. Viernes, T. Yodong, B. Lou Estrada, D. Valdez, T. Binwag, Antibacterial, Prooxidative and Genotoxic Activities of Gallic Acid and its Copper and Iron Complexes against Escherichia coli, Asia Pacific J. Multidiscip. Res. P. 2 (2014) 2350–7756. www.apjmr.com.

[108] S. Parveen, A.H. Wani, M.A. Shah, H.S. Devi, M.Y. Bhat, J.A. Koka, Preparation, characterization and antifungal activity of iron oxide nanoparticles, Microb. Pathog. 115 (2018) 287–292. https://doi.org/https://doi.org/10.1016/j.micpath.2017.12.068.

[109] S. Arokiyaraj, M. Saravanan, N.K. Udaya Prakash, M. Valan Arasu, B. Vijayakumar, S. Vincent, Enhanced antibacterial activity of iron oxide magnetic nanoparticles treated with Argemone mexicana L. leaf extract: An in vitro study, Mater. Res. Bull. 48 (2013) 3323–3327. https://doi.org/https://doi.org/10.1016/j.materresbull.2013.05.059.

[110] M. Thukkaram, S. Sitaram, S. kumar Kannaiyan, G. Subbiahdoss, Antibacterial Efficacy of Iron-Oxide Nanoparticles against Biofilms on Different Biomaterial Surfaces, Int. J. Biomater. 2014 (2014) 716080. https://doi.org/10.1155/2014/716080.

[111] M. Arakha, S. Pal, D. Samantarrai, T.K. Panigrahi, B.C. Mallick, K. Pramanik, B. Mallick, S. Jha, Antimicrobial activity of iron oxide nanoparticle upon modulation of nanoparticle-bacteria interface, Sci. Rep. 5 (2015) 1–12. https://doi.org/10.1038/srep14813.

[112] S.A. Ansari, M. Oves, R. Satar, A. Khan, S.I. Ahmad, M.A. Jafri, S.K. Zaidi, M.H. Alqahtani, Antibacterial activity of iron oxide nanoparticles synthesized by co-precipitation technology against Bacillus cereus and Klebsiella pneumoniae, Polish J. Chem. Technol. 19 (2017) 110–115. https://doi.org/10.1515/pjct-2017-0076.

[113] K.B. Myint, L.C. Sing, Z. Wei, Tannic Acid as Phytochemical Potentiator for Antibiotic Resistance Adaptation, APCBEE Procedia. 7 (2013) 175–181. https://doi.org/10.1016/j.apcbee.2013.08.030.

[114] Y. Vitta, M. Figueroa, M. Calderon, C. Ciangherotti, Synthesis of iron nanoparticles from aqueous extract of Eucalyptus robusta Sm and evaluation of antioxidant and antimicrobial activity, Mater. Sci. Energy Technol. 3 (2020) 97–103.

https://doi.org/10.1016/j.mset.2019.10.014.

Chapter-II

Synthesis and Characterization of Iron-Plant Polyphenol Metal Complexes

2.1. Introduction

Materials from plant polyphenols and iron salts attracted our interest. The chemistry of polyphenols with iron is multifaceted. Several types of polyphenols were used in the materials synthesis [1,2]. Depending upon the pH, oxidation state of iron, metal-ligand ratio, and presence of oxygen, gallic acid or tannic acid and iron salts can react in a number of ways, for instance: (a) iron(II) binds with gallic acid forming an iron(II) complex, which gets oxidized to iron(III) complex in air, usually at pH > 4 or (b) iron(III) binds with gallic acid forming a transient iron(III) complex that undergoes a redox reaction to yield iron(II) and quinone as products [3–5]. The second path at acidic pH has been observed for tannic acid [6,7]. On the other hand, the first path may lead to oxo-bridged iron(III) complex [8]. Considering the metal-ligand ratio as an additional factor, the number of possible products further increases [3,9].

The presence of multiple components in the starting plant extract creates difficulty in the process of identification of active components. The insoluble form of the product limits the understanding of the identity of active ingredients and their mechanism of action. In many of the observations related to the reaction of iron(II) alone with plant extracted polyphenols, the reported active species varied from zero-valent iron [10,11] to iron(III)oxide [12,13] with various degrees of certainty. Products of iron salt and tannic acid, which are available in a purer form, have been studied before [6,14,15]. However, different conditions employed in the synthesis and different set of characterization tools makes it difficult to unify the chemical factors responsible for the observed function. It is rational to keep all except one reaction condition constant and study the effect.

The Fe (II) complexes of two different types of polyphenols under quite identical conditions were synthesized. The iron-polyphenol ratio would play a role in determining the type of complexation; the ratio was fixed at 1:1. In Mat-1, the iron: tannic acid was fixed at 10:1, which is equivalent to iron: gallic acid unit of 1:1. In Mat-2, guava leaf extract was used, which is rich in catechol-containing polyphenols, mainly 3-O-glycosides (example: quercetin) and flavan-3-ol (example: catechin) [16,17] (Scheme 2.1).

2.2. Experimental Section

2.2.1. Materials and Methods

Tannic acid and $FeSO_4.7H_2O$ were purchased from Alfa Aesar and RankemTM, respectively. Besides, $Fe(NO_3)_3.9H_2O$, sodium hydroxide, potassium nitrate, activated charcoal, acetonitrile, and methanol were purchased from Merck, India. Gallic acid, α-Cyano-4-hydroxycinnamic acid (HCCA), and trifluoroacetic acid (TFA) were bought from Sigma Aldrich company. Folin-Ciocalteu reagent was bought from SRL Pvt. Ltd and HiMedia, India, respectively. Purified water collected from the Amtrol reverse osmosis system.

UV and visible spectra were recorded using a Perkin Elmer Lambda 25 spectrophotometer. The Perkin-Elmer Spectrum one spectrophotometer with KBr discs was used for FTIR spectra. Solid-state magnetic susceptibilities were measured using Sherwood Scientific magnetic balance MSB-1 [18]. The Elemental analyses were measured on FLASHEA 1112 series CHNS analyzer at SAIF, IIT Bombay, India. Thermo-gravimetric analyses (TGA) were performed using Netzsch STA449F3A00 thermogravimetric analyzer under N_2 atmosphere. The Lindberg Blue M Muffle furnace manufactured by Thermo Scientific was used to convert materials to ferric oxide at 800° C. The Powder X-ray diffraction pattern of materials was recorded using Rigaku SmartLab X-ray diffractometer (CuKα radiation λ=1.5405 Å). The surface morphology of the materials was studied using Zeiss Sigma 300 and Zeiss Gemini field emission scanning electron microscope (FESEM). The size of the materials was analyzed using Jeol 2100F field

emission transmission electron microscopy (FETEM). Particle size distribution was measured using Malvern Panalytical Mastersizer 2000 dynamic light scattering (DLS) analyzer. BET surface area analysis was performed with Quantachrome Autosorb-IQ MP surface area and a pore size analyzer. Solid-state X-band EPR spectra were recorded on Jeol JES-FA200 spectrometer. XPS spectra were acquired using Thermo Fisher Scientific ESCALAB Xi+ photoelectron spectrometer. Electrospray Ionization mass (ESI-MS) spectra for tannic acid and extract were recorded using Agilent Q-TOF 6520 high-resolution mass spectrometer. The MALDI mass spectra of the insoluble materials were obtained using Brukner autoflex speed MALDI-TOF spectrometer. The pH of the solutions was measured using a Thermo Scientific Orion 3 Star pH meter.

2.2.2. Sample Preparation

For ESI-MS measurement, tannic acid (3 mg) was dissolved in 2 mL of distilled water and sonicated for 1 minute. This solution was filtered through a 0.2 μ membrane filter before measurement. The pH of the solution was 3.2. Further, 2 mL of the guava leaf extract was filtered through a 0.2 μ membrane before recording the mass spectra.

For MALDI-mass measurement, 3 mg of sample was added in 2 mL of HCCA matrix and sonicated for 2 minutes. The matrix was prepared by dissolving 1.4 mg/mL of HCCA in a solvent mixture containing 85% acetonitrile, 15% water, and 0.1% TFA.

The gravimetric method was used to estimate the amount of iron in the samples. 100 mg of the material were taken in covered crucibles and placed inside the muffle furnace at 800°C for 2 h. The process converted materials to iron (III)oxide. After cooling, the crucibles were kept in a desiccator for 10-15 minutes, followed by final weight measurement.

2.2.3. Material Synthesis

2.2.3.1. Synthesis of Mat-1

A tannic acid solution (7.00 g, 4.11 mmol) in 100 mL water was added to another solution of $FeSO_4 \cdot 7H_2O$ (11.44 g, 41.14 mmol) in 100 mL water. The pH of the mixture was adjusted to 7 using a dilute solution of NaOH and stirred continuously for 2 h. A blue-black colored precipitate was formed, which was isolated by centrifugation at 8000 rpm for 5 minutes. The precipitate was washed sequentially with water and methanol and kept in a desiccator over anhydrous calcium chloride for four days. Dried Mat-1 (12.2 g) was stored over silica gel in the refrigerator to retain the activity for at least a year.

2.2.3.2. Synthesis of Mat-2

For the preparation of Mat-2, freshly collected young guava leaves (*Psidium guajava*) were washed with plenty of water and dried with water-absorbing tissue paper. Pulping was done by grinding these leaves using a kitchen mixer with 400 mL of water. The paste obtained was heated at 50°C for 15 minutes and filtered using a Büchner funnel. The residue was further extracted with another 400mL of distilled water. A total of 750 mL solution was collected, and the pH was found to be 4.4.

The phenolic content of the extract was determined using the Folin-Coicalteu test (ISO 14502) [19] and measured in mg of gallic acid equivalent per mL. The value varied from 4.3 to 5.48 mg/mL, depending on the batch. Further, 633 mL of this extract (phenolic content 4.3 mg/mL, 0.016 mol gallic acid) was stirred with a solution of $FeSO_4 \cdot 7H_2O$ (4.90 g, 0.018 mol in 5 mL water). For batches with different phenolic content, the quantity of iron (II) salt was adjusted to keep the mole ratio constant. The pH of the solution was adjusted to 7 by adding a dilute solution of NaOH. A blue-black precipitate was formed because of continuous agitation of the above solution for 2 h. The precipitate was isolated by centrifugation (8000 rpm for 5 min) and washed with deionized water followed by methanol. Afterward, the solid was kept inside a

vacuum desiccator, having anhydrous $CaCl_2$ for four days. The final yield of Mat-2 was 9 g as a black powder. Drying and storage conditions are as described for Mat-1.

2.2.3.3. Synthesis of Mat-3

For Mat-3, a solution of tannic acid (2.00 g, 1.17 mmol in 50 mL of water) was mixed with $Fe(NO_3)_3 \cdot 9H_2O$ (4.75 g, 11.75 mmol in 50 mL water). The pH of the solution was adjusted to 7.0 using a dilute solution of NaOH. After 2 h of continuous stirring, a blue-black precipitate was formed, which was isolated by centrifugation. The residue was washed with water and methanol, subsequently. The solid was dried in a vacuum desiccator over anhydrous calcium chloride for four days. The final yield of Mat-3 was 3 g. Drying and storage conditions were kept identical as that for Mat-1.

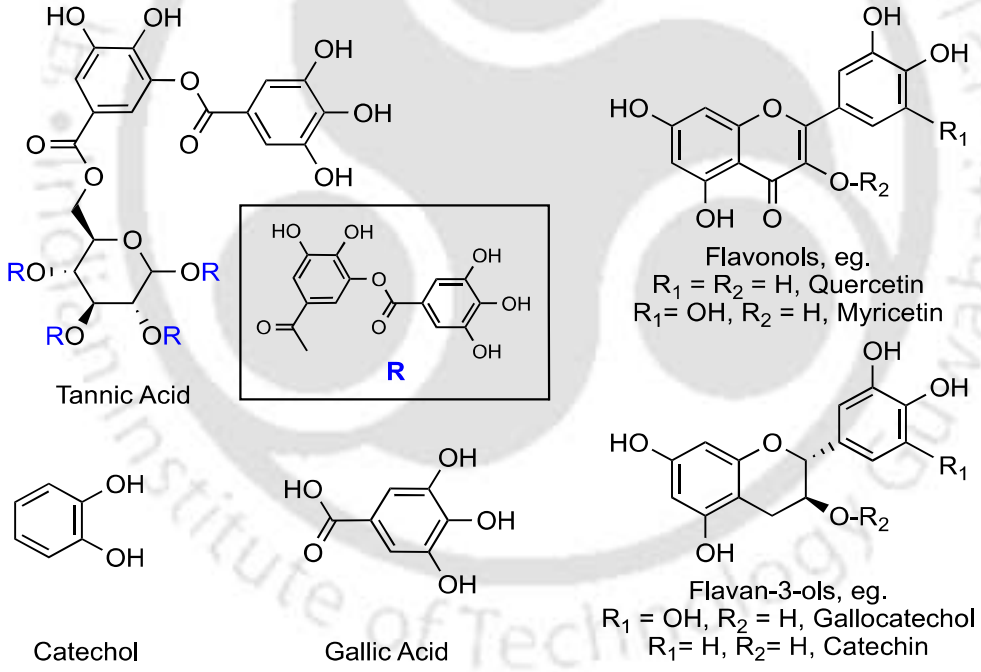

Synthesis

1. Tannic Acid + $Fe^{II}SO_4$ (Fe: gallic acid unit, 1:1) ⟶ Mat-1

2. Guava Leaves extract + $Fe^{II}SO_4$ (Fe: gallic acid equivalent, 1:1) ⟶ Mat-2

3. Tannic Acid + $Fe^{III}(NO_3)_3$ (Fe: gallic acid unit, 1:1) ⟶ Mat-3

All three materials were isolated as black power at pH 7

Scheme 2.1. Structure of polyphenols related to this chapter and the synthesis protocol of the materials.

2.3. Results and Discussion

2.3.1. Synthesis and Characterization

2.3.1.1. Synthesis and Imaging

Materials were synthesized by mixing the polyphenols and either ferrous sulfate (Mat-1 and Mat-2) or ferric nitrate (Mat-3) in water with an iron:gallic equivalent ratio kept constant at ~ 1:1. The tannic acid (TA) contains 10 gallic acid units, hence iron:TA used for Mat-1 and Mat-3 are 10:1. In guava leaf extract, a mixture of polyphenols are present, we determined the gallic acid equivalent was determined using the Folin Ciocalteu reagents [19] and the amount of iron salt to be added was calculated so as to maintain a 1:1 ratio (gallic acid:iron). This ratio compensates for the variation of polyphenol content in the extract from batch to batch. This particular ratio was chosen to be used based on a preliminary spectrophotometric titration of TA with ferrous sulfate, which showed the maximum absorbance at TA:Fe ratio of 1:10-12 i.e., iron and gallic unit ratio of ~1:1(Figure 2.1). Incidentally, all the known structurally characterized iron gallate complexes had an iron: gallate ratio of 1:1 [3,4,9].

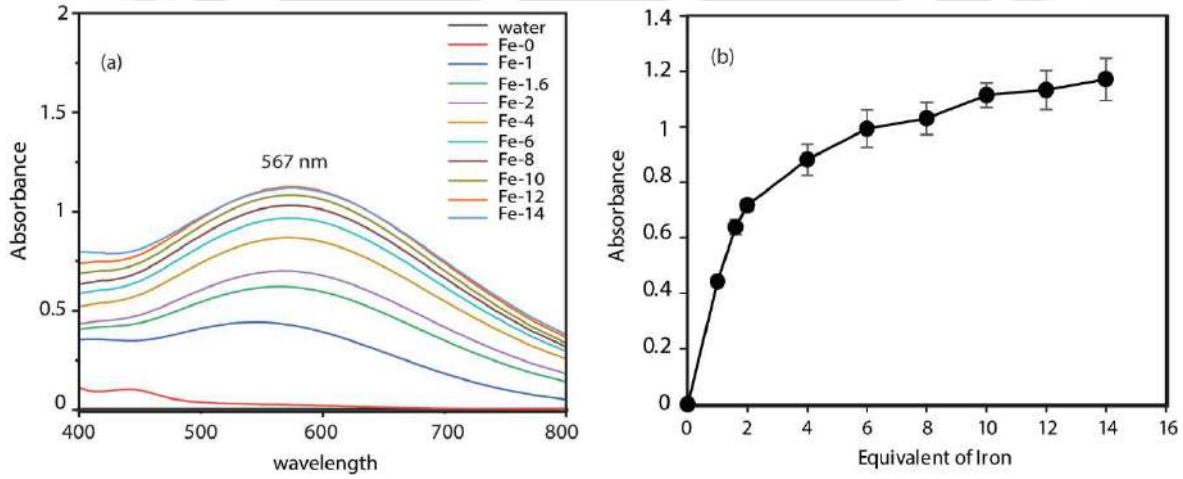

Figure 2.1. (a) UV spectra of tannic acid titrated with increasing amount of iron (II) salt, and (b) absorbance vs. iron equivalent plot of the titration monitored at 567nm.

Mixing polyphenol with iron salt instantly changes the color to dark blue. The pH of the solution is ~3.5. Dynamic light scattering (DLS) measurement of the solution showed the

solution contains colloid particles with an average particle size of 339 nm and 187 nm for Mat-1 (from TA) and Mat-2 (from leaf extract), respectively (Figure 2.2).

The pH of the solution was adjusted to 7 using dilute sodium hydroxide. The materials started precipitating at pH 5. The complete precipitation was observed at pH 7. Materials were isolated in black-blue solid forms after centrifugation for 5 minutes at 8000 rpm. Further studies were performed on these solids.

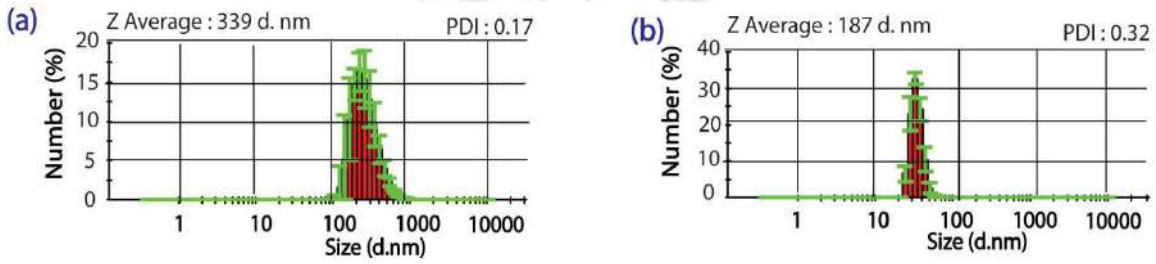

Figure 2.2. Particle size distribution plot from DLS experiment of (a) Mat-1 before centrifuge, (b) Mat-2 before centrifuge.

FESEM images of Mat-1 and Mat-2 before redispersion showed particles of less than 50 nm size agglomerated to clusters of ~1micron size (Figure 2.3a, 2.3b). Mat-3 was isolated as chunky clumps but, after dispersion, it has the same morphology as Mat -1 and Mat-2 (Figure 2.3f). FESEM images of synthesized Mat-2, before and after dispersion are not very different (Figure 2.3b and Figure 2.3d).

Nanoparticle from Fe(II) and tannic acid (1:5 ratio) for coating mouse hair have been observed by Cui and co-workers, but re-dispersibility has not been reported [20]. Moustafa and co-workers reported Fe_3O_4 nanoparticle formation from ferrous sulfate and dried guava leaf extract without isolation of the material in the solid-state [21]. FESEM images and DLS experiments confirmed that the present iron-phenol materials formed nanoparticles similar other reports. The FETEM images illustrate the size and shape of Mat-1 and Mat-2. Figure 2.4 shows the agglomerated form of materials with the size of < 50nm.

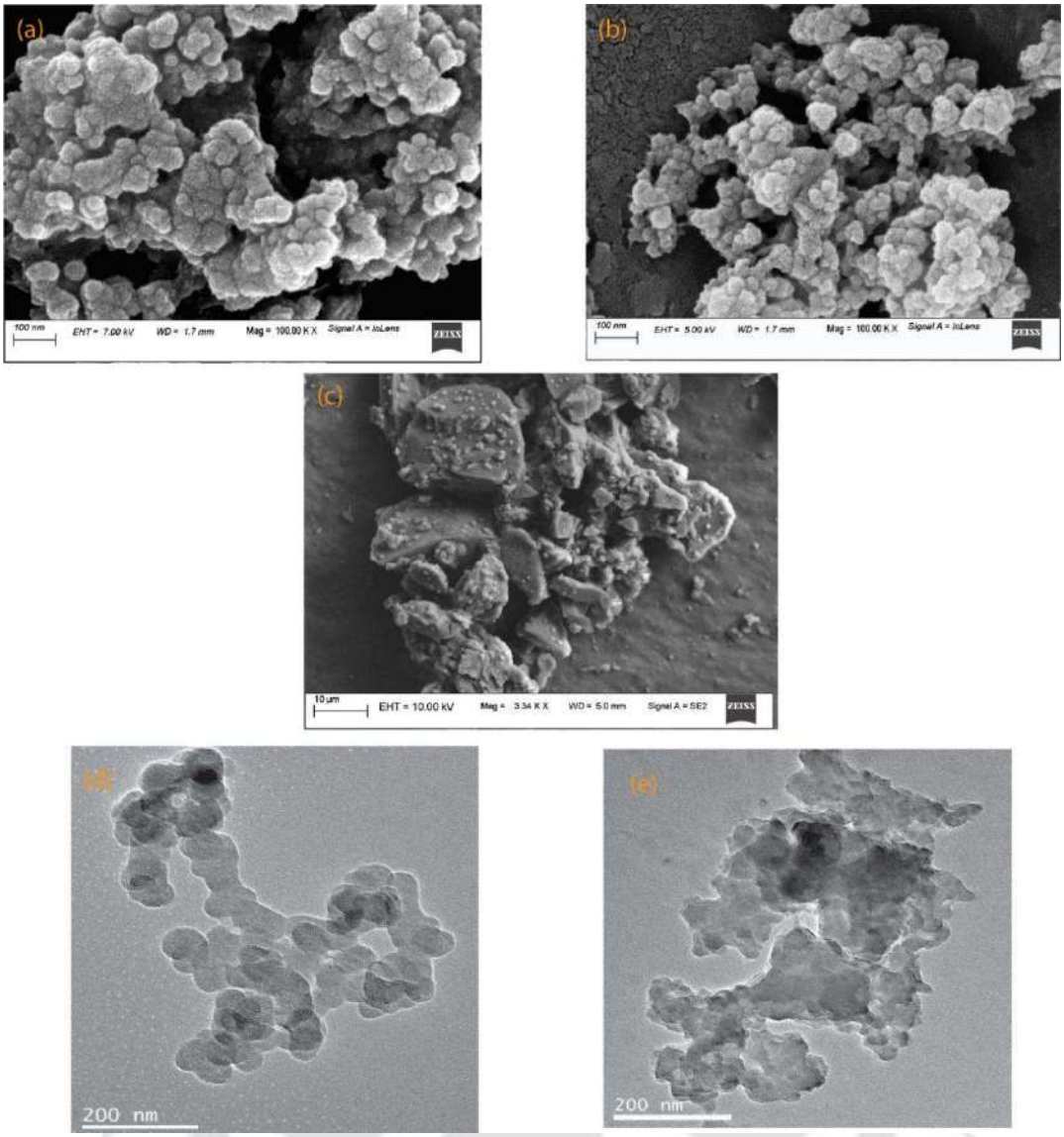

Figure 2.3. FESEM images of isolated solids of (a) Mat-1, (b) Mat-2 and (c) Mat-3; FETEM images of (d) Mat-1 and (e) Mat-2.

2.3.2. Chemical Characterizations

2.3.2.1. Elemental Analysis

Elemental analyses of the materials are presented in Table 2.1. These values are the average of three-sets from three different batches. As the synthesis did not involve any carbon source other than polyphenols, the Fe:C ratio for Mat-1 is found to be 1:8.6, close to the value 1:8.4 expected for 9 iron per tannic acid (Molecular formula $C_{76}H_{52}O_{46}$). Mat-2 shows Fe:C ratio of 1:11 as guava extract has mainly 3-O-glycosides (for example, quercetin) and flavan-3-ol (for instance,

catechin), most of which has a larger carbon framework than gallic acid units in Mat-1 [16,17,22]. The extra carbon would increase molecular weight and thus increase the carbon ratio to 1:11 even when iron:polyphenol ratio was 1:1. Mat-3 could not be analyzed due to the presence of nitrate counter ions, which undergo exploitation above 80°C.

Table 2.1. Characterization data of the synthesized materials.[a]

	Analysis C%, H%, Fe%	Fe:C	TGA[b] %	Susceptibility, cm3 g-1	X-Band g, 298K	EPR g, 77K
Mat-1	29.66 (± 1.2), 3.78 (± 0.21), 15.98	1:8.6	18	2.14 × 10–5 (± 0.11)	2.091	4.99[c]
Mat-2	29.66 (± 0.74), 4.17 (± 0.15), 12.4	1:11.2	22	1.67 × 10–5 (± 0.17)	2.099	5.05[c]
Mat-3	-	-	-	6.8 × 10–5 (± 0.3)	2.127	2.26

[a] elemental analyses are an average of three measurements, while iron % is an average of two measurements. Weight loss was monitored up to 450 °C. Magnetic susceptibilities are the average of three measurements. Standard deviations are in parenthesis. Mat-3 explodes at ~80 °C as it contains nitrate counter ion. Elemental analysis and thermogravimetric analysis were not performed for Mat-3. [b] weight loss up to 200 °C. [c] Very weak signal.

2.3.2.2. FTIR Analysis

The three prominent FTIR peaks of tannic acid at 1717 (νC=O, ester), 1609, and 1535 cm^{-1} were shifted to approximately 1690, 1630, and 1580 cm^{-1} respectively after binding with iron in Mat-1 and Mat-3 (Figure 2.4). Tannic acid, Mat-1, and Mat-3 had a prominent peak at ~758 cm^{-1}, usually because of in-plane aromatic ring vibration. The same was also observed in the FTIR of gallic acid, which is a constituent of tannic acid [23]. The FTIR spectrum of the polyphenols in the extract could not be obtained as the solution was dilute and the medium was water. The FTIR of the material synthesized from it (Mat-2) was recorded (Figure 2.4). The absence of peak ~1700 cm^{-1} or higher shows the absence of the carboxylic or ester group in it

[24]. If the sulfate anion (from $FeSO_4$) is present in Mat-1 and Mat-2, it should show a vibration peak at 1100 cm^{-1}. However, it is fairly obscured by the 1100 cm^{-1} peak present in starting polyphenol itself. Although, XPS spectra confirmed the presence of sulfur in Mat-1 and Mat-2 (2.3.2.5). A sharp and intense peak at 1380 cm^{-1} in FTIR of Mat-3 confirmed the presence of nitrate (Figure 2.4) [24]. We concluded that all the materials contain counter anions.

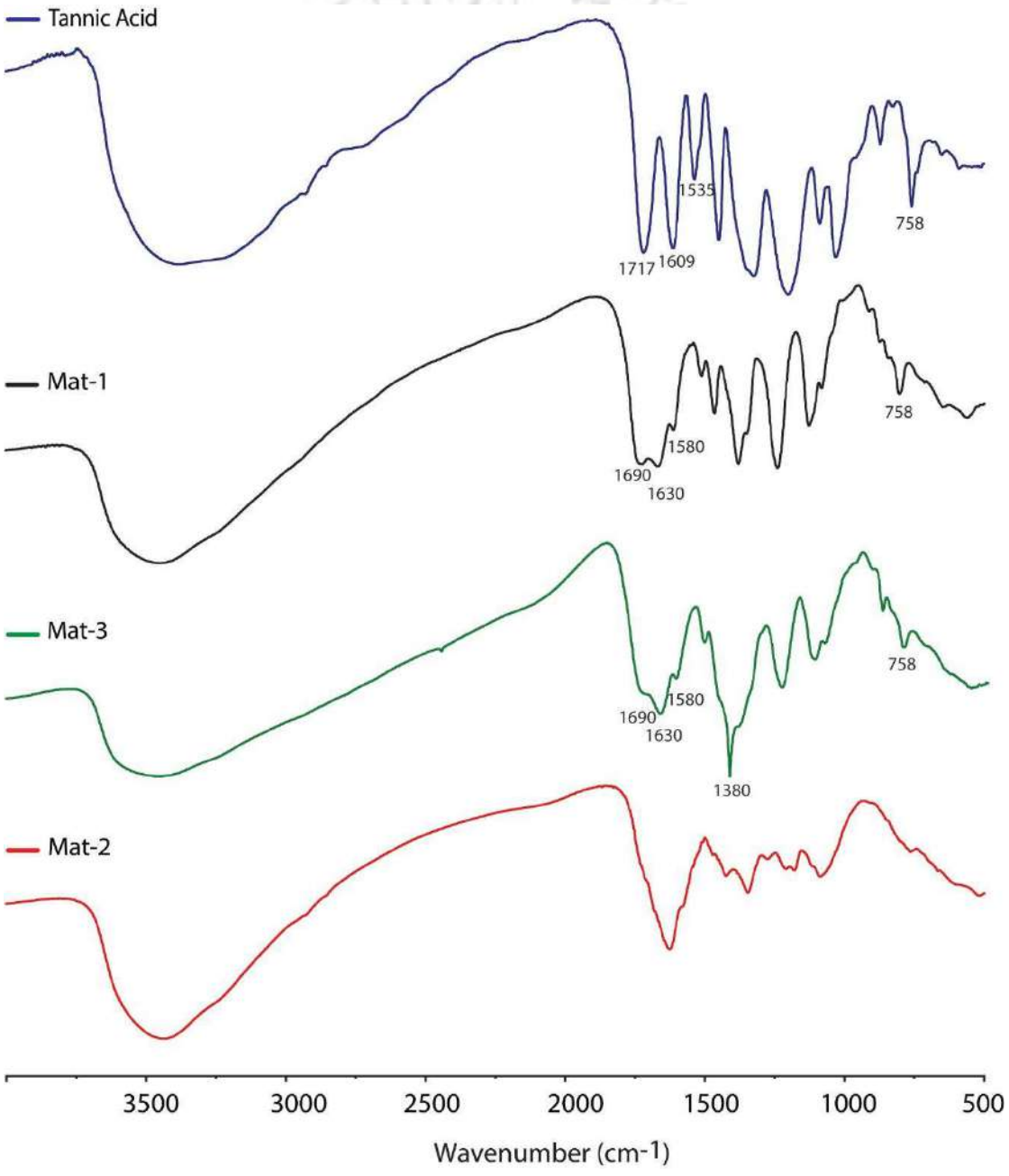

Figure 2.4. FTIR spectra of Mat-1, Mat-2, Mat-3, and tannic acid.

2.3.2.3. Mass spectral Analysis

Mass spectra of starting polyphenols in aqueous solutions were recorded using the electrospray ionization technique (ESI-Mass). Polyphenols easily lose acidic protons forming anions; hence negative ion mode was used. Corresponding iron-polyphenol materials, which are insoluble, were recorded using the matrix-assisted laser desorption (MALDI) technique. In this case, positive ion mode was used as the presence of counter ions confirmed their overall positive charge.

The ESI-Mass spectrum of tannic acid (Figure 2.5, Table 2.2) shows molecular ion peak for monoanionic form at 1699.49 (calculated for $[M\text{-}H^+]^-$, 1699.16) and dianionic form at 849.24 (calculated for $[M\text{-}2H^+]^{2-}$, 849.08). Monoanionic and dianionic mass ions could be easily distinguished as they have different line separations. Due to charge difference, the line separation for monoanionic is 1 a.m.u. while for the dianionic it is 0.5 a.m.u. unit. Apart from molecular ion peaks, it showed a sequential fragmentation pattern with successive loss of 152.03 mass units (calculated for $C_7H_4O_4$, 152.01), which corresponds to the loss of one gallic acid unit. A similar loss of 76 mass units between the dianionic forms (76 x 2 = 152) was observed as well (Figure 2.5, Table 2.2). It corresponds well with the tannic acid used, having esters of 10 gallic acid units with a central sugar unit (Scheme 2.1).

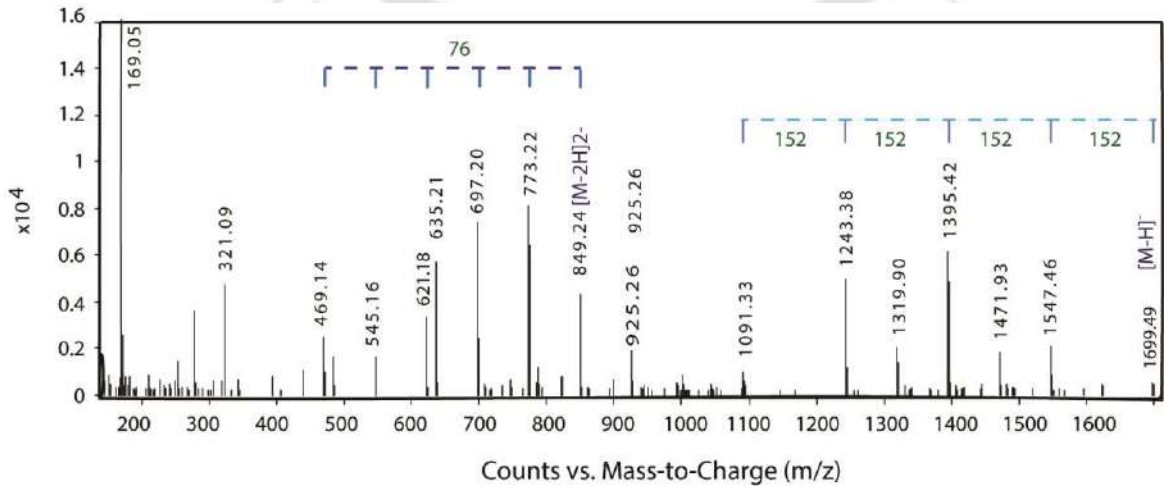

Figure 2.5. ESI mass of tannic acid in negative mode.

Table 2.2 Molecular ion and other fragments observed in ESI-Mass spectra of Tannic acid.

	Formula		Calc. for [M]-H^+	Found	Calc. for [M]-$2H^+$	Found
Tannic acid	$C_{76}H_{52}O_{46}$	1700.17	1699.16	1699.49	849.08	849.24
Fragments						
Sugar+9 gallic acid	$C_{69}H_{48}O_{42}$	1548.16	1547.15	1547.46	773.07	773.22
Sugar+8 gallic acid	$C_{62}H_{44}O_{38}$	1396.15	1395.14	1395.42	697.07	697.20
Sugar+7 gallic acid	$C_{55}H_{40}O_{34}$	1244.14	1243.13	1243.37	621.06	621.18
Sugar+6 gallic acid	$C_{48}H_{36}O_{30}$	1092.13	1091.12	1091.33	545.06	545.16
Sugar+5 gallic acid	$C_{41}H_{32}O_{26}$	940.12	939.11	n.o.	469.05	469.14
Sugar+3 gallic acid	$C_{27}H_{24}O_{18}$	636.1	635.09	635.21	317.04	n.o.
Gallic acid	$C_7H_6O_5$	170.12	169.11	169.04	84.05	n.o.

Tannic acid is an ester of one sugar unit and 10 gallic acid unit. n. o. = not observed.

MALDI for Mat-1 was scanned up to 2000 mass units. However, mass peaks with significant intensity were observed only up to 1200 mass units. MALDI is a harsh technique compared to ESI-mass. The peaks were assigned based on the fragmentation patterns and distinctive isotopic patterns caused by naturally occurring iron isotopes ^{54}Fe (5.8%),^{56}Fe (91.7%), ^{57}Fe (2.2%), and ^{58}Fe (0.3%). Therefore, extensive fragmentation was observed (Figure 2.6). The highest mass peak observed at 1114.8 could be assigned having oxidized sugar unit, five gallic acid unit complexed with three iron (calculated for $[C_{41}H_{23}Fe_3O_{27}]^+$, 1114.84, Figure 2.6b). The reason being, oxidation of sugar is justified under the oxidizing condition in the positive ion mode. Less intense peaks were observed due to the fragmentation of the highest peak. Two types of fragmentation were observed. Each prominent peak was fragmented stepwise by 16 units (mass of oxygen, 15.9997), presumably due to loss of phenolic oxygen. The other type of fragmentation is the loss of 205.5 units between sets of peaks. The loss of 205.5 mass units could be assigned to iron (III) bound to gallic acid (Figure 2.6a).

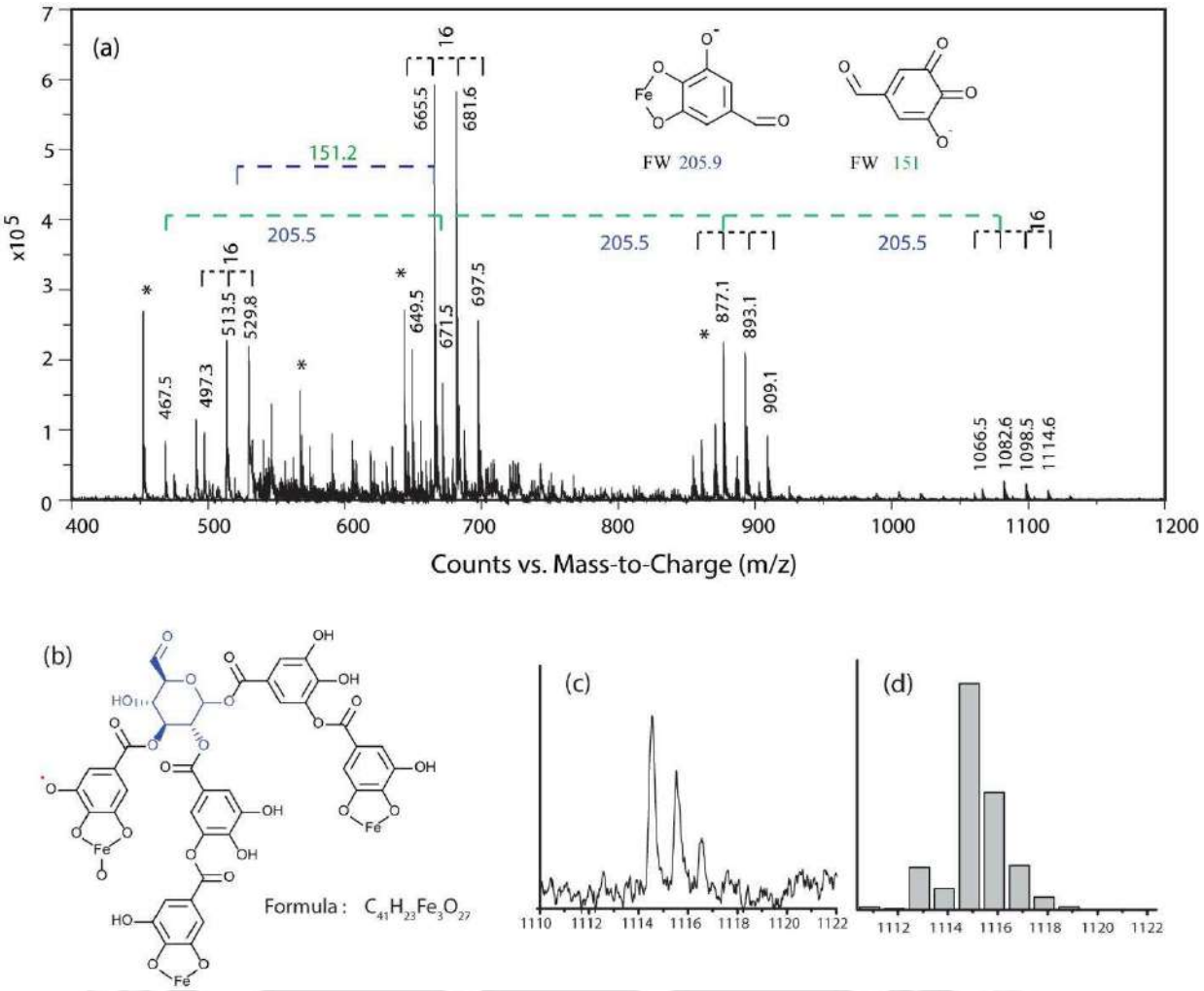

Figure 2.6. (a) MALDI Mass of Mat-1 (Tannic acid- Iron Complex) (b) chemical formula of at MW 1114.6 (c) tannic-iron mass complexed observed (MW 1114.6) (d) calculated isotopic distribution.

This supports the binding of iron to gallic acid units of tannic acid. The other notable feature is the presence of oxygen bound to Fe (III). Compared to tannic acid, extract from guava leaves is a multi-component mixture. Díaz-de-Cerio and other literature identified many polyphenols in the cold alcoholic extract of leaves of a different guava species [17,22]. They found that flavonols (alcohol) and flavan-3-ols (ketone) type of polyphenols together constitute over 70% of the extract with gallic acid derivatives are ~20% [17]. In the present work, some of these polyphenols in the hot aqueous extract used in the present work, using ESI-Mass spectrometry, were being identified (Figure 2.7, and Table 2.3). Some of the peaks that were identified and tentatively assigned are as listed below in Table 2.3.

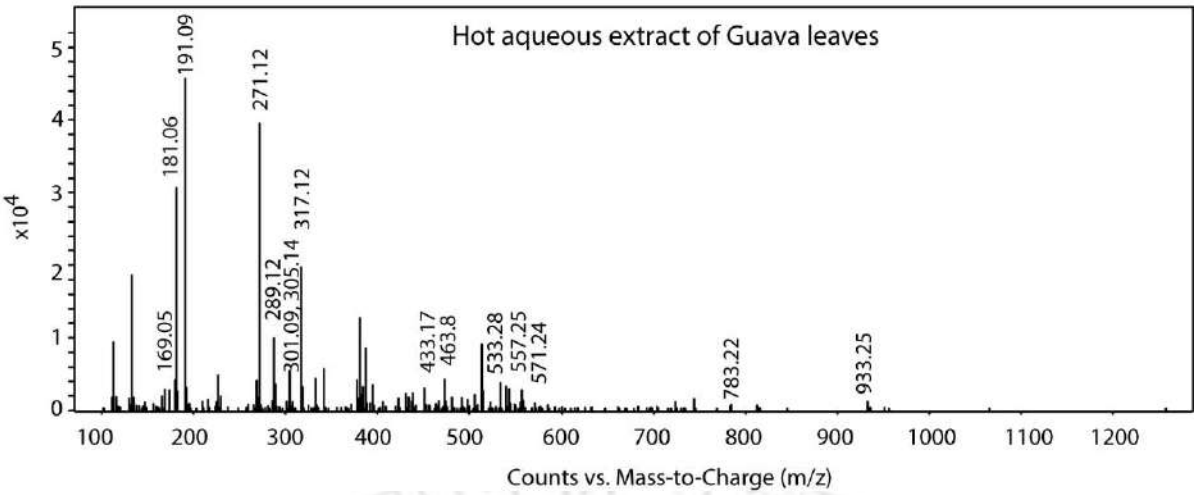

Figure 2.7. ESI mass of guava extract in negative mode.

Table 2.3. Chemicals identified in Guava leaf extract from the ESI-Mass spectrum.

Found	Formula $[M-H]^-$	Mass unit	Tentative Assignment
933.26	$C_{41}H_{25}O_{26}$	933.07	Stenophyllanin A / Vescalagin/castalagin Isomer
783.22	$C_{34}H_{23}O_{22}$	783.07	Pedunculagin/casuarinin isomer
571.	$C_{28}H_{27}O_{13}$	571.15	Guavinoside B
557.2	$C_{27}H_{25}O_{13}$	557.13	2,6-dihydroxy-3-methyl-4- O-(6″-O-galloyl-β-D-glucopyranosyl)- benzophenone
533.28	$C_{26}H_{29}O_{12}$	533.17	Phellatin
463.18	$C_{21}H_{19}O_{12}$	463.08	Isoquercitrin, hyperin
433.16	$C_{20}H_{17}O_{11}$	433.07	Reynoutrin, Guajaverin, Avicularin
317.10	$C_{15}H_9O_8$	317.03	Myricetin
305.19	$C_{15}H_{13}O_7$	305.07	Gallocatechol
301.09	$C_{15}H_9O_7$	301.03	Quercetin/Morin
289.13	$C_{15}H_{14}O_6$	289.07	Catechin
271.1	$C_{15}H_{11}O_5$	271.06	Naringenin
191.10	$C_7H_{11}O_6$ / $C_6H_7O_7$	191.05 / 191.02	Quinic Acid / citric acid
181.06	$C_6H_{13}O_6$	181.07	Galactitol, by reduction of galactose
169.06	$C_7H_5O_5$	169.11	*Gallic acid*

[a] Assignments were in conjunction with other reports of guava leaves under different extraction conditions. The polyphenols with the same mass value are clubbed together in the assignment.

The identifying peaks in the MALDI mass spectra of the corresponding Mat-2 were assigned in Figure 2.8. We were able to assign two iron (III) Fe_2O and Fe_2O_2 (presumably oxo-bridged complexes) units with Pedunculagin or casuarinin isomer ($[Fe^{III}_2O_2(C_{34}H_{21}O_{22})]^+$ at 925.14, which is much closer to the calculated value i.e. 924.91) and Guavinoside B ($[Fe^{III}_2O(C_{28}H_{25}O_{13})]^+$ at 697.5, calculated = 696.99). These complexes showed multiple loss of 16 mass units (O, 15.9997) due to the loss of uncoordinated phenols, just like Mat-1 (Figure 2.8). Unlike tannic acid, the guava leaf extract has mainly low molecular weight (< 1000 mass unit) polyphenols (Table 2.3). However, compared to tannic acid, these polyphenols have a higher carbon content. The C:O ratio of tannic acid is 1.5, whereas most of the polyphenols in the extract are close to 2 and above. Considering approximately one polyphenol bound to one iron supports the higher C ratio observed in the elemental analysis of Mat-2 (Table 2.1).

Combining results of elemental analysis and mass spectrometry, it can be confirmed that the Mat-1 is an iron complex of tannic acid having ~1 gallic acid unit per iron. At the same time, Mat-2 is a mixture of iron complexes of low molecular weight (low compared to tannic acid but higher than gallic acid units) polyphenols. The presence of $Fe^{III}O$ fragments in Mat-1 and Fe_2O and Fe_2O_2 in Mat-2 is indicative of oxo bridged binuclear iron (III) formed during oxidation of Fe (II) in the presence of aerial oxygen [8]. Oxo iron bridges are known to form during aerial oxidation of Fe (II) [8] but confirming its presence here needs additional support. MALDI spectrum of Mat-3 was recorded multiple times, which showed peaks of only up to 400 mass units (Figure 2.9). It did not fragment enough to analyze.

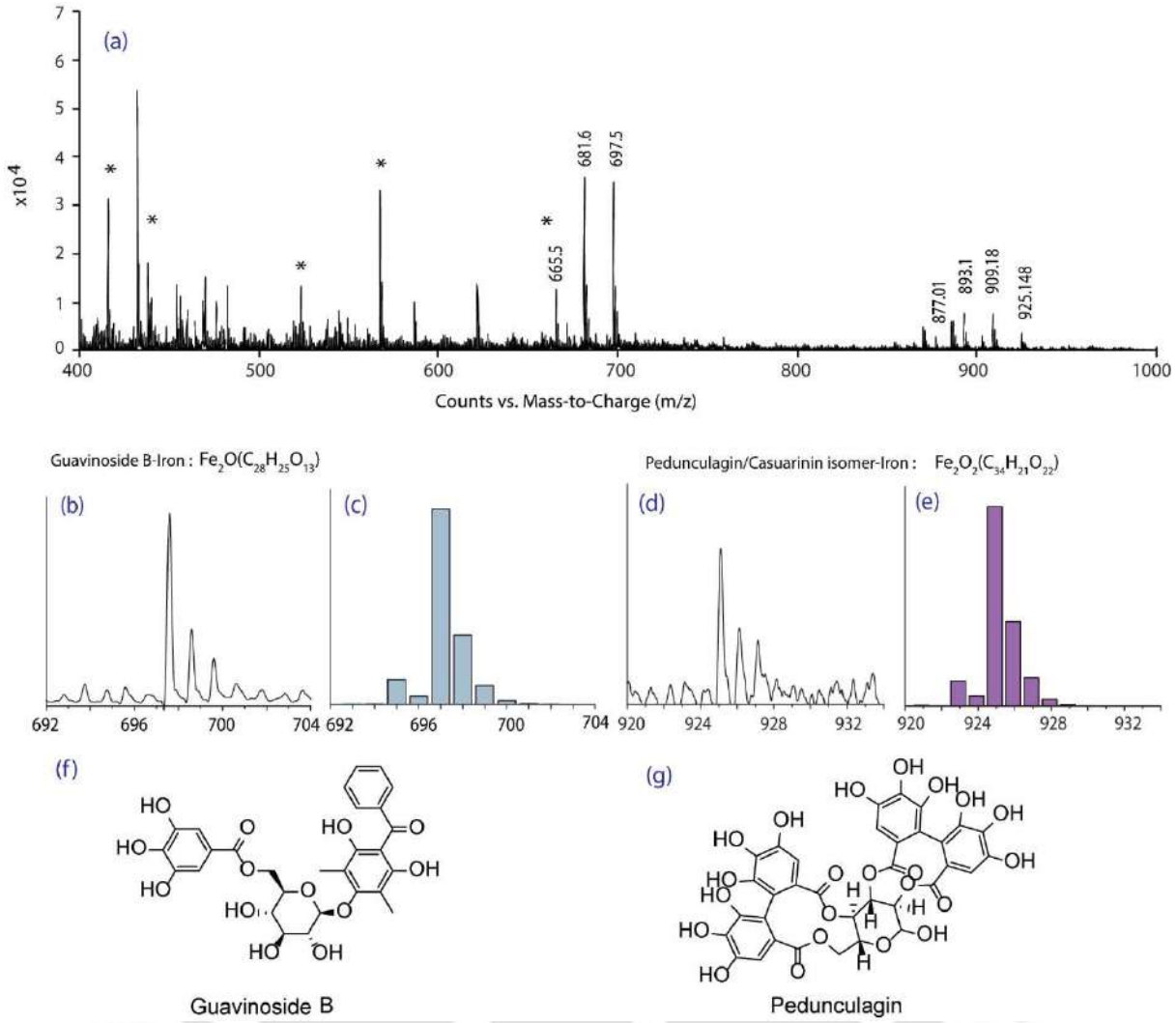

Figure 2.8. MALDI mass analysis of Mat-2 in HCCA matrix (a); Observed and calculated isotopic distribution of Guavinoside b-Iron complex (b) and (c) and Pedunculagin/Casuarinin Iron complex (d) and (e), respectively; Structure of (f) Guavinoside B and (g) Pedunculagin. * Marks the peak positions expected for the HCCA matrix used in measurements.

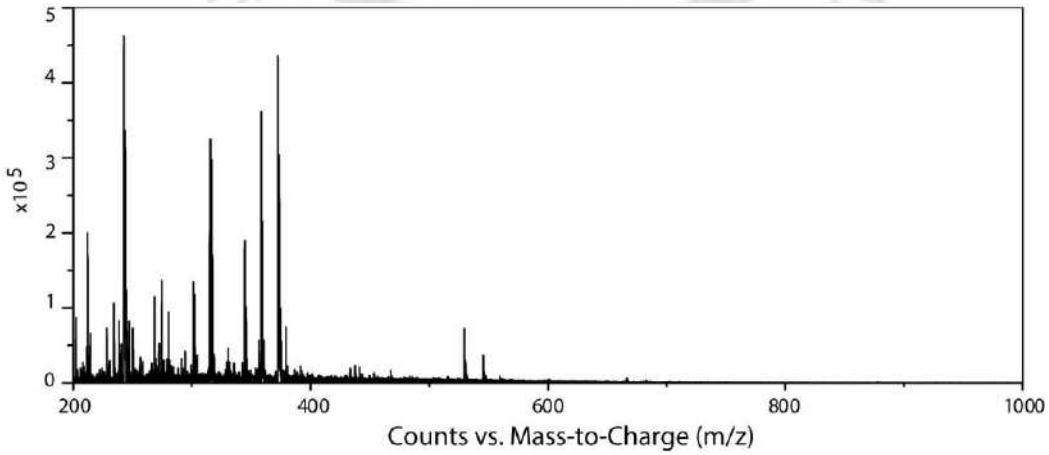

Figure 2.9. MALDI mass spectrum of Mat-3 in HCCA matrix.

2.3.2.4. EPR Analysis

In principle, X-Band Electron paramagnetic resonance (EPR) spectroscopy can distinguish magnetically uncoupled iron (III) which is EPR active, and oxo-bridged anti-ferromagnetically coupled Fe (III). The later is usually EPR active at room temperature (depends on extent of coupling), but EPR inactive at low temperature [25]. Iron (II) is not EPR active in the X-band range. EPR spectra of the solid powder of Mat-1, Mat-2, and Mat-3 were recorded at room temperature and 77K (Figure 2.10). We compared their intensity using an identical setting and a fixed sample size. Diphenyl picryl hydrazide (DPPH) served as a reference. At room temperature, all show broad signal at g =2, symptomatic of iron (III). Mat-3 showed a significantly intense signal as compared to the other two materials. At 77K, the signal for Mat-1 and Mat-2 almost disappeared, barring a very weak signal at g =4.2, symptomatic of rhombic high spin iron (III) [25]. This disappearance of signal supports the presence of magnetically coupled iron (III) (ground state S=0) as the majority of iron (III) is present in Mat-1 and Mat-2. The EPR signal of Mat-3 at 77K was intense (Figure 2.10b). This confirms the presence of a significant amount of uncoupled mononuclear high-spin iron (III) in Mat-3. The broad curvature in spectra at low temperature is due to dissolved oxygen in liquid nitrogen used to lower temperature. As the Fe (II) is not EPR active in this range. Its presence can be identified from X-ray photoelectron spectroscopy (XPS) (Section 2.3.2.5).

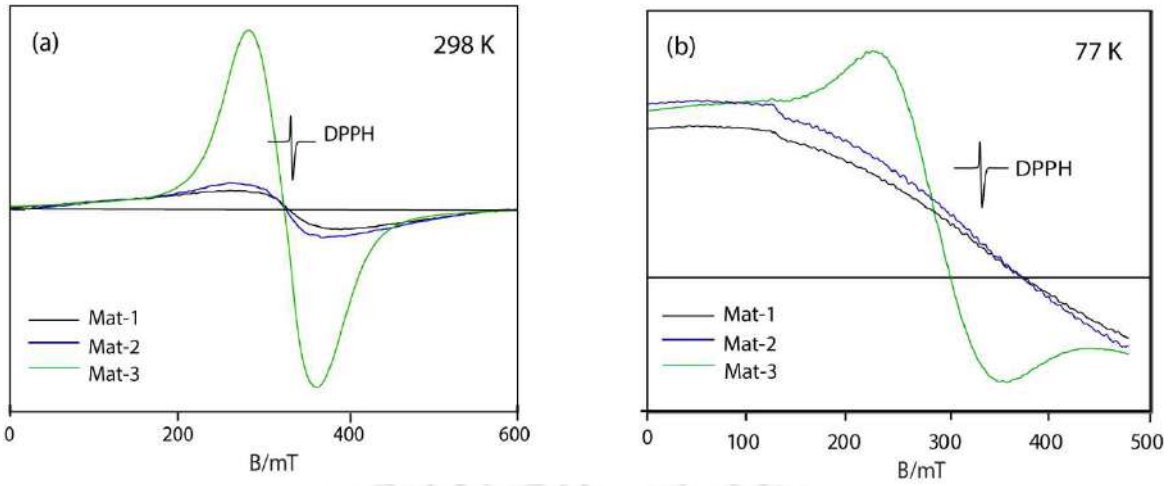

Figure 2.10. EPR plot of Mat-1, Mat-2, and Mat-3 at (a) room temperature and (b) at liquid nitrogen temperature (77K).

2.3.2.5. XPS Analysis

The composition and valency state of elements present in Mat-1, Mat-2, and Mat-3 were investigated using XPS. The spectra showed the peaks of Fe, O, C, S in Mat-1, Fe, O, C, S, N in Mat-2, and Fe, O, C, N in Mat-3 (Figure 2.11, Table 2.4). The oxidation states of the iron were determined by fitting the profiles at 710 eV (Fe^{+2}) and 711.8 eV (Fe^{+3}) for Mat-1, 709.8 eV (Fe^{+2}) and 711.3eV (Fe^{+3}) for Mat-2 711.29 eV (Fe^{+3}) for Mat-3 at Fe $2P_{3/2}$ region (Figure 5) [26,27]. We found that Mat-1 and Mat-2 contain Fe^{+3} and Fe^{+2}, whereas, Mat-3 contains Fe^{+3} only (Figure 2.11). Measuring area covered under the fitted graph, the Fe^{+2} and Fe^{+3} were found to be 25% and 75% for Mat-1; 38.5% and 61.5% for Mat-2 (Table 2.4).

The peaks for S in Mat-1 and Mat-2 confirmed the presence of sulphate anions (Figure 2.11a, 2.11b, Table 2.4). Additionally, N peaks in XPS were observed in Mat-2 and Mat-3. Further, the N peak in Mat-3, synthesized from iron (III) nitrate, was from the nitrate anion. The characteristic sharp peak of nitrate vibration at 1380 cm^{-1} is present in FTIR, supporting nitrate's presence (Figure 2.11c). The N in XPS is not expected in XPS of Mat-2 as it was not synthesized using nitrate salt, and FTIR did not show a nitrate peak at 1380 cm^{-1}. We tested for protein [28] in the guava leaf extract to know the nitrogen source, but none was found. The

source and nature of N in Mat-2 are unknown at this point. The C1s XPS spectra indicated the presence of C-C at 284 eV and C=O at 288 eV (Figure 2.12) [29]. The O 1s XPS spectra showed the presence of C-O at 533 eV and 532 eV for Organic C=O as well as structural -OH [30].

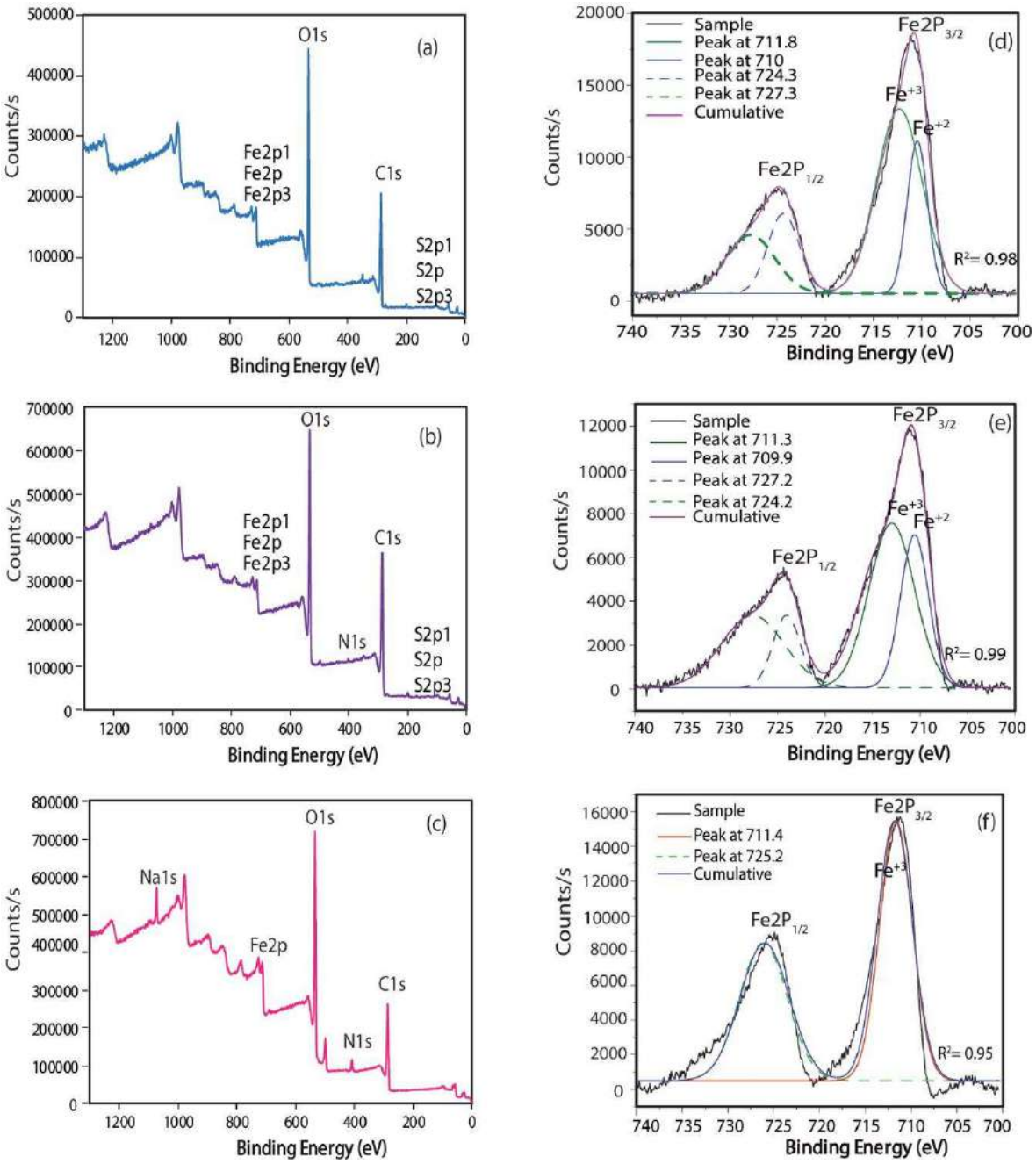

Figure 2.11. Elemental analysis of (a) Mat-1, (b) Mat-2 and Mat-3.

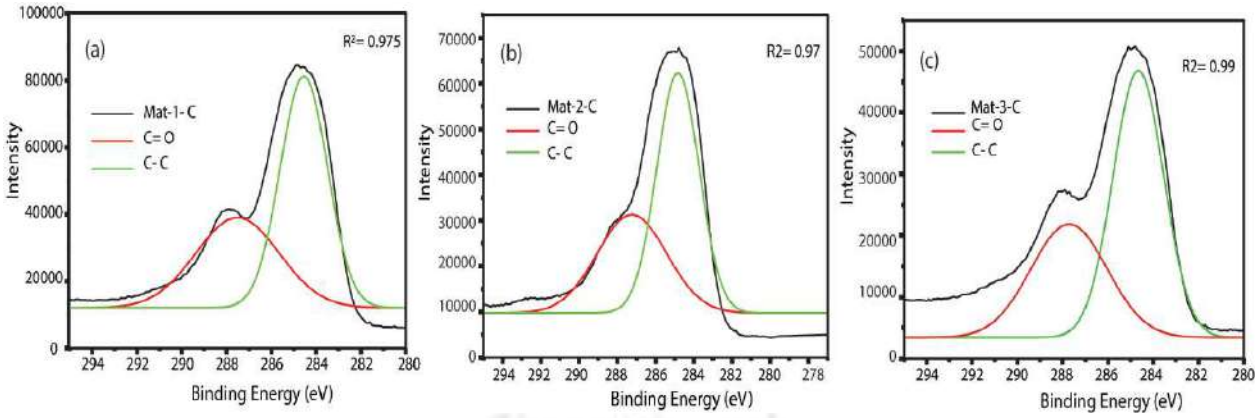

Figure 2.12. XPS spectra of carbon (a) Mat-1, (2) Mat-2, and (3) Mat-3.

Table 2.4. XPS data table of Mat-1, Mat-2, and Mat-3.

Material	Name	Ref Peak	Found peak	Atomic %	Area %	Confirm
Mat-1	O	531.5–532	531.74	38.1		Organic C=O
	C	284.8	284.67	58.26		C-C
	S		167.27	1.1		
	Fe2p1		725.1(724.3,727.3)	0.24		
	Fe2P		711.8	1.5	75.8%	Fe^{+3}
	Fe2P3		710.	0.6	24.2%	Fe^{+2}
Mat-2	O1s		531.78	36.33		Organic C=O
	C1s		284.89	60.72		C-C
	N1s		400.2	0.81		
	S		167.79	0.8		
	Fe2p1		724.5(724.2,727.2)	0.03		
	Fe2P		711.3	0.92	61.5%	Fe^{+3}
	Fe2P3	709.6	709.9	0.4	38.5%	Fe^{+2}
Mat-3	O1s		531.69	42.55		
	C1s		284.79	46.47		
	N1s		406.65	2.48		
	Fe2P1		725.2	5.38		
	Fe2p		711.29		100%	Fe^{+3}

2.3.2.6. Magnetic Susceptibility and Powder X-Ray Diffraction

The magnetic susceptibilities of the materials were measured (Table 1.1). The significantly higher magnetic susceptibility of Mat-3, compared to Mat-1 and Mat-2, supports the observation (EPR section) that it contains uncoupled high-spin iron(III) while the other two most likely have magnetically coupled iron(III) (Table 2.1) [31]. Powder X-ray results were noisy and hardly showed any peak (Figure 2.13). The materials are amorphous and do not contain any Fe(0) or iron oxides [10][32]. Furthermore, we pyrolyzed Mat-1 and Mat-2 at 800 °C to convert to oxide and recorded FESEM and powder X-ray (Figure 2.14, 2.13d). FESEM images of oxides look very clean and evenly sized (Figure 2.14). Comparison of powder X-ray pattern before and after pyrolysis (Figure 2.13) showed that Mat-1 did not have any significant amount of oxide before pyrolysis. Similar conclusions can be drawn for the other two materials (Figure 2.13) [33][34].

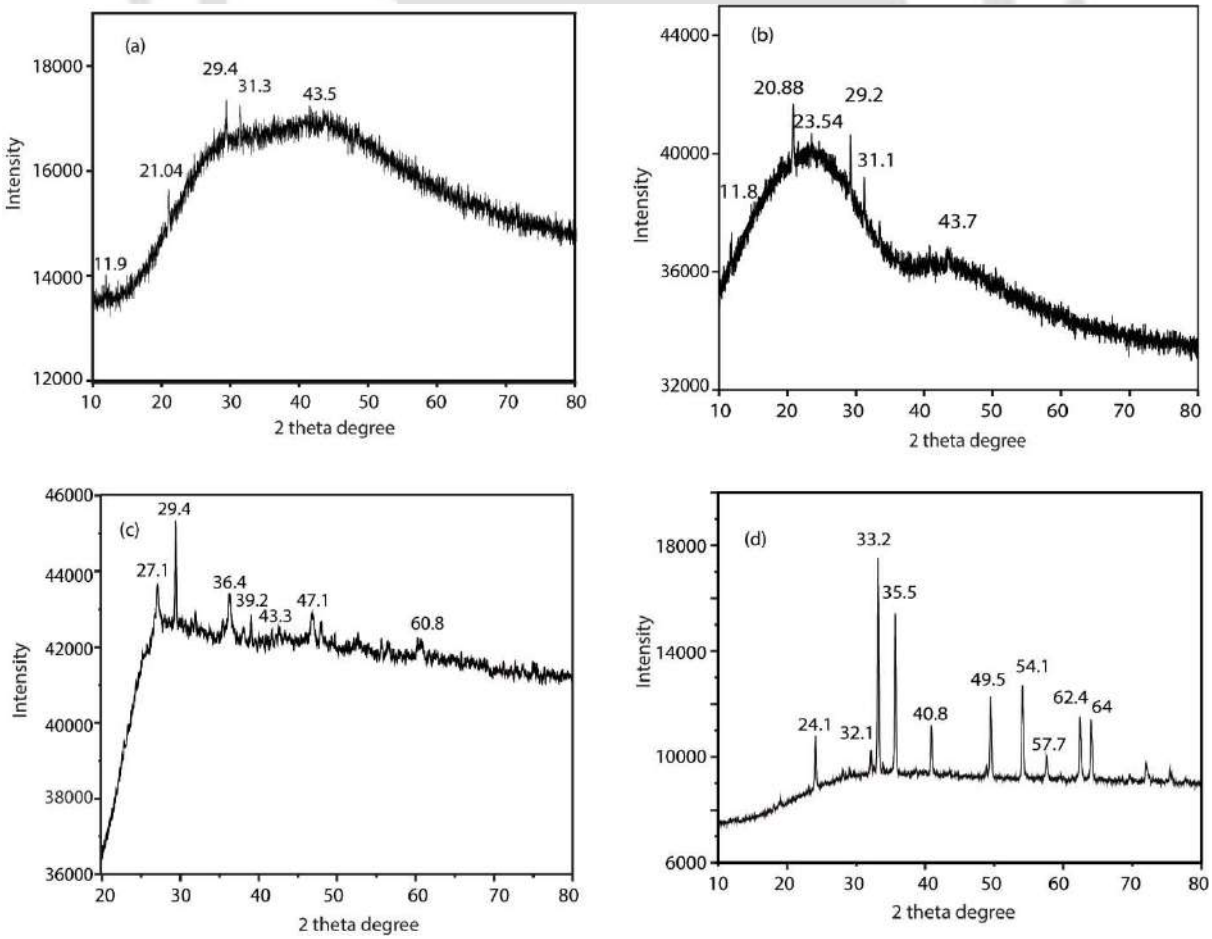

Figure 2.13. Powder XRD of (a) Mat-1, (b) Mat-2, (c) Mat-3 and (d) oxide of Mat-1.

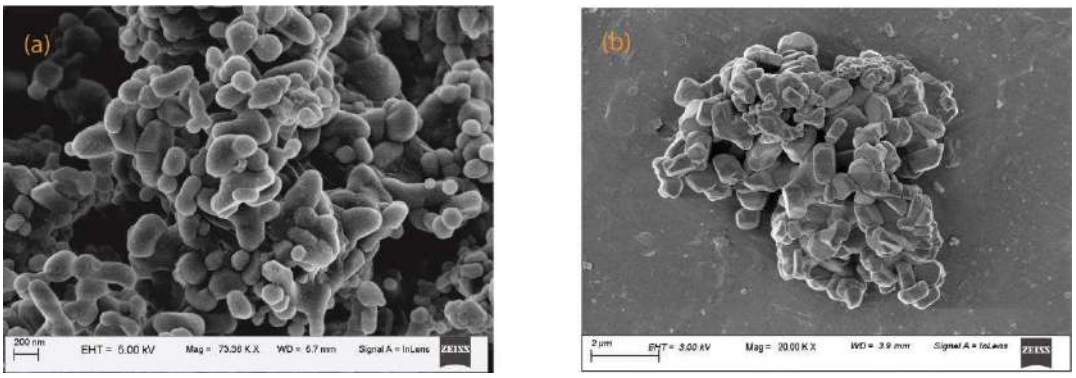

Figure 2.14. FESEM images of oxide of (a) Mat-1 and (b) Mat-2.

2.3.3. Thermal Stability

The thermal stability of the materials was analyzed by thermogravimetric analysis (TGA). The TGA of both Mat-1 and Mat-2 were recorded between 20°C to 450 °C (Figure 2.15). The first weight loss started at ~60°C and continued up to ~160°C. The weight losses were ~18% for Mat-1 and 22% for Mat-2, likely due to water evaporation (Table 2.1). With the increase in temperature, further weight losses of 43% and 38% occurred for Mat-1 and Mat-2, respectively, above 250°C, mainly due to the material's decomposition. Mat-1 and Mat-2 are thermally stable at <160°C. Mat-3 explodes beyond 60°C due to nitrate counter ion.

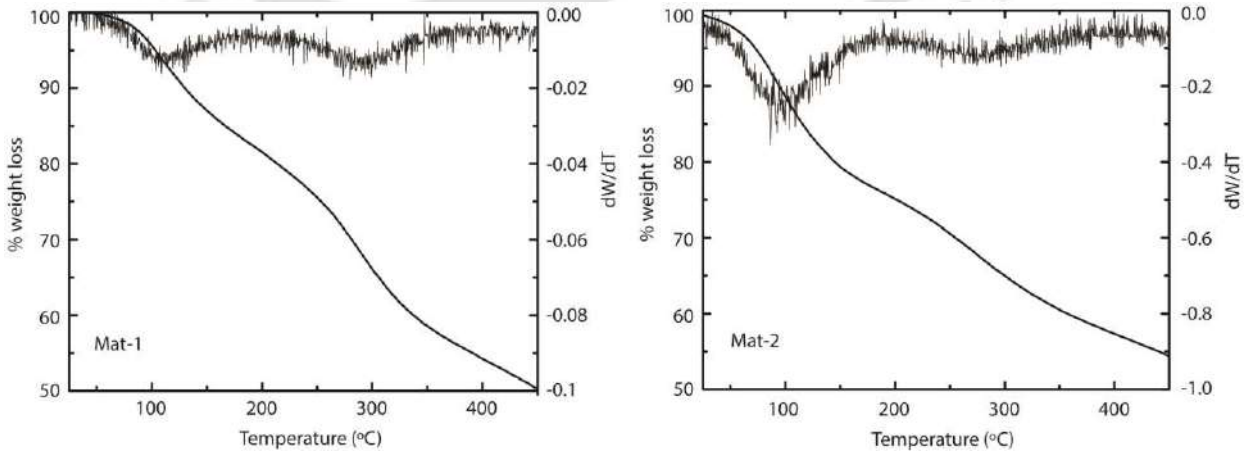

Figure 2.15. TGA of Mat-1 and Mat-2.

2.3.4. Surface Area Measurement

The surface area of the materials was estimated using nitrogen adsorption-desorption studies at 77 K temperature (Figure 2.16). The surface area determined from multipoint BET analysis of Mat-1 and Mat-2 were 99.6 and 100.9 m^2/g, respectively, which are very close to each other (Table 2.5). The present materials have a surface area within the range found for other related nanomaterials. The (BET) surface area of Fe_2O_3 NPs of Plantain extract showed a surface area of 11.31 m^2/g [35]. Singh et al. (2017) showed the surface area of Fe_3O_4 coated-tea polyphenol is 126.8 m^2/g [36]. The surface area of Mat-3 is low at 3.0 m^2/g. The adsorption−desorption isotherm of Mat-1 and Mat-2 were very similar (Figure 2.16). Both showed an H3-type of the hysteresis loop that demonstrated the presence of non-rigid aggregates of plate-like particles or assemblages of slit-shaped pores (Figure 2.16) [37,38]. Mat-3 showed H4 type of hysteresis, which signifies particles with internal voids of irregular shape and broad size distribution or hollow spheres with walls. The pore diameter and pore volume of Mat-3 were also the highest among the three materials (Table 2.5). Overall, Mat-1 and Mat-2 have very similar adsorption surfaces consisting of rigid aggregates. The surface area of both is much lower than activated charcoal.

Table 2.5. BET isotherm parameters of all synthesized materials.

Method	Parameter	Mat-1	Mat-2	Mat-3
Multi-point BET	Surface Area, m^2/g	99.557	100.882	3.045
	Average pore diameter, nm	14.64	24.82	41.81
	Total pore volume, cc/g	0.364	0.626	0.032
adsorption	Surface Area, m^2/g	77.77	74.90	10.14
	Pore diameter, nm	3.814	3.601	6.513
	Pore volume, cc/g	0.350	0.611	0.029
desorption	Surface Area, m^2/g	92.78	81.11	25.05
	Pore diameter, nm	3.75	17.18	3.79
	Pore volume, cc/g	0.350	0.610	0.036

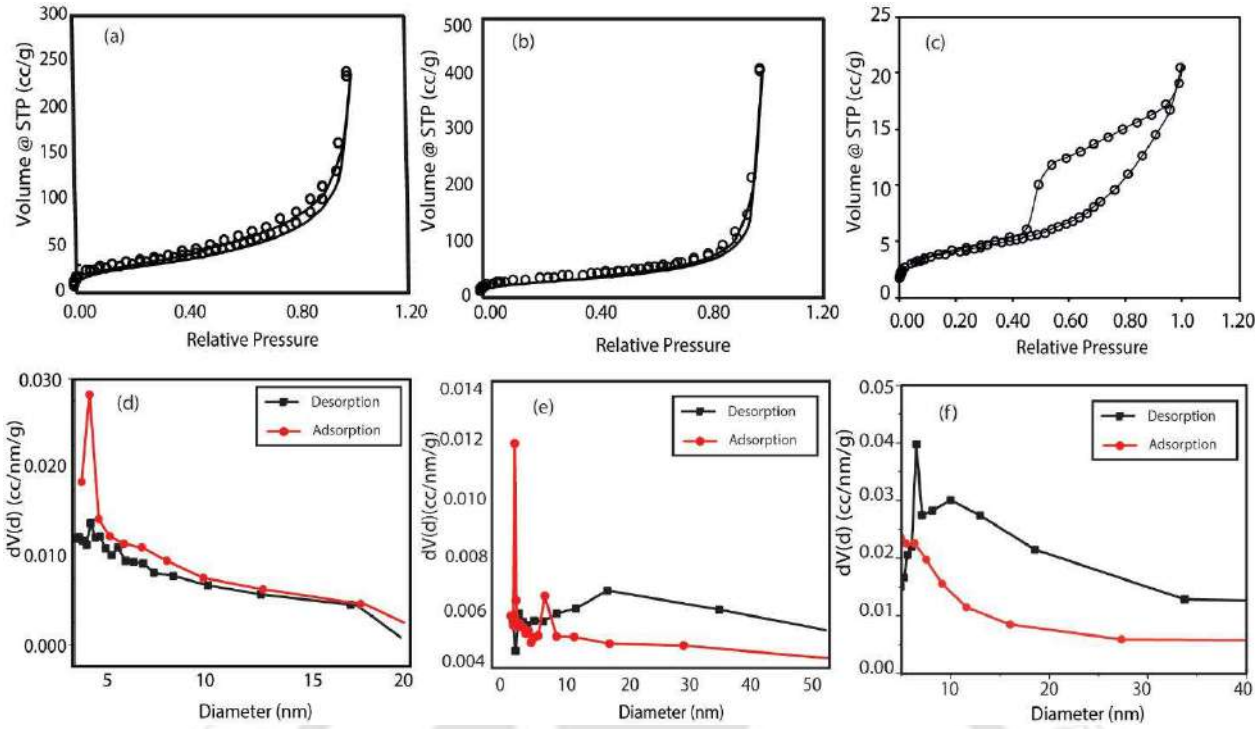

Figure 2.16. BET isotherms of (a), (d) Mat-1; (b), (e) Mat-2; (c), (f) Mat-3**.**

2.3.5. Determination of Point of Zero Charge (pH_{zpc})

The surface charge is one of the most important parameters controlling the adsorption process. Therefore, the point of zero charges (pH_{zpc}) was determined by two methods, mass titration and immersion technique [39] . In the mass titration method, materials were varied in quantity with 5, 10, and 15 g/L in 0.03 M KNO_3 solution and kept in a magnetic stirrer for 24 h at 250 rpm. After agitation, the measured pH_{zpc} of solutions for Mat-1, Mat-2, and Mat-3 was 3.9, 4.2, and 2.6, respectively (Figure 2.17). In the mass titration method, pH_{zpc} was estimated by plotting equilibrium pH versus mass of the materials. In the immersion technique, the pH_{zpc} was determined by varying the pH of KNO_3 solution from 2-10 with 1 N HCl/ NaOH at a fixed material dose of 5 g/L and kept in a shaker for 24 h at 250 rpm. (Figure 2.17). In immersion technique, the change of pH (ΔpH) versus initial pH plot was analyzed.

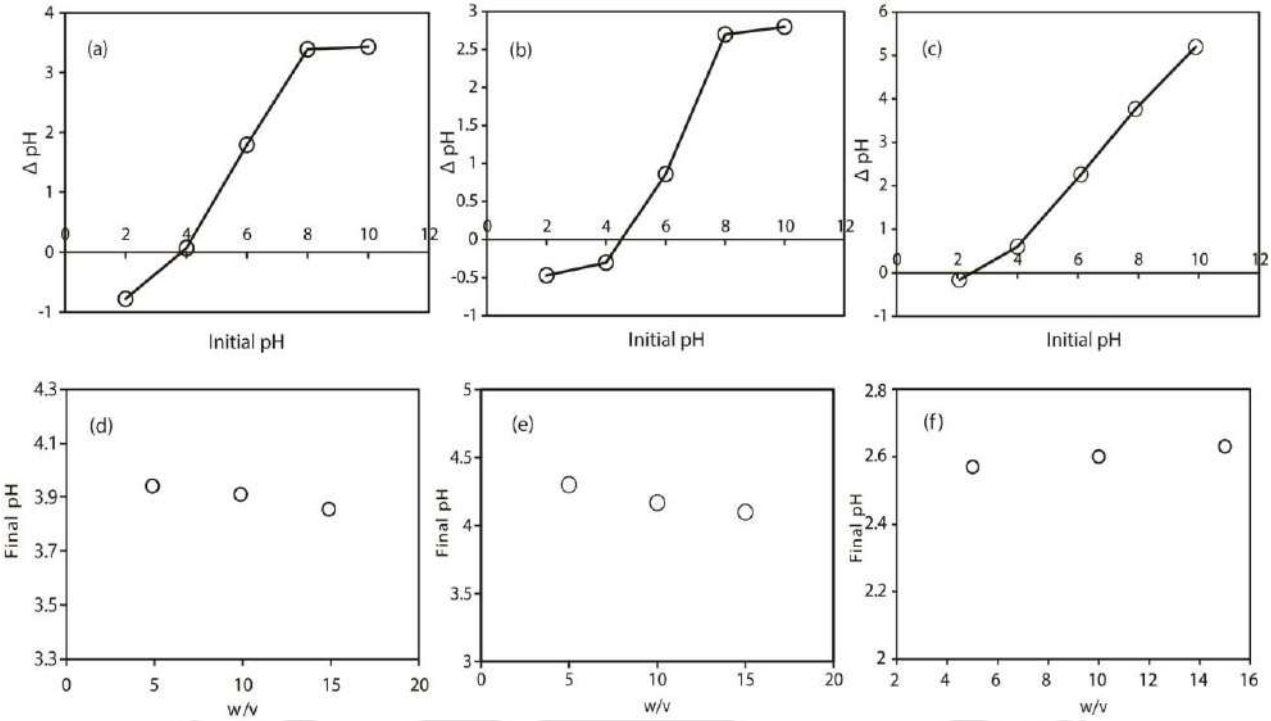

Figure 2.17. (a), (b), (c) represent the pH_{zpc} of Mat-1, Mat- 2, and Mat-3 by immersion technique, and (d), (e), (f) represent the pH_{zpc} determination by mass titration method of respective materials.

From the immersion method, the pH_{zpc} was found to be 3.9, 4.5, and 2.5 for Mat-1, Mat-2, and Mat-3, respectively. Values obtained from both techniques were very close. The value indicated the pH at which the net charge of the total particle surface is zero and above which the surface has a negative charge. All three values were lower than 7, which means that it would produce an acidic solution after adding into neutral water. This could be more likely due to presence of acidic phenols in all the materials. The other possibility is that iron (III) absorbs the hydroxyl group from water, resulting in an acidic solution (hydrolysis). The value of Mat-3 confirmed that it is the most acidic out of all the three materials.

2.3.6. Re-dispersibility

Dispersibility of the solids was tested with water: methanol of 1:1 at different pH (4-9) under sonication for 4 min. Both Mat-1 and Mat-2 dispersed at pH 7 and stayed dispersed for at

least 24 h. In contrast, a small quantity of Mat-3 was dispersed, which precipitated in less than an hour. DLS on the dispersed solutions showed particles with an average size of 740-800 nm (Figure 2.18). It is a useful property in terms of storage. Other reports did not explore this property.

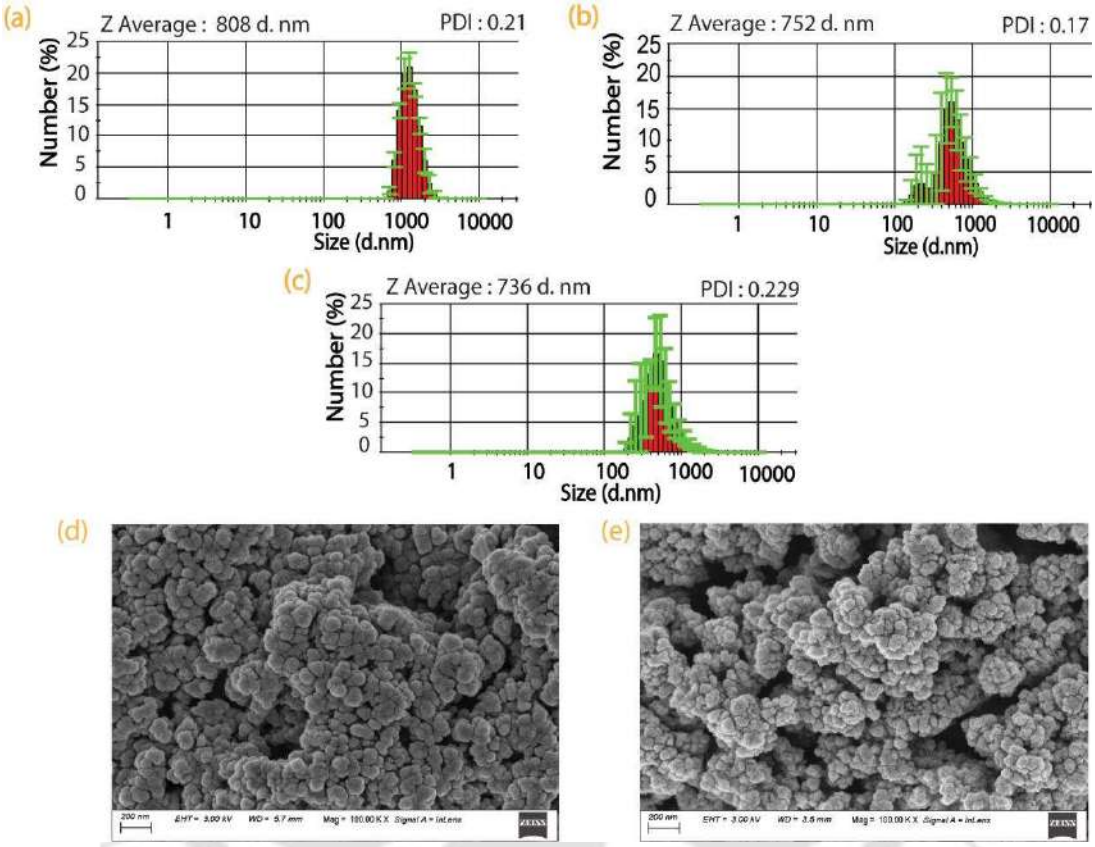

Figure 2.18. Particle size distribution plot from DLS experiment, after re-dispersibility in 1:1 MeOH: H2O of (a) Mat-1, (b) Mat-2 and (c) Mat-3 respectively. FESEM of after re-dispersibility in 1:1 MeOH: H2O of (d) Mat-2 and (e) Mat-3.

2.4. Conclusion

Materials were synthesized by using two different types of plant-based polyphenol and reacting it with iron (II) salt under similar conditions. One of the polyphenols is tannic acid, common in many plants, including gall nuts. This is commercially available in pure form, and the structure contains ten esterified gallic acid (Scheme 2.1). The other one is a raw extract of guava leaves (*Psidium guajava*), which is known to have a large quantity 3-O-glycosides and

flavan-3-ol type of polyphenols (Scheme 2.1) [35-37]. Both Mat-1 and Mat-2 are very similar in color and morphology (Section 2.3.1). Both materials were identified as clusters of nanoparticles (Figure 2.1) which re-disperses in nanoparticulate in Methanol (Figure 2.2, 2.3, 2.4). MALDI-mass (Figure 2.7, 2.9) and XPS analysis (Figure 2.12) revealed that these contain mostly Fe(III) complexes of polyphenols with either one or two oxygen bound to Fe(III). Moreover, both materials have Fe(II) as a minor component. Another material, Mat-3, prepared from Fe(III) salt and tannic acid, showed only Fe(III) presence (Figure 2.12). EPR at low temperature and room temperature susceptibility supported oxo-bridged Fe(III) in Mat-1 and Mat-2 but not in Mat-3. The surface area of Mat-1 and Mat-2 were found similar but higher than Mat-3 (Section 2.3.4, Table 2.5). Thus, Mat-1 and Mat-2, despite being synthesized from different polyphenols, were found to be very similar in chemical and physical properties but unlike from Mat-3.

References

[1] N.R. Perron, H.C. Wang, S.N. Deguire, M. Jenkins, M. Lawson, J.L. Brumaghim, Kinetics of iron oxidation upon polyphenol binding, Dalt. Trans. 39 (2010) 9982–9987. https://doi.org/10.1039/c0dt00752h.

[2] M.I. Din, A. Zahoor, Z. Hussain, R. Khalid, A review on green synthesis of iron (Fe) nanomaterials, its alloys and oxides, Inorg. Nano-Metal Chem. 0 (2020) 1–17. https://doi.org/10.1080/24701556.2020.1862229.

[3] A. Ponce, L.B. Brostoff, S.K. Gibbons, P. Zavalij, C. Viragh, J. Hooper, S. Alnemrat, K.J. Gaskell, B. Eichhorn, Elucidation of the Fe(III) Gallate Structure in Historical Iron Gall Ink, Anal. Chem. 88 (2016) 5152–5158. https://doi.org/10.1021/acs.analchem.6b00088.

[4] R.K. Feller, A.K. Cheetham, Fe(III), Mn(II), Co(II), and Ni(II) 3,4,5-trihydroxybenzoate (gallate) dihydrates; a new family of hybrid framework materials, Solid State Sci. 8 (2006) 1121–1125. https://doi.org/10.1016/j.solidstatesciences.2006.04.013.

[5] N.R. Perron, H.C. Wang, S.N. Deguire, M. Jenkins, M. Lawson, J.L. Brumaghim, Kinetics of iron oxidation upon polyphenol binding, Dalt. Trans. 39 (2010) 9982–9987. https://doi.org/10.1039/c0dt00752h.

[6] J.D. Hem, Complexes of Ferrous Iron With Tannic Acid, Chem. Iron Nat. Water. 1459 (1960) 75–94. https://pubs.usgs.gov/wsp/1459d/report.pdf.

[7] V. Rouchon, M. Duranton, C. Burgaud, E. Pellizzi, B. Lavédrine, K. Janssens, W. De Nolf, G. Nuyts, F. Vanmeert, K. Hellemans, Room-temperature study of iron gall ink impregnated paper degradation under various oxygen and humidity conditions: Time-dependent monitoring by viscosity and X-ray absorption near-edge spectrometry measurements, Anal. Chem. 83 (2011) 2589–2597. https://doi.org/10.1021/ac1029242.

[8] M.J. Sever, J.J. Wilker, Visible absorption spectra of metal – catecholate and metal – tironate, (2004) 1061–1072.

[9] C. -H Wunderlich, R. Weber, G. Bergerhoff, Über Eisengallustinte, ZAAC - J. Inorg. Gen. Chem. 598 (1991) 371–376. https://doi.org/10.1002/zaac.19915980134.

[10] V. Madhavi, T.N.V.K.V. Prasad, A.V.B. Reddy, B. Ravindra Reddy, G. Madhavi, Application of phytogenic zerovalent iron nanoparticles in the adsorption of hexavalent chromium, Spectrochim. Acta - Part A Mol. Biomol. Spectrosc. 116 (2013) 17–25. https://doi.org/10.1016/j.saa.2013.06.045.

[11] F. Luo, Z. Chen, M. Megharaj, R. Naidu, Biomolecules in grape leaf extract involved in one-step synthesis of iron-based nanoparticles, RSC Adv. 4 (2014) 53467–53474. https://doi.org/10.1039/C4RA08808E.

[12] T. Shahwan, S. Abu Sirriah, M. Nairat, E. Boyaci, A.E. Eroglu, T.B. Scott, K.R. Hallam, Green synthesis of iron nanoparticles and their application as a Fenton-like catalyst for the degradation of aqueous cationic and anionic dyes, Chem. Eng. J. 172 (2011) 258–266. https://doi.org/10.1016/j.cej.2011.05.103.

[13] S. Groiss, R. Selvaraj, T. Varadavenkatesan, R. Vinayagam, Structural characterization, antibacterial and catalytic effect of iron oxide nanoparticles synthesised using the leaf extract of Cynometra ramiflora, J. Mol. Struct. 1128 (2017) 572–578. https://doi.org/10.1016/j.molstruc.2016.09.031.

[14] Z. Fu, R. Chen, Study of complexes of tannic acid with Fe(III) and Fe(II), J. Anal. Methods Chem. 2019 (2019). https://doi.org/10.1155/2019/3894571.

[15] Y.M. Li, X. Miao, Z.G. Wei, J. Cui, S.Y. Li, R.M. Han, Y. Zhang, W. Wei, P. Control, R. Development, Iron-tannic acid nanocomplexes : facile synthesis and application for removal of methylene blue from aqueous solution, 11 (2016) 1045–1061.

[16] W. Nantitanon, S. Yotsawimonwat, S. Okonogi, Factors influencing antioxidant activities and total phenolic content of guava leaf extract, LWT - Food Sci. Technol. 43 (2010) 1095–1103. https://doi.org/10.1016/j.lwt.2010.02.015.

[17] E. Díaz-de-Cerio, A.M. Gomez-Caravaca, V. Verardo, A. Fernandez-Gutierrez, A. Segura-Carretero, Determination of guava (Psidium guajava L.) leaf phenolic compounds using HPLC-DAD-QTOF-MS, J. Funct. Foods. 22 (2016) 376–388. https://doi.org/10.1016/j.jff.2016.01.040.

[18] D.F. Evans, A new type of magnetic balance, J. Phys. E. 7 (1974) 247–249. https://doi.org/10.1088/0022-3735/7/4/007.

[19] I. Standard, ISO 14502-1 Content of total polyphenols in tea — Colorimetric method using Folin- Ciocalteu reagent, Int. Stand. (2005) 1–10.

[20] H. Geng, L. Zhuang, M. Li, H. Liu, F. Caruso, J. Hao, J. Cui, Interfacial Assembly of Metal-Phenolic Networks for Hair Dyeing, ACS Appl. Mater. Interfaces. 12 (2020) 29826–29834. https://doi.org/10.1021/acsami.0c06928.

[21] M. Moustafa, R. shams Al Din, Green Synthesis and Characterization of Iron-Oxide Nanoparticles By Guava Aqueous Leaves Extract for Doxorubicin Drug Loading, J. Biosci. Appl. Res. 3 (2017) 177–180. https://doi.org/10.21608/jbaar.2017.126138.

[22] E. Díaz-De-Cerio, V. Verardo, A.M. Gómez-Caravaca, A. Fernández-Gutiérrez, A.

Segura-Carretero, Determination of polar compounds in guava leaves infusions and ultrasound aqueous extract by HPLC-ESI-MS, J. Chem. 2015 (2015) 1–9. https://doi.org/10.1155/2015/250919.

[23] Y.P. Neo, S. Ray, J. Jin, M. Gizdavic-Nikolaidis, M.K. Nieuwoudt, D. Liu, S.Y. Quek, Encapsulation of food grade antioxidant in natural biopolymer by electrospinning technique: A physicochemical study based on zein-gallic acid system, Food Chem. 136 (2013) 1013–1021. https://doi.org/10.1016/j.foodchem.2012.09.010.

[24] K. Nakamoto, Infrared and Raman Spectra of Inorganic and Coordination Compounds, 2008. https://doi.org/10.1002/9780470405840.

[25] J.T. Weisser, M.J. Nilges, M.J. Sever, J.J. Wilker, EPR investigation and spectral simulations of iron-catecholate complexes and iron-peptide models of marine adhesive cross-links, Inorg. Chem. 45 (2006) 7736–7747. https://doi.org/10.1021/ic060685p.

[26] J.F. Moulder, W.F. Stickle, P.E. Sobol, K.D. Bomben, Handbook of X-ray photoelectron spectroscopy: a reference book of standard spectra for identification and interpretation of XPS data, 1992. https://www.cnyn.unam.mx/~wencel/XPS/MANXPS.pdf.

[27] V. V. Makarov, S.S. Makarova, A.J. Love, O. V. Sinitsyna, A.O. Dudnik, I. V. Yaminsky, M.E. Taliansky, N.O. Kalinina, Biosynthesis of stable iron oxide nanoparticles in aqueous extracts of hordeum vulgare and rumex acetosa plants, Langmuir. 30 (2014) 5982–5988. https://doi.org/10.1021/la5011924.

[28] M. Friedman, Applications of the Ninhydrin Reaction for Analysis of Amino Acids, Peptides, and Proteins to Agricultural and Biomedical Sciences, J. Agric. Food Chem. 52 (2004) 385–406. https://doi.org/10.1021/jf030490p.

[29] D. Gan, W. Xing, L. Jiang, J. Fang, C. Zhao, F. Ren, L. Fang, K. Wang, X. Lu, Plant-inspired adhesive and tough hydrogel based on Ag-Lignin nanoparticles-triggered dynamic redox catechol chemistry, Nat. Commun. 10 (2019) 1–10. https://doi.org/10.1038/s41467-019-09351-2.

[30] C. Xiao, H. Li, Y. Zhao, X. Zhang, X. Wang, Green synthesis of iron nanoparticle by tea extract (polyphenols) and its selective removal of cationic dyes, J. Environ. Manage. 275 (2020) 111262. https://doi.org/10.1016/j.jenvman.2020.111262.

[31] C.J. O'Connor, Magnetochemistry-Advances in Theory and Experimentation, in: 2007: pp. 203–283. https://doi.org/10.1002/9780470166307.ch4.

[32] Y.P. Sun, X. qin Li, J. Cao, W. xian Zhang, H.P. Wang, Characterization of zero-valent iron nanoparticles, Adv. Colloid Interface Sci. 120 (2006) 47–56.

https://doi.org/10.1016/j.cis.2006.03.001.

[33] Y. Yi, G. Tu, P. Eric, S. Xiao, Z. Fang, Green synthesis of iron-based nanoparticles from extracts of Nephrolepis auriculata and applications for Cr (VI) removal, Mater. Lett. 234 (2019) 388–391. https://doi.org/10.1016/j.matlet.2018.09.137.

[34] Z. Wang, C. Yu, C. Fang, M. Megharaj, Removal of acid red 94 and methylene blue using iron-polyphenol nanomaterials synthesized by various plant leaves: A comparison study, Proc. 2014 Int. Conf. Nanosci. Nanotechnology, ICONN 2014. (2014) 39–42. https://doi.org/10.1109/ICONN.2014.6965256.

[35] S. Venkateswarlu, Y.S. Rao, T. Balaji, B. Prathima, N.V.V. Jyothi, Biogenic synthesis of Fe3O4 magnetic nanoparticles using plantain peel extract, Mater. Lett. 100 (2013) 241–244. https://doi.org/10.1016/j.matlet.2013.03.018.

[36] K.K. Singh, K.K. Senapati, K.C. Sarma, Synthesis of superparamagnetic Fe_3O_4 nanoparticles coated with green tea polyphenols and their use for removal of dye pollutant from aqueous solution, J. Environ. Chem. Eng. 5 (2017) 2214–2221. https://doi.org/10.1016/j.jece.2017.04.022.

[37] M. Thommes, K.A. Cychosz, Physical adsorption characterization of nanoporous materials: Progress and challenges, Adsorption. 20 (2014) 233–250. https://doi.org/10.1007/s10450-014-9606-z.

[38] K.A. Cychosz, M. Thommes, Progress in the Physisorption Characterization of Nanoporous Gas Storage Materials, Engineering. 4 (2018) 559–566. https://doi.org/10.1016/j.eng.2018.06.001.

[39] N. Fiol, I. Villaescusa, Determination of sorbent point zero charge: Usefulness in sorption studies, Environ. Chem. Lett. 7 (2009) 79–84. https://doi.org/10.1007/s10311-008-0139-0.

Chapter III

Methylene Blue Removal Using Materials Synthesized in Chapter II

3.1. Introduction

In the previous chapter, two materials were synthesized and characterized using two polyphenols and iron (II) salt, was discussed. From the characterization, it was concluded that both the materials are complexes of iron-polyphenol, where iron is bound with polyphenol through oxo bridge. In materials, Fe(III) is present as the major component, and Fe(II) is present as a minor component. The pH_{zpc} values of Mat-1 and Mat-2 was 3.9 and 4.5, respectively. Above these pH_{zpc} values, the surface of materials is expected to be negatively charged. Therefore, they might be capable of removing positively charged pollutants. Hence, methylene blue was used as a probe to check the removal capability of both Mat-1 and Mat-2.

Methylene blue (MB) is a heterocyclic cationic dye that is extensively used in textile, wool, food, paper, printing, and pharmaceutical sectors [1]. It is highly toxic to living organisms because it can easily bond to oppositely charged cellular membrane surfaces [2]. Additionally, MB has a high color value and it gives noticeably color in minimal concentration (1 mg/L). It is nevertheless regarded as a dangerous colorant. Even a minimal concentration of it can pollute the water. The presence of dyes in water bodies reduces light penetration, and this consequently thwarts the photosynthesis of aqueous flora [3]. MB is a cationic dye with multiple biogenic activities and is harmful to humans and the environment [1,4,5].

3.2. Experimental Section

3.2.1. Adsorption Experiments

Dye removal efficiencies of Mat-1 and Mat-2 were studied using batch processes at room temperature. Batch processes were carried out with different pH (2, 3, 4, 5, 7, 8); concentration of dye (1, 5, 10, 20, 40, 80, 150 mg/L); with dose of adsorbent (0.5, 1, 2, 4 g/L) and time (5, 15, 30, 60, 120 min). The pH of the solutions was adjusted with 1N HCl and 1N NaOH. Methylene blue (MB) is a water-soluble cationic dye (FW, 319.85) with λ_{max} of 664nm [6]. For the stock solution of MB, 1g of MB was dissolved in 1 L of water. Different concentrations of MB were prepared after appropriate dilutions. A calibration curve was prepared from 1 to 150 mg/L of dye concentration, and it was observed that the estimation curve was linear with a correlation coefficient of 0.99 (Figure 3.1). The amount of dye removal was calculated by initial (C_0) and final concentration (C_e) of MB dye using equation (1). All experiments were studied in 3 sets.

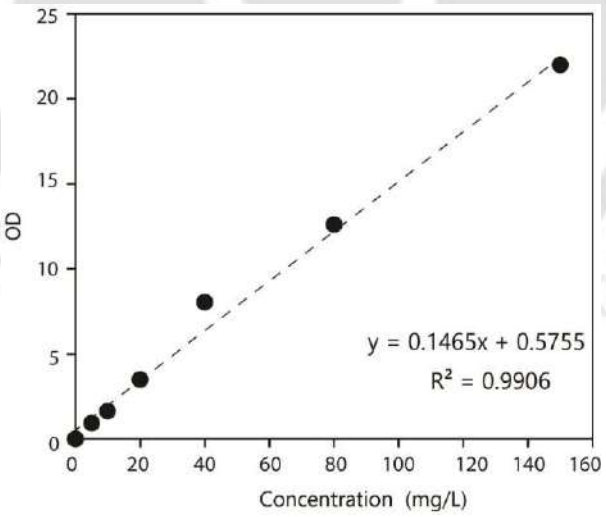

Figure 3.1. Calibration curve of MB dye. A stock solution was prepared by dissolving 1 g of MB with water in 1000 mL volumetric flask. Different concentration of MB was prepared by serial dilutions.

The amount of dye removal was calculated by initial (C_0) and final concentration (C_e) of MB dye using equation (1). All experiments were studied in 3 sets.

$$\% \, Removal \, of \, dye = \frac{C_0 - C_e}{C_0} \times 100 \quad (1)$$

Where,

C_0 = Initial concentration (mg/L)

C_e = Final concentration (mg/L)

The uptake capacity was calculated considering the concentration of absorbed dye (mg/L), solution volume and adsorbent dose (g).

$$q_e = \frac{(C_0 - C_e)V}{m} \quad (2)$$

Where,

q_e = Uptake capacity (mg/g)

V = Volume of solution (L)

m = dose of adsorbent (g)

3.2.2. Desorption Studies

Desorption studies were conducted, followed by the adsorption process. At first, adsorption of MB dye was carried out with 40 mg/L of dye concentration, treated with either Mat-1 or Mat-2 with two different dose variances of 0.5 g/L and 1 g/L. The adsorption experiment was carried out after equilibration for 2 h of continuous shaking. The pH of the solution was 7 at the beginning of the equilibration process. After the shaking, the mixtures were centrifuged at 8000 rpm for 3 min, and the filtrate was spectrophotometrically analyzed to check the dye adsorption. The residue (dye-containing adsorbent) was further utilized for desorption study. The desorption study was carried out by adding 10 ml of methanol (desorbent) with methylene blue-containing Mat-1 and Mat-2 and agitated continuously for 1 h. Further, the mixtures were centrifuged, and the filtrates were analyzed in UV-spectrophotometer. The percentage of desorption was calculated using equation (3) [7]. The

adsorption-desorption process was performed for four cycles.

All experiments were studied in 3 sets.

$$Desorption\% = \frac{V_{des} \times C_{des}}{(C_0 - C_e) \times V_{ads}} \times 100 \quad (3)$$

Where, V_{des} is the volume of methanol used (10 mL), C_{des} is the final concentration of methylene blue dye in solution after desorption (mg/L), and V_{ads} is the volume of dye solution used for adsorption.

3.3. Results and Discussion

Initially, the adsorption property of Mat-1 and Mat-2 was tested with five cationic and two anionic dyes (Table 3.1). Among all the dyes tested, methylene blue and bismarck brown R showed the highest adsorption, in case of both the materials. Both had the near-identical removal property at higher doses, but the differences cropped up at lower doses. A detailed batch study was performed with methylene blue only.

Table 3.1. Comparison between different dye removal by Mat-1 and Mat-2.[1]

Name	**Dose (g/L)**	**% of removal**			**Dose (g/L)**	**% of removal**	
		Mat-1	**Mat-2**			**Mat-1**	**Mat-2**
Cationic dye				*Anionic dye*			
Rhodamine B	0.5	12	26	Acid orange 7	0.5	14	27
	1	32	59		1	31	46
Methylene blue	0.5	71.5	94.9	Acid blue 9	0.5	19	31
	1	94	99		1	33	51
Malachite Green	0.5	13	51				
	1	23	70				
Bismarck Brown R	0.5	90	80				
	1	98	97				
Safranin	0.5	42	59				
	1	65	85				

[1] Initial dye concentration 40 mg/L, 1 h of contact time, and at 250 rpm.

3.3.1. Effect of pH

The effect of solution pH was investigated within the 2-8 pH range, at two different initial concentrations of 10 and 40 mg/L with the dosage of materials with 0.5 g/L (Figure 3.2a, 3.2b, Table 3.2). The contact time used was 1 h. Both materials are equally effective at 10 mg/L dye concentration in the entire range of pH, with the removal of 96-100%. Therefore, indicating that the adsorption capacity is not exhausted. Rightly so, the differences were observed when dye concentration was increased fourfold to 40 mg/L. At this condition, the removal dropped marginally for Mat-2 but significantly for Mat-1. The Mat-1 showed pH dependence with a dip at ~4.5 pH. It is close to its pH_{zpc} value of 4. Expectedly, the removal rises above this pH as the surface becomes more and more negative and the dye is positively charged (Figure 3.2a, 3.2b). It's not easy to explain the higher adsorption at pH < pH_{zpc} value. However, one possibility is protonation, as a result of which self-association of MB dye and its depositing on the material's surface may occur.

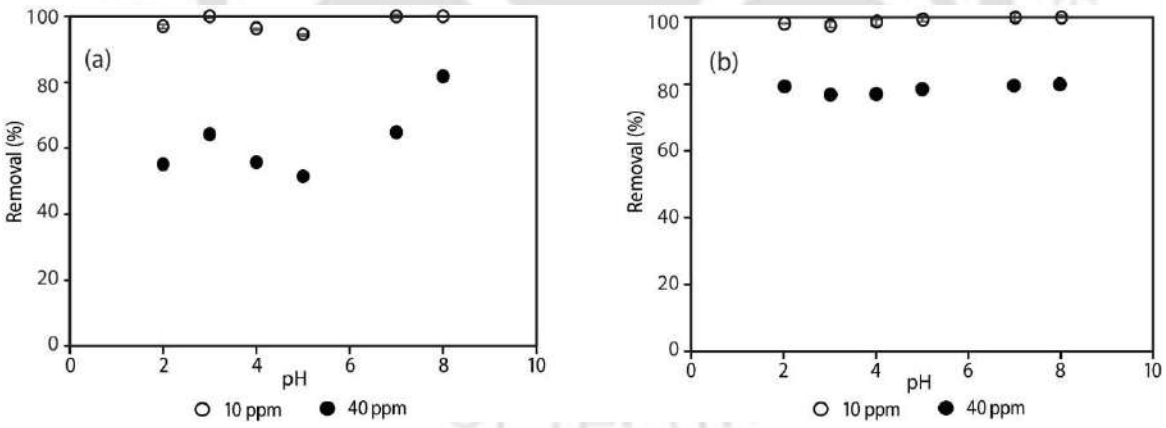

Figure 3.2. (a), (b) Effect of solution pH (2-8) on methylene blue removal by Mat-1 and Mat-2, respectively (Conditions: C_0= 10, 40 mg/L, pH=2-8, Adsorbent dose=0.5g/L, rpm=250, t=60min).

The self-association of MB dye at lower pH is reported in previous literature [8]. The other possible factor is the aromatic π–π interaction between the aromatic rings of polyphenols and the dye. As the materials possess a negatively charged surface at pH 7 and show good removal

capacity at that pH, the rest of the adsorption processes were carried out at pH 7. Considering the use of the materials in water treatment, results at pH 7 are more useful than alkaline pH. Interestingly, plant extract-based Mat-2 hardly showed any pH dependence (Figure 3.2b). As it has many polyphenols and an unknown N-containing substance, we could not identify the component responsible for the observation.

Table 3.2. Effect of different pH variations, at 10 and 40 mg/L of MB concentration.

pH	Concentration (mg/L)	Removal % Mat-1	Uptake (mg/g) Mat-1	Removal % Mat-2	Uptake (mg/g) Mat-2
2	10	96.7 1± 0.44	19.3± 0.88	97.82 ±0.95	19.56± 0.19
3	10	99.4 5±0.12	19.89 ±0.024	97.51±0.89	19.5± 0.18
4	10	95.9 1±0.3	19.18 ±0.055	98.38 ± 0.81	19.6 ±0.16
5	10	94.05 ± 0.07	18.81 ±0.07	99.35 ± 1.1	19.8 ±0.22
7	10	99.55± 0.64	19.91 ±0.13	99.71± 0.4	19.9 ±0.08
8	10	99.89± 0.18	19.9 ±0.036	100	20
2	40	54.9 ±0.13	54.32±0.6	80.30±0.07	64.81±0.3
3	40	63.9 ±0.2	63.24±0.06	77.84±0.45	57.79±0.1
4	40	55.7 ±0.08	55.14±0.16	78.08±0.4	58.46±0.1
5	40	51.6 ± 0.13	51.08±0.2	79.54±0.6	56.44±0.2
7	40	64.73± 0.22	64.05±0.04	80.57±0.1	58.06±0.3
8	40	81.66± 0.1	80.81±0.12	80.91±0.2	58.33±0.2

(With dose 0.5 g/L, 1 h of contact time, and 250 rpm agitation).

3.3.2. Effect of Concentration

Adsorption was studied at initial concentrations from 5 to 150 mg/L, with 0.5 g/L of material dose, at pH 7 and 1 h contact time (Figure 3.3a, 3.3b). Both the materials showed 99% removal in lower adsorbate (MB) concentrations of 5 and 10 mg/L. With increasing dye concentration of 20, 40, 80, 150 mg/L, Mat-1 showed 91, 70, 61, 62% of removal, while Mat-2 showed 99, 95, 91, 85%, respectively. Both the materials are effective; however, Mat-2 is more efficient.

The dye concentration variance is an important factor for exploring the uptake capacity of Mat-1 and Mat-2. Results showed that maximum adsorption capacities of 187 and 255 mg/g at 150 mg/L of dye concentration for Mat-1 and Mat-2, respectively (Table 3.3). Due to the saturation of adsorption sites at high concentrations, the removal percentage was decreased [9].

However, even at a maximum dye concentration of 150 mg/L and a dose of 0.5 g/L, Mat-2 remains very effective (80 % removal). Compared to other reported materials, only two other materials are more effective than the present two materials as mentioned in Table 3.4.

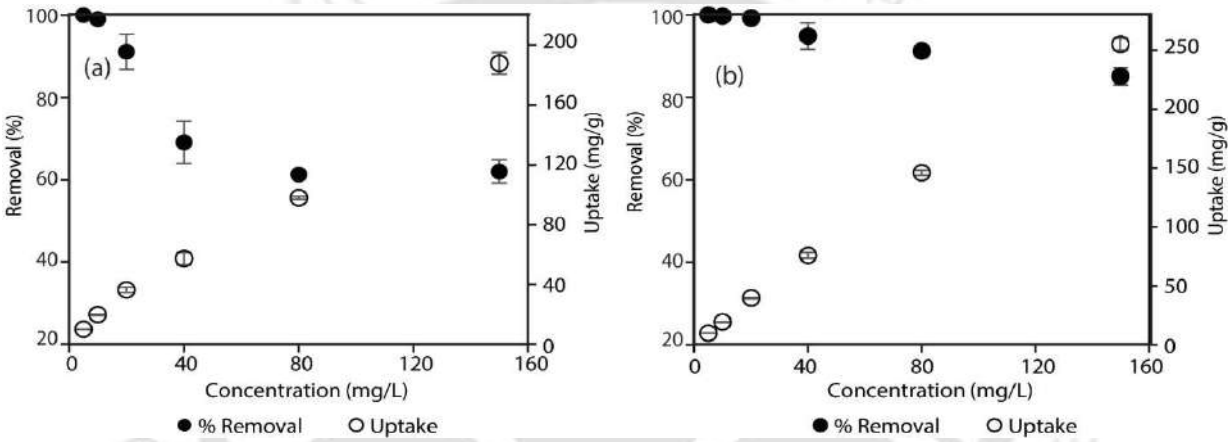

Figure 3.3. (a), (b) Effect of initial concentration on removal percentage and adsorption capacity of MB by Mat-1 and Mat-2, respectively. (Conditions: C_0=5-150 mg/L, pH= 7, Adsorbent dose=0.5g/L, rpm=250, t=60min).

Table 3.3. Effect of initial fluoride concentration on MB removal.

Concentration (mg/L)	Removal % Mat-1	Uptake (mg/g) Mat-1	Removal % Mat-2	Uptake (mg/g) Mat-2
5	100.00±0	10.00±0	100.00	10.00
10	99.01±0.34	19.80±0.34	99.69±0.53	19.38±0.1
20	91.02±4.27	36.41±1.7	99.24±.94	39.70±0.38
40	69.08±5.1	55.26±4.1	94.89±3.2	75.91±2.56
80	61.20±0.59	97.92±.95	91.27±1.3	146.03±5.96
150	62.57±8.3	187.71±8.3	85.09±2.12	255.28±6.3

(At pH 7, with dose of 0.5 g/L, 1 h contact time, and 250 rpm agitation).

Table 3.4. Comparison of MB removal percentage and uptake with various adsorbents.

Composition	pH	Initial conc (mg/L)	Dose (g/L)	Time (min)	% Removal	Exp Uptake (mg/g)	References
Activated carbon from coconut coil	8	80	4	100	83	16.6	[10]
Modified activated carbon	8	600	1	60	38	230	[11]
Activated carbon	8	100	1		42	42	
Modified multi-walled carbon nanotube	7	20	0.75	15	95	25.3	[12]
Activated carbon (Merck)	7.2	600	2	35	95	285	[13]
Bamboo dust carbon		200	10		93	18.5	
Annona squmosa seed	6	200	4	60	15	7.5	[14]
Poly *m*-phenylenediamine grafted dextrin bio adsorbent	8	50	0.06	60	5	42	[15]
polyaniline hydrogel	6.5	50	2.5	720		71.2	[16]
Hydrogel bead of tannic acid -PVA/sodium alginate	9	120	0.5	720	54	130	[17]
CMC-PAA-GO nanocomposite hydrogels	7	125	0.01	250	90	138	[5]
Magnetic Porous Organic Polymers	8	50	1	5	<95	47.5	[18]
Polyaniline Nanotubes	7	3.1	0.05	120	7.7	4.8	[9]
Magnetic ferrite nanoparticle	8	50	0.5	60	55	55	[19]
Iron oxide nanoparticles	7	200	2	-	5	1	[20]
Iron (III) tannate	9	50	0.5	240	50	45	[21]
Tea leaf-Fe nanoparticle	6	50	0.01	100	93	186.9	[22]
Fe_3O_4 coated-tea polyphenol	7	8.5	1	60	95	5	[23]
Iron nanoparticle with eucalyptus extract	-	2000	-	1440	-	64	[21]
Fe-zero valent with Guava leaf	-	50	2.4	>300	94		[24]
Mat-1 (Tannic-Iron complex)	7	40	0.5	60	71	57	This study
		150	0.5	60	62	**187**	
Mat-2 (Guava-Iron complex)	7	40	0.5	60	95	76	This study
		150	0.5	60	85	**255**	

Isotherms are beneficial for explaining the adsorption mechanism and theoretical uptake capacity of different adsorptive materials. The data have been fitted to all three standard models of Langmuir, Freundlich, and Temkin equations (Table 3.5 and Figure 3.4). The Langmuir isotherm is expressed as:

$$q_e = \frac{q_{max}.k_b.C_e}{1 + k_b.C_e} \quad (4)$$

Where q_e (mg/g) is the equilibrium amount of MB adsorbed in per gram of adsorbent, C_e (mg/L) is the equilibrium concentration of contaminant in solution. The q_{max} (mg/g) and k_b (l/mg) are the parameters describing the maximum uptake capacity of the solid surface and the energy constant, respectively. This Freundlich Adsorption Isotherm equation is denoted by:

$$q_e = K_F C_e^{1/n} \quad (5)$$

Where K_F is the constant indicative of relative adsorption capacity and $1/n$ is adsorption intensity. The Temkin isotherm equation is denoted by:

$$q_e = \frac{RT}{b} \ln(K_T C_e) \quad (6)$$

Where K_T is the equilibrium binding energy constant (1/mol), the R and T are the gas constant (8.314 J/mol K), and absolute temperature (K), respectively.

By comparing the data obtained from the isotherm models, we conclude that both the Langmuir and Freundlich models fitted the data due to their R^2 value being closer to unity, as shown in Table 3.5. However, the Temkin model did not fit.

Table 3.5. Isotherm parameters of methylene blue in Mat-1 and Mat-2.

Material	Langmuir			Freundlich			Temkin		
	Q_{max}	K_b	R^2	n	K_F	R^2	K_T	b	R^2
Mat-1	296.2	0.03	0.95	1.9	22	0.97	48.4	54.1	0.7
Mat-2	347.6	0.12	0.95	2.2	61.5	0.98	104.7	73.6	0.8

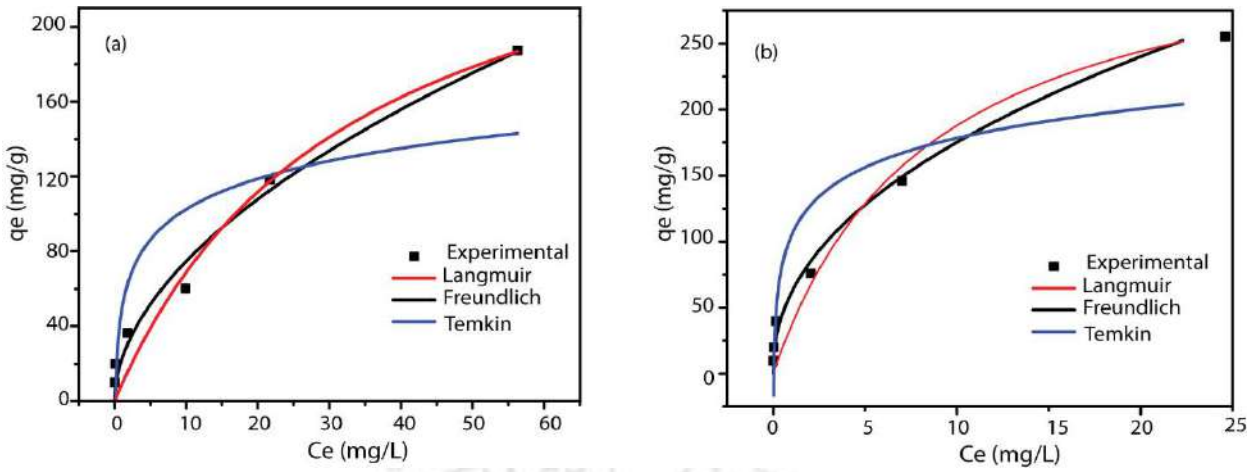

Figure 3.4. Isotherm plot of MB removal by (a) Mat-1 and (b) Mat-2.

3.3.3. Effect of Adsorbent Dose

The effect of different material dosages on MB removal and uptake capacity was studied (Figure 3.5 and Table 3.6). The removal efficiency was investigated at different dosages of 0.5, 1, 2, 4 g/L and different concentrations of MB as 40, 80, and 150 mg/L. The results showed that with the increment in dosages, the percentage removal also increase from 71.6 to 99.7% for 40 mg/L MB concentration, 64.9 to 98.6% for 80 mg/L MB and 62.5 to 99.6% for 150 mg/L MB concentration, in case of Mat-1. For Mat-2, the removal percentage increased from 95.7 to 99.8% for 40 mg/L MB concentration, 82.7 to 99.3% for 80 mg/L MB and 85 to 99.5% for 150 mg/L of MB concentration. The percentage of dye removal increased with the increment of adsorbent dose due to an increase in surface area and availability of more adsorbent sites [19]. In general, the adsorption capacity decreases with the increase in adsorbent dose due to a reduction in available surface area. In the present study, Mat-1 and especially Mat-2 showed good removal capacity with significantly high uptake values compared to other materials listed in Table 3.4.

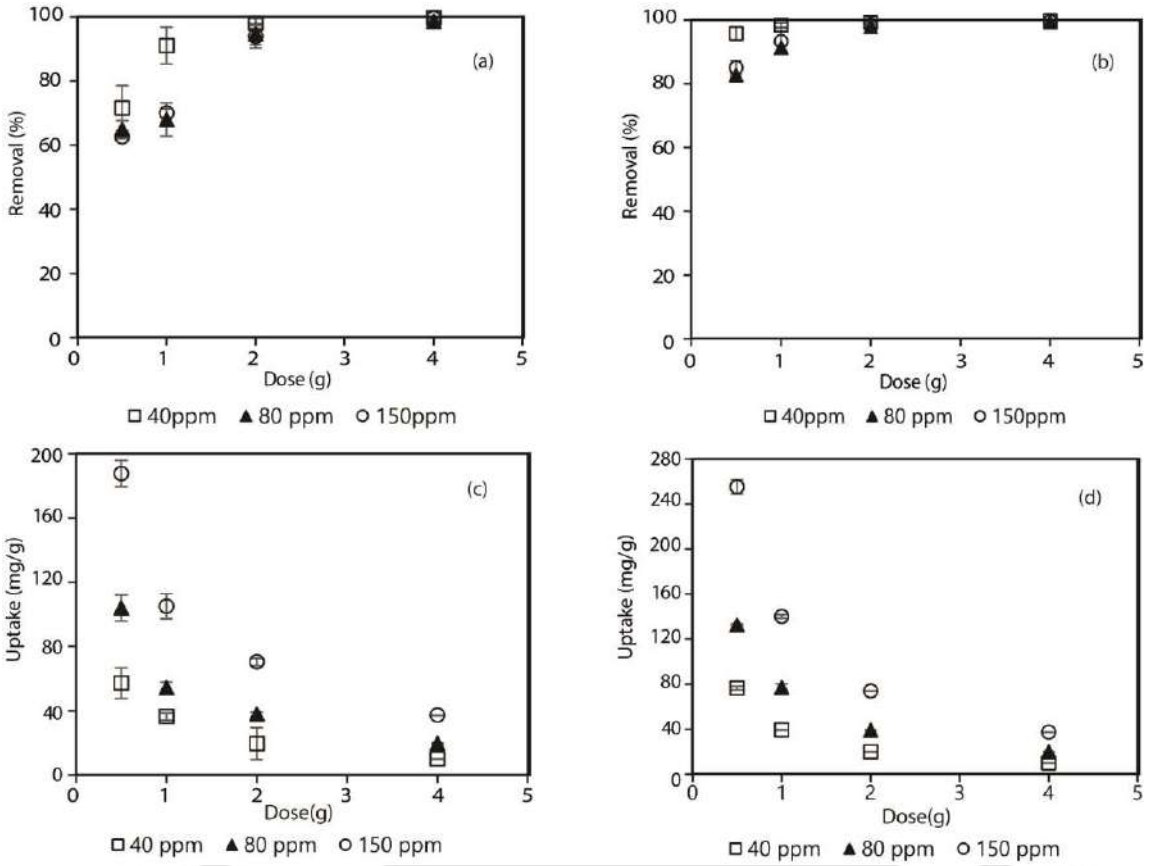

Figure 3.5. Effect of dosage of Mat-1 and Mat-2 on different MB concentration variance, (a, b) removal percentage vs adsorbent dose and (c, d) Uptake vs adsorbent dose plot respectively. (Conditions: Adsorbent dose=0.5-4 g/L, C_0=40, 80, 150 mg/L, pH=7, rpm=250, t=60 min).

Table 3.6. Effect of dose on MB removal.

Concentration (mg/L)	Dose (g/L)	Removal % Mat-1	Uptake (mg/g) Mat-1	Removal % Mat-2	Uptake (mg/g) Mat-2
40	0.5	71.57±7	57.26±9.5	95.75±2.23	76.60±1.79
40	1	91.09±5.78	36.44±2.3	98.43±0.67	39.37±0.27
40	2	98.00±1.56	19.60±9.99	99.22±0.23	19.84±0.04
40	4	99.75±0.39	9.96±0.03	99.87±0.22	9.99±0.03
80	0.5	64.93±0.47	103.88±8.1	82.72±0.63	132.35±1.01
80	1	67.99±1.3	54.4±3.6	91.36±0.67	77.13±3.03
80	2	94.61±3.5	37.85±1.4	97.98±.35	39.19±0.14
80	4	98.6±0.93	19.56±0.29	99.38±0.31	19.88±0.06
150	0.5	62.57±2.76	187.71±8.3	85.09±2.12	255.28±6.3

150	1	70.02±5.18	105.03±7.77	93.36±4.05	140.04±1.6
150	2	93.91±3.2	70.43±2.4	98.66±0.28	73.99±0.21
150	4	99.61±0.06	37.35±0.23	99.57±0.31	37.34±0.11

(At pH 7, 1 h contact time and 250 rpm agitation).

3.3.4. Effect of Time

Effect of contact time on the MB dye removal was examined at different times from 5 to 300 min, at 40 mg/L of dye concentration, with the dosage of 1 g/L, at pH 7 (Figure 3.6, Table 3.7). With only 5 min of contact time, 60% and 84% MB removal by Mat-1 and Mat-2 were observed. Moreover, at 30 min of contact time, Mat-1 and Mat-2 showed 80 and 97% of dye removal, respectively. With the increase in contact time, the available binding sites were occupied by MB, ultimately reinforcing the slow adsorption rate and saturation of sites [25]. Among the materials, Mat-2 is the fastest to reach equilibrium within 30 min (97% removal), and the removal stays constant till 120 min (~98).

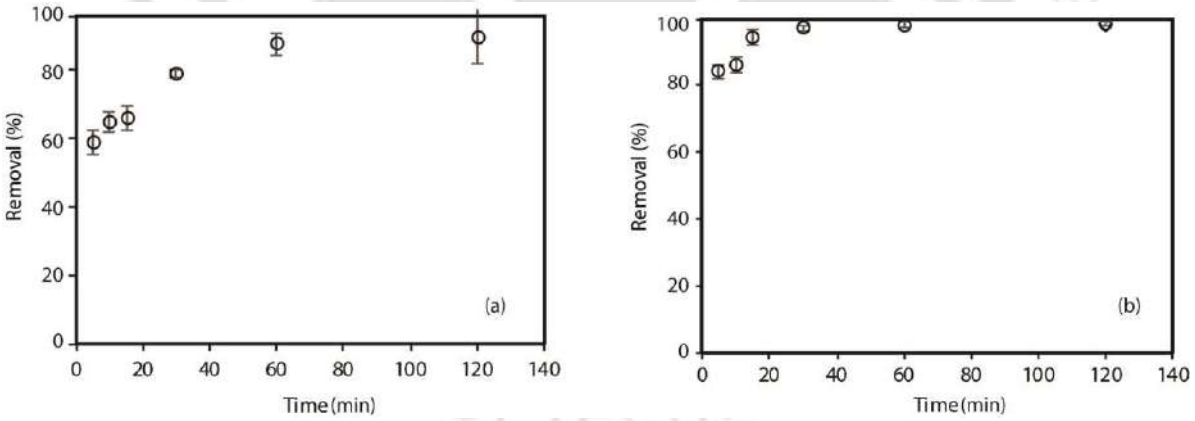

Figure 3.6. Effect of contact time for removal of 40 mg/L methylene blue removal by (a) Mat-1 and (b) Mat-2. (Conditions: t=5-120 min, C_0=40 mg/L, Adsorbent dose=1g/L, pH=7, rpm=250).

Both materials did 100% removal of dye after 300 min of contact time. Compared to this, adsorption of MB on modified multi-walled carbon nanotube reaches equilibrium within 15 min (dose, 0.75 g/L, removal 95%) [12]. Huang et al. reported adsorption on magnetic porous

organic polymers reaches equilibrium within 5 min (dose 1g/L, removal <95%) [26]. Except for these two examples, the equilibrium time for MB removal of Mat-1 is faster than other reported materials listed in Table 3.4.

Table 3.7. Effect of contact time for MB removal.

Time (min)	Removal % Mat-1	Uptake (mg/g) Mat-1	Removal % Mat-2	Uptake (mg/g) Mat-2
5	59.3 ±3.4	23.7± 1.36	84.09±2.07	33.6± 0.83
10	64.96± 3	25.9 ±1.22	85.76±2.3	34.31 ±0.93
15	66.32 ±3.5	26.5 ±1.4	94.13±2.1	37.69± 0.85
30	79.0± 1.12	31.6 ±0.45	96.74±1.05	38.69 ±0.42
60	87.5± 3	35.0 ±1.2	97.88±0.62	39.15 ±0.25
120	89.69±7.9	35.9± 3.2	98.43±0.60	39.37 ±0.24
300	100	40	100	40

(At pH 7, with a dose of 1 g/L, 40 mg/L of dye concentration, and 250 rpm agitation).

Data were fitted to both pseudo-first-order (Eq. 7) and pseudo-second-order (Eq. 8).

$$q_t = q_e\,(1 - e^{-k_1 t}) \tag{7}$$

$$q_t = \frac{k_2\, q_e^2\, t}{1 + k_2\, q_e\, t} \tag{8}$$

Where, k_1 and k_2 are the rates constant of pseudo-first-order and pseudo-second-order kinetics, q_t is the adsorption capacity at time t, and q_e is the equilibrium adsorption capacity. The plots and parameters of the fit are given in Figure 3.7 and Table 3.8. The data fits better with the second-order rate plot, which means the adsorption process is chemisorption (Table 3.8). We noted that MB removal with commercially available activated charcoal also followed second-

order kinetics [13]. Similar second-order kinetics was observed for MB on tannic acid–poly(vinyl alcohol)/sodium alginate hydrogel beads (equilibrium time of 12 h) [17].

Table 3.8. Non-linear kinetics data of methylene blue removal by Mat-1 and Mat-2.

Sample	Qe_{exp}	Pseudo 1st order			Pseudo 2nd order		
		Qe_{cal}	k_1	R^2	Qe_{cal}	k_2	R^2
Mat-1	40	35.05	0.35	0.53	37	0.005	0.84
Mat-2	40	38.6	0.86	0.52	39.2	0.023	0.94

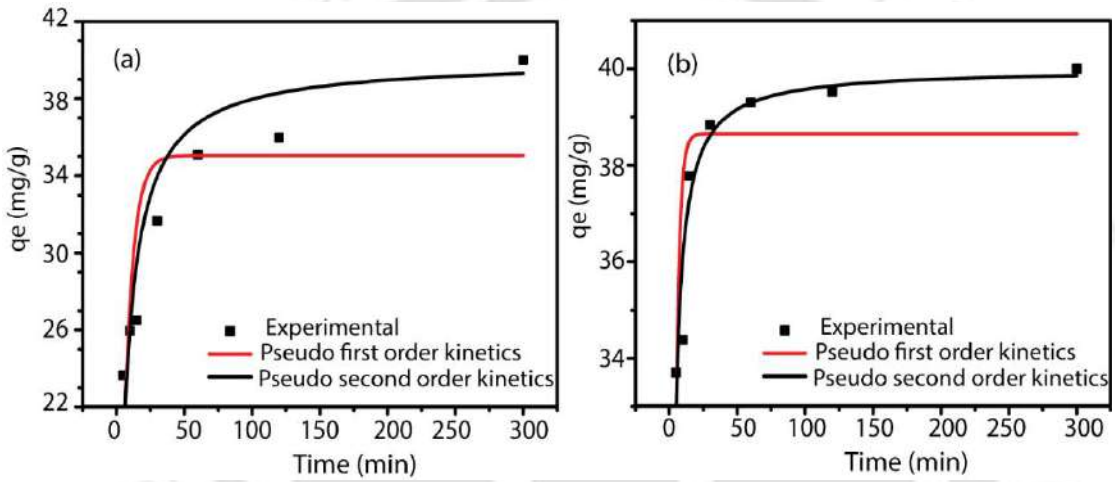

Figure 3.7. Kinetics study of MB removal by (a) Mat-1 and (b) Mat-2.

3.4. Desorption of MB

Desorption and recyclability of the materials were tested with several organic solvents: methanol, ethanol, ethyl acetate, acetone, and hexane. Methanol and ethanol can disrupt H-bond as they can act both as strong H-bond donors or acceptors. Ethyl acetate and acetone are weak H-bond acceptors, and hexane is incapable of H-bond formation. Among the organic solvents, desorption is most effective with methanol and ethanol. It must be because of its ability to disrupt the H-bonds between MB and phenolic -OH groups of the materials. All the materials have multiple phenolic (from catechol) groups. MB is a potential H-bond acceptor at

the heterocyclic N or charged S. The methyl substitutions at both the amine N of MB robs their H-bond donor capability. Ethyl acetate, acetone, and hexane are incapable of breaking the H-bonds. Thus, desorption in these solvents is either negligible or does not occur at all. It means that H-bond with phenolic -OH is one of the factors in adsorption.

Under similar conditions, desorption works best with methanol. Therefore, the recyclability was tested in MeOH at two different doses (0.5 g/L and 1 g/L) of material up to 4 cycles (Figure 3.8a). At a lower dosage of 0.5 g/L, adsorption capacity decreases in the successive cycle (~10%) up to the third cycle. The re-absorption drops steeply in the fourth cycle. One of the feature observed is that the quantity desorbed is much less than the re-absorption quantity. We think the methanol is unable to desorb more than ~20% of the adsorbed dye. Instead, methanol exposes new surfaces on the adsorbent particles by breaking H-bonds within the cluster of the adsorbent particles. Hence the successive adsorption is higher than the amount desorbed (Figure 3.8a). Mat-2 retains re-adsorption capacity better than Mat -1. Recyclability works with the simple addition of methanol or ethanol but not due to the efficient desorption but the ability of the solvent to expose new adsorption sites. The occurrence of desorption was less than 50% in first cycle le which indicates that the H-bond may not be the only contributor to the dye binding.

The other factor could be the ionic interaction between the cationic dye and the adsorbent. To test this, we checked desorption with Na^{+}, K^{+}, Ca^{+2}, Ba^{+2}, and Al^{+3} salts under identical conditions (Figure 3.8b). The cations were chosen based on increasing size and charge (K^{+} is larger than Na^{+} and Ba^{2+} larger than Ca^{+2}). The desorption shows that higher charge and larger cations are increasingly more effective in displacing dye from adsorbent (Figure 3.8b). Al^{+3} is similar in size and charge with Fe^{+3} and is known to bind strongly with catechol/polyphenols, which may have resulted in a very high desorption value in the case of Al^{+3}. From this experiment it can be concluded that the ionic interaction is present, in dye binding but as the

values are not higher than 50% (except Al^{+3}), ionic interaction alone is not responsible. Combining results of solvents and salts, the dye adsorption on these materials seems to be a combination of H-bond and ionic interactions. The possibility of aromatic π–π interactions cannot be ruled out.

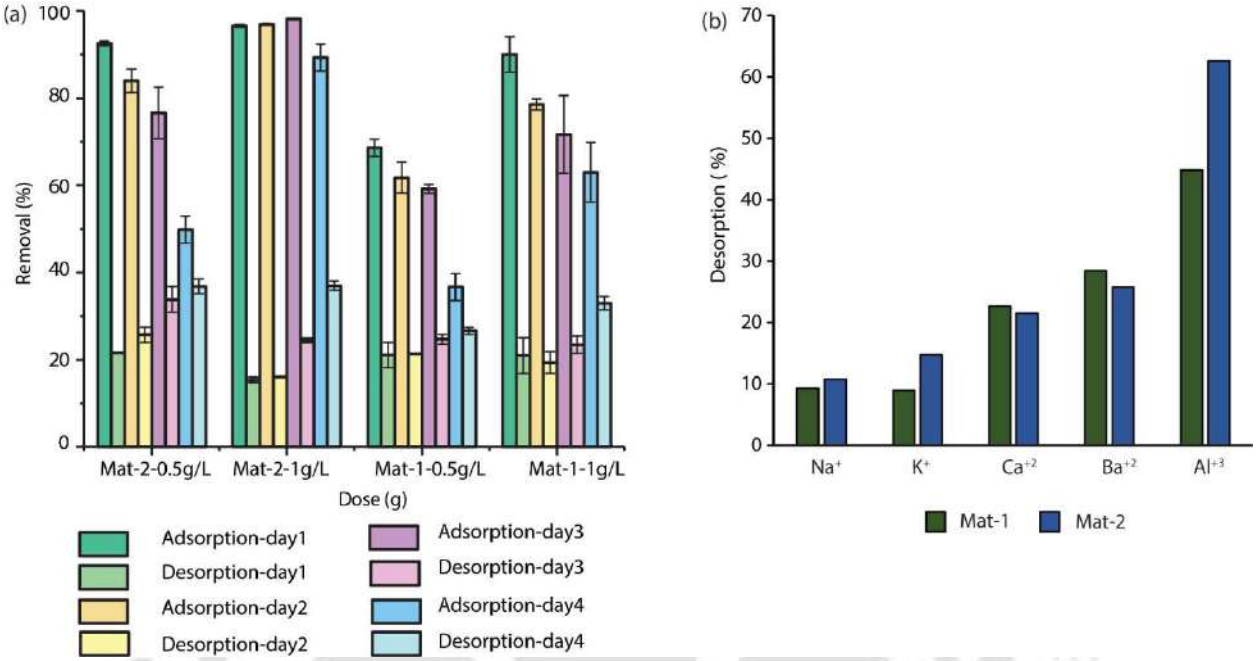

Figure 3.8. Desorption study of MB from Mat-1 and Mat-2 with (a) MeOH and (b) different metal salts. (Condition: 0.01g of salt, initial pH 4).

3.5. Comparison with Charcoal

Activated charcoal is a well-known efficient adsorbent for dye removal from wastewater [10,11]. Due to their high surface area and porous structure, activated carbon showed very high adsorption capacity for dye removal [11–13]. Activated charcoal was used as a reference to compare the dye removal property under identical conditions with the materials synthesized in chapter 2. The surface area of the activated charcoal is very high at 688.4 m^2/g. The value found for charcoal is consistent with previous reports [27,28]. The significantly higher surface area gives charcoal an advantage over other adsorbents. For activated charcoal, the adsorption-

desorption isotherm belongs to type-1 as reported by other literature (Figure 3.9) [28]. Effectivity is also comparable to activated charcoal (Table 3.10) despite having 1/7th of surface area (Table 3.9). Mat-3 is the least effective (Table 3.10).

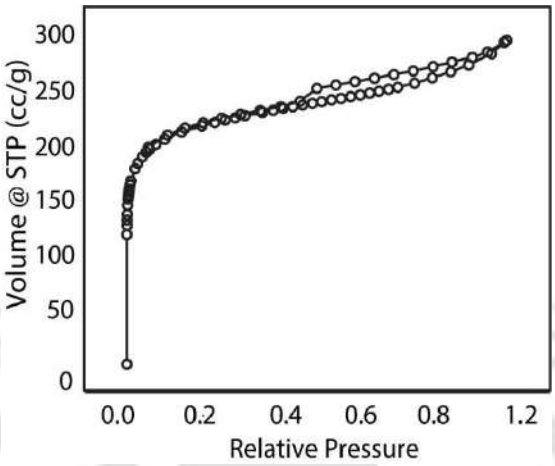

Figure 3.9. BET isotherm of activated charcoal.

Table 3.9. BET isotherm parameters of activated charcoal.

Method	Parameter	Activated Charcoal
Multi-point BET	Surface Area, m^2/g	688.409
	Average pore diameter, nm	2.678
	Total pore volume, cc/g	0.461
adsorption	Surface Area, m^2/g	69.04
	Pore diameter, nm	3.010
	Pore volume, cc/g	0.136
desorption	Surface Area, m^2/g	90.85
	Pore diameter, nm	3.82
	Pore volume, cc/g	0.140

Table 3.10. Comparison of methylene blue removal by different materials at pH 7.[1]

	Removal (%)	q_e (mg/g)	Removal (%)	q_e (mg/g)
Dose, 0.5 g/L; Dye conc. 40 mg/L			*Dose, 1 g/L; Dye conc. 40 mg/L*	
Mat 1	71.5	57.2	94	37
Mat 2	94.9	75.9	99	39.8
Mat 3	36.6	29.3	78.5	31.4
Charcoal	100	80	100	40

[1] (Contact time=1 h, rpm= 250).

3.6. Conclusions

Both materials were found capable of removing 99% of 10 mg/L methylene blue with a dose of 0.5 g/L and contact time of 1 h. At lower dye concentrations, both Mat-1 and Mat-2 are equally effective in a wide pH range from 2-9, with 96-100% removal. With the dose of 2 g/L, more than 98% removal of 150 mg/L of MB dye was observed by both the materials. In adsorption isotherm processes, the Freundlich model was better fitted in both materials than Langmuir and Temkin models. Pseudo-second-order kinetics was best fitted in both Mat-1 and Mat-2. MB dye removal capacities of materials were also compared with activated charcoal. It was observed that Mat-2 could match performance with activated charcoal with the added advantage of less energy consumption and no greenhouse gas emission. Desorption study revealed that dye binding on adsorbent has a significant contribution from ionic interaction and H-bonding along with aromatic π-π interaction.

References

[1] M. Ghaedi, S. Heidarpour, S. Nasiri Kokhdan, R. Sahraie, A. Daneshfar, B. Brazesh, Comparison of silver and palladium nanoparticles loaded on activated carbon for efficient removal of Methylene blue: Kinetic and isotherm study of removal process, Powder Technol. 228 (2012) 18–25. https://doi.org/10.1016/j.powtec.2012.04.030.

[2] T. Hu, Q. Liu, T. Gao, K. Dong, G. Wei, J. Yao, Q. Liu, T. Gao, K. Dong, G. Wei, J. Yao, Facile Preparation of Tannic Acid–Poly(vinyl alcohol)/Sodium Alginate Hydrogel Beads for Methylene Blue Removal from Simulated Solution, ACS Omega. (2018) 7523−7531. https://doi.org/10.1021/acsomega.8b00577.

[3] M. Roosta, M. Ghaedi, A. Daneshfar, R. Sahraei, A. Asghari, Optimization of the ultrasonic assisted removal of methylene blue by gold nanoparticles loaded on activated carbon using experimental design methodology, Ultrason. Sonochem. 21 (2014) 242–252. https://doi.org/10.1016/j.ultsonch.2013.05.014.

[4] C.C. Coddington, T.L. Anderson, C.R. Accetta, J. Swanson, T. Kruger, G.D. Hodgen, Adverse effects of methylene blue on human sperm motility, components of human reproductive tract fluids, and mouse embryo cleavage, Fertil. Steril. 51 (1989) 480–485. https://doi.org/10.1016/S0015-0282(16)60558-7.

[5] H. Hosseini, A. Zirakjou, D.J. McClements, V. Goodarzi, W.-H. Chen, Removal of methylene blue from wastewater using ternary nanocomposite aerogel systems: Carboxymethyl cellulose grafted by polyacrylic acid and decorated with graphene oxide, J. Hazard. Mater. 421 (2022) 126752. https://doi.org/10.1016/j.jhazmat.2021.126752.

[6] K.C. Bedin, A.C. Martins, A.L. Cazetta, O. Pezoti, V.C. Almeida, KOH-activated carbon prepared from sucrose spherical carbon: Adsorption equilibrium, kinetic and thermodynamic studies for Methylene Blue removal, Chem. Eng. J. 286 (2016) 476–484. https://doi.org/10.1016/j.cej.2015.10.099.

[7] P. Terangpi, S. Chakraborty, M. Ray, Improved removal of hexavalent chromium from 10 mg/L solution by new micron sized polymer clusters of aniline formaldehyde condensate, Chem. Eng. J. 350 (2018) 599–607. https://doi.org/10.1016/j.cej.2018.05.171.

[8] A.K. Ghosh, Study of the self-association of methylene blue from protonation equilibriums, J. Am. Chem. Soc. 92 (1970) 6415–6418. https://doi.org/10.1021/ja00725a005.

[9] M.M. Ayad, A.A. El-Nasr, Adsorption of cationic dye (methylene blue) from water

using polyaniline nanotubes base, J. Phys. Chem. C. 114 (2010) 14377–14383. https://doi.org/10.1021/jp103780w.

[10] Y.C. Sharma, Uma, S.N. Upadhyay, Removal of a cationic dye from wastewaters by adsorption on activated carbon developed from coconut coir, Energy and Fuels. 23 (2009) 2983–2988. https://doi.org/10.1021/ef9001132.

[11] J.A.B. Tech, E. Am, A.E. Wm, A.A.A. Oudah, Methylene Blue Dye Removal from Aqueous Solution Using Several Solid Stationary Phases Prepared from Papyrus Plant, J. Anal. Bioanal. Tech. (2016). https://doi.org/10.4172/2155-9872.s13-003.

[12] T. Madrakian, A. Afkhami, M. Ahmadi, H. Bagheri, Removal of some cationic dyes from aqueous solutions using magnetic-modified multi-walled carbon nanotubes, J. Hazard. Mater. 196 (2011) 109–114. https://doi.org/10.1016/j.jhazmat.2011.08.078.

[13] N. Kannan, M.M. Sundaram, Kinetics and mechanism of removal of methylene blue by adsorption on various carbons - A comparative study, Dye. Pigment. 51 (2001) 25–40. https://doi.org/10.1016/S0143-7208(01)00056-0.

[14] T. Santhi, S. Manonmani, V.S. Vasantha, Y.T. Chang, A new alternative adsorbent for the removal of cationic dyes from aqueous solution, Arab. J. Chem. 9 (2016) S466–S474. https://doi.org/10.1016/j.arabjc.2011.06.004.

[15] W.J. Luo, Q. Gao, X.L. Wu, C.G. Zhou, Removal of Cationic Dye (Methylene Blue) from Aqueous Solution by Humic Acid-Modified Expanded Perlite: Experiment and Theory, Sep. Sci. Technol. 49 (2014) 2400–2411. https://doi.org/10.1080/01496395.2014.920395.

[16] B. Yan, Z. Chen, L. Cai, Z. Chen, J. Fu, Q. Xu, Fabrication of polyaniline hydrogel: Synthesis, characterization and adsorption of methylene blue, Appl. Surf. Sci. 356 (2015) 39–47. https://doi.org/10.1016/j.apsusc.2015.08.024.

[17] T. Hu, Q. Liu, T. Gao, K. Dong, G. Wei, J. Yao, Facile Preparation of Tannic Acid-Poly(vinyl alcohol)/Sodium Alginate Hydrogel Beads for Methylene Blue Removal from Simulated Solution, ACS Omega. 3 (2018) 7523–7531. https://doi.org/10.1021/acsomega.8b00577.

[18] L. Huang, M. He, B. Chen, Q. Cheng, B. Hu, Facile Green Synthesis of Magnetic Porous Organic Polymers for Rapid Removal and Separation of Methylene Blue, ACS Sustain. Chem. Eng. 5 (2017) 4050–4055. https://doi.org/10.1021/acssuschemeng.7b00031.

[19] N.M. Mahmoodi, Magnetic ferrite nanoparticle-alginate composite: Synthesis, characterization and binary system dye removal, J. Taiwan Inst. Chem. Eng. 44 (2013) 322–330. https://doi.org/10.1016/j.jtice.2012.11.014.

[20] B. Saha, S. Das, J. Saikia, G. Das, Preferential and enhanced adsorption of different dyes on iron oxide nanoparticles: A comparative study, J. Phys. Chem. C. 115 (2011) 8024–8033. https://doi.org/10.1021/jp109258f.

[21] Z. Wang, C. Yu, C. Fang, M. Megharaj, Removal of acid red 94 and methylene blue using iron-polyphenol nanomaterials synthesized by various plant leaves: A comparison study, Proc. 2014 Int. Conf. Nanosci. Nanotechnology, ICONN 2014. (2014) 39–42. https://doi.org/10.1109/ICONN.2014.6965256.

[22] C. Xiao, H. Li, Y. Zhao, X. Zhang, X. Wang, Green synthesis of iron nanoparticle by tea extract (polyphenols) and its selective removal of cationic dyes, J. Environ. Manage. 275 (2020) 111262. https://doi.org/10.1016/j.jenvman.2020.111262.

[23] K.K. Singh, K.K. Senapati, K.C. Sarma, Synthesis of superparamagnetic Fe3O4 nanoparticles coated with green tea polyphenols and their use for removal of dye pollutant from aqueous solution, J. Environ. Chem. Eng. 5 (2017) 2214–2221. https://doi.org/10.1016/j.jece.2017.04.022.

[24] P. Somchaidee, K. Tedsree, Green synthesis of high dispersion and narrow size distribution of zero-valent iron nanoparticles using guava leaf (Psidium guajava L) extract, Adv. Nat. Sci. Nanosci. Nanotechnol. 9 (2018). https://doi.org/10.1088/2043-6254/aad5d7.

[25] T.L. Silva, A. Ronix, O. Pezoti, L.S. Souza, P.K.T. Leandro, K.C. Bedin, K.K. Beltrame, A.L. Cazetta, V.C. Almeida, Mesoporous activated carbon from industrial laundry sewage sludge : Adsorption studies of reactive dye Remazol Brilliant Blue R, 303 (2016) 467–476. https://doi.org/10.1016/j.cej.2016.06.009.

[26] L. Huang, X. Weng, Z. Chen, M. Megharaj, R. Naidu, Synthesis of iron-based nanoparticles using oolong tea extract for the degradation of malachite green, Spectrochim. Acta - Part A Mol. Biomol. Spectrosc. 117 (2014) 801–804. https://doi.org/10.1016/j.saa.2013.09.054.

[27] P.K. Malik, Dye removal from wastewater using activated carbon developed from sawdust: Adsorption equilibrium and kinetics, J. Hazard. Mater. 113 (2004) 81–88. https://doi.org/10.1016/j.jhazmat.2004.05.022.

[28] J. Abdulsalam, J. Mulopo, B. Oboirien, S. Bada, R. Falcon, Experimental evaluation of activated carbon derived from South Africa discard coal for natural gas storage, Int. J. Coal Sci. Technol. 6 (2019) 459–477. https://doi.org/10.1007/s40789-019-0262-5.

Chapter-IV

Bismarck Brown Dye Removal Capacity and Cytotoxic Assessment of Dye on *Allium cepa*

4.1. Introduction

In the previous chapter, the removal capacity of Mat-1 and Mat-2 against one heterocyclic cationic dye (MB) was investigated. In this chapter, we wanted to test the material's efficacy in the removal of another cationic dye. Bismarck brown (BB), an azo dye, was chosen to check the removal capacity of Mat-1 and Mat-2 against it. Over 700,000 tons of dyes are annually produced throughout the world, of which 60–70% are azo dyes [1,2]. Different azo dyes are produced from the textile, leather, printing, paper, food, and cosmetic industries. Dyes are known as important contaminants which can be dangerous to humans, animals, and other living organisms [3–6]. Therefore, it demands considerable attention to remove them from industrial wastewater before being discharged into the environment.

Indian Government has banned 70 azo dyes since June 1997, Basic brown-4 or Bismarck brown R (BB) (Colour Index Constitution No. 21010) is one of them. Bismarck brown is a cationic azo dye used in textile industries, shows a significant peak at 464 nm. Azo dyes are organic compounds with one or more -N = N- functional groups associated with the aromatic ring. It was reported that azo dyes could show carcinogenic nature and induce genetic abnormalities in human beings and animals [4,7]. *Allium cepa* (*A. cepa*) is considered an efficient material for studying chromosomal aberration for environmental stress because of its large and low chromosomal number and easy availability, and affordability [8,9].

Materials synthesized in Chapter II were applied for the removal of Bismarck brown R dye. The optimization parameters were carried out at different dye concentrations, material dose,

contact times. As BB is a toxic dye, the cytotoxic effect of BB dye was investigated by applying it on *Allium cepa.* The effect was checked by directly using the stock solution of BB dye on *Allium cepa*. *Besides,* the reduction of the toxicological impact of BB dye residual solutions after adsorption by Mat-1 and Mat-2. Since post-treated water will be used for different purposes, it is important to check the toxicity of the post-treated water due to the possibility of presence of residual toxicity.

4.2. Experimental Section

4.2.1. Materials and Methods

Tannic acid ($C_{76}H_{52}O_{46}$) and ferrous sulfate ($FeSO_4.7H_2O$) were purchased from Alfa Aesar, and Rankem respectively, and were used as supplied without further purification. Sodium hydroxide, potassium nitrate, acetonitrile, and methanol were purchased from Merck, India. Gallic acid was bought from Sigma Aldrich. Folin Ciocalteu reagent and Bismarck brown (BB) dye were purchased from SRL Pvt. Ltd and HiMedia, respectively. Purified water from a Amtrol reverse osmosis system was used for all experiments.

The UV spectra were measured on Perkin Elmer Lambda 25 UV-vis spectrophotometer. pH of the solutions was measured using Thermo scientific, Orion 3 Star pH meter. Cytotoxic observations were studied using Zeiss Axio Vert A1 microscope.

4.2.2. Adsorption Experiments

The batch process was carried out to check the removal efficiencies of Bismarck brown dye by Mat-1, and Mat-2 was studied in batch mode at room temperature. Batch processes were executed with diffirent concentration of dye (10, 20, 40, 80, 100, 200, 400 mg/L); dose of adsorbent (0.5, 1, 1.5, 2, 3 g/L) and time (5, 10, 15, 30, 60, 120 minutes). The pH of the solution was adjusted with 1N HCl and 1N NaOH. Bismarck brown r is a cationic dye with λ_{max} of 464nm. A stock solution was prepared by dissolving 1g of BB with water in 1000 mL

volumetric flask. Different concentration of BB was prepared by serial dilutions. A calibration curve was prepared from 0 to 400 mg/L of dye concentration, and it was observed that the estimation curve was linear with a correlation coefficient of 0.98 (Figure 4.1). The amount of dye removal was calculated by BB dye's initial (C_0) and final concentration (C_e). All experiments were studied in 3 sets.

$$\%\ Removal\ of\ dye = \frac{C_0 - C_e}{C_0} \times 100 \quad (1)$$

Where,

C_0 = Initial concentration (mg/L)

C_e = Final concentration (mg/L)

The uptake capacity was calculated considering the concentration of absorbed dye (mg/L), solution volume, and adsorbent dose (g).

$$q_e = \frac{(C_0 - C_e)V}{m} \quad (2)$$

Where,

q_e = Uptake capacity (mg/g)

V = Volume of solution (L)

m= dose of adsorbent (g)

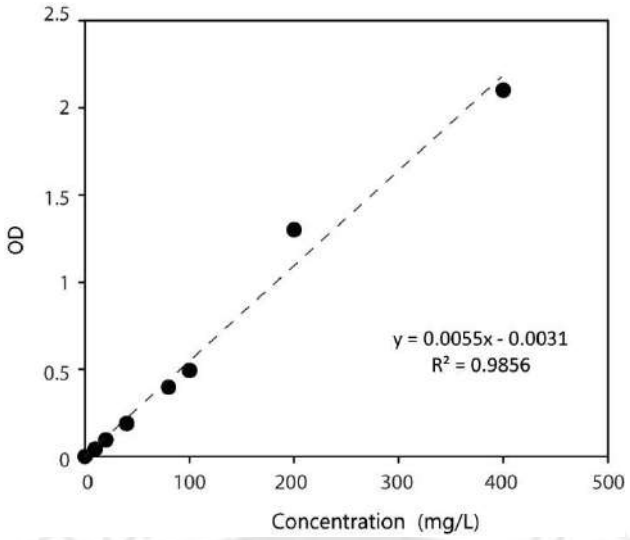

Figure 4.1. Calibration curve of BB dye. A stock solution was prepared by dissolving 1 g of BB with water in 1000 mL volumetric flask. Different concentration of BB was prepared by serial dilutions.

4.2.3. Desorption Studies

The desorption or recyclability study was executed, followed by the adsorption process. At first, adsorption of BB dye was carried out with 400 mg/L of dye concentration, treated with Mat-1 and 2 with two different dose variances of 0.5 g/L and 1 g/L. The adsorption experiment was carried out after equilibration for 2 h of continuous shaking. The pH of the solution was 7 at the beginning of the equilibration process. After the shaking, the mixtures were centrifuged at 8000 rpm for 3 minutes, and the filtrate was spectrophotometrically analyzed to check the dye adsorption. The residue (dye-containing adsorbent) was further utilized for desorption study.

The recyclability study was carried out using various organic solvents: methanol, ethanol, ethyl acetate, acetone, hexane, and salts of Na^{+}, K^{+}, Ca^{+2}, Ba^{+2}, Al^{+3}. Using 10 ml of solvents or 0.01g of salts to Bismarck brown-adsorbed Mat-1 and Mat-2 and agitated continuously for 2 h. Further, the mixtures were centrifuged, and the filtrates were analyzed in UV-spectrophotometer. The percentage of desorption was calculated using equation (3) [10]. The

adsorption-desorption process was performed for 3 cycles. All experiments were studied in 3 sets.

$$Desorption\% = \frac{V_{des} \times C_{des}}{(C_0 - C_e) \times V_{ads}} \times 100 \quad (3)$$

Where V_{des} is the volume of acetone used (10 mL), C_{des} is the final concentration of BB dye in solution after desorption (mg/L), and V_{ads} is the volume of dye solution used for adsorption.

4.2.4. Cytotoxicity Test

Allium cepa (2n=16) was used as an indicator to check the cytotoxicity against BB dye. The *Allium cepa* (onion bulbs) was purchased from domestic, commercial sources. The onion bulbs were placed on the sand containing paper cups, and roots were emerged in it and treated for 5days at 25°C. The distilled water treated root was used as control standard, while root treated with a stock solution of 200 and 400 mg/L of Bismarck brown r dye was also used to check the adverse effect of the dye. The post-treated solutions of BB with Mat-1 and Mat-2 used for all the sets were done in two batches.

After treatment of 5 days, 2 cm size of root tips were dipped in ethanol: acetic acid (3:1) solution for 24h for fixation purposes. The root tips were hydrolyzed with 1N HCl at 50°C for 1min and stained with aceto-orceine. Squashed on slides and observe the mitotic index and cytological changes in the light microscope.

The following equations calculated the mitotic index and cell aberration percentage [11].

Mitotic index (MI) =

$$Mitotic\ index(MI)\% = \frac{Number\ of\ deviding\ cells}{Total\ number\ of\ cells} \times 100 \quad (4)$$

$$Abnormality\ percentage\ (AP)\% = \frac{Number\ of\ abnormal\ cells}{Total\ cells\ observed} \times 100 \quad (5)$$

4.3. Result and Discussion

4.3.1. Bismarck Brown Removal by the Batch Study

4.3.1.1. Effect of Concentration

The effect of different concentrations of BB on removal and measurement of adsorption capacity of Mat-1 and Mat-2 were studied and depicted in Figure 4.2, Table. 4.1. Batch processes were carried out with varying concentrations of BB 20, 40, 80, 100, 200, 400 mg/L, with the dose of 0.5g/L of materials, at pH 7, and contact time of 1 h.

The Figure 4.2 showed > 80% removal of BB in a wide range of dye concentrations, from 20-400 mg/L by Mat-1, and showed similar results in the case of Mat-2. With the rise of BB concentration from 20, 40, 80, 100, 200, 400 mg/L Mat-1 exhibited 80, 91, 87, 85, 85, 81% of removal, while Mat-2 showed 66, 79, 89, 87, 89, 85 %, respectively. The results showed the adsorption capacity of material rapidly increased with increasing concentration. Both Mat-1 and Mat-2 showed very high adsorption capacity, i.e., 652 mg/g and 680 mg/g for BB dye at 400 mg/L of concentration.

Table 4.1. Effect of concentration on BB removal.

Conc (mg/L)	Removal % by Mat-1	Removal % by Mat-2	Uptake (mg/g) Mat-1	Uptake (mg/g) Mat-2
20	80.6±6.8	66.6±3.7	32.2±2.7	25.2±3.7
40	90.65±0.1	79.75±3.5	72.52±0.1	63.8±2.7
80	87.55±2.3	89.64±1.8	140.08±3.7	143.4±1.8
100	85.29±1.3	87.98±5.1	170.1±3.5	175.9±10.2
200	85.45±0.4	89.7±1.2	341.8±1.5	358.87±5.1
400	81.53±4.8	85.01±3.6	652.2±35	680.08±29

(At pH 7, with a dose of 0.5 g/L, 1 h contact time and 250 rpm agitation).

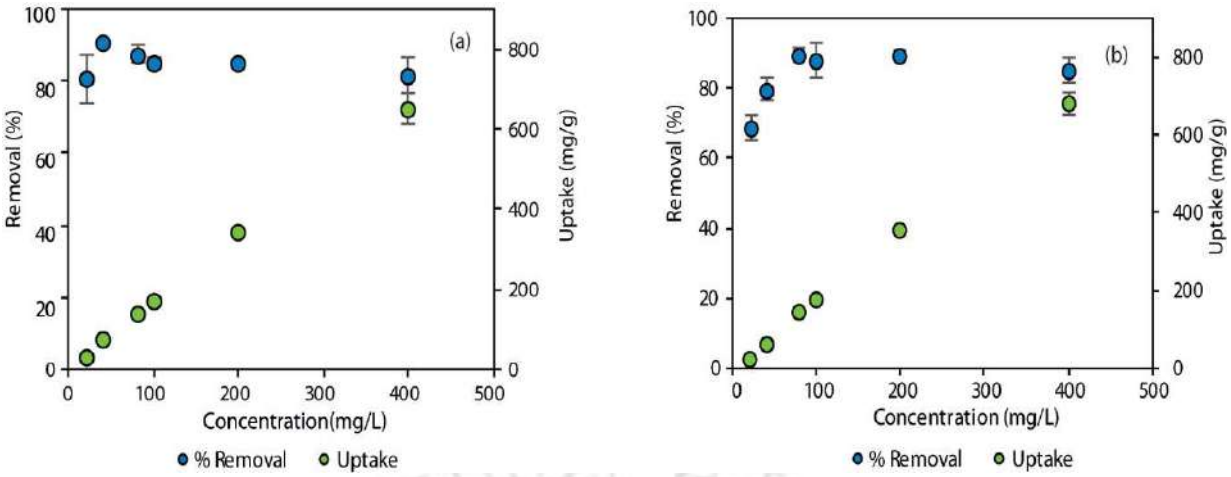

Figure 4.2. Effect of initial dye concentration on removal percentage and adsorption capacity of BB by Material-1 and 2, respectively. (Conditions: C_0=20-400 mg/L, pH= 7, Adsorbent dose=0.5 g/L, rpm=250, t=60min.

From the comparison of the data obtained from the three isotherm models, it was observed that the R^2 value of the Langmuir and Freundlich models was very close. Therefore, there was a possibility of both the fitting well due to their higher R^2 values.

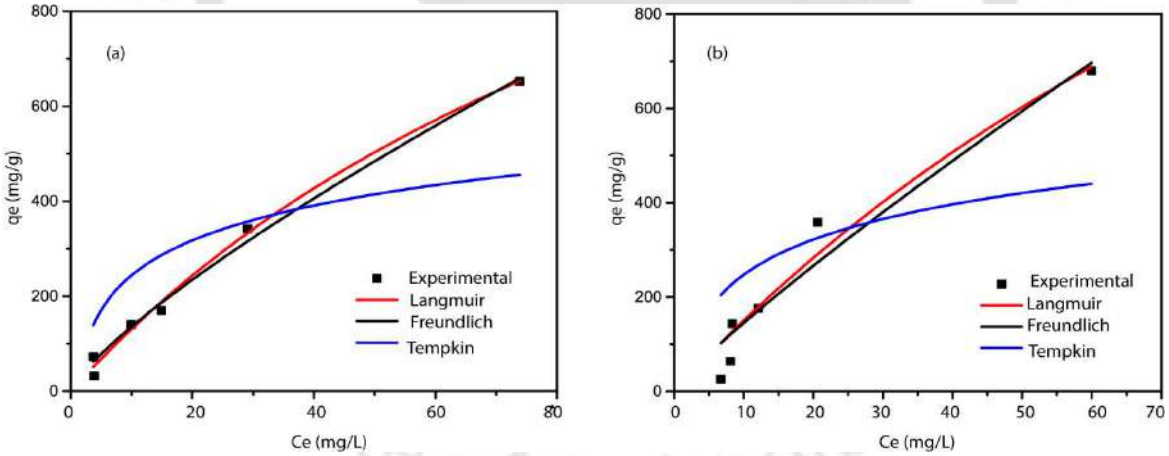

Figure 4.3. Non-linear isotherm study of BB removal by (a) Mat-1 and (b) Mat-2.

Table 4.2. Non-linear isotherm data of Bismarck brown removal by Mat-1 and Mat-2.

Material	Langmuir			Freundlich			Temkin		
	Q_{max} (mg/g^{-1})	K_b	R^2	n	K_f	R^2	K_T	b	R^2
Mat-1	1743	0.008	0.99	1.26	22	0.99	1E-12	244	0.62
Mat-2	2425.8	0.007	0.94	1.14	19.4	0.93	1E-12	247.6	0.45

4.3.1.2. Effect of Dose

Adsorption of BB dye on Mat-1 (Tannic iron complex) and Mat-2 (Guava iron complex) was investigated with different dose of 0.5, 1, 1.5, 2, 3 g/L at initial concentration of 400 mg/L of BB at pH 7 (Table 4.3. and Figure 4.4) With the varying dose of 0.5, 1, 1.5, 2, 3 g/L the removal percentage was 81, 95, 96, 97, 98% and 86, 96, 97, 97, 97% for Mat-1 and Mat-2, respectively at 400 mg/L concentration. Results showed that saturation occurred after the dose of 1 g/L in both materials. The dye uptake decreased from 651 to 131 mg/g with an increment of adsorbent dose from 0.5-3 mg/g for Mat-1. The decrease in adsorption capacities with an increment of material dose resulted from the less available surface area. In this study, both materials showed significantly good removal and adsorption capacities compared to the literature in Table 4.4

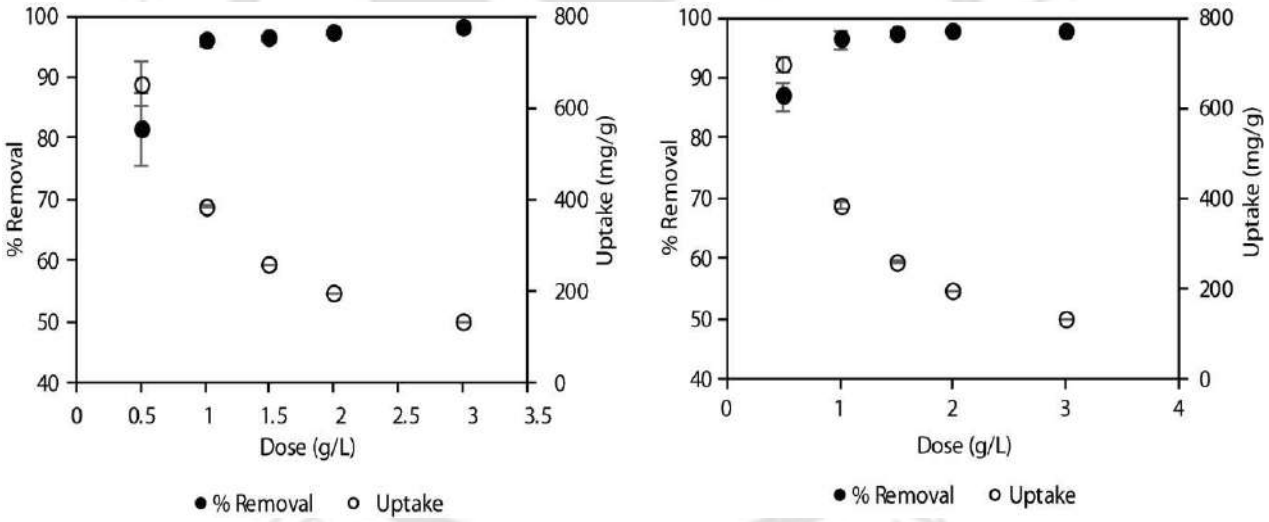

Figure 4.4. Effect of dosage of Mat-1 and 2 on BB (Conditions: Adsorbent dose=0.5-3 g/L, C_0=400 mg/L, pH=7, rpm=250, t=60 min).

Table 4.3. Effect of dose on BB removal.

Dose	Removal % by Mat-1	Removal % by Mat-2	Uptake (mg/g) Mat-1	Uptake (mg/g) Mat-2
0.5	81.4±6	86.9±2.2	651.6±48.8	695.2±17.9
1	95.7±0.6	96.3±1.4	383.07±2.6	385.3±8.3
1.5	96.3±0.5	97.3±0.3	256.9±1.4	259.6±0.8
2	97.1±0.5	97.6±.03	194.2±1	195.3±0.6
3	98.3±0.32	97.4±0.1	131.08±0.4	129.9±0.1

(At pH 7, 1 h contact time, 400 mg/L of dye concentration, and 250 rpm agitation.

Table 4.4. Comparison with previous reports for BB removal.

Composition	PH	Initial concentration (mg/L)	Dose (g/L)	Time (min)	Removal (%)	Experimental Uptake (mg/g)	References
(Co/Ni)-MOF		30	0.5	600	80	48	[12]
Brassica rapa leaf-based f-CdWO4	7	10	1.6	90	90	5.6	[4]
Sewage Sludge	-	50	0.5	240	86.7	86	[13]
Hen feather	3	10 × 10−5M	0.2	120	95.2	-	[7]
Pea peels	-	20	10	60	89	1.8	[14]
Modified biochar	3	150	1.7	60	49	45	[15]
Multi-wall carbon nanotube	5	5 × 10−5M	0.025	60	90	17.8	[16]
Iron Oxide Nanosphere (IONs)	7	40	1	24	50	20	[17]
multiwalled carbon nanotubes modified with Iron	7	25	0.1	80	86	177	[18]
Mat-1 (Tannic-Iron complex)	7	100	0.5	60	85	170	This study
		400	0.5	60	81.5	652	
Mat-2 (Guava-Iron complex)	7	100	0.5	60	88	176	This study
		400	0.5	60	85	680	

4.3.1.3. Effect of Time.

The effect of contact time in BB adsorption was investigated and depicted in Figure 4.5 (Table 4.5). The batch process was carried out with 400 mg/L of BB dye solution, with 1 g/L of material dose and 5-120 minutes time variances. The adsorption rate has been found to be very fast in both cases. The removal percentage of 400 mg/L of BB by Mat-1 and Mat-2 was 80 and 83%, respectively, in only 5 min of contact time. Mat-1 and Mat-2 showed 87% and 91% of dye removal, respectively, at 30 min of contact time. Saturation of materials occurred after 30 minutes of contact time in both of the materials.

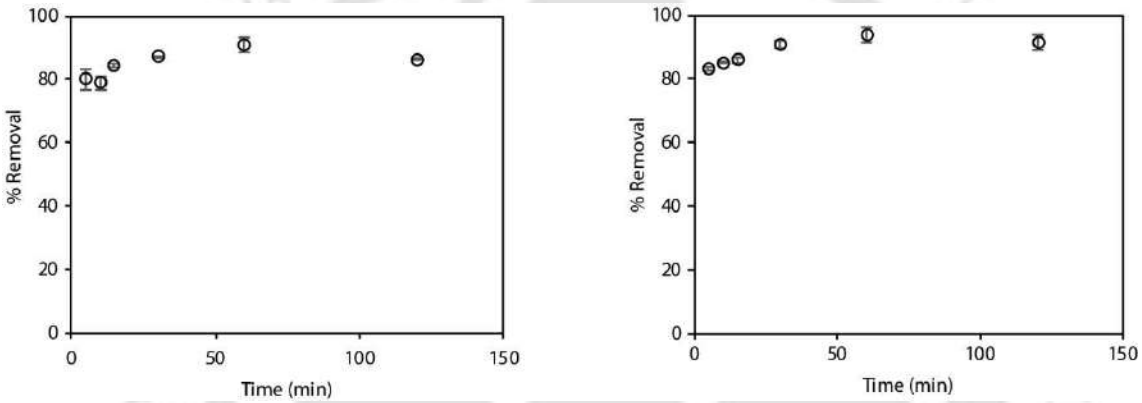

Figure 4.5. Effect of time for removal of 400 mg/L BB removal by (a) Mat-1 and Mat-2. (Conditions: t=5-120 min, C_0=400 mg/L, Adsorbent dose=1g/L, pH=7, rpm=250).

Table 4.5. Effect of contact time for BB removal.

Time(min)	Removal % by Mat-1	Removal % by Mat-2	Uptake (mg/g) Mat-1	Uptake (mg/g) Mat-2
5	80 ±3.47	83.3±0.6	320.04±13.8	333.3± 2.77
10	78.9± 2	85.16±0.26	314.6± 8.1	340.68 ±1.05
15	84 ±0.5	85.9±0.94	337 ±2.09	343.6± 3.78
30	87± 0.4	90.7±1.05	348.52 ±1.8	363.07 ±4.8
60	90.9± 2.2	93.72±2.25	363.98 ±8.99	374.89 ±8.9
120	86.4±0.26	91.5±2.5	345.5± 1.04	366.1 ±10.

(At pH 7, with dose of 1 g/L, 400 mg/L of dye concentration, and 250 rpm agitation)

The adsorption kinetics can assume the removal rate of the pollutant from aqueous solutions and gives important data for understanding the mechanism of adsorption in the batch process [19]. There are two phases in adsorption kinetics: initially rapid removal phase followed by a slow phase towards equilibrium stage.

The rate constants and the corresponding R^2 values of pseudo-first-order and pseudo-second-order are given in Table 4.6, and Figure 4.6. The correlation coefficient values of pseudo-second-order show better results in both Mat-1 and Mat-2 for BB removal. In all cases, q_e experimental values were matched with q_e calculated values (Qe_{cal}) in pseudo-second-order.

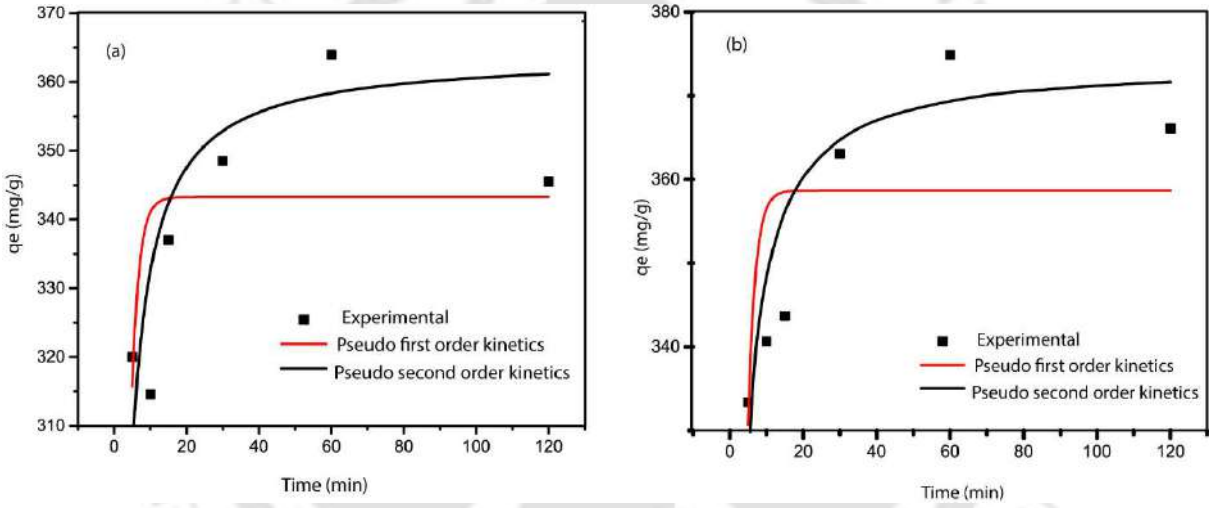

Figure 4.6. Kinetics study of BB removal by (a) Mat-1 and (b) Mat-2.

Table 4.6. Non-linear kinetics data of Bismarck brown removal by Mat-1 and Mat-2.

Sample	Qe_{exp}	Pseudo 1st order			Pseudo 2nd order		
		Qe_{cal}	k_1	R^2	Qe_{cal}	k_2	R^2
Mat-1	363	343	1.17	0.12	344.8	0.0029	0.6
Mat-2	374	358	1.2	0.23	370	0.0035	0.75

4.3.2. Desorption Study of BB

For bismarck brown, the adsorption-desorption studies were carried out with Mat-1 and Mat-2 with a dose of 0.5, 1 g/L in 3 days of cycles. Out of all solvents, methanol implied most for the desorption of the bismarck brown dye. Figure 4.7 showed a reduction of adsorption percentage from 91 to 85% after 3 days cycle, while the increase in desorption percentage from 71 to 86% in the case of Mat- 2, 0.5 g/L of dose. For mat-2, with the dose of 1 g/L, adsorption decreased from 95 to 89%, and desorption increased from 65 to 78%. Moreover, for Mat-1, with dose 0.5 g/L, adsorption percentage decreased 87 to 85%, desorption increased from 75 to 99 %, and material with dose 1g/L showed decreasing adsorption pattern from 91 to 90 % and increased desorption pattern of 60-97%.

We also checked the desorption of BB dye with Na^{+}, K^{+}, Ca^{+2}, Ba^{+2}, and Al^{+3} salts under similar conditions (Figure 4.7b). The cations were selected depending on the increasing size and charge. The results showed that more efficacious displacement of bb dye from materials has occurred with the increase in size and charges of cations. (Figure 4.7b). In the presence of aluminum salt, maximum desorption of 80% and 85% from Mat-1 and Mat-2 was observed. Due to the similar size and charge to iron, aluminum can bind strongly with the polyphenols of the materials.

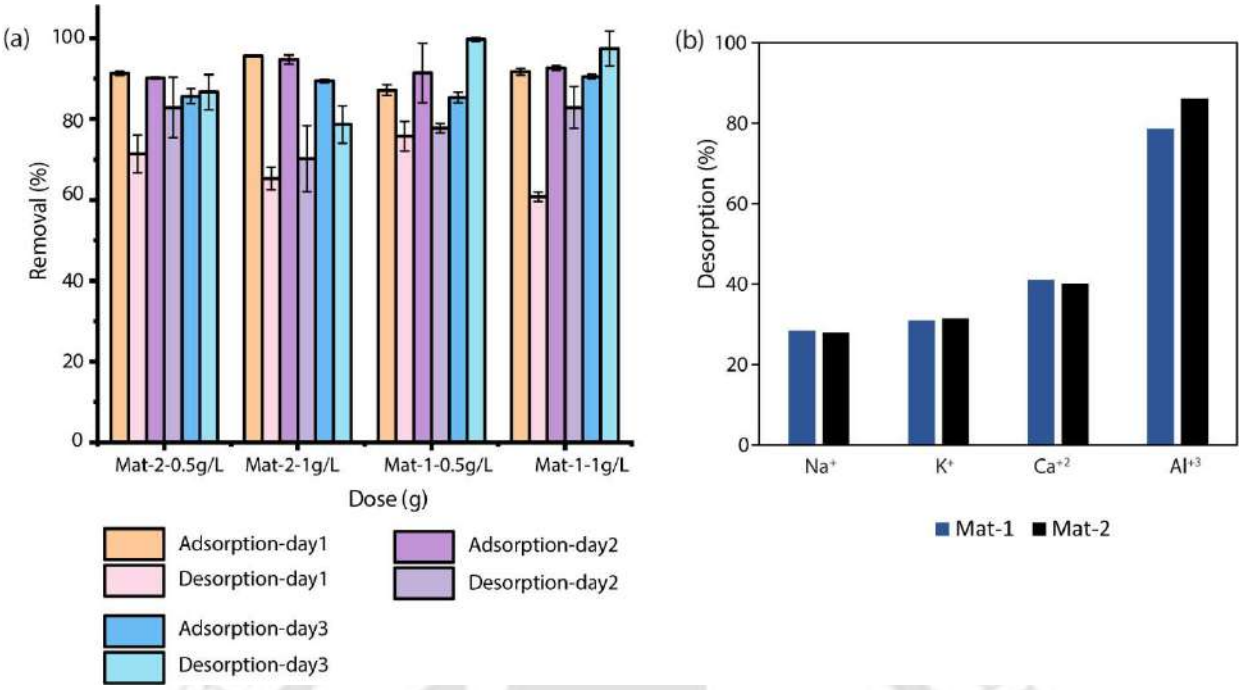

Figure 4.7. (a) Adsorption-desorption study of Mat-1 and Mat-2 for BB in MeOH, (b) desorption study with salt.

4.3.3. Cytotoxicity Test

The pre-treated and post-treated BB solutions were applied on *Allium cepa* to check the cytotoxic effect of the solutions. The effect of BB dye on *Allium cepa* root cells having mitosis is shown in Table.4.7 in terms of MI and chromosomal aberration. In this study, the root of *A. cepa* was treated for five days with distilled water (DW) as control, two different concentrations of 200 mg/L and 400 mg/L of BB dye, and after treated water of 400 mg/L concentration of BB by Mat-1 and Mat-2.

It was noticed that in both 200 mg/L and 400 mg/L of dye treated *A. cepa* root cells, the mitotic index decreased compared to the control treatment (DW). *A. cepa* root cell treated with BB stock solution showed the mitotic index of 12.3% at 200 mg/L and 11.7% at 400 mg/L of dye concentration compared to distilled water treated *A. cepa* (MI= 15.7%). The MI data confirmed that miotic inhibition of 21 and 24% occurred with increasing Bismarck brown (BB) dye

concentration of 200 to 400 mg/L. The decrease in MI might be due to mitotic inhibition or cell death. On the other side, 19 and 12% increase in MI was observed in the case of Mat-1, and Mat-1 adsorbed residual dye solution.

Table 4.7. Cytootoxic analysis of on *A. cepa.*

	Total no. cell	Prophase	Metaphase	Anaphase	Telophase	MI %	Deform cell %
Mat-1	300	47	2	5	2	18.7	-
Mat-2	300	48	1	4	0	17.7	-
BB-200	300	31	1	3	2	12.3	41
BB-400	300	35	0	0	0	11.7	95
Control	300	39	2	4	2	15.7	-

After the treatment with 400 mg/L of stock BB dye on allium root cell, no such mitotic stages were observed. In most of the cells, the interphase stage was observed and the change in cell structures (elongated cells) was observed (Figure. 4.8c, 4.9h). In the case of 200 mg/L of BB dye treated *Allium cepa* root tip cell, chromosomal aberration in metaphase and anaphase was observed. The degradation of cell walls and agglomeration of cells was also observed (Figure. 4.8b, 4.9g). At 200 mg/L of concentration, 7% of chromosomal abnormalities with 41% cell deformation were found. However, at 400 mg/L of dye concentration, >90% of cell deformation was observed, as elongation of all the cells was noticed.

No chromosomal aberration was identified in control as well as in both after Mat-1 and Mat-2 treated BB solution applied *A. cepa* root cells. Here all cells are intact without any cell and chromosomal deformation. However, with the increase of dye concentration, the change in cell structure and elongated cells were observed (Figure 4.8a, 4.8d, 8e; 4.9a, 4.9b, 4.9c, 4.9d). With the increase of stress, such configuration of cells in *A. cepa* was also observed by Azeez et al., (2020) [20]. Thus, from the MI % and cell abnormality % and the microscopic images, it was

clear that, after treatment of 400 mg/L of BB dye solution with Mat-1 and Mat-2, the treated water showed no negative effect on *A. cepa* cells.

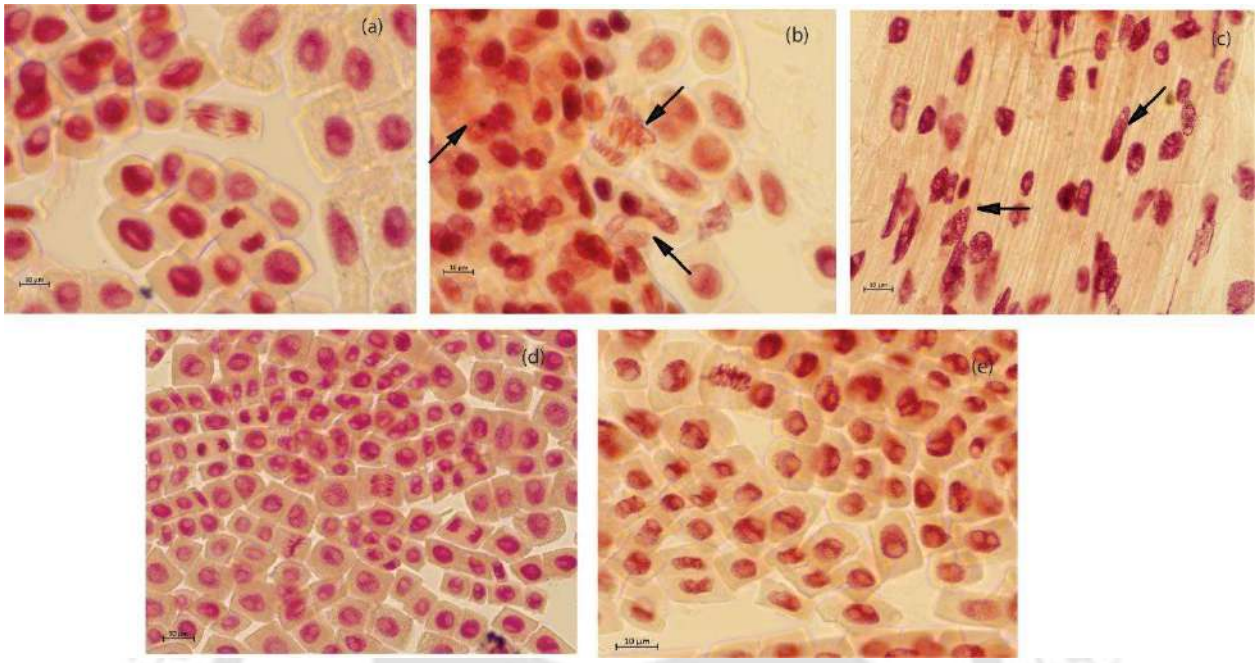

Figure 4.8. Microscopic observation of *A. cepa* cell. (a) Control (b) treated with 200 mg/L of BB (c) treated with 400 mg/L of BB (d) after treatment of Mat-1 and (e)Mat-2.

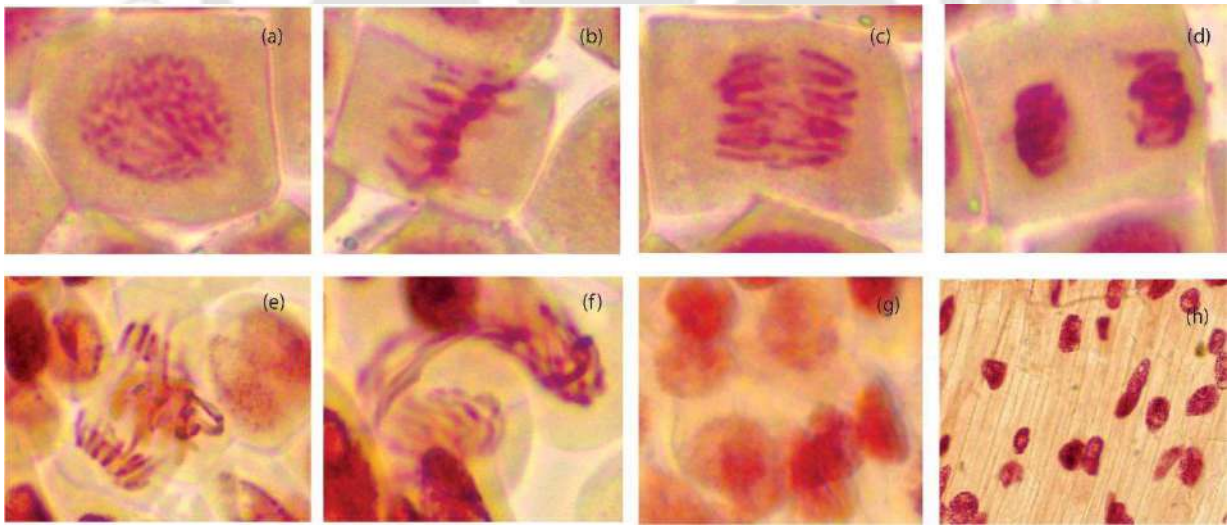

Figure 4.9. Chromosomal observation of *A. cepa* cell. (a) normal prophase; (b) normal metaphase; (c) normal anaphase; (d) normal telophase; (e) anaphase with chromosomal aberration in exposure of BB; (f) chromosomal deformation chromosomal aberration, (g) cellular agglomeration with cell wall degradation; and (h) cell elongation.

4.4. Conclusion

In this chapter, the removal efficiency of iron-polyphenol complexes (Mat-1 and Mat-2) were checked on Bismarck brown R (BB) dye. Both materials showed ~80% removal efficiency at a wide range of dye concentrations (20-400 mg/L). Mat-1 exhibited the adsorption capacities of 652 mg/g of BB dye. Moreover, Mat-2 showed 680 mg/g of adsorption capacity with the dose of 0.5g/L, 400 mg/L of dye concentration at pH 7. The adsorption-desorption study indicates the reusability of both Mat-1 and Mat-2 more than 3 times. After the dye adsorption, solutions were applied for the further cytotoxic test on *A. cepa,* as BB is a carcinogenic dye.

The decrease in cytotoxic effect was observed after adsorption of BB solution by iron-polyphenol complexes. With direct application of BB dye, the chromosomal deformation, decrease in MI %, and elongation of cell morphology was observed. After the adsorption of BB solution by Mat-1 and Mat-2, the residual solutions have not shown any toxic effect in the *A. cepa* root cells in terms of the mitotic index and chromosomal deformation. 95% of cell deformation was observed with direct treatment of 400 mg/L of stock BB solution. While Mat-1 and Mat-2 effectively reduce the carcinogenic effect of azo dye.

References

[1] L. Bulgariu, L.B. Escudero, O.S. Bello, M. Iqbal, J. Nisar, K.A. Adegoke, F. Alakhras, M. Kornaros, I. Anastopoulos, The utilization of leaf-based adsorbents for dyes removal: A review, J. Mol. Liq. 276 (2019) 728–747. https://doi.org/10.1016/j.molliq.2018.12.001.

[2] V. Katheresan, J. Kansedo, S.Y. Lau, Efficiency of various recent wastewater dye removal methods: A review, J. Environ. Chem. Eng. 6 (2018) 4676–4697. https://doi.org/10.1016/j.jece.2018.06.060.

[3] J. Mittal, V. Thakur, A. Mittal, Batch removal of hazardous azo dye Bismark Brown R using waste material hen feather, Ecol. Eng. 60 (2013) 249–253. https://doi.org/10.1016/j.ecoleng.2013.07.025.

[4] B. Fatima, S.I. Siddiqui, R. Ahmed, S.A. Chaudhry, Green synthesis of f-CdWO 4 for photocatalytic degradation and adsorptive removal of Bismarck Brown R dye from water, 22 (2019).

[5] V. Ponnusami, V. Gunasekar, S.N. Srivastava, Kinetics of methylene blue removal from aqueous solution using gulmohar (Delonix regia) plant leaf powder: Multivariate regression analysis, J. Hazard. Mater. 169 (2009) 119–127. https://doi.org/10.1016/j.jhazmat.2009.03.066.

[6] H. Hosseini, A. Zirakjou, D.J. McClements, V. Goodarzi, W.-H. Chen, Removal of methylene blue from wastewater using ternary nanocomposite aerogel systems: Carboxymethyl cellulose grafted by polyacrylic acid and decorated with graphene oxide, J. Hazard. Mater. 421 (2022) 126752. https://doi.org/10.1016/j.jhazmat.2021.126752.

[7] A.M. Jyoti Mittal, Vijay Thakur, Batch removal of hazardous azo dye Bismark Brown R using waste material hen feather, Ecol. Eng. 60 (2013) 249– 253. https://doi.org/10.1016/j.ecoleng.2013.07.025.

[8] B. de C. Ventura-Camargo, D. de F. de Angelis, M.A. Marin-Morales, Assessment of the cytotoxic, genotoxic and mutagenic effects of the commercial black dye in Allium cepa cells before and after bacterial biodegradation treatment, Chemosphere. 161 (2016) 325–332. https://doi.org/https://doi.org/10.1016/j.chemosphere.2016.06.085.

[9] I.S. Khan, M.N. Ali, R. Hamid, S.A. Ganie, Genotoxic effect of two commonly used food dyes metanil yellow and carmoisine using Allium cepa L. as indicator, Toxicol. Reports. 7 (2020) 370–375. https://doi.org/https://doi.org/10.1016/j.toxrep.2020.02.009.

[10] P. Terangpi, S. Chakraborty, M. Ray, Improved removal of hexavalent chromium from 10 mg/L solution by new micron sized polymer clusters of aniline formaldehyde condensate, Chem. Eng. J. 350 (2018) 599–607. https://doi.org/10.1016/j.cej.2018.05.171.

[11] I. Shafi, N. Ali, R. Hamid, S. Ahmad, Genotoxic effect of two commonly used food dyes metanil yellow and carmoisine using Allium cepa L . as indicator, Toxicol. Reports. 7 (2020) 370–375. https://doi.org/10.1016/j.toxrep.2020.02.009.

[12] A. Abbasi, M. Soleimani, M. Najafi, S. Geranmayeh, Inorganica Chimica Acta New interpenetrated mixed (Co / Ni) metal – organic framework for dye removal under mild conditions, 439 (2016) 18–23. https://doi.org/10.1016/j.ica.2015.09.028.

[13] S.H. Ali, T.E. Jassim, Thermodynamics and Kinetic study of Bismarck Brown R Dye Adsorption from Aqueous Solution using Sewage Sludge, xxx (2020).

[14] T.A. Khan, R. Rahman, E.A. Khan, Decolorization of bismarck brown R and crystal violet in liquid phase using modified pea peels : non-linear isotherm and kinetics modeling, Model. Earth Syst. Environ. 2 (2016) 1–11. https://doi.org/10.1007/s40808-016-0195-6.

[15] I.W.A. Publishing, W. Science, Magnetically modi fi ed biochar for organic xenobiotics removal Ivo S afarik , Zdenka Made rova, Kristyna Pospis kova , Hans-Peter Schmidt , ˇ j Malina Eva Baldíkova, Jan Filip , Michal Krizek , Ondr e and Mirka S afar ikova, (2016) 1706–1715. https://doi.org/10.2166/wst.2016.335.

[16] A.F.H. and F.H.H. Ahmed M. Kamil, Firas H. Abdalrazak, Adsorption of Bismarck Brown R Dye Onto Multiwall Carbon Nanotubes, J. Environ. Anal. Chem. 1 (2014). https://doi.org/10.4172/jreac.1000104.

[17] M. Khosravi, B. Yahyaei, S. Azizian, M. Khosravi, B. Yahyaei, S. Azizian, Adsorption of Bismarck Brown by Iron Oxide Nanosphere and Its Modified Form, J. Dispers. Sci. Technol. 35 (2014) 1135–1142. https://doi.org/10.1080/01932691.2013.833484.

[18] T.A. Khan, M. Nazir, E.A. Khan, Magnetically modified multiwalled carbon nanotubes for the adsorption of bismarck brown R and Cd (II) from aqueous solution : batch and column studies, 3994 (2015) 0–17. https://doi.org/10.1080/19443994.2015.1100553.

[19] B. Cheng, Y. Le, W. Cai, J. Yu, Synthesis of hierarchical Ni(OH)2 and NiO nanosheets and their adsorption kinetics and isotherms to Congo red in water, J. Hazard. Mater. 185 (2011) 889–897. https://doi.org/10.1016/j.jhazmat.2010.09.104.

[20] S.O. Azeez, R.A. Ayo-lawal, I.J. Olawuni, O.G. Abraham, Evaluation of the bio-toxicity and cytogenetic effects of methanolic leaf extract of Heliotropium indicum L ., 14 (2020) 1–10.

Chapter V

Removal of Fluoride Using Mat-1 and Mat-2

5.1. Introduction

In the previous chapters, two cationic dyes were efficiently removed at above the values of pH_{zpc} in Mat-1 and Mat-2. The results showed that both the adsorbents were capable of removing cationic dyes from an aqueous solution at pH 7. Moreover, below pH_{zpc} values, as the surfaces of the materials are positively charged, they are expected to be capable of removing the negatively charged ions. In this chapter, we choose fluoride to check the materials removal capacity.

One of the most environmental contaminants in underground water is fluoride. Fluoride contamination of groundwater is caused by geological and human activities. Apart from pollution, fluoride has adverse effects on human beings due to toxicity at lower concentrations and low discharge limits (CPCB, 2010). Estimation of the toxic effects of fluoride shows that millions of people suffer from their hazardous effects worldwide [1]. According to the studies, drinking water is the primary source of fluoride; daily and prolonged intake of drinking water with high fluoride concentrations (>1.5 mg/L) can cause birth, fertility, and immunological deformities [2]; dental and skeletal fluorosis [3][4] etc. Because of these probable severe adversities, permissible values of 1500 µg/L for fluoride are formulated by WHO and Indian Standard (IS 10500) guidelines. The Assam region of NE India has been recognized as a fluoride-affected area (Central Ground Water Board, Ministry of Water Resources, Government of India, 2010) [5].

To the best of our knowledge, guava leaf iron complexes or tannic-iron complexes have not been used in fluoride removal studies. In the present study, two iron-polyphenol complexes were synthesized and applied as a probe to remove fluoride from aqueous solutions. A comparison of fluoride removal efficiency was also carried out among the tannic acid-iron complex and guava leaf iron complex. The batch process was carried out at different variances of pH, concentration, dose, and time. Materials were also applied on real fluoride contaminated water of 15 sites of Guwahati city.

5.2. Experimental Section

5.2.1. Materials and Methods

Tannic acid ($C_{76}H_{52}O_{46}$) and ferrous sulfate ($FeSO_4.7H_2O$) were purchased from Alfa Aesar, and Rankem respectively. Sodium hydroxide, potassium nitrate, and methanol were purchased from Merck, India. Gallic acid and Folin Ciocalteu reagent were bought from Sigma Aldrich and SRL Pvt. Ltd, respectively. Standard fluoride solution (100 mg/L) (Thermo Orion, USA), Total ionic strength adjustment buffer (TISAB III) was purchased from Thermo scientific. Purified water from an Amtrol reverse osmosis system was used for all experiments.

5.2.2. Fluoride Measurement Using ISE

Fluoride concentration in solution was measured using Thermo Orion Benchtop multiparameter kit with fluoride ion-selective electrode. The instrument was repeatedly calibrated using a standard solution.

5.2.3. Adsorption Experiments

Adsorption experiments for fluoride removal by Mat-1 and Mat-2 were carried out using batch processes at room temperature. Adsorption processes were executed at different pH variance of 2, 3, 4, 5, 7, 9; with fluoride concentrations of 5, 10, 20, 40, 50, and 60 mg/L; adsorbent

dose of 0.5, 1, 2, 4, 6, 8, and 10 g/L; and contact time of 5, 10, 30, 60, 120, 180 min. The pH of the solutions was adjusted with 1N HCl and 1N NaOH. A calibration curve of fluoride was prepared from 1 to 100 mg/L of concentration, using commercially available standard fluoride stock solution.

5.3. Result and Discussion

5.3.1. Fluoride Adsorption Study

5.3.1.1. Effect of pH

The influence of solution pH on fluoride removal by Mat-1 and Mat-2 was studied using the batch adsorption process. Batch experiments were performed at different pH of 2, 3, 4, 5, 7, 9. The other experimental variables have remained constant with 10 mg/L concentration of fluoride, 250 rpm, a material dose of 4 g/L, and 60 min of contact time (Figure 5.1). The results showed that with the increase in pH, removal percentage for both cases of Mat-1 and Mat-2 decreases. Mat-1 showed a significant decline in removal from 63% to 8% upon the increase in pH from 2 to 9. Mat-2 showed a similar decrease in removal pattern from 50% to 11%. Similarly, Viswanathan et. al. (2016) reported that Fe_3O_4 fabricated nano polymeric composite showed maximum fluoride removal took place at pH 3, and with increasing pH, the removal declined [6]. The point of zero charges (pH_{zpc}) of Mat-1 and Mat-2 were 3.9 and 4.5. Therefore, in acidic pH, the surface of the materials becomes positively charged, and due to electrostatic attraction, the removal of negatively charged fluoride has occurred. However, at pH > pH_{pzc}, negatively charged in the material surface caused the repulsion of fluoride. With increase in pH, the decrease of removal percentage was observed in both the cases.

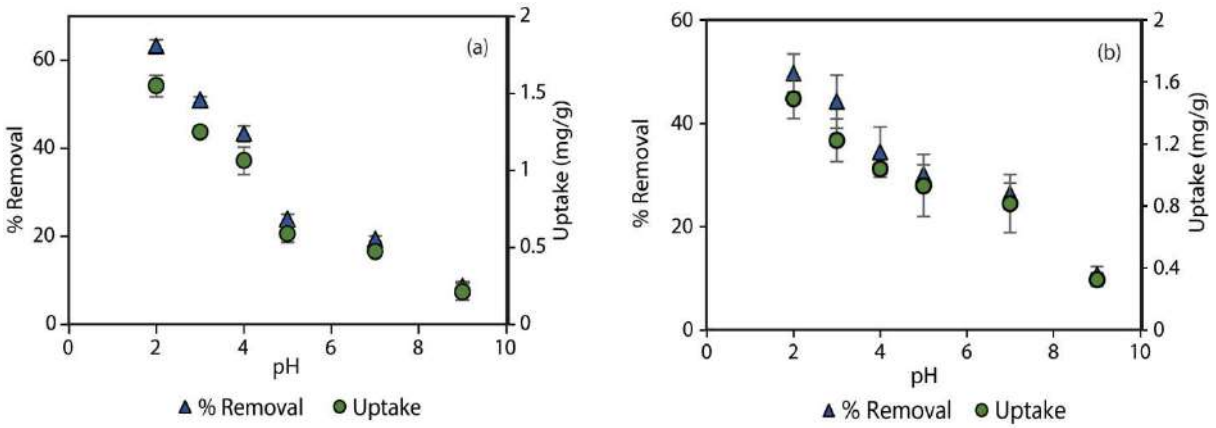

Figure 5.1. Effect of pH on fluoride removal by (a) Mat-1 and (b) Mat-2.

5.3.1.2. Effect of Concentration

The fluoride removal by Mat-1 and Mat-2 was studied by varying the initial fluoride concentration of 5, 10, 20, 40, 50, and 60 mg/L, with a contact time of 60 min, pH 2, and material dose of 4 g/L at 250 rpm (Figure 5.2). The result showed that with the increase in concentration, the adsorption capacities of Mat-1 and Mat-2 also increased. For Mat-1, the fluoride uptake reached 7 mg/g at 60 mg/L of fluoride concentration. While, at 10 mg/L of concentration Mat-1 showed 60% removal with adsorption of 1.6 mg/g. For Mat-2, at 60 mg/L concentration the fluoride adsorption capacity was 5.1 mg/g. The fluoride adsorption capacity increased with the increased fluoride concentration, as the maximum adsorption sites in Mat-1 and Mat-2 were utilized.

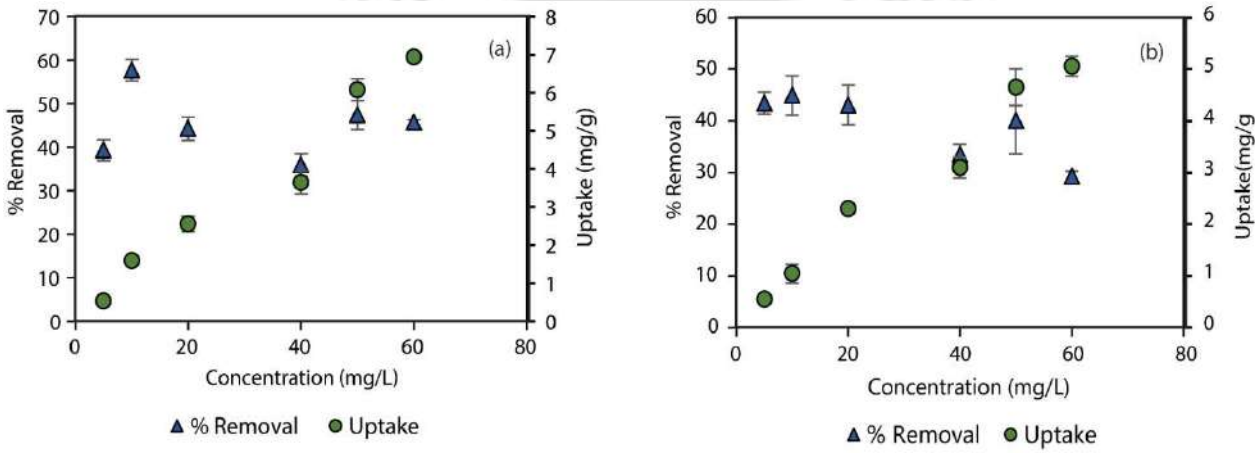

Figure 5.2. Effect of concentration on fluoride removal by (a) Mat-1 and (b) Mat-2.1

5.3.1.3. Effect of Dose

The effect of dose on fluoride removal by Mat-1 and Mat-2 was investigated with material doses of 0.5, 1, 2, 4, 6, 8, and 10 g/L; on two different concentrations of 10 and 50 mg/L, at pH 2 for 60 min of contact time and 250 rpm (Figure 5.3). In Mat-1, with the increase of dose from 0.5 to 10 g/L, the removal percentage also increased from 16 to 71 % for 10 mg/L and 12 to 64% for 40 mg/L of fluoride observed. For Mat-2, it was found that the percentage removal also increased from 17 to 72% for 10 mg/L and 7.5 to 57% for 40 mg/L of fluoride, respectively. While with the rise in dose, the decrease in adsorption capacity was observed in all the cases. With increments of material dose from 0.05 to 10 g/L, reduction of adsorption capacity from 12.3 to 3.2 mg/g for Mat-1 and 7.5 to 2.8 mg/g for Mat-2 was noticed at 50 mg/L concentration. At higher fluoride concentration, the binding capacity of the adsorbent approaches saturation, resulting in an overall decrease in adsorption capacity [7,8]. The result showed the maximum fluoride uptake capacities of Mat-1 and Mat-2 were 12.3 and 7.5 mg/g. Materials removal capacities were also compared with similar kinds of material in the literature (Table 5.1).

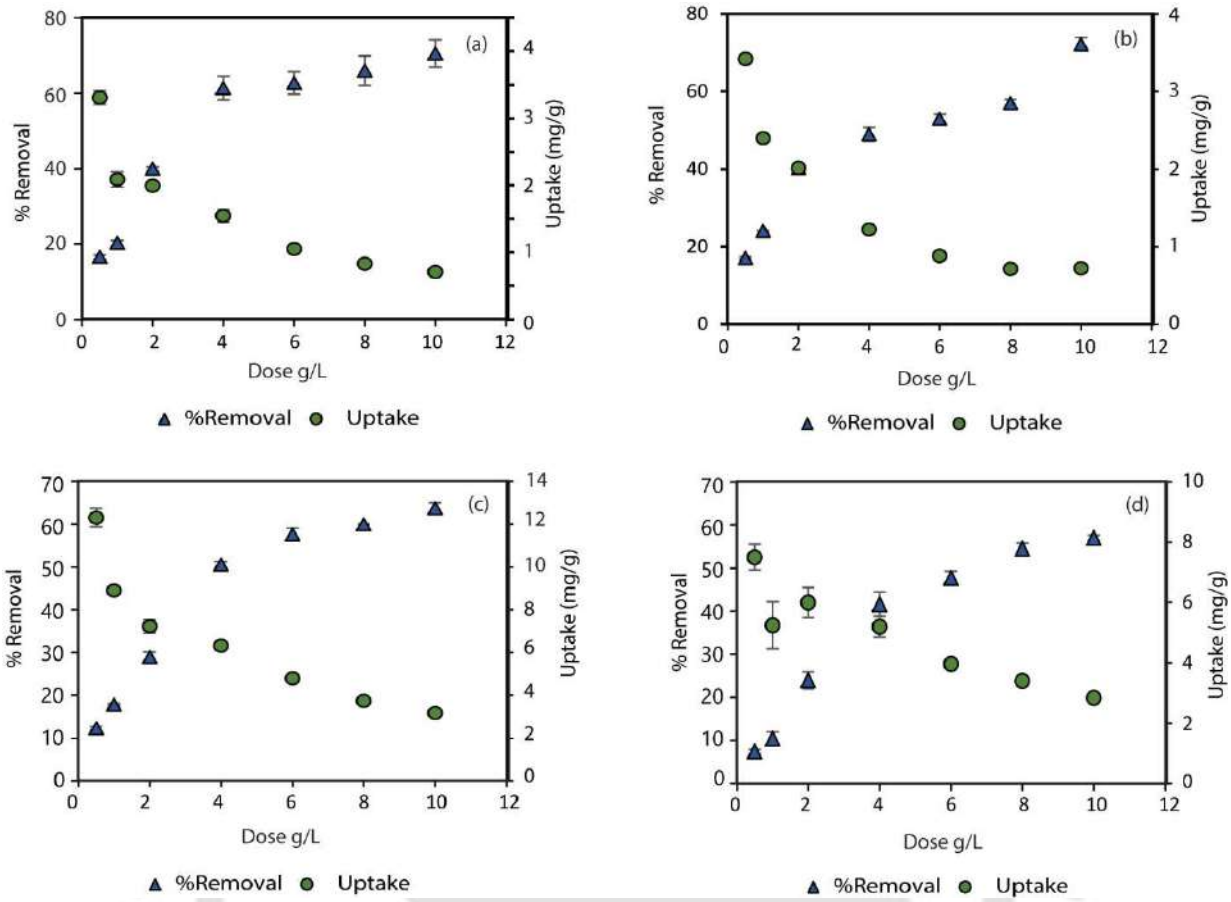

Figure 5.3. Effect of dose in fluoride removal by (a) Mat-1 and (b) Mat-2.

Table 5.1. Comparison of fluoride removal capability of synthesized materials with literature.

Materials Used	C_0	pH	dose	Time (min)	Removal %	q_e (mg/g)	References
Iron oxide nano with *Moringa oleifera* leaf extract	6	7	0.5g	40	12.5	1.4	[7]
Iron oxyhydroxide NP coated rice husk	30	4	0.8g	45	68	18	[9]
Al_2O_3–Fe_3O_4–expanded graphite nano-sandwich	5	4	0.4	120	77	2.2	[10]
Mesoporous 2-line ferrihydrite	10	7	1	30	90	9	[11]
Iron e aluminum nanocomposite	20		2.5	60	79	3.28	[12]
Chitosan based Ti–Al binary metal oxide	10		4	1440	70	2.2	[13]
Iron Nano-with tea	4	7	2.5	30	87	1.4	[14]
Fe_3O_4 NP with *Simmondsia*	2 10	5		80	93 21		[15]

chinensis (jojoba) extract							
Iron based MOF	10	7	0.1	30		4.9	[16]
cerium (IV)-incorporated hydrous iron (III) oxide	10	7	2	120	34	1.7	[17]
Mat-1	10	2	4	60	66.2	1.85	Present study
Mat-2					54.4	1.55	
	40		0.5	60	12.3	12.3	
					7.5	7.5	

Isotherms are beneficial for explaining the mechanism of adsorption and the theoretical uptake capacity of all the materials. We have fitted the data to all three standard models of Langmuir, Freundlich, and Temkin linear equations (Table 5.2 and Figure 5.4). The non-linear equation was not fitted well. Therefore, we applied the linear isotherm equation in this chapter. By comparing the data obtained from the isotherm models, we conclude that both the Langmuir and Freundlich models fitted the data due to their R^2 value being closer to unity in Mat-1 (Table 5.2). However, the Temkin model did not fit. In Mat-2, Freundlich isotherm was better fitted.

Table 5.2. Isotherm parameters of fluoride in Mat-1 and Mat-2.

Material	Langmuir			Freundlich			Temkin		
	Q_{max}	K_b	R^2	n	K_f	R^2	K_T	b	R^2
Mat-1	18.8	0.008	0.95	0.77	13.8	0.95	0.077	8.3	0.89
Mat-2	20	0.006	0.96	0.47	13.8	0.97	0.073	5.9	0.95

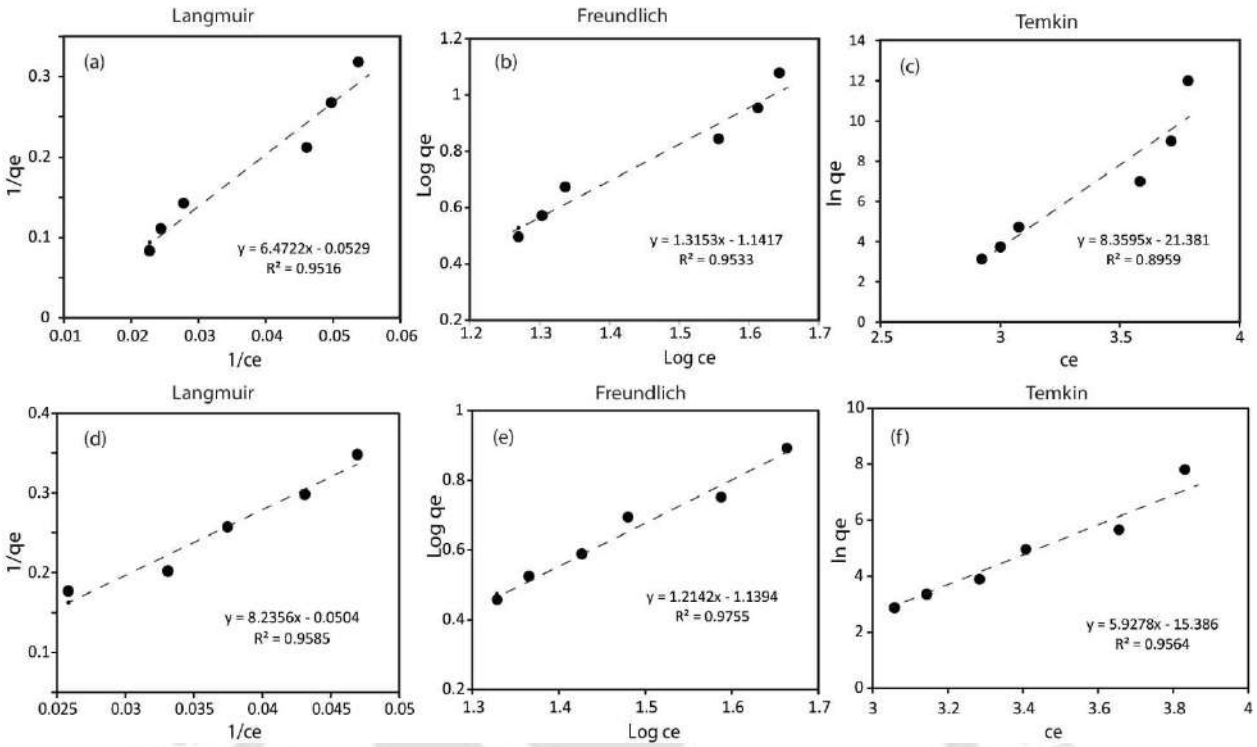

Figure 5.4. Linear Isotherm of Mat-1 (a) Langmuir, (b) Freundlich, (c) Temkin; Mat-2 (d) Langmuir, (e) Freundlich, (f) Temkin.

5.3.1.4. Effect of Time

Effect of contact time for both Mat-1 and Mat-2 were optimized through experimentation with 5, 10, 30, 60, 120, 180 min time period, with 10 mg/L fluoride concentration, at pH 2 and dose 4 g/L. It was observed that the fluoride removal percentage and adsorption capacity of Mat-1 and Mat-2 increased with increasing contact time (Figure 5.5). Results showed 66.2% of removal fluoride with 1.85 mg/g of uptake capacity by Mat-1. In contrast, Mat-2 showed 54.4 % of removal with 1.55 mg/g of uptake at 10 mg/L fluoride concentration. The pseudo first-order (Eq. 4) and pseudo second-order (Eq. 5) models were used to estimate the adsorption kinetics of fluoride adsorption by Mat-1 and Mat-2 (Figure 5.6, Table 5.3).

$$q_t = q_e\,(1 - e^{-k_1 t}) \qquad (4)$$

$$q_t = \frac{k_2\, q_e^2\, t}{1 + k_2\, q_e\, t} \qquad (5)$$

Where k_1 and k_2 are the rates constant of pseudo-first order and second-order kinetics; q_t is adsorption capacity at time t, and q_e is equilibrium adsorption capacity. The data fits better with the second-order rate plot in both cases, which means the chemisorption processes were carried out.

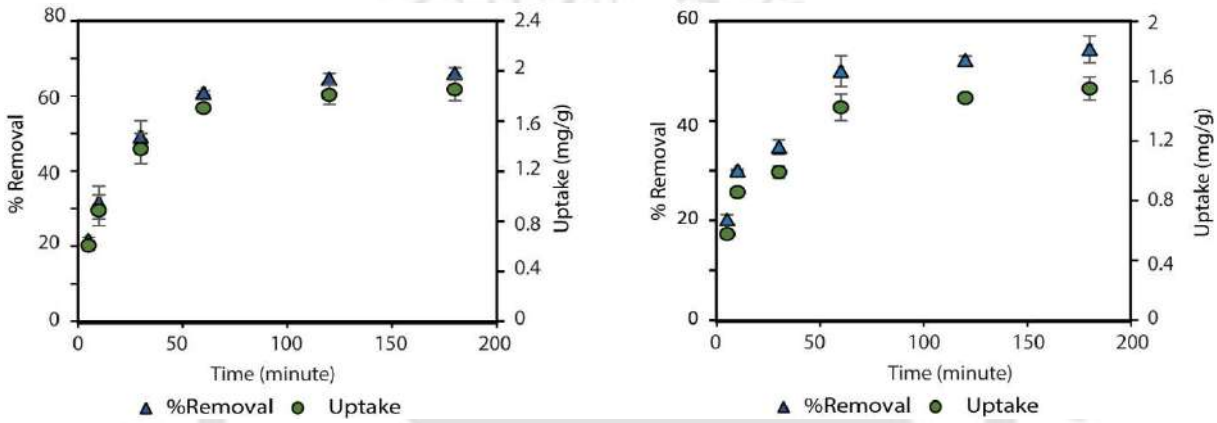

Figure 5.5. Effect of time for fluoride removal by Mat-1 and Mat-2.

Table 5.3. Non-linear kinetics data of 10 mg/L of fluoride removal by Mat-1 and Mat-2.

Sample	Qe exp	Pseudo 1st order			Pseudo 2nd order		
		Qe cal	k_1	R^2	Qe cal	k_2	R^2
Mat-1	1.85	1.78	0.149	0.96	1.83	0.056	0.97
Mat-2	1.55	1.44	0.173	0.8	1.5	0.0702	0.93

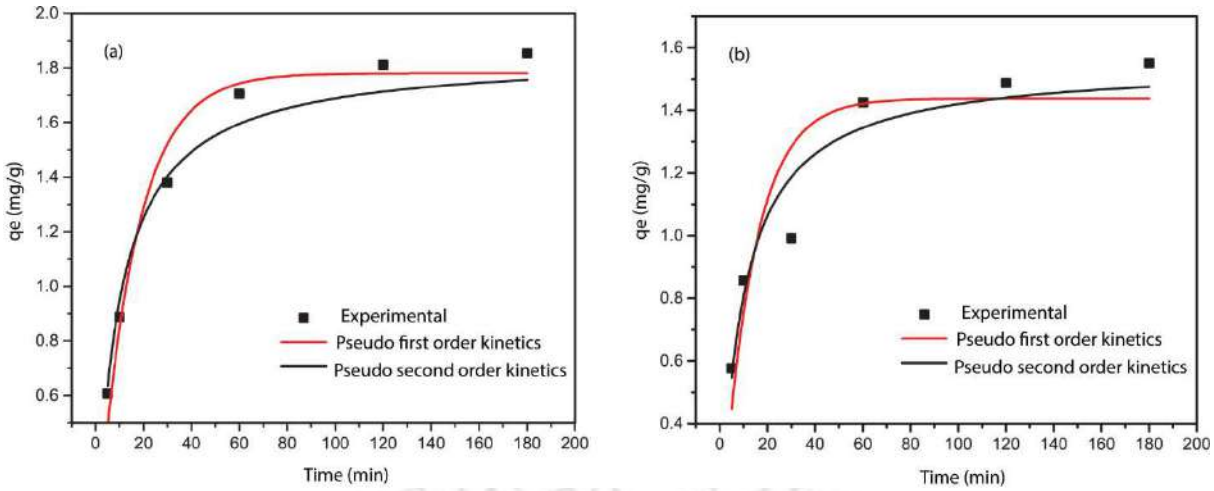

Figure 5.6. Kinetics of fluoride removal by Mat-1 and Mat-2.

5.3.2. Desorption Study

The desorption study was carried out, followed by adsorption processes. The fluoride adsorbed Mat-1 and Mat-2 were used for the desorption study. The desorption of fluoride from Mat-1 and Mat-2 was carried out using NaOH solution. Mat-1 and Mat-2 were treated with 0.02, 0.04, 0.06,0.08 and 0.1 M of NaOH for 1 h. fluoride desorption. For Mat-1 the fluoride desorption capacities using NaOH solutions of 0.02, 0.04, 0.06,0.08 and 0.1 M were 45, 47, 56, 62, 68%. In Mat-2 the desorption efficiencies were 48, 55, 56, 61, 69%. Both materials showed similar kinds of desorption values at a high alkaline medium.

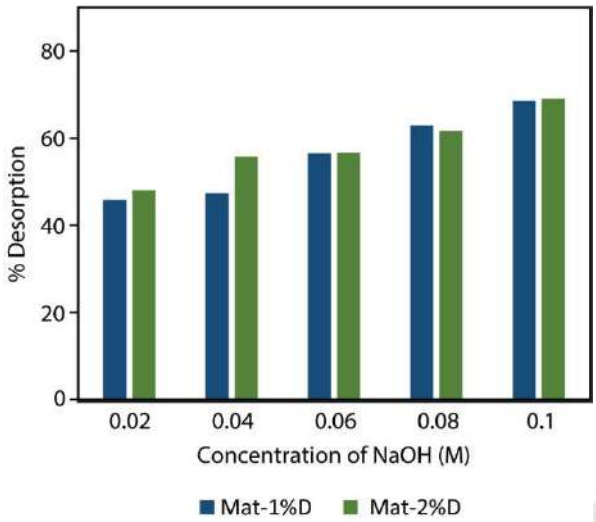

Figure 5.7. Desorption of fluoride using different concentrations of fluoride.

5.3.3. Fluoride Removal from Real Water Sample

For authentication of Mat-1 and Mat-2 on fluoride removal capacity, all the materials were applied to real fluoride contaminated water. Groundwater samples were collected from 15 different sites of Guwahati city: Birkuchi, Satgaon, Narengi, Sixmile, Beltala, Khanapara, Downtown, Adabari and Amingaon. Some areas of Guwahati city belong to fluoride affected zone. Among them, the water sample of six sites crossed the threshold limit (Table 5.4).

After treatment of water, four samples were reached below the WHO recommended permissible limit (1.5 mg/L) with 2 g/L doses of Mat-1 and Mat-2 and contact time of 1 h. For the other two samples, the fluoride concentration reached 2.2 and 2.4 mg/L from 4.04 and 4.4 mg/L with a dosage of 2 g/L of the materials. After the increase in dose to 3 g/L, those two samples also reached within the permissible limit. The physio-chemical parameters like pH and conductivity were also checked. The results clearly indicate that Mat-1 and Mat-2 are applicable for the removal of fluoride from groundwater.

Table 5.4. Removal of fluoride-affected water samples in Guwahati, Assam using Mat-1 and Mat-2.

place	Initial-F (conc)	Final F (conc)		Mat-1 (% R)	Mat-2 (%R)
		Mat-1	Mat-2		
Birkuchi	2.06	1.02	1.13	50.49	45.15
Satgaon	1.63	0.46	0.53	64.38	59.23
Narengi-1	4.08	1.31	1.36	66.67	65.44
Narengi-2	4.43	1.45	1.48	67.27	66.14
Sixmile-3	2.66	0.9	1.01	62.84	57.85
Sixmile-2	1.68	0.37	0.41	77.9	76.2

5.3.4. XPS and EDX

The elemental analysis of Mat-1 and Mat-2 before and after fluoride removal was measured using XPS (Figure 5.8). A new peak was observed at 685 eV in Mat-1, Mat-2 after the adsorption samples, indicating fluoride was effectively adsorbed by Materials (Figure 5.8a, 5.8b). The F1s spectra also confirm the adsorption of fluoride in the materials. The comparison of before and after adsorption spectra of materials clearly signified the presence of a new peak of fluoride at 684 eV, which was absent in the material before the adsorption process (Figure 5.8c, 5.8d). The EDX spectra of the materials before and after adsorption of fluoride are presented in Figure 5.9. Results also supported the XPS data and signified the presence of fluoride in both adsorbed materials.

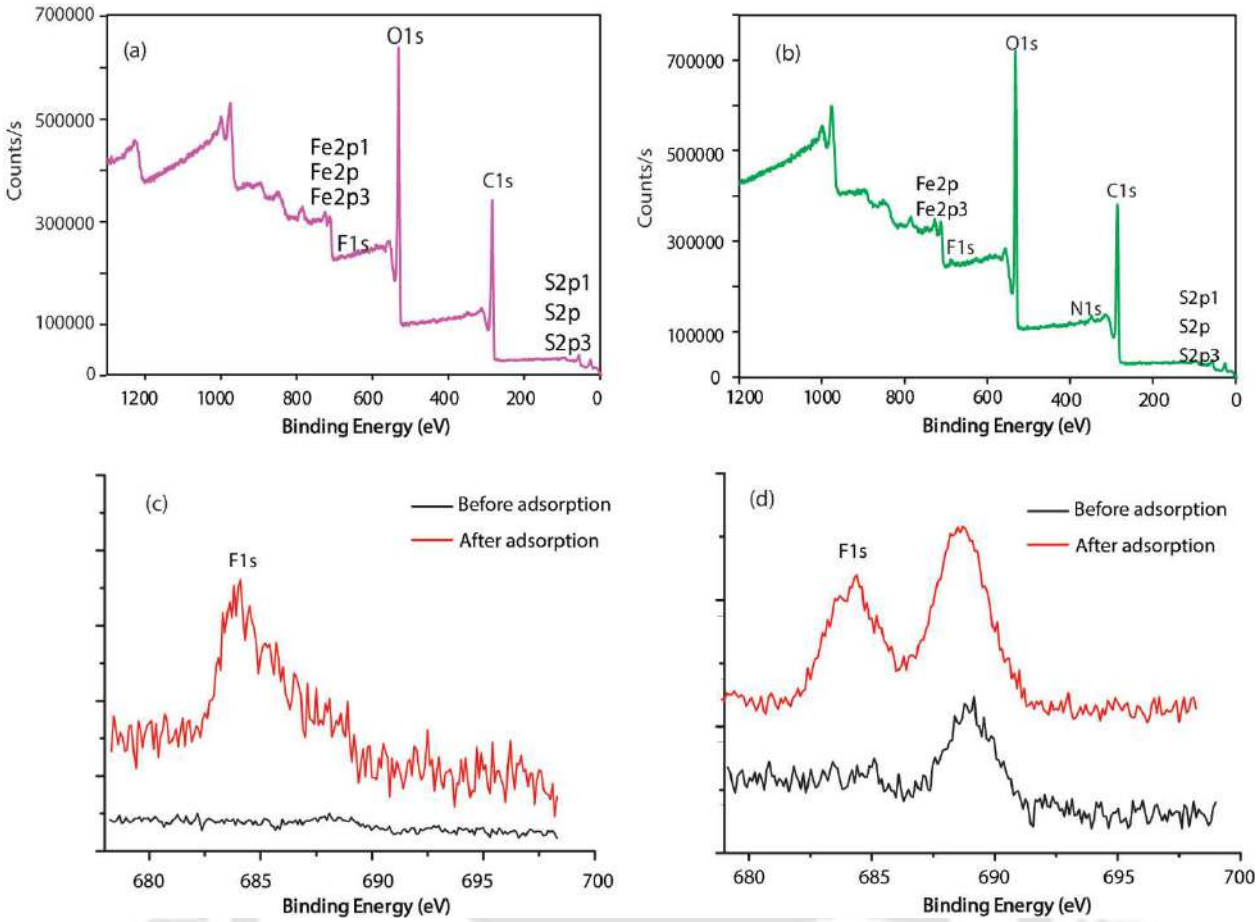

Figure 5.8. XPS spectra of elemental analysis after adsorption of fluoride (a) Mat-1 (b) Mat-2; XPS spectra of fluoride (c) Mat-1 and (d) Mat-2 before and after adsorption.

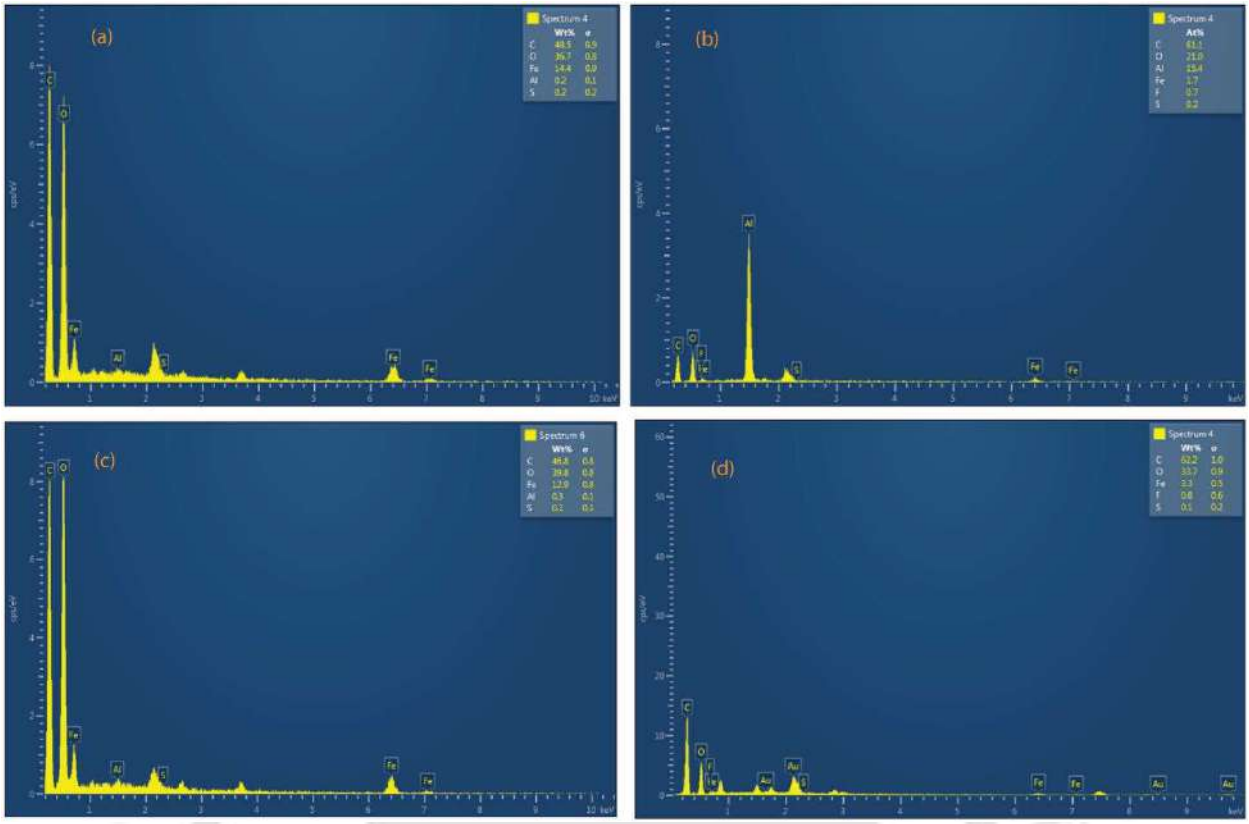

.

Figure 5.9. EDX of (a) Mat-1 before adsorption (b) Mat-1 after adsorption; (c) Mat-2 before adsorption (d) Mat-2 after adsorption.

5.4. Conclusion

This chapter summarizes the fluoride removal application of both iron polyphenol complexes. The removal efficiency of iron-polyphenol complexes declined drastically with the increase of solution pH from 2-9. Materials were used for the removal of fluoride at pH below the zero-point charge values of the materials at pH 2. The maximum adsorption capacities of the materials were 12.3 and 7.5 by Mat-1 and Mat-2, respectively. Both Langmuir and Freundlich models fitted the data due to their R^2 value being closer to unity in Mat-1. In Mat-2, the Freundlich models fitted better in comparison to Langmuir and Temkin.

XPS supported the fluoride adsorption mechanism with a peak at 685 eV and the elemental analysis by EDX. Desorption studies were carried out using NaOH solution. Real water

samples were collected from 15 sites of Guwahati city for practical application of Mat-1 and Mat-2. Materials are capable of the successful removal of real contaminated samples.

References

[1] L. Li, J. Li, C. Shao, K. Zhang, S. Yu, N. Gao, Y. Deng, D. Yin, Arsenic removal in synthetic ground water using iron electrolysis, Sep. Purif. Technol. 122 (2014) 225–230. https://doi.org/10.1016/j.seppur.2013.11.012.

[2] L. Valdez-Jiménez, C. Soria Fregozo, M.L. Miranda Beltrán, O. Gutiérrez Coronado, M.I. Pérez Vega, Effects of the fluoride on the central nervous system, Neurol. (English Ed. 26 (2011) 297–300. https://doi.org/10.1016/s2173-5808(11)70062-1.

[3] S. Jagtap, M.K. Yenkie, N. Labhsetwar, S. Rayalu, Fluoride in Drinking Water and Defluoridation of Water, Chem. Rev. 112 (2012) 2454–2466. https://doi.org/10.1021/cr2002855.

[4] Z. Mandinic, M. Curcic, B. Antonijevic, M. Carevic, J. Mandic, D. Djukic-Cosic, C.P. Lekic, Fluoride in drinking water and dental fluorosis, Sci. Total Environ. 408 (2010) 3507–3512. https://doi.org/10.1016/j.scitotenv.2010.04.029.

[5] R. Bordoloi, Existence of Arsenic in Ground water and its Effect on Health, Int. J. Comput. Appl. Eng. Sci. II (2012) 270–272. http://www.caesjournals.org/uploads/IJCAES-CSE-2012-138.pdf.

[6] K. Pandi, N. Viswanathan, In Situ Fabrication of Magnetic Iron Oxide over Nano-hydroxyapatite Gelatin Eco-polymeric Composite for Defluoridation Studies, J. Chem. Eng. Data. 61 (2016) 571–578. https://doi.org/10.1021/acs.jced.5b00727.

[7] C. Silveira, Q.L. Shimabuku, M. Fernandes Silva, R. Bergamasco, Iron-oxide nanoparticles by the green synthesis method using Moringa oleifera leaf extract for fluoride removal, Environ. Technol. (United Kingdom). 39 (2018) 2926–2936. https://doi.org/10.1080/09593330.2017.1369582.

[8] A. Jeyaseelan, M. Naushad, T. Ahamad, N. Viswanathan, Journal of Environmental Chemical Engineering Design and development of amine functionalized iron based metal organic frameworks for selective fluoride removal from water environment, (2020).

[9] P. Pillai, Y. Lakhtaria, S. Dharaskar, M. Khalid, Synthesis, characterization, and application of iron oxyhydroxide coated with rice husk for fluoride removal from aqueous media, Environ. Sci. Pollut. Res. 27 (2020) 20606–20620.

https://doi.org/10.1007/s11356-019-05948-8.

[10] C. Xu, J. Li, F. He, Y. Cui, C. Huang, H. Jin, S. Hou, Al2O3-Fe3O4-expanded graphite nano-sandwich structure for fluoride removal from aqueous solution, RSC Adv. 6 (2016) 97376–97384. https://doi.org/10.1039/c6ra19390k.

[11] B.S. Zhu, Y. Jia, Z. Jin, B. Sun, T. Luo, L.T. Kong, J.H. Liu, A facile precipitation synthesis of mesoporous 2-line ferrihydrite with good fluoride removal properties, RSC Adv. 5 (2015) 84389–84397. https://doi.org/10.1039/c5ra15619j.

[12] P. Mondal, M.K. Purkait, Preparation and characterization of novel green synthesized iron–aluminum nanocomposite and studying its efficiency in fluoride removal, Chemosphere. 235 (2019) 391–402. https://doi.org/10.1016/j.chemosphere.2019.06.189.

[13] D. Thakre, S. Jagtap, N. Sakhare, N. Labhsetwar, S. Meshram, S. Rayalu, Chitosan based mesoporous Ti-Al binary metal oxide supported beads for defluoridation of water, Chem. Eng. J. 158 (2010) 315–324. https://doi.org/10.1016/j.cej.2010.01.008.

[14] I. Ali, Z.A. Alothman, M.M. Sanagi, Green Synthesis of Iron Nano-Impregnated Adsorbent for Fast Removal of Fluoride from Water, J. Mol. Liq. 211 (2015) 457–465. https://doi.org/10.1016/j.molliq.2015.07.034.

[15] S. Kumari, S. Khan, Defluoridation technology for drinking water and tea by green synthesized Fe3O4/Al2O3 nanoparticles coated polyurethane foams for rural communities, Sci. Rep. 7 (2017) 1–12. https://doi.org/10.1038/s41598-017-08594-7.

[16] A. Jeyaseelan, M. Naushad, T. Ahamad, N. Viswanathan, Design and development of amine functionalized iron based metal organic frameworks for selective fluoride removal from water environment, J. Environ. Chem. Eng. (2020) 104563. https://doi.org/10.1016/j.jece.2020.104563.

[17] K. Mukhopadhyay, A. Ghosh, S.K. Das, B. Show, P. Sasikumar, U. Chand Ghosh, Synthesis and characterisation of cerium(IV)-incorporated hydrous iron(III) oxide as an adsorbent for fluoride removal from water, RSC Adv. 7 (2017) 26037–26051. https://doi.org/10.1039/c7ra00265c.

Chapter-VI

In Vitro Investigation of Mat-1 and Mat-2 on Physio-Chemical Responses in *Vigna Radiata* and Antimicrobial Activity Against Pathogenic Bacteria

6.1. Introduction

In previous chapters, Mat-1 and Mat-2 were used for the removal of different cationic dyes as well as the adsorption of fluoride. Metal-polyphenol complexes are proven effective in different applications, namely biomedical field, adsorbent development, wastewater treatment, food packaging, agriculture, biosensor, pigment synthesis, antimicrobial agent, environmental remediation, etc. [1,2]. The use of plant polyphenols in material synthesis introduces a greener route and cost-effective procedure [3]. The toxicity test of synthesized materials is preliminary criteria before it introducing it into the field-level application. In recent times, the use of nanoparticles (NPs) in commercial and industrial applications has rapidly increased. However, understanding the molecular level's interaction mechanisms between NPs and biological systems is largely lacking. Therefore, it's very essential to know whether these materials may impose any environmental toxicity or not. In literature, there is a debate about the beneficial or harmful effects of iron-based nano metal complexes on the environment [4–7]. According to the literature reports, the accretion of iron oxide NPs on the root surface inhibits the water uptake capacity of plants [6]. Moreover, iron oxide nanoparticle also causes stress and reduces the chlorophyll content and the nutrient uptake capacity of the *Helianthus annuus* plant [8]. The leaching of metal ions from nanoparticles also causes suppression in plant growth [9]. In the study by Libralato et al. (2016), no plant toxicity or adverse effect of iron complexes were detected, and seedling growth and the increase in biomass productivity were studied [5].

Similarly, Reyes et al. (2014) studied no changes in physicochemical properties were observed in the post-application effect of Fe_3O_4 on *L. sativa* [10].

Polyphenol-metal complexes interact with microbial organisms and show resistance against them [11]. Iron oxide nanoparticles can also show resistant efficiency against *Escherichia coli* [12]. In a study, Parveen et al. (2018) showed the antifungal activity of iron-tannic-nanoparticle [13]. Literature also showed that various plant species are resistant to different pathogenic microorganisms due to the presence of different phytochemicals in plant materials such as alkaloids, flavonoids, tannins, terpenoids, glycosides, etc. [14]. These phytochemicals are produced from the secondary metabolism of plants. In these phytochemicals, Tannins, a high molecular weight compound, is present, which acts as an antiseptic agent due to the presence of the phenolic group. In ancient India, tannin-rich plants were applied to treat abdominal diseases [15].

The use of Guava (*Psidium guajava)* plant extracts to synthesize the iron-polyphenol complex as it contains several phenolic compounds such as Guaijaverin, epicatechin, quercetin, gallic acid, among other polyphenols these also can show antimicrobial properties [16,17]. Guava is a common, traditional medicinal plant found in India and other tropical parts of the world. Leaves of the plants have different antigenotoxic, antimicrobial, anti-inflammatory properties [18]. It also exhibits high antioxidant activity [16]. There are few studies on the effect of plant-polyphenol iron on the bacteria and plant system.

In this study, seed germination, biomass, microscopic study, and biochemical experiments were performed on *Vigna radiata* to investigate the phytotoxicity of Mat-1 (tannic-iron complex) and Mat-2 (guava-iron complex). The germination index, root-shoot elongation, biomass, morphology, and other physiological and biochemical parameters, which are sensitive to environmental stress, worked as toxicity indicators. This study provided valuable

information for the application of iron polyphenol complexes in agriculture and environmental safety assessment. This research also aimed to determine the antibacterial activity and properties as well as minimum inhibitory concentrations (MIC) of Mat-1 and Mat-2. Since Mat-1 was synthesized from TA, which has well-known antibacterial properties [19,20] the test for antimicrobial activity of TA was also performed against four Gram-positive and four Gram-negative bacteria.

6.2. Materials and Methods

6.2.1. Phytotoxicity Test on Vigna radiata (Mung Bean)

Phytotoxicity tests of Mat-1, Mat-2, and tannic acid were checked on *Vigna radiata.* The germination (%), seedling elongation and morphology, germination index (GI%), biomass production, biochemical parameters of mung beans were analyzed.

6.2.1.1. Preparation of Seeds

Mung beans were chosen for this work because they are easily available, easy to handle, can be grown at any season, and germinate easily. Mung bean seeds were bought from the market and soaked in water for 2 h.

6.2.1.2. The Treatment of Seeds with Mat-1, Mat-2, and Tannic Acid (TA)

Experiments were conducted in four Petri plates; each contains 50 mung bean seeds for the germination process. Seeds were partially immersed in 5 ml aqueous solutions of TA, Mat-1, and Mat-2, each having 1 mg/ml concentration. Mat-1and Mat-2 were sonicated for 1 minute before adding to the petri dish. These experiments were conducted for a period of 10 days at room temperature. Further, the control study was carried by applying distilled water for the seed germination and growth.

6.2.2. Analytical Analysis

6.2.2.1. Seed Germination and Growth Test

The mung bean seed germination and seedling growth were tested by evaluating the germination percentage [21] (Eq. 1), germination index [22] (Eq. 2), relative elongation ratio of shoot (RERS) (Eq. 3), root (RERR) [22] (Eq. 4), and seedling vigor index (SVI) [22] (Eq. 5).

Germination Indices

$$\text{Germination percentage (GP)} = \frac{\text{Total number of seed germinated}}{\text{Total number of seeds sown}} \times 100 \quad (1)$$

$$\text{Germination index (GI)} = \frac{\text{No. of germinated seeds}}{\text{Days of first count}} + \ldots\ldots + \frac{\text{No. of germinated seeds}}{\text{Days of final}} \quad (2)$$

Seedling Growth Indices

Relative elongation ratio of root (RERR) and shoot (RERS):

$$\text{RER of shoot} = \frac{\text{Mean shoot length of tested plant}}{\text{Mean shoot length of control}} \times 100 \quad (3)$$

$$\text{RER of root} = \frac{\text{Mean root length of tested plant}}{\text{Mean root length of control}} \times 100 \quad (4)$$

$$\text{Seedling Vigor Index (SVI)} = \text{Germination \%} \times \text{Root lenght (cm)} \quad (5)$$

6.2.2.2. Biomass Test

Biomass was checked using the fresh roots, and shoots were separately taken, cleaned, and weighed, followed by drying them in a hot air oven at 60°C for 48 h.

6.2.2.3. Membrane Stability Index (MSI)

The MSI of leaves was measured by the method established by Premachanda et al. and Sairam [23,24]. Membrane stability of all the tested plants was evaluated by measuring the electrical conductivity (Thermo Scientific, Orion 3 star) of leaf sample solution boiled in 40°C and 100°C.

$$\text{MIS of leaf} = 100\text{-}\{(C_1/C_2)\times 100\} \quad (6)$$

Where C_1= electrical conductivity at 40°C

C_2= electrical conductivity at 100°C

6.2.2.4. Biochemical Parameters

6.2.2.4.1. Estimation of Chlorophyll and Carotenoid (Arnon, 1949)

0.1 g of leaves were used to extract chlorophyll in 80% acetone, and the absorbances were read at 663 nm and 645 nm in a spectrophotometer (Perkin Elmer, Lambda 25). The amount of chlorophyll was calculated using the following equations. The concentrations of chlorophyll 'a,' 'b,' total chlorophyll, and carotenoid were calculated by using the equations as follows [25] (Eq. 6, 7, 8, 9).

$$\text{Chl "a"}\ (\text{mg g}^{-1}\text{fw}) = [12.7 \times \text{D663} - 2.69 \times \text{D645}] \times \frac{\text{V}}{1000} \times \text{W} \quad (6)$$

$$\text{Chl "b"}\ (\text{mg g}^{-1}\text{fw}) = [22.9 \times \text{D645} - 4.68 \times \text{D663}] \times \frac{\text{V}}{1000} \times \text{W} \quad (7)$$

$$\text{Total Chl}\ (\text{mg g}^{-1}\text{fw}) = \text{D652} \times 1000 \times \frac{\text{V}}{1000} \times \text{W} \quad (8)$$

$$\text{Total carotenoid content (mg g}^{-1}) = [7.6 \times \text{D480} - 1.49 \times \text{D510}] \times \frac{\text{V}}{1000} \times \text{W} \quad (9)$$

6.2.2.4.2. Estimation of Total Phenol Content

Total phenolic contents were measured by the Folin-Coicalteu method [26]. 0.05 g of fresh leaves were pulped by grinding with 5 ml of distilled water and boiled for 15 min. Then 2 ml of 10% Folin-Coicalteu reagent was mixed with 0.4 ml of plant extract. After 3 min, 1.6 ml sodium carbonate was added. The mixture was allowed to stand for 1 h before the absorbance was measured at 765 nm. The value was determined considering gallic acid as the phenol and reported as mg of gallic acid equivalent per mL of solution.

6.2.2.4.3. Estimation of Total Carbohydrate

The anthrone method estimated the total carbohydrate of treated and control plant leaves (Hedge and Hofreiter, 1962). A paste with 0.5 g of fresh leaves and 10 ml of distilled water was centrifuged, and 1 ml of prepared plant extract was taken. Then 4 ml of anthrone reagent was added to each extract. Subsequently, incubation of test tubes was carried out under boiling water for 8 minutes. After cooling the solutions, the absorption spectrum was evaluated at 630 nm. The unknown concentration of total carbohydrate content in the samples was determined from the glucose calibration plot.

6.2.2.4.4. Estimation of Proline

Proline content in the plant was measured by ninhydrin-based colorimetric assay [27]. 0.1 g of the plant was homogenized separately in 3% of sulpho-salicylic acid and centrifuged for 5 min. The supernatant was administered with an equal volume of 5% ninhydrin solution, glacial acetic acid followed by 1 h of heating in the water bath. The reaction was quenched using an

ice bath. At last, toluene was added to the reaction mixture and vortexed. The absorbance of chromophore-containing toluene was recorded using a spectrophotometer at 520 nm, and proline content was calculated using a standard curve.

6.2.3. Antimicrobial Assay

6.2.3.1. Bacteria Type and Preparation of Standardized Media

The antimicrobial study was performed against four Gram-negative bacterial strains viz., *Klebsiella pneumoniae* (KP), *Escherichia coli* (EC), *Pseudomonas aeruginosa* (PA), *Enterobacter aerogenes* (EA**),** and four Gram-positive strains *Bacillus subtilis* (BS), *Staphylococcus aureus* (SA), *Staphylococcus epidermis* (SE), *Micrococcus luteus* (ML). The bacterial inoculums were cultivated following the CSLI recommendation, where the OD 600 value was adjusted to the equivalent of $5x10^5$ CFU mL^{-1} cultivated in Mueller-Hinton broth (MHB). Diffusion plates on Mueller-Hinton agar (MHA) were incubated for 24 h at 37°C

6.2.3.2. Determination of Minimum Inhibitory Concentration (MIC) by Resazurin Microtitre Assay (REMA) Method

The antibacterial activity of Mat-1, Mat-2, and tannic acid against eight pathogenic bacteria was analyzed by REMA assay [28]. It was an easy, less time-consuming method, giving more accurate results than other methods [29]. All the materials were dissolved in 5% DMSO. Mat-1 and Mat-2 were insoluble powder in nature, so, therefore, it needs sonication before adding the sterile well plate. 50 µL of each sample solution was added to the wells. The highest concentration of the tested materials was 12.5 mg/mL. Then the concentration of materials was serially diluted in the next column. The resazurin (Sigma-Aldrich) stock solution was prepared with a concentration of 10 g/L in sterile water and saved frozen at –20°C. Every experimental wall contained a total 100 µL of solution where it includes 50 µL of materials solution, 10 µL of bacterial suspension (5 x 10^5 CFU/mL), 10 µL of resazurin indicator, and 30 µL of growth

medium (LB broth) were added in every well. The plates were kept incubated for 24 h at 37°C. In a positive control, bacteria were not added, and an antibiotic mixture made up of piperacillin and tazobactam was added.

6.2.3.3. Disc Diffusion Technique

All bacterial inoculum was then swabbed into the sterile MHA with sterile cotton swabs. Three well per plate were bored, and 40 µL of Minimum inhibitory concentration (MIC) of Mat-1, Mat-2, and tannic acid solution were poured for each bacterium and were left for diffusion. The plates were invertedly incubated at 37°C for 24 h. The mixture of 25 µg/mL of Piperacillin and Tazobactum was used as a control experiment. The zone of inhibition was then measured by using a scale. Antibacterial studied by the disc diffusion method is shown in Table 6.3.

6.3. Results and discussion

6.3.1. Phytotoxicity Test

6.3.1.1. The Effect of Iron-Polyphenol Complexes on Germination and Root-Shoot Growth

Table 6.1 summarizes the phytotoxic impact of materials on the mung bean in terms of germination test and seedling growth. From the results, 100% of seed germination was observed in all cases. Therefore, it can be concluded that there is no adverse effect on seed germination observed.

The results obtained for mung bean root growth (Table 6.1) indicate a significant positive impact with 200% of the relative elongation of plant root (RERR) for the Mat-1 treated plant. Similarly, Mat-2 also showed an increase in root growth with 150% of RERR value. However, tannic acid showed a negative impact on root growth in comparison to control. Moreover, the RERR was found to be 26.6% for tannic acid-affected plants.

The best growth response of shoot for *Vigna radiata* was observed in Mat-2 treated one. It showed RERS of 177.8% for shoot growth compared to control. The RERS of 155.5% in the shoot was also observed in the case of the Mat-1 treated plant.

Table 6.1. Germination and morphology of *Vigna radiata* under treatment.

Plant type	Seed germination (SG)	Relative seed germination	GI	Seedling Vigor Index (SVI)	(RERR)	(RERS)
Control-plant	100	100	61	153.33		
TA-plant	100	100	62	54.054	26.7	81.5
Mat-1 plant	100	100	63	286.18	200	155.5
Mat-2 plant	100	100	63	140	150	177.7

The effect of iron polyphenol complex on root and shoot length of *Vigan radiata* was depicted in Figure 6.2. On day 7, the average shoot length of control, Mat-1, Mat-2, and tannic acid-treated *Vigan radiata* were 6.7, 10.5, 12, 5.5 cm, respectively, and root length was 3, 6, 4.5, 0.8 cm, respectively. It revealed that the twofold growth of root length in Mat-1 treated plant and 50% increase in growth in Mat-2 treated plant compared to control plant. Moreover, 55 and 77% increase of shoot length in Mat-1 and Mat-2 treated plants was observed in comparison control plants. The literature also exhibited that small doses of iron helped increase the seedling root, shoot length, and biomass yield [30]. Ghafariyan et al. (2013) also studied the elongation of the soybean root after treatment with iron nanoparticles [31].

In this study the disturbance of root formation was studied in tannic asid treated plants. The root formation was impeded to such an extent that the root could not grow more than 0.8 cm, while the average growth of the root of control was 3 cm. (Figure 6.2).

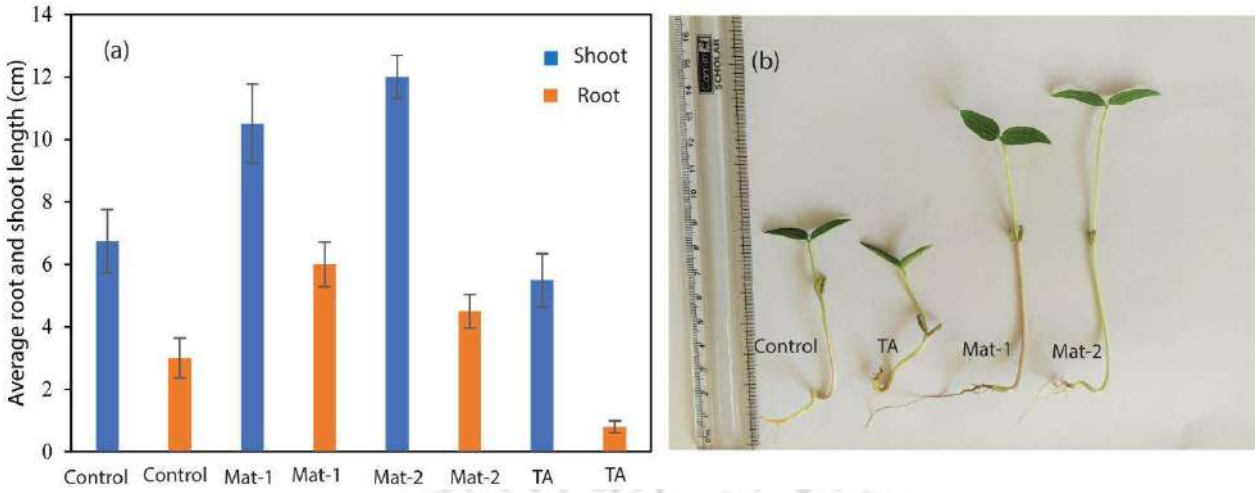

Figure 6.1. Comparison of average root shoot length on day 7 in (a) graphical presentation (b) photo image.

A polyphenol, quinone derivatives showed the suppression of 70% in the lettuce root growth was also observed in the literature [32]. In another study, Muzaffar and Ali et al. (2012) observed the inhibitory effect of polyphenol on the seedling length on cucumber plants [33]. A similar report also observed where caffeic acid inhibited the root formation of *Vigna radiata* [34].

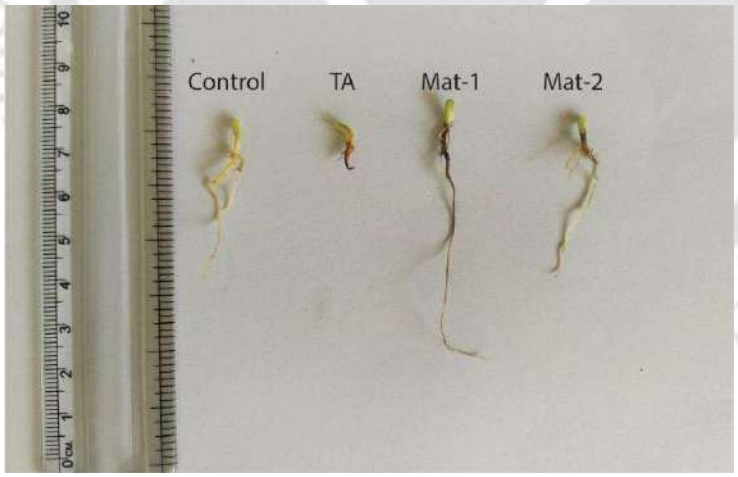

Figure 6.2. Effect of material's application on *Vigna radiata* root formation.

Tannic acid might be acting as an inhibitor of growth hormones causing suppression of root, shoot elongation. In literature, phenolic acids showed the inactivation of growth hormone (indole-3-acetic acid), which eventually suppresses the growth of plants [32,35].

6.3.1.2. Biomass Analysis

The effect of treatments on the biomass production of root and shoot of mung bean seedlings was analyzed and depicted in Figure 6.3. For Mat-1, treatment of mung bean seedlings showed 55% increase in fresh root mass and 23% increase in fresh shoot mass over control. Moreover, after drying, biomass weight of root and shoot increased to 61% and 17%, respectively, over the control. Mat-2 treated seedlings exhibited 57% and 31% increase in fresh root and shoot mass compared to control. In addition, an increment of 37% and 13% dry weight of root and shoot biomass was observed compared with the control. Plaksenkova et al., 2019 also observed the stimulation of biomass as an effect of Fe_3O_4 on *Eruca sativa* [36].

However, for tannic acid-treated seedlings, 16% and 7% decrease in fresh root and shoot mass was observed. In the case of dry biomass, 8% and 5% decrease in root and shoot mass was also found for tannic acid-treated plants. The reduction of biomass compared to control seedling biomass considers a toxic effect of material on plants [37].

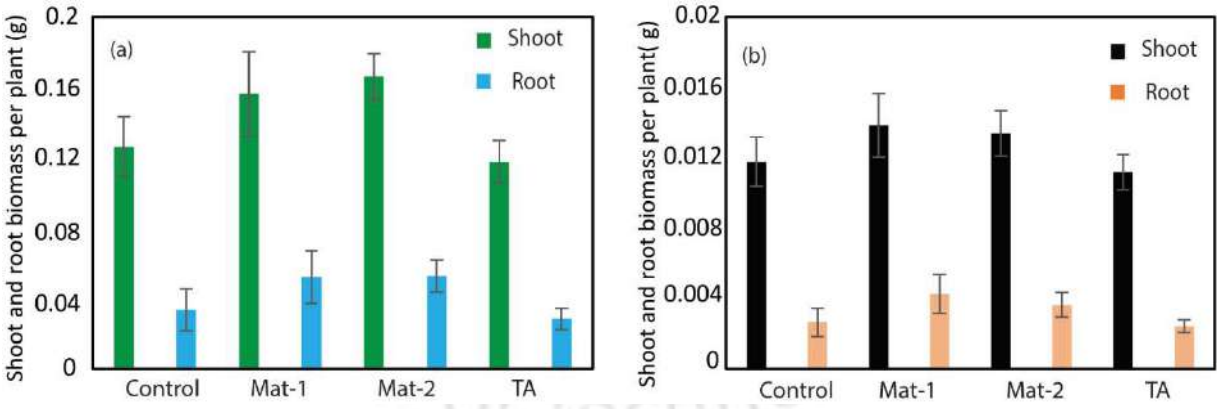

Figure 6.3. Fresh and Dry biomass of root and shoot of mung bean seedlings after 7days of growth.

6.3.1.3. Membrane Stability Index (MSI)

The membrane stability index clearly showed that no difference in Mat-1 and Mat-2 treated plant membrane compared to control (Figure 6.4). However, in tannic acid-treated plants, MSI considerably decreased from 87% to 82% in comparison to control. The decrease in membrane stability is due to increase in permeability of cell membrane [38].

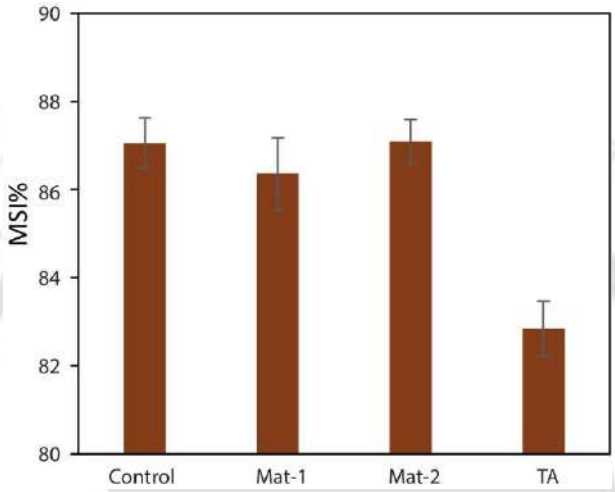

Figure 6.4. Membrane stability index of the treated plant leaf of *Vigna radiata*.

6.3.1.4. Biochemical Parameter

The experimental values disclosed that the variation in (Chl-a, Chl-b, total Chl, and carotenoid content was affected under the influence of different materials (Table 6.2). For Mat-1 and Mat-2, no significant change was found in Chl-a, Chl-b, total chlorophyll content, and Chl-a/Chl-b ratio of plants compared to the control. Therefore, the results suggested that Mat-1 and Mat-2 have no negative impact on photosynthesis capacity. Generally, iron is an important element for plant growth, photosynthesis, and essential for different biochemical processes. Iron is a crucial element for the structure of chloroplasts and Fe-S group, which is vital in electron transport. [39]. Iron also has a pivot role in the synthesis of Chl-b from Chl-a via chlorophyllide a oxygenase [40]. However, a significant decrease in all pigments was observed in the tannic acid-treated plants. It showed 22.5% reduction in total chlorophyll content, while 20%

decrement in Chl-a and 29% in Chl-b was observed compared to control. The 13% increase of Chl-a/ Chl-b ratio represents the unhealthy condition of plants treated with tannic acid [41].

Compared to control, proline content was highly increased (3 times) when the plants were treated with tannic acid. In contrast, lower proline content was observed in Mat-1, and Mat-2 treated plants compared to control. The decrease of proline content of 14% and 21% was observed in Mat-1 and Mat-2. Due to the lower stress, all the metabolic functions of Mat-1 and Mat-2 treated plants worked properly. However, in tannic acid-treated plants, the rise in proline content was observed that signified the stress response effect [42]. In this study, it was noted that the direct application of tannic acid induces stress on the plants. However, after the complexation with iron, i.e., iron-tannic acid complex (Mat-1) changes the whole behavioral pattern on *Vigna radiata* was observed. The reduction in stress level and increase in the productivity of plants were observed.

Table 6.2. Biochemical parameters of mung bean (*Vigna radiata*) plant under different treatment.

Parameters	Control	Literature	Mat-1	Mat-2	TA
Chl -a (mg/g)	0.74±0.005	0.07 mg/g. [43] on 15th day	0.74±0.003	0.77±0.013	0.59±0.004
Chl -b (mg/g)	0.27±0.0015	0.06 mg/g	0.27±0.0005	0.28±0.001	0.19±0.0005
Total Chl (mg/g)	1.01±0.005	1.7 mg/100 g on 15th day	1.01±0.004	1.05±0.02	0.78±0.007
Chl a/ Chl b	2.76	-	3.13	2.76	2.78
Carotenoid	0.33	0.45 at 25 day [44]	0.24	0.28	0.29
Carbohydrate mg/g	0.058±0.003	-	0.065±0.002	0.063±0.001	0.062±0.004
Polyphenol mg/g	6.033±0.4	-	5.95±0.4	6.174±0.5	11.813±0.7
Proline µg/0.1g	11.4±0.5	8.4mg/g in leaf on 21day [45] 250 µ mol/1g of leaf [38]	9.7±0.4	9.3±0.0.7	29.7±1.8

6.3.1.5. Microscopic Observation

The transverse section of treated shoots and roots of *Vigna radiata* was observed under a bright-field optical microscope (OLYMPUS, CX41) (Figure 6.5). The microscopic view of the transverse section of the shoot exhibited epidermis, cortex, peri circle, xylem, and phloem region. Black dots were observed on the epidermis region after the treatments of Mat-1 and Mat-2. It could be due to the aggregation of materials outside the cell walls. Black particles were also observed throughout the cortex region and peri circle in Mat-1 and Mat-2 treated plant shoots. This could be due to the penetration of both iron-polyphenol complexes in plant cells during water transport. The induced growth of the plants, biomass yield, and the presence of iron particles in the vascular bundle suggests the penetration of the iron polyphenol complex improved the productivity of the plant. A similar kind of iron aggregation in the cell wall was observed by Libralato *et al*. (2016) in the microscopic view of both *S. alba* and *S. saccharatum* [5]. Compared to control, no changes or deformation of the xylem and phloem were observed in shoot and root for Mat-1, and Mat-2 treated plants. However, the microscopic view of the root section treated with tannic acid showed a negative impact on root structure, which deforms the xylem and phloem (Figure. 6.5h).

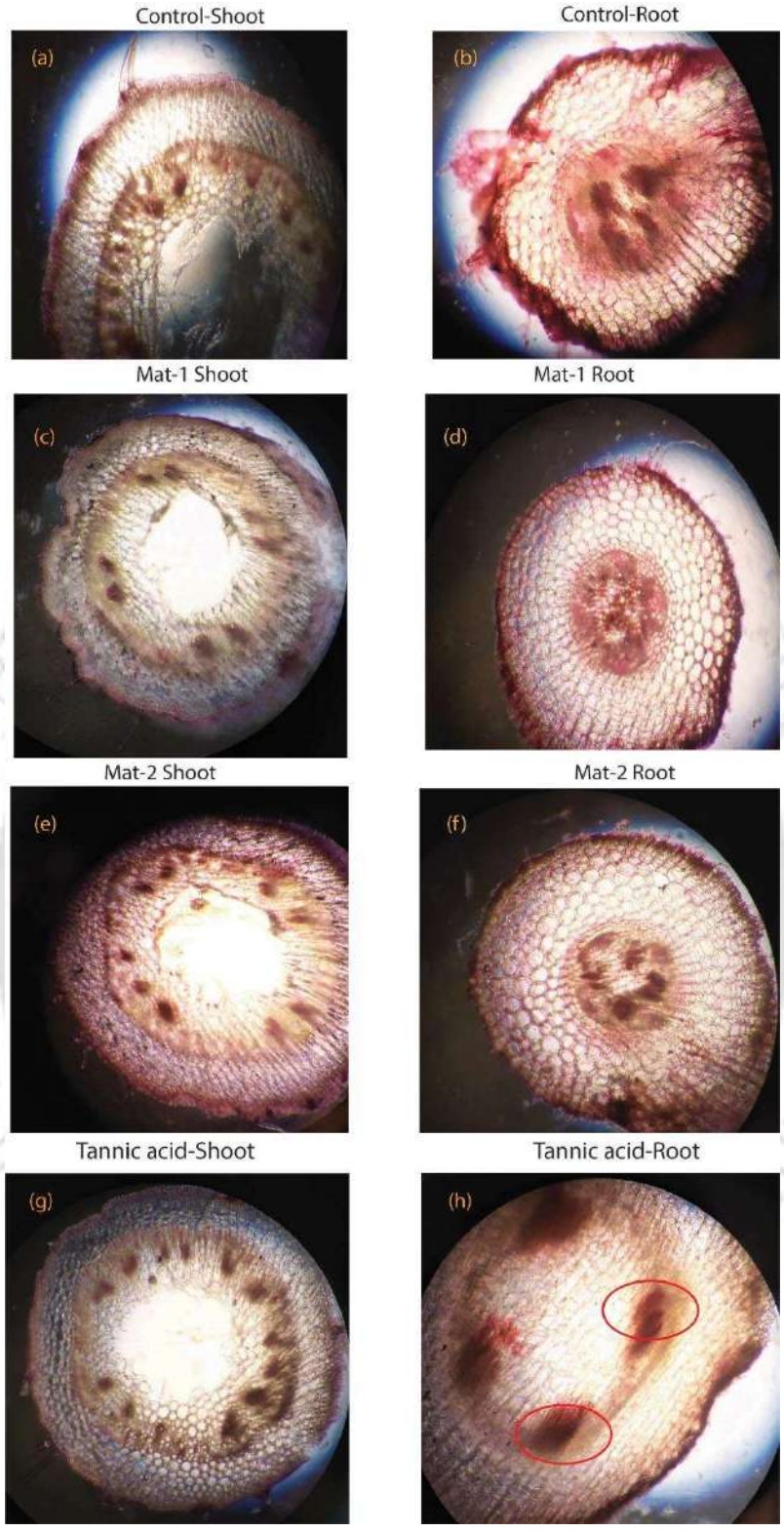

Figure 6.5. Transverse section of shoots and roots of (a), (b) control, (c), (d) Mat-1, (e), (f) Mat-2 and (g), (h) TA treated plants.

6.3.1.6. FESEM and EDS Analysis of Root and Shoot

The accumulation or aggregation of iron-polyphenol complexes on cell tissue of root were determined using EDS (Zeiss, Sigma). In the FESEM image, the aggregation of Mat-1 and Mat-2 was observed on the root's surface (Figure 6.6). In previous studies, it was reported that the aggregation of particles outer side of the root decreases the water uptake capacity of the plant. As a result, it reduces the growth and chlorophyll content in plants [46]. FESEM and EDS analysis confirmed the presence of particles in the root surface. However, no adverse effects on plant growth and chlorophyll content indicated that the plants had no water blocking issues. The EDS confirms the presence of the iron compounds in the inner part of roots treated by Mat-1 and Mat-2 (Figure 6.6). Hence, it can be concluded that the penetration of materials occurred through the xylem and phloem. The FESEM image and EDS analysis of the root of control also confirm the absence of iron.

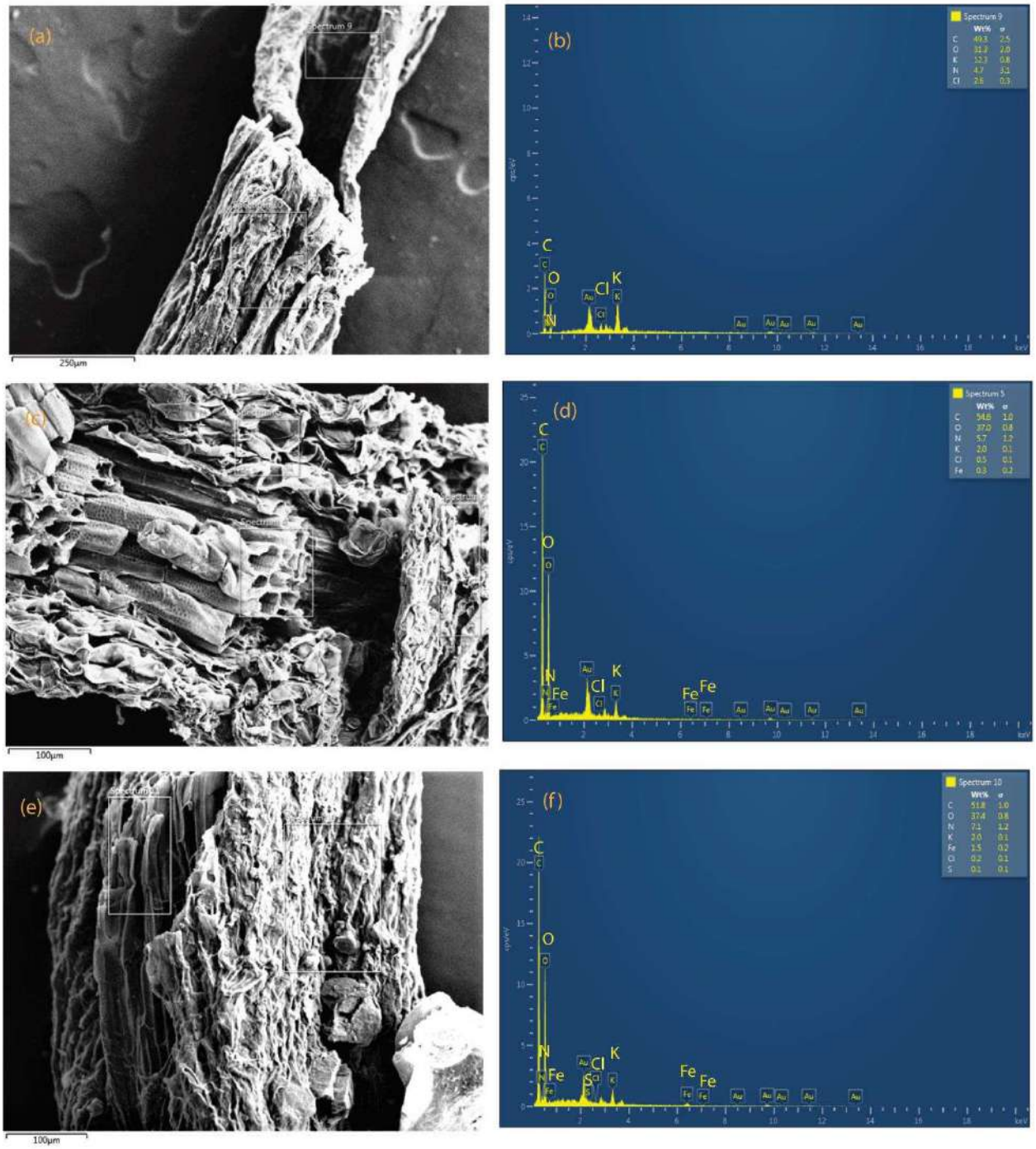

Figure. 6.6. FESEM and EDS of the root of (a)(b) control, (c)(d) Mat-1, (e) (f) Mat-2 treated plant respectively.

6.3.2. Antimicrobial Test

6.3.2.1. Minimum Inhibitory Concentration (MIC)

The minimum inhibitory concentration (MIC) was measured by the colorimetric method using the resazurin dye as an indicator of cell growth. The non-toxic blue-colored dye is converted to resorufin, a pink compound, when reacts with oxidoreductase enzyme present in living cells [28]. Thus, the blue color indicates no bacterial growth, while the pink color indicates the presence of living bacteria.

Mat-1 was active against all the four Gram-negative bacteria at MIC of 6.25 mg/mL. Mat-2 showed similar results against *Escherichia coli, Klebsiella pneumoniae,* and *Enterococcus aerogenes* at 6.25 mg/mL. However, Mat-2 showed better results against *Pseudomonas aeruginosa* with MIC of 3.13 mg/mL (Figure 6.7). On the other hand, tannic acid showed the MIC at 0.36 mg/mL for *Escherichia coli* and *Pseudomonas aeruginosa* and 3.13 mg/mL for *Klebsiella pneumoniae* and *Enterococcus aerogenes*.

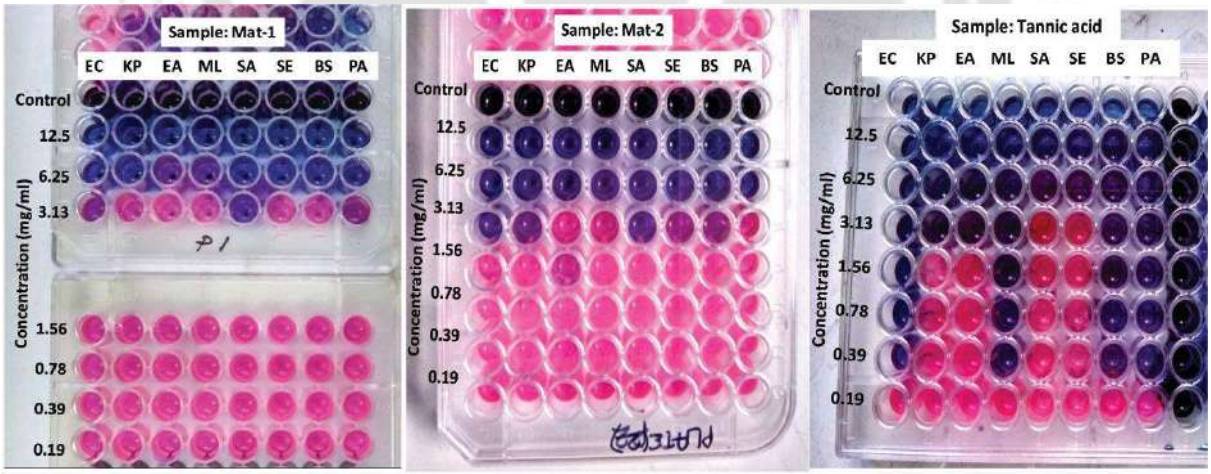

Figure 6.7. MIC test of Mat-1, Mat-2, and Tannic acid against Gram-positive and Gram-negative bacteria.

On the other side, Mat-1, Mat-2, and tannic acid also showed inhibition activity against all four Gram-positive bacteria. MIC of Mat-1 against *Staphylococcus aureus* was 3.13 mg/mL, and

for the rest of the three Gram-positive bacteria were 6.25 mg/mL. On the other hand, MIC of Mat-2 for *Micrococcus luteus* and *Bacillus subtilis* was 3.13 mg/mL and against *Staphylococcus aureus* and *Staphylococcus epidermidis* was 6.25 mg/mL. Tannic acid showed strong microbial resistance against *Micrococcus luteus* and *Bacillus subtilis* with MIC of 0.39 mg/mL and 6.25 mg/mL against *Staphylococcus aureus* and *Staphylococcus epidermidis*. Sendamangalam et al., (2011) observed that tannic acid also showed similar results against *Streptococcus mutans* at MIC of 0.4 mg/mL [47]. Mat-1 and Mat-2 showed better inhibition activity against *Staphylococcus aureus* in comparison to tannic acid.

6.3.2.2. Zone of Inhibition (ZOI) Determination with the MIC of Each Extract for Each Bacterium

The activity against bacteria was studied by the disc diffusion method, as shown in Table 6.3. Results exhibited significant zone of inhibition for *Escherichia coli* with diameter of 14 mm by Mat-1 and 13 mm by Mat-2. Against *Enterococcus aerogenes,* both Mat-1 and Mat-2 showed bacterial inhibition with 9 mm of ZOI. Among Gram-negative bacteria, both iron-polyphenol complexes expressed the ZOI of 9 mm against *Staphylococcus aureus.* Moreover, against *Staphylococcus epidermidis,* Mat-1 exhibited better inhibition potential with 12 mm of inhibition area, while Mat-2 produced a zone of inhibition of 9 mm. Both Mat-1 and Mat-2 did not exhibit any ZOI against *Klebsiella pneumoniae, Pseudomonas aeruginosa Micrococcus luteus, Bacillus subtilis* bacteria. Due to the low solubility of Mat-1 and Mat-2, the dispersion in the agar plates becomes resistant. Because of low dispersibility, it becomes difficult to get an accurate result in this technique. It was one of the drawbacks of this method. Besides, it was unable to estimate the minimum inhibitory concentration of materials [29].

The zone of inhibition was shown by tannic acid against all 4 Gram-negative bacteria species like *Escherichia coli* (20 mm), *Klebsiella pneumoniae* (19 mm), *Enterococcus aerogenes* (23 mm), *Pseudomonas aeruginosa* (17 mm), and all 4 Gram-positive bacteria species like

Micrococcus luteus (19 mm), *Staphylococcus aureus* (22 mm) and *Staphylococcus epidermidis* (22 mm), *Bacillus subtilis* (17 mm). Tannic acid showed a maximum zone of inhibition of 20 mm for E. coli with only 0.39 mg/mL of concentration.

Table 6.3. Minimum inhibitory concentration and zone of inhibition of materials against eight bacteria.

Bacteria	MIC (mg/mL)			ZOI (mm)		
	Tannic	Mat -1	Mat -2	Tannic	Mat -1	Mat -2
Gram-negative bacteria						
Escherichia coli	0.39	6.25	3.13	20	14	13
Klebsiella pneumoniae	3.13	6.25	6.25	19	-	-
Enterococcus aerogenes	3.13	6.25	6.25	23	9	9
Pseudomonas aeruginosa	0.39	6.25	6.25	17	-	-
Gram-positive bacteria						
Micrococcus luteus	0.39	6.25	6.25	19	-	-
Staphylococcus aureus	6.25	3.13	3.13	22	9	9
Staphylococcus epidermidis	6.25	6.25	6.25	22	12	9
Bacillus subtilis	0.39	6.25	3.13	17	-	-

6.3.2.3. Mechanism

The results of MIC and ZOI in culture media indicate the significant antibacterial activity of both iron polyphenol complexes as well as tannic acid. The mechanism of antimicrobial action of iron polyphenol complex may differ from species to species of bacteria and as well as the size of the material.

Tannic acid showed microbial resistance through complexation with protein molecules by covalent and non-covalent interaction. Literature also showed tannic acid deformed the germ tube structure of *Crinipellis perniciosa* [13].

There are different possibilities of mechanism due to which the materials were showing significant antimicrobial activity. Due to the production of different reactive oxygen species in

the cells, such as hydroxyl radicals, singlet oxygen, etc., damages the cells by inducing stress and causing resistance against bacteria [13,48]. Iron can damage the biomolecules like lipid, DNA, etc., and cause damage to the cell [14]. A similar observation was reported where iron nanoparticles affected the protein and DNA. Lee et al. (2008) have shown that iron nanoparticles penetrate through the cell membranes and damage cells of E. coli by Fenton reaction [49]. Another process behind the antibacterial activity may be due to the large surface-to-volume ratio, which effectively covers the bacteria and reduces oxygen supply for respiration.

6.4. Conclusion

In this study, the treatment of plants with iron-polyphenol complexes such as Mat-1 and Mat-2 significantly impacted the plant's growth. As compared with the control plants, Mat-1 treated plants showed a twofold increase in root length. Mat-2 exhibits 77% more growth in the shoot length of the mung bean plants. Moreover, the increase in biomass in Mat-1 and Mat-2 treated plants signified the positive impact of iron-polyphenol complexes on plants. In addition, microscopic view showed no deformation in the epidermis, cortex, peri circle, xylem, and phloem in Mat-1 and Mat-2 treated plants. The FESEM and EDX analysis also support the presence of iron in the inner part of the plant, which penetrates during water transport. Both Mat-1 and Mat-2 did not impose any negative effect on biochemical parameters and the morphology of plants. In contrast, tannic acid did not affect the germination of seeds, but it showed an adverse effect on the elongation of plants, chlorophyll content, biomass, and rise in proline content. The blunt in root growth (Figure. 6.2) and deformation of the root vascular bundle were observed after tannic acid treatment due to the suppression of growth hormone. Therefore, treatment of plants with tannic acid alone induces stress, change of physiological and biological parameters, which eventually affect plant health. However, after the

complexation with iron, i.e., iron-tannic acid complex (Mat-1) changes the whole behavioral pattern with *Vigna radiata*, it reduces the stress level and increases the productivity of plants.

So, both Mat-1 and Mat-2 showed positive impact on the growth and health of *Vigna radiata.* On the other side, both materials also comprised antibacterial activity against all eight pathogenic bacteria. Results showed that REMA assay gives more authentic results in the antibacterial resistant method than disc diffusion assay as diffusion became obstetrical in this study. Results suggest that Mat-1 showed inhibition of *Staphylococcus aureus* at the dose of 3.13 mg/L with 9 mm of ZOI, while with the higher dose of 6.26 mg/L, it showed the ZOI of 14 mm against *E. coli*. Mat-2 is more effective against *E. coli, Staphylococcus aureus* and *Bacillus subtilis* with a dose of 3.13 mg/mL and showed ZOI of 13, 9, 9 mm.

References

[1] E. Akyüz, K.S. Başkan, E. Tütem, R. Apak, C. Ii, À.I. Assay, Novel Iron (III) − Induced Prooxidant Activity Measurement Using a Solid Protein Sensor in Comparison with a Copper (II) − Induced Assay Novel Iron (III) À Induced Prooxidant Activity Measurement, Anal. Lett. 53 (2020) 1489–1503. https://doi.org/10.1080/00032719.2019.1710180.

[2] C.P. Devatha, K. Jagadeesh, M. Patil, Environmental Nanotechnology , Monitoring & Management E ff ect of Green synthesized iron nanoparticles by Azardirachta Indica in di ff erent proportions on antibacterial activity, Environ. Nanotechnology, Monit. Manag. 9 (2018) 85–94. https://doi.org/10.1016/j.enmm.2017.11.007.

[3] R.S. Yehia, A.M. Ali, Biosynthesis and characterization of iron nanoparticles produced by Thymus vulgaris L . and their antimicrobial activity, ACTA BOT. CROAT. 79(2) (2020) 192–125. https://doi.org/10.37427/botcro-2020-032.

[4] W. Du, J.A. Hernandez-viezcas, N. Bonilla-bird, L.L. Martha, J.R. Peralta-videa, M. Kom, Plant Physiology and Biochemistry Exposure of engineered nanomaterials to plants : Insights into the physiological and biochemical responses-A review *, 110 (2017). https://doi.org/10.1016/j.plaphy.2016.05.037.

[5] G. Libralato, A. Costa Devoti, M. Zanella, E. Sabbioni, I. Mičetić, L. Manodori, A. Pigozzo, S. Manenti, F. Groppi, A. Volpi Ghirardini, Phytotoxicity of ionic, micro- and nano-sized iron in three plant species, Ecotoxicol. Environ. Saf. 123 (2016) 81–88. https://doi.org/10.1016/j.ecoenv.2015.07.024.

[6] X. Ma, A. Gurung, Y. Deng, Phytotoxicity and uptake of nanoscale zero-valent iron (nZVI) by two plant species, Sci. Total Environ. 443 (2013) 844–849. https://doi.org/10.1016/j.scitotenv.2012.11.073.

[7] N. Shabnam, M. Kim, H. Kim, Iron (III) oxide nanoparticles alleviate arsenic induced stunting in *Vigna radiata*, Ecotoxicol. Environ. Saf. 183 (2019) 109496. https://doi.org/10.1016/j.ecoenv.2019.109496.

[8] D. Martinez-Fernandez, D. Barroso, M. Komárek, Root water transport of Helianthus annuus L. under iron oxide nanoparticle exposure, Environ. Sci. Pollut. Res. 23 (2016) 1732–1741. https://doi.org/10.1007/s11356-015-5423-5.

[9] C.O. Dimkpa, J.E. McLean, N. Martineau, D.W. Britt, R. Haverkamp, A.J. Anderson, Silver nanoparticles disrupt wheat (Triticum aestivum L.) growth in a sand matrix,

Environ. Sci. Technol. 47 (2013) 1082–1090. https://doi.org/10.1021/es302973y.

[10] J. Trujillo-Reyes, S. Majumdar, C.E. Botez, J.R. Peralta-Videa, J.L. Gardea-Torresdey, Exposure studies of core-shell Fe/Fe3O4 and Cu/CuO NPs to lettuce (Lactuca sativa) plants: Are they a potential physiological and nutritional hazard?, J. Hazard. Mater. 267 (2014) 255–263. https://doi.org/10.1016/j.jhazmat.2013.11.067.

[11] P. Plachtová, Z. Medříková, R. Zbořil, J. Tuček, R.S. Varma, B. Maršálek, Iron and Iron Oxide Nanoparticles Synthesized with Green Tea Extract: Differences in Ecotoxicological Profile and Ability to Degrade Malachite Green, ACS Sustain. Chem. Eng. 6 (2018) 8679–8687. https://doi.org/10.1021/acssuschemeng.8b00986.

[12] S. Arokiyaraj, M. Saravanan, N.K. Udaya Prakash, M. Valan Arasu, B. Vijayakumar, S. Vincent, Enhanced antibacterial activity of iron oxide magnetic nanoparticles treated with Argemone mexicana L. leaf extract: An in vitro study, Mater. Res. Bull. 48 (2013) 3323–3327. https://doi.org/https://doi.org/10.1016/j.materresbull.2013.05.059.

[13] S. Parveen, A. Hamid, M. Ashraf, H. Sylvia, M. Yaqub, J. Abdullah, Microbial Pathogenesis Preparation , characterization and antifungal activity of iron oxide nanoparticles, Microb. Pthogenes. 115 (2018) 287–292. https://doi.org/10.1016/j.micpath.2017.12.068.

[14] N.R. Perron, J.L. Brumaghim, A review of the antioxidant mechanisms of polyphenol compounds related to iron binding, Cell Biochem. Biophys. 53 (2009) 75–100. https://doi.org/10.1007/s12013-009-9043-x.

[15] G.C. Omojate, F.O. Enwa, A.O. Jewo, C.O. Eze, Mechanisms of Antimicrobial Actions of Phytochemicals against Enteric Pathogens – A Review, J. Pharm. Chem. Biol. Sci. 2 (2014) 77–85.

[16] W. Nantitanon, S. Yotsawimonwat, S. Okonogi, Factors influencing antioxidant activities and total phenolic content of guava leaf extract, LWT - Food Sci. Technol. 43 (2010) 1095–1103. https://doi.org/10.1016/j.lwt.2010.02.015.

[17] M.N. Mailoa, M. Mahendradatta, A. Laga, N. Djide, Tannin Extract Of Guava Leaves (Psidium Guajava L) Variation With Concentration Organic Solvents, Int. J. Sci. Technol. Res. 2 (2013) 106–110.

[18] E. Díaz-de-Cerio, A.M. Gómez-Caravaca, V. Verardo, A. Fernández-Gutiérrez, A. Segura-Carretero, Determination of guava (Psidium guajava L.) leaf phenolic compounds using HPLC-DAD-QTOF-MS, J. Funct. Foods. 22 (2016) 376–388. https://doi.org/10.1016/j.jff.2016.01.040.

[19] G. Dong, H. Liu, X. Yu, X. Zhang, H. Lu, T. Zhou, J. Cao, Antimicrobial and anti-biofilm activity of tannic acid against Staphylococcus aureus, Nat. Prod. Res. 32 (2018) 2225–2228. https://doi.org/10.1080/14786419.2017.1366485.

[20] K.B. Myint, L.C. Sing, Z. Wei, Tannic Acid as Phytochemical Potentiator for Antibiotic Resistance Adaptation, APCBEE Procedia. 7 (2013) 175–181. https://doi.org/10.1016/j.apcbee.2013.08.030.

[21] Y. Luo, J. Liang, G. Zeng, M. Chen, D. Mo, G. Li, D. Zhang, Seed germination test for toxicity evaluation of compost: Its roles, problems and prospects, Waste Manag. 71 (2018) 109–114. https://doi.org/10.1016/j.wasman.2017.09.023.

[22] B. Iddy, A. Mwilawa, D. Maleko, E. Mtengeti, Allelopathic effect of Chromolaena odorata aqueous leaf extracts on seed germination and seedling growth of selected crop and pasture species in Tanzania, Int. J. Bot. 3 (2018) No. 41-48.

[23] G.S. Premachandra, H. Saneoka, M. Kanaya, S. Ogata, Cell membrane stability and leaf surface wax content as affected by increasing water deficits in maize, J. Exp. Bot. 42 (1991) 167–171. https://doi.org/10.1093/jxb/42.2.167.

[24] Sairam R. K., Effect of Moisture Stress on Physiological Activities of Two Contrasting Wheat Genotypes, Indian J. Exp. Biol. 32 (1994) 584–593. https://www.researchgate.net/profile/Raj_Kumar_Sairam/publication/316189772_Effect_of_moisture_stress_on_physiological_activities_of_two_contrasting_wheat_genotypes/links/58f5cdc1a6fdcc11e56a0364/Effect-of-moisture-stress-on-physiological-activities-of-tw.

[25] D.I. Arnon, Copper Enzymes in Isolated Chloroplasts. Polyphenoloxidase in Beta Vulgaris , Plant Physiol. 24 (1949) 1–15. https://doi.org/10.1104/pp.24.1.1.

[26] I. Standard, ISO 14502-1 Content of total polyphenols in tea — Colorimetric method using Folin- Ciocalteu reagent, Int. Stand. (2005) 1–10.

[27] I.. Bates, L.S., Waldren, R.P. and Teare, Rapid determination of free proline for water stress w a t e r - s t r e s s studies, Plant Soil. 39 (1973) 205–207.

[28] S.D. Sarker, L. Nahar, Y. Kumarasamy, Microtitre plate-based antibacterial assay incorporating resazurin as an indicator of cell growth , and its application in the in vitro antibacterial screening of phytochemicals, 42 (2007) 321–324. https://doi.org/10.1016/j.ymeth.2007.01.006.

[29] N.D. Fajarningsih, I. Munifah, D.S. Zilda, F.P. Processing, Evaluation of Antibacterial Assays for Screening of Marine Invertebrate, (2018). https://doi.org/10.15578/squalen.v13i1.294.

[30] T. Guha, K.V.G. Ravikumar, A. Mukherjee, A. Mukherjee, R. Kundu, Nanopriming with zero valent iron (nZVI) enhances germination and growth in aromatic rice cultivar (Oryza sativa cv. Gobindabhog L.), Plant Physiol. Biochem. 127 (2018) 403–413. https://doi.org/10.1016/j.plaphy.2018.04.014.

[31] M.H. Ghafariyan, M.J. Malakouti, M.R. Dadpour, P. Stroeve, M. Mahmoudi, Effects of magnetite nanoparticles on soybean chlorophyll, Environ. Sci. Technol. 47 (2013) 10645–10652. https://doi.org/10.1021/es402249b.

[32] R. Growth, Germination Phenolic compounds in high concentrations suppress the growth processes in various biotests (KEn ' ELI 1974). Plants are able to oxidize certain phenols (Lucx ~ . B 1977). Some authors discussing the problems of interconnection between phe, 24 (1982) 1–6.

[33] and N.A.W. Muzaffar, S., B. Ali, Effect of Catechol , Gallic Acid and Pyrogallic Acid on the Germination , Seedling Growth and the Level of Endogenous Phenolics, Int. J. Life Sci. Biotechnol. Pharma Res. 1 (2012) 50–55.

[34] D.R. Batish, H.P. Singh, S. Kaur, R.K. Kohli, S.S. Yadav, Caffeic acid affects early growth, and morphogenetic response of hypocotyl cuttings of mung bean (Phaseolus aureus), J. Plant Physiol. 165 (2008) 297–305. https://doi.org/10.1016/j.jplph.2007.05.003.

[35] T.T. Lee, F. Skoog, Effects of Hydroxybenzoic Acids on Indoleacetic Acid Inactivation by Tobacco Callus Extracts, Physiol. Plant. 18 (1965) 577–585. https://doi.org/10.1111/j.1399-3054.1965.tb06919.x.

[36] I. Plaksenkova, M. Jermaļonoka, L. Bankovska, I. Gavarāne, V. Gerbreders, E. Sledevskis, J. Sniķeris, I. Kokina, Effects of Fe3O4 Nanoparticle Stress on the Growth and Development of Rocket Eruca sativa, J. Nanomater. 2019 (2019). https://doi.org/10.1155/2019/2678247.

[37] S.K. Dhoke, P. Mahajan, A.S. Khanna, Effect of nano-ZnO particle suspension on growth of mung (Vigna radiata) and gram (Cicer arietinum) seedlings using plant agar method, J. Nanotechnol. 13 (2011) 54–61. https://doi.org/10.1155/2011/696535.

[38] B.B. and N. Gogoi, Effect of induced drought on different growth and biochemical attributes of black gram (Vigna mungo L.) and green gram (Vigna radiata L.), J. Environ. Res. Dev. 6 (2012).

[39] J.F. Briat, C. Dubos, F. Gaymard, Iron nutrition, biomass production, and plant product quality, Trends Plant Sci. 20 (2015) 33–40. https://doi.org/10.1016/j.tplants.2014.07.005.

[40] A. Tanaka, R. Tanaka, Chlorophyll metabolism, Curr. Opin. Plant Biol. 9 (2006) 248–255. https://doi.org/10.1016/j.pbi.2006.03.011.

[41] L.R.R. Souza, L.E. Bernardes, M.F.S. Barbetta, M.A.M.S. da Veiga, Iron oxide nanoparticle phytotoxicity to the aquatic plant Lemna minor: effect on reactive oxygen species (ROS) production and chlorophyll a/chlorophyll b ratio, Environ. Sci. Pollut. Res. 26 (2019) 24121–24131. https://doi.org/10.1007/s11356-019-05713-x.

[42] P.M. Gopalakrishnan Nair, S.H. Kim, I.M. Chung, Copper oxide nanoparticle toxicity in mung bean (Vigna radiata L.) seedlings: physiological and molecular level responses of in vitro grown plants, Acta Physiol. Plant. 36 (2014) 2947–2958. https://doi.org/10.1007/s11738-014-1667-9.

[43] L. Baskaran, P. Sundaramoorthy, A.L.A. Chidambaram, K.S. Ganesh, Growth and Physiological Activity of Greengram (Vigna radiata L.) Under Effluent Stress, Bot. Res. Int. 2 (2009) 107–114.

[44] S.B. Agrawal, D. Rathore, Changes in oxidative stress defense system in wheat (Triticum aestivum L.) and mung bean (Vigna radiata L.) cultivars grown with and without mineral nutrients and irradiated by supplemental ultraviolet-B, Environ. Exp. Bot. 59 (2007) 21–33. https://doi.org/10.1016/j.envexpbot.2005.09.009.

[45] B. Ali, S.A. Hasan, S. Hayat, Q. Hayat, S. Yadav, Q. Fariduddin, A. Ahmad, A role for brassinosteroids in the amelioration of aluminium stress through antioxidant system in mung bean (Vigna radiata L . Wilczek), 62 (2008) 153–159. https://doi.org/10.1016/j.envexpbot.2007.07.014.

[46] N. Zuverza-Mena, D. Martínez-Fernández, W. Du, J.A. Hernandez-Viezcas, N. Bonilla-Bird, M.L. López-Moreno, M. Komárek, J.R. Peralta-Videa, J.L. Gardea-Torresdey, Exposure of engineered nanomaterials to plants: Insights into the physiological and biochemical responses-A review, Plant Physiol. Biochem. 110 (2017) 236–264. https://doi.org/10.1016/j.plaphy.2016.05.037.

[47] V. Sendamangalam, O.K. Choi, Y. Seo, D. Kim, Antimicrobial and Antioxidant Activities of Polyphenols against Streptococcus mutans, 1 (2011). https://doi.org/10.5530/ax.2011.3.7.

[48] F. Length, Mycosynthesis of iron nanoparticles by Alternaria alternata and its antibacterial activity, 14 (2015) 1234–1241. https://doi.org/10.5897/AJB2014.14286.

[49] C. Lee, J.E.E.Y. Kim, W.O.N.I.L. Lee, K.L. Nelson, Bactericidal Effect of Zero-Valent Iron Nanoparticles on Escherichia coli, (2008) 4927–4933. https://doi.org/10.1021/es800408u.

Chapter VII

Conclusion and Future work

Materials were synthesized using two different types of plant-based polyphenol after reacting with iron(II) salt under similar conditions. One polyphenol is tannic acid, commercially available in pure form, and the structure contains ten esterified gallic acid (Scheme 2.1). The other one is a raw extract of guava leaves (*Psidium guajva*).

7.1. Main Findings

i. Materials were synthesized at room temperature by simple mixing of the polyphenols and iron in 1:1 ratio at pH 7. The synthesis procedure was optimized for making the materials reproducible. It was proven through rigorous experimentation that bulk production and storage is also possible for 3 years without changing the properties of the materials and proved to be efficient adsorbents.

ii. Magnetic susceptibility, EPR spectra, and mass analysis supported that most of the bound iron in Mat-1 and Mat-2 are oxo bridged Fe(III). However, both EPR and XPS confirmed that Mat-3 consists of magnetically uncoupled mononuclear Fe(III) complex of Tannic Acid. XPS showed in both Mat-1 and Mat-2, Fe(III) present as major component and Fe(II) as minor.

iii. The surface area of Mat-1 and Mat-2 are 99.6 and 100.9 m^2/g, respectively, with the H3-type of the hysteresis loop that exhibited the presence of non-rigid aggregates of plate-like particles. However, Mat-3 had a low surface area, 3.0 m^2/g, with H4 hysteresis denoted irregular shape and broad size distribution. FESEM images also supported the similar morphology and size distribution of Mat-1, Mat-2, and Mat-3.

iv. The pH_{zpc} value of Mat-1, Mat-2, and Mat-3, was found to be 3.9, 4.5, and 2.5 for respectively. At that specific pH, the net surface charge of the materials is zero, and above that pH material's surface has a negative charge and is able to attract positively charged pollutants. However, below that pH, materials are able to remove the anionic pollutants.

v. Both synthesized materials were found capable of removing cationic dyes at neutral pH. A detailed study of MB dye removal was carried out. Mat-1 and Mat-2 showed maximum adsorption capacities of 187 and 255 mg/g, respectively, with the dose of 0.5 g/L, dye concentration of 150 mg/L at pH 7. MB dye removal capacities of materials were also compared with activated charcoal. Particularly, it was observed that Mat-2 could match performance with activated charcoal with the added advantage of less energy consumption and no greenhouse gas emission.

vi. Desorption study revealed that dye binding on iron-polyphenol complexes has a significant contribution from ionic interaction and H-bonding along with aromatic π-π interaction which is also possible.

vii. Materials are also effective in the removal of a toxic azo dye, Bismarck brown (BB), with a wide range of concentrations (20-400 mg/L). The very high adsorption capacity of 652 and 680 mg/g by Mat-1 and Mat-2 were observed with the dose of 0.5 g/L, 400 mg/L of dye concentration, and at pH 7.

viii. The cytotoxic study on *A. cepa* root cell showed, with direct application of 400 mg/L of stock dye concentration >90% of cell deformation was observed. However, after adsorption with Mat-1 and Mat-2, the residual solution exhibited no chromosomal aberration and cell deformation on *A. cepa* root cells.

ix. Both materials were able to remove fluoride at pH 2 (below the pHzpc), and the maximum fluoride uptake capacities of Mat-1 and Mat-2 were 12.3 and 7.5 mg/g for

40 mg/L of concentration. Both materials were capable of removing fluoride from contaminated real groundwater samples.

x. After the direct application of Mat-1 and Mat-2 on *Vigna radiata*, the growth of root-shoot length, the increase in biomass, decreasing stress in terms of proline content signified the positive impact of iron-polyphenol complexes on plants and also any negative effect on biochemical parameters, microscopic observations and the morphology of plant was observed.

xi. Mat-1 and Mat-2 are capable of showing antimicrobial activities against all of the eight disease-causing bacteria: *Klebsiella pneumoniae* (KP), *Escherichia coli* (EC), *Pseudomonas aeruginosa* (PA), *Enterobacter aerogenes* (EA.**)** *Bacillus subtilis* (BS), *Staphylococcus aureus* (SA), *Staphylococcus epidermis* (SE), and *Micrococcus luteus* (ML).

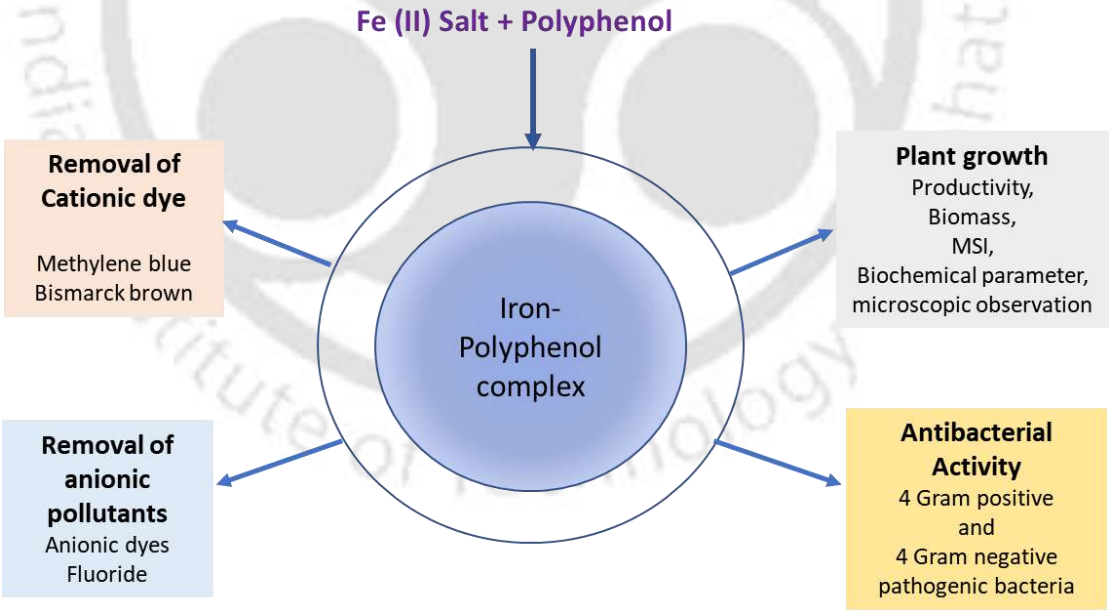

Scheme 7.1. Synthesis and applications of iron-polyphenol complexes (Mat-1 and Mat-2) and their environmental applications

7.2. Recommendation for Future Work

Based on the above conclusions, the future scope of the Tannic-iron complex and Guava-iron complex are as follows:

i. Application of the materials on other toxic ions like cadmium, lead, etc.

ii. The adsorption study in continuous mode can be carried out.

iii. The application and behavior of iron-polyphenol complexes in the presence of multi-pollutant can also be studied.

iv. The behavioral pattern of iron-polyphenol complexes in presence of UV-light can be examined.

v. Field application of materials in the growth of plants and effect on phyto-enzymes can also be carried out.

Research Outcomes

Research papers

1. J. Aktar, M. Ray, Iron-polyphenol nanomaterial removes fluoride and methylene blue dye from water and promotes plant growth, J. Environ. Chem. Eng. 10 (2022) 107707. https://doi.org/10.1016/j.jece.2022.107707.
2. J. Aktar, M. Ray, State of Iron in two Iron-plant polyphenol complexes: MALDI-Mass, EPR and volume susceptibility analysis, *Manuscript under preparation*.
3. J. Aktar, M. Ray, Adsorption of carcinogenic Bismarck Brown R dye from water using iron-plant polyphenol complex and assessment of the cytotoxic effect of dye, before and after adsorption, *Manuscript under preparation.*
4. J. Aktar, M. Ray, Removal of fluoride by iron-plant polyphenol metal complexes, *Manuscript under preparation*.

Book Chapter

J. Aktar, Batch adsorption process in water treatment, in: Intell. Environ. Data Monit. Pollut. Manag., Elsevier, 2021: pp. 1–24. https://doi.org/10.1016/b978-0-12-819671-7.00001-4. Academic Press.

List of Conferences

1. J. Aktar, (2016) Beneficial Conversion of Domestic Bio-waste. International conference, *Recycle-2016*, IIT Guwahati (Poster Presentation).
2. J. Aktar, (2017). Application of pond mud in chromium removal. Research conclave-2017, IIT Guwahati. (Poster Presentation).

3. J. Aktar, M. Ray, (2018). Formation of Iron based metal complex and its application in fluoride removal. I*nternational Conference on Frontiers in Chemical Sciences (FICS - 2018)* from 6- 8th Dec, IIT Guwahati (Poster Presentation).
4. J. Aktar, M. Ray, (2018). Green synthesis of Iron nanoparticles and its Characterization. International conference, *Recycle-2018*, IIT Guwahati (Poster Presentation).
5. J. Aktar, M. Ray, (2019). Formation of Iron based Metal Complex and Its Application. Research conclave, IIT Guwahati. (Poster Presentation).
6. J. Aktar, M. Ray, (2019). Efficient MB dye removal property of Iron(III) complexes of lant polyphenol and tannic acid in an insoluble powder form. International conference, *Modern trends in inorganic chemistry*, 11-14th Dec, 2019, IIT Guwahati (Poster Presentation).
7. J. Aktar, M. Ray, (2019). Synthesis of Iron-Polyphenol Metal complex and Its Application. National conference *CHEMCON 2019*, 15-19th Dec, 2019, IIT Delhi (Oral Presentation).
8. J. Aktar, M. Ray, S. Chakraborty, (2020). Efficient dye removal property of materials synthesized from plant polyphenols and iron in an insoluble powder form. National Conference *on Issues and Challenges in Water Treatment and Allied Research for Sustainable, Water-2020*, Centre for the Environment, IIT Guwahati, 23-25 Jan, 2020 (Poster Presentation).
9. J. Aktar, M. Ray, (2020). Efficient pollutants removal property of materials synthesized from plant polyphenols and iron, *DST-UKIERI supported WORKSHOP CUM SYMPOSIUM ON Bio-inspired Nanomaterials for Environmental Applications*, IIT Guwahati, 12 - 13 Feb, 2020 (Poster Presentation).

10. J. Aktar, M. Ray, S. Chakraborty, (2020). Usefulness of nanomaterials from plant extract and Iron as fluoride remover. *International conference, ICONN-2021*, Feb 01-03, 2021(Poster Presentation).

Awards

1. Department of Science and Technology (DST)-INSPIRE Fellowship, 2016, Government of India.
2. Best poster presentation in International conference, ICONN-2021, February 01-03, 2021.
3. Best poster presentation in DST-UKIERI supported WORKSHOP CUM SYMPOSIUM ON Bio-inspired Nanomaterials for Environmental Applications, IIT Guwahati, 12 - 13 February 2020.
4. 3rd position in poster presentation in National Conference on Issues and Challenges in Water Treatment and Allied Research for Sustainable Environment (Water 2020), IIT Guwahati, 23-25 January 2020.
5. Best poster presentation Recycle-2016, International conference, IIT Guwahati.